UNIVERSITY OF BIRMINGHAM

ADSORPTION SYSTEM FOR COOLING AND POWER GENERATION USING ADVANCED ADSORBENT MATERIALS

By

Fadhel Noraldeen Abed Al-Mousawi

A thesis submitted to the University of Birmingham for the Degree of Doctor of Philosophy

Department of Mechanical Engineering
School of Engineering
College of Engineering and Physical Sciences
The University of Birmingham
Edgbaston, Birmingham, UK

February- 2018

ABSTRACT

This thesis investigates the feasibility of producing electricity and cooling simultaneously utilising low-grade heat sources. This was studied through (i) incorporating an expander within the adsorption cooling system and (ii) integrating an Organic Rankine Cycle (ORC) with the water adsorption cooling system. Novel configurations and scenarios of adsorption system have been developed to enhance the adsorption cooling system performance so that it can produce cooling and electricity simultaneously. Such new configurations can help exploiting the available low-grade heat in developing countries to generate green cooling and electricity.

Advanced physical adsorbent materials have been investigated for the first time to generate cooling and electricity simultaneously utilising CPO-27(Ni), MIL101(Cr), and Aluminium-Fumarate Metal Organic Framework MOF materials and AQSOA-Z02 zeolite, and compared to commonly used Silica-gel. MOFs consist of metal ions coordinated to organic ligands which form crystalline materials with ultrahigh porosity and enormous surface areas and pore volume, while AQSOA-Z02 is a synthetic zeolite with a unique adsorption characteristics produced by Mitsubishi Chemical Company. Two innovative configurations of water adsorption systems for cooling and electricity were investigated in this study to compare their performances and offer more options for energy designers. In the first configuration, the two-bed basic adsorption cooling system (BACS) is improved by including an expander within the system so that it can generate electricity and cooling simultaneously (ASCE).

In the second configuration, the basic adsorption cooling system (BACS) and ORC cycle are integrated to produce cooling and electricity simultaneously (IAOSCE). Four different scenarios of systems integration based on the way of powering the ORC and the adsorption

system were investigated to find out the best way of combining adsorption cooling system with ORC. In the first three scenarios, the adsorption cooling system is used as a topping system while the ORC is used as a bottoming system. In scenario 1, an external heat source is used to drive the adsorption system while the ORC is powered using the cooling fluid leaving the adsorption system. This happens after recovering the heat rejected during the adsorption process. Scenario 2 is similar to scenario 1, but the ORC is driven by the heating fluid after leaving the adsorption system. In scenario 3, the recovered heat from the adsorption process mixes with the return heating fluid to produce new heat source that can be used to power the ORC. In scenario 4 ORC is set up as a topping system so that the heating fluid leaving the ORC is used to power the adsorption side. The IAOSCE can also include in addition to the ORC turbine a steam turbine in the adsorption side (similar to ASCE) so that the integrated system has two expanders which increases the electric power generated with similar four integration scenarios.

MATLAB Simulink software is used to simulate the different configurations/scenarios investigated in this study. Results show that generating cooling and power simultaneously is feasible where for the ASCE, the equivalent coefficient of performance COP increased from 0.7 to 0.8. Scenario 1 of IAOSCE shows higher equivalent COP of 1.27 compared to 0.7 and 0.8 of BACS and ASCE respectively, while scenario 2 shows higher equivalent specific cooling power than those of ASCE and BACS.

Also, detailed CFD simulations of small-scale radial inflow turbines are developed using the k-ω SST turbulence model provided by ANSYS CFX$^{@2018}$ for the cases of the ASCE (steam turbine) and the IAOSCE (ORC turbines). CFD results show that an efficient radial inflow turbine can be developed to meet the requirements of the ASCE configuration, also efficient ORC radial turbines can be designed to meet the requirement of the different scenarios of the

IAOSCE configuration. Also, based on the numerical modelling results, a novel experimental facility is developed to integrate ORC with two-bed adsorption cooling system to validate the numerical models and proof the concept of producing power as well as cooling, where maximum specific cooling power (SCP) of 252 W/kg_{ads} and specific power (SP) of 162 W/kg_{ads} are achieved. Experimental data showed good agreements with the numerical results with a maximum deviation of less than 17%.

To

The Soul of My lovely Mother

My beloved Father

ACKNOWLEDGEMENT

My thanks are extended to my Ph.D. supervisor Dr. Raya Al-Dadah for her guidance, encouragement, support, motivation and wide knowledge that cover all aspects of my project throughout my Ph.D. study.

Also, I am very grateful to Dr. Saad Mahmoud for his valuable suggestions and continuous support during my Ph.D. study.

I would like to thank Mr. Simon Rowan for his support in constructing my experimental facility and for his advice regarding the health and safety measures.

I would like to thank my fellow researchers and Ph.D. students for their cooperation and useful comments. In addition, I would like to thank the university staff in the main library and the post graduate administration office of the mechanical engineering department.

Many thanks to, my lovely big family, my father, brothers, sister for their support and inspiration. Many thanks to my lovely wife and children. You really encouraged and supported me along the way.

Finally, I thankfully acknowledge my sponsor, The Iraqi Government, for their financial support during my study. Also, I would like to thank the staff in the Iraqi cultural Attaché in London.

Fadhel Al-Mousawi
Birmingham February 2018

TABLE OF CONTENTS

LIST OF FIGURES

LIST OF TABLES

NOMENCLATURE

Symbols

A	Adsorption potential, (J/mole)
A	Area, (m^2)
C_p	Specific heat at constant pressure, (J/kg/K)
C_s	Spouting velocity (m/s)
COP	Coefficient of performance
COPe	Equivalent coefficient of performance
d	Diameter (m)
D_{so}	Pre-exponential constant
E	Exergy (W)
k_o	Empirical constant (1/s)
E_a	Activation energy, (J/kg)
f	Correction/friction coefficient's
F	Shape factor, factor equivalent to the typical COP of vapour compression refrigeration system
h	Enthalpy, (J/kg)
h_{fg}	Latent heat of evaporation (J/kg)
M	Mass, (kg)
l	Length, (m)
K	Losses coefficient
K_o	Pre-exponential constant
$\dot{m}$	Fluid mass flow rate, (kg/s)
P	Pressure, (Pa)
Q_{st}	Adsorption isosteric heat, (J/kg)
R	Adsorption/desorption time ratio
R_w	Water vapour gas constant, (J/kg/K)
r	Radius, (m)
U	Overall heat transfer coefficient, ($W/m^2/K$)

U_4	Inlet rotor velocity (m/s)
U_5	Outlet rotor velocity (m/s)
UA	Overall conductance (W/K)
SP	Specific power (W/kg_{ads})
SCP	Specific cooling power (W/kg_{ads})
SCPe	Equivalent specific cooling power (W/kg_{ads})
R_p	Particle radius (m)
T	Temperature, (K)
t	Time, (s)
W	Power (W), work (J/kg)
x	Water uptake, (kg/kg_{ads})
x_{eq}	Equilibrium water uptake, (kg/kg_{ads})
Z	Blades number

Greek letters

α	Absolute flow angle (degree)
β	Relative flow angle (degree)
η	Efficiency
ρ	Density kg/m^3
φ	Flag
ϕ	Flow coefficient
ψ	Loading coefficient
ω	Rotational speed (rad/s)

Subscripts

ads, a	adsorbent
ads	adsorption
amb	ambient temperature
bed	adsorbent bed
chill	chilled water
cond	condenser
des	desorption

eff	effective
evap, e	evaporator
exp	expander
ex	exergy
f	liquid
g	gas
hyd	hydraulic
in	inlet
j	Heating/cooling source
h	heat source
n	constant
o	outlet
s	saturation
w	water

Abbreviations

1D, 3D	One and three dimensional
ASCE	Adsorption system for cooling and electricity
Al	Aluminum
AC	Activated carbon
ATM	Automatic topology and meshing
BACS	Basic adsorption cooling system
CFD	Computational fluid dynamics
CCHP	Combined cooling heating power
CS	Cooling sink
DVS	Dynamic vapour sorption
GWP	Global warming potential
HASCE	Hybrid adsorption system for cooling and electricity
HS	Heat source
HFC	Hydrofluorocarbons
IAOSCE	Integrated adsorption-ORC system for cooling and electricity
LMTD	Logarithmic mean temperature difference

LPM	Liter per minute
KC	Kalina Cycle
MOF	Metal Organic Framework
RD	Regular density
RTD	Resistance temperature detector
SEM	Scanning electron microscope

LIST OF PUBLICATIONS

JOURNAL PAPERS

1) Al-Mousawi, F.N., R. Al-Dadah, and S. Mahmoud, Low-grade heat driven adsorption system for cooling and power generation using advanced adsorbent materials. Energy Conversion and Management, 2016. 126: p. 373-384.
2) Al-Mousawi, F.N., R. Al-Dadah, and S. Mahmoud, Low-grade heat driven adsorption system for cooling and power generation with small-scale radial inflow turbine. Applied Energy, 2016. 183: p. 1302-1316.
3) Al-Mousawi, F.N., R. Al-Dadah, and S. Mahmoud, Integrated adsorption-ORC system: Comparative study of four scenarios to generate cooling and power simultaneously. Applied Thermal Engineering, 2017. 114: p. 1038-1052.
4) Al-Mousawi, F.N., R. Al-Dadah, and S. Mahmoud, Novel system for cooling and electricity: Four different integrated adsorption-ORC configurations with two expanders. Energy Conversion and Management, 2017. 152: p. 72-87.
5) Al-Mousawi, F.N., R. Al-Dadah, and S. Mahmoud, Different bed configurations and time ratios: Performance analysis of low-grade heat driven adsorption system for cooling and electricity. Energy Conversion and Management, 2017. 148: p. 1028-1040.

CONFERENCE PAPERS

1) Al-Mousawi, R. Al-Dadah, and S. Mahmoud, "MIL101(Cr) MOF – Water Adsorption System for Cooling and Power Generation Using Waste Heat," SusTEM2015 Conference Proceedings, pp. 291–301, 2015.
2) Al-Mousawi, F.N., Raya Al-Dadah, and Saad Mahmoud, Novel adsorption system for cooling and power generation utilizing low-grade heat sources. Students on Applied Engineering (ISCAE), International Conference for. IEEE, 2016.
3) Al-Mousawi, F.N., Raya Al-Dadah, and Saad Mahmoud "Performance evaluation of multi-bed adsorption systems for cooling and power generation", HPC2016 Conference proceedings, June 2016.

CHAPTER ONE

INTRODUCTION

1.1 Background

For decades, fossil fuels have been the main energy source for various applications; however, the abundant low-grade heat resources like solar thermal energy, geothermal energy or waste heat can be converted into cooling and electricity using promising clean energy technologies like absorption, adsorption and Organic Rankine cycle (ORC). Such technologies can be used to reduce reliance on fossil fuels and associated CO_2 emissions thus alleviating the adverse impacts of global warming [1]. A notable example of the low-grade heat sources is the waste heat, where in the UK only the waste heat from industrial processes is ranging from 10 to 40 TWh [2]. Also, another useful example is the solar energy, where sun emits 3.8×10^{14} TW, out of which about 1.8×10^{5} TW reaches our planet [3]. However, millions of people who live in developing countries still lack access to secure electricity and the problem is worse in hot countries where large power capacities are required for building air conditioning. For example in Iraq as a hot climate country, there is a big gap between the electricity supply and demand as shown in Figure 1-1. ORC is one of the important technologies in this field that converts low-grade heat sources into useful power (electricity) using different types of heat sources including waste heat [4], and solar energy [5]. Although ORC systems are able to utilize a wide range of low-grade heat sources to generate electricity, it shows relatively low efficiency compared to other low-grade heat utilization technologies [6].

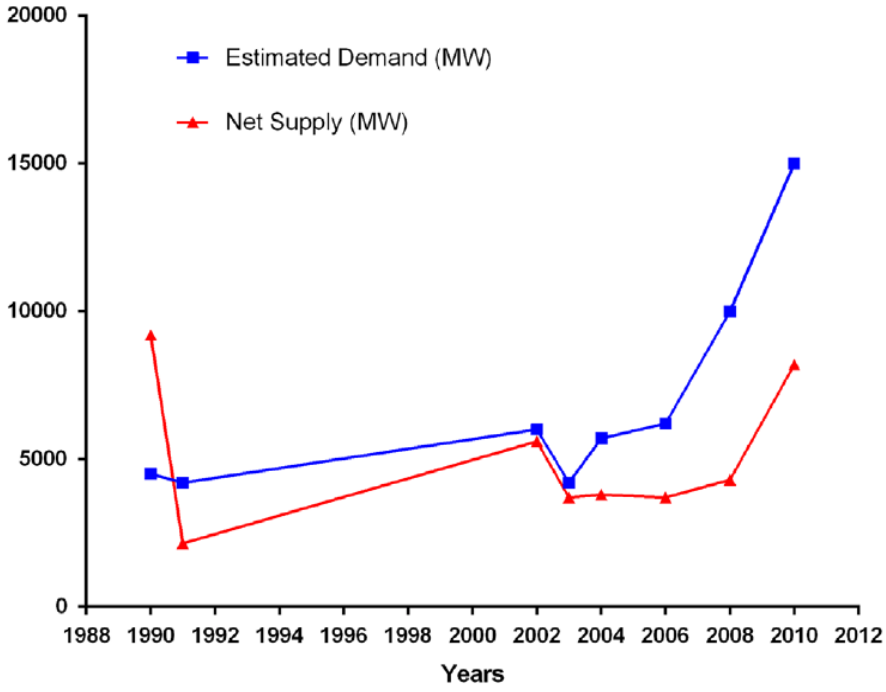

Figure 1-1: Electric power demand /supply in Iraq for the period between 1990 and 2010 [7]

Air conditioning systems generally consume a large amount of electricity especially in hot countries, so it would be more practical to convert the low grade-heat sources into cooling and electricity directly and simultaneously to enhance the overall efficiency of power systems and decrease losses in energy conversion. The production of cooling and electricity using absorption technology is investigated by a number of researchers [8-10], however, this technology has a number of disadvantages like the large size, ammonia risks, and corrosiveness of lithium bromide salt [11]. On the other hand, adsorption technology can utilise the large amount of low-grade heat sources to produce electricity and cooling simultaneously with the advantage of using a wide range of heat source temperature, and relatively long life compared to absorption systems [12]. Generating cooling and electricity using chemical adsorbent materials was investigated by several researchers [13-19], by incorporating an expander within the adsorption cooling cycle, however, this system showed a limited power output with the problem of ammonia risks and salts corrosiveness.

1.2 Aim and objectives

The aim of this Ph.D. research is to develop an adsorption system for cooling and power generation at the same time utilising low-grade heat sources and using advanced physical adsorbent materials [20]. The research aim is achieved through the following objectives:

1. Review published literature of absorption cooling systems, adsorption cooling systems, power generation cycles and heat driven systems for cooling and power generation including absorption and adsorption technologies. This helps to understand the background of these systems and highlight their advantages and disadvantages.
2. Investigate the feasibility of modifying the basic adsorption cooling system (BACS) to generate cooling and electricity at the same time utilizing low-grade heat sources by integrating an expander (turbine) between the hot bed (desorber) and the condenser. This can be achieved through thermodynamic modelling using MATLAB Simulink platform.
3. Investigate various possible scenarios of integrating adsorption cooling system with Organic Rankine Cycle (ORC) to produce cooling and electricity simultaneously. This can be achieved through thermodynamic modelling utilising a range of adsorbent materials, ORC working fluids and operating conditions using MATLAB Simulink [20].
4. Detailed 3D CFD modelling of small-scale radial inflow steam turbine to be incorporated in the adsorption system, and small-scale ORC turbines to be used in the ORC system integrated with adsorption system [20]. This analysis helps to evaluate the performance of the different turbines in terms of power and efficiency and find the suitable turbines that meet the requirement of the different cases.
5. Develop an experimental test rig to validate the simulation of the proposed adsorption system for cooling and electricity generation.

1.3 Research novelty and contribution

Using clean technologies like adsorption system to generate cooling and electricity simultaneously can reduce reliance on fossil fuels, and help to solve the problem of electricity shortage especially in developing countries. Figure 1-2 summarises the main technologies that use low-grade heat sources to produce cooling and electricity and highlights research areas where there is a knowledge gap. Particularly, no research works on using physical adsorption systems to produce cooling and power simultaneously was found. Also, limited research work on integrated physical adsorption systems with ORC to produce power and cooling simultaneously was found. Furthermore, advanced adsorbent materials like Metal Organic Framework MOF materials have not been used for producing electricity and cooling at the same time.

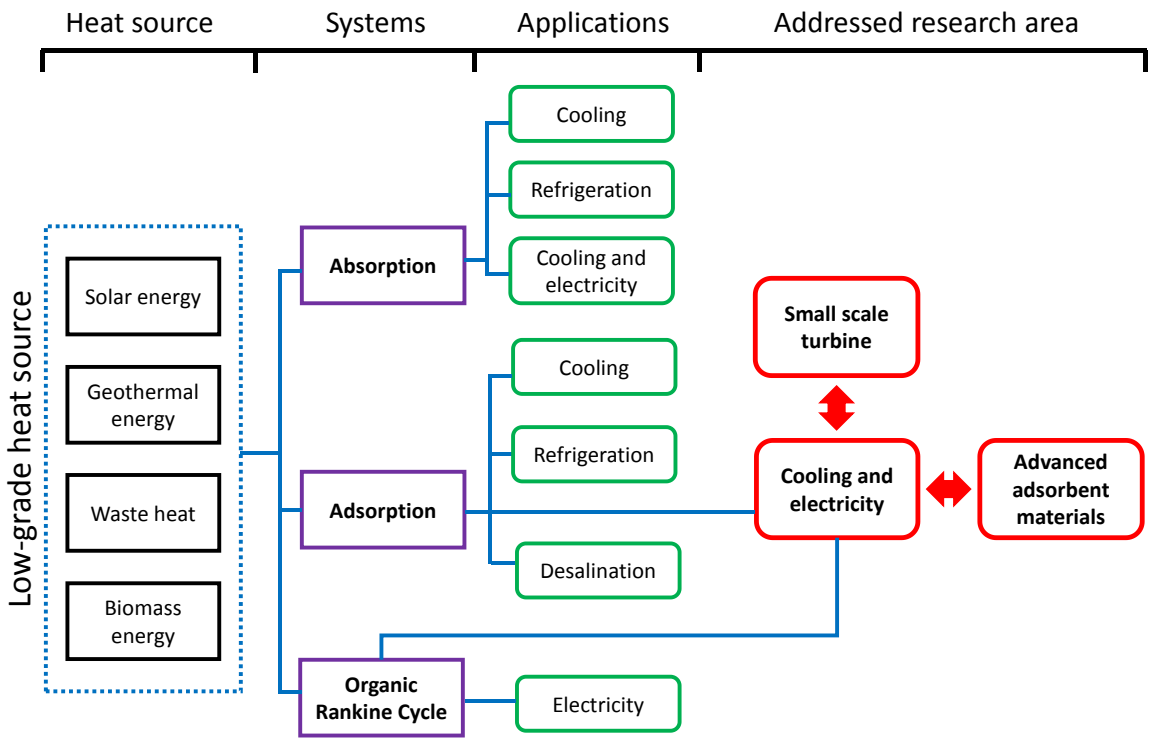

Figure 1-2: Cooling and power generation systems classification and the knowledge gap of this study

Two new adsorption system configurations to generate cooling and power simultaneously are investigated in this study as shown in Figure 1-3. Regarding the use of physical adsorption systems for cooling and electricity, the two-bed basic adsorption cooling system (BACS) is modified to generate electricity and cooling at the same time by integrating an expander (turbine) between the hot bed (desorber) and the condenser [20, 21]. This configuration can also utilise multiple bed arrangements like three, four, five or six beds. Also, a small-scale steam radial inflow turbine (RIT) is developed using detailed CFD modelling that work efficiently at the operating vacuum conditions of the adsorption system to generate electricity [20] as shown in configuration 1 in Figure 1-3.

Regarding integrating adsorption system with Organic Rankine Cycle to generate cooling and electricity simultaneously four different scenarios depending on the method of integration were investigated [20, 22]. Configuration 2 in Figure 1-3 shows two integrations concepts; one for integrating adsorption cooling system with ORC and the second one is for integrating adsorption cooling and power generation system with ORC where power can be produced from both the adsorption and ORC systems. Experimental testing of integrating adsorption system with ORC is carried out, which proved the feasibility of this technique with good agreement with modelling.

Regarding the use of advanced physical adsorbent materials AQSOA-Z02 zeolite, Metal Organic Framework MOF materials such as CPO-27(Ni), Al-Fumarate (Aluminium-Fumarate) and MIL101(Cr), are used and all the new adsorbent materials are compared to the frequently used Silica-gel [20]. Water is utilised as an adsorption refrigerant, while R245fa, R365mfc and R141b are investigated as ORC working fluids.

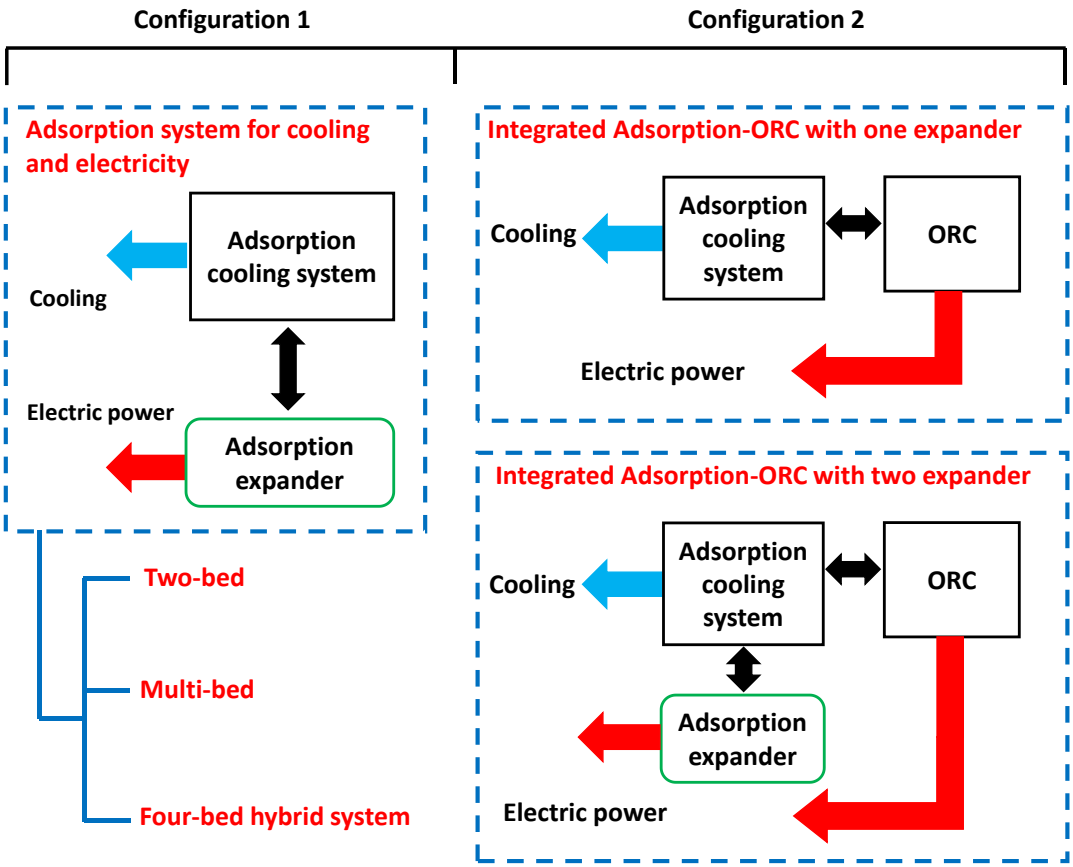

Figure 1-3: Main configurations and technologies used in this thesis to generate cooling and electricity

1.4 Thesis outline

This thesis consists of eight chapters, where chapter one introduces the main points of this thesis including research topic, research aim and objectives, research novelty and thesis outline furthermore, this chapter discusses the background of the research work.

Chapter two reviews the latest research work on adsorption systems that simultaneously generate cooling and electricity utilising low-grade heat sources such as industrial waste heat and solar thermal energy [20]. In addition, this chapter reviews the up to date literature of other technologies that generate cooling and electricity like absorption systems, and Organic

Rankine cycle (ORC). Also, this chapter assesses the newest literature work in the field of small-scale expanders and turbines used in power generation systems.

Chapter three defines the main properties of the different adsorbent materials used in this study, where the experimental data from the DVS (Dynamic Vapour Sorption) analyser is employed to investigate the water adsorption characteristics of AQSOA-Z02, and MIL101(Cr). For Al-Fumarate, CPO-27(Ni), and Silica-gel the adsorption characteristics are already available in the literature. Also, in this chapter, the experimental water uptake for all the studied adsorption materials are compared to each other.

In chapter four, mathematical models of water adsorption system for cooling and electricity (ASCE) are developed where, the two-bed BACS is improved to generate electricity and cooling at the same time by integrating an expander (turbine) between the hot bed (desorber) and the condenser [20, 21]. Also, the effect of using a number of advanced adsorbent materials such as CPO-27(Ni), MIL101(Cr), Al-Fumarate MOFs and AQSOA-Z02 zeolite on the overall system performance is studied and compared to that of Silica-gel. Also, this chapter studied the effect of using different bed arrangements either in series or in parallel beside the effect of adsorption and desorption times on the overall adsorption system performance. In addition, a hybrid adsorption system for cooling and electricity (HASCE) is developed which comprises of four adsorber beds, two evaporators, condenser and an expander (turbine) and results are compared in terms of using various system performance criterion like coefficient of performance (COP), specific cooling power (SCP), and specific power (SP) [20].

In chapter five, the two-bed BACS is integrated with an ORC system (IAOSCE) to simultaneously generate electricity and cooling utilising CPO-27(Ni)/water, AQSOA-ZO2/water, Al-Fumarate, and Silica-gel/water as adsorption pairs and R245fa, R365mfc and R141b as ORC working fluids. Four different scenarios of the integrated adsorption-ORC system have been simulated, where in the first three scenarios, an adsorption system is set up as a topping system, while ORC is set up as a bottoming system. The first scenario utilizes the waste heat of adsorption to power the ORC system with no additional heat. In the second scenario, the adsorption return heating fluid is used to power the ORC system, in the third scenario, the cooling and heating sources leaving the adsorption system are mixed, where the new heat source is generated to power the ORC system. In the fourth scenario, the ORC used as a topping system, while the adsorption system acted as a bottoming system and the return ORC heating fluid can be used to power the adsorption cycle. In addition, the second configuration can be presented in a novel method of integrating adsorption cooling system with ORC to simultaneously generate cooling and electricity. This can be carried out by incorporating a steam expander to the adsorption side so that the system has two expanders in order to increase the amount of electricity generated, while similar four scenarios are simulated using this configuration. Again results are compared in terms of COP, SCP, SP and adsorption power efficiency, ORC efficiency besides the system exergy efficiency.

In chapter six, detailed CFD modelling for three small-scale radial inflow turbines namely Steam, ORC1 and ORC2 have been established to meet the requirements of the main adsorption configurations adopted in this thesis including the adsorption system for cooling and electricity (ASCE) and the integrated adsorption-ORC system for cooling and electricity (IAOSCE). The baseline design is developed using VISTA RTD ANSYS$^{@2018}$, where the design is improved using the three dimensional CFD modelling utilising ANSYS$^{@2018}$ CFX.

Chapter seven describes the main components of the experimental facility of the integrated adsorption-ORC system for cooling and electricity. Two scenarios of integrating adsorption system with ORC cycle utilising CPO-27(Ni) as an adsorbent material and R245fa as an ORC working fluid have been investigated experimentally. This chapter includes the validations of the numerical models of the two-bed adsorption cooling system, the ORC cycle, and the integrated adsorption-ORC system (as one system) using the two proposed scenarios in terms of COP, SCP, SP, and ORC efficiency, against the experimental results for range of heat source temperatures [22]. Also, the effect of various operating parameters on the performance of the adsorption cooling system has been investigated experimentally. Chapter eight illustrates the key conclusions of this work and the recommendations.

CHAPTER TWO
LITERATURE REVIEW

2.1 Introduction

Mechanical vapour compression refrigeration systems consume a large amount of power (electricity), leading to fossil fuel consumption and CO_2 emissions. In addition, working fluids used in these systems usually including hydrofluorocarbons (HFCs) which have a negative impact on the environment [11]. Absorption and adsorption can produce cooling for different applications using the widespread low-grade heat sources like geothermal energy, industrial waste heat, and solar thermal energy [20]. Absorption cooling is based on the principle that absorbing a refrigerant like ammonia in an absorbent like water decreases the pressure of refrigerant vapour which allows more refrigerant to evaporate generating a cooling effect in the evaporator [23, 24]. The principle of adsorption cooling is similar to that of absorption but with the adsorbent being solid porous material that has high affinity for the refrigerant. Adsorption cooling systems are promising heat driven technology and this technology has a number of advantages, like its ability to use low-grade heat sources, utilizing environmentally friendly refrigerant such as water, they are quiet with less moving parts, no crystallization or corrosion problems and low maintenance [25, 26].

Furthermore, the performance of such systems is not affected considerably by the deviation of the heat source, which makes them good candidates for using solar energy [27]. This chapter reviews the latest work on absorption and adsorption cooling systems utilising low-grade heat source, also it reviews the thermal power cycles generating electricity by utilizing low-grade heat sources like Kalina and ORC cycles. However, the chapter focuses on published work regarding the absorption and adsorption systems that generate cooling and electricity simultaneously. In addition, it assesses the newest literature work on the small-scale expanders used in power generation cycles.

2.2 Low-grade heat sources

The abundant amount of the low-grade heat sources like solar thermal energy, geothermal energy and industrial waste heat can be converted into useful outputs like heating, cooling, and electricity using various clean technologies [20, 28]. Enormous amounts of the waste heat from the different industrial processes and power stations are discharged to the atmosphere [29]. For example, in the UK, the waste heat from the industrial processes is estimated to be about 40TWhr every year, which is enough for heating of about two million houses [30]. For geothermal energy, globally the electricity capacity is projected to increase to 16 GW in 2020 and deliver about 104 TWh [31]. For solar energy, the amount of solar energy generated from glazed or unglazed solar collectors is likely to increase significantly. Figure 2-1 shows the increase in the global solar thermal capacity and energy yield for the years between 2000 and 2015 [32].

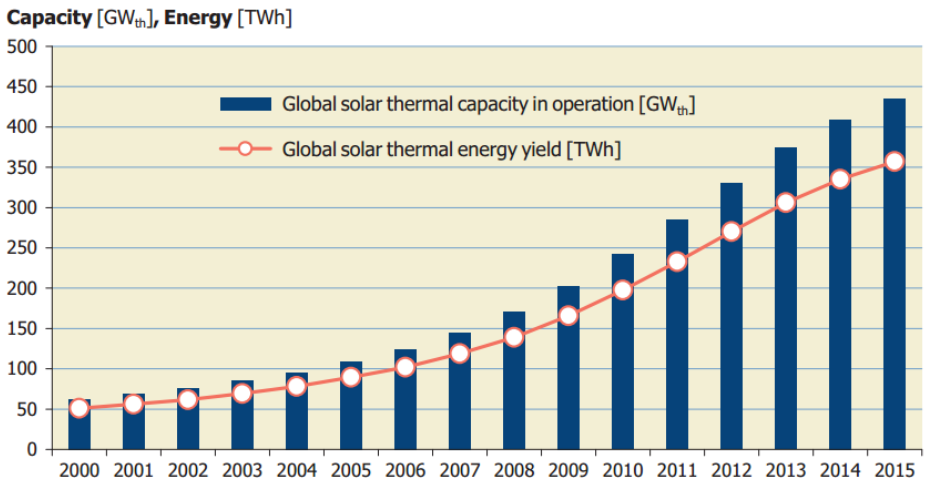

Figure 2-1: Global annual solar thermal capacity and energy yields for the period between 2000 and 2015 [32]

Many researchers developed several technologies that can convert such low-grade heat sources into heating, cooling, and electricity using absorption cooling cycle, adsorption cooling cycle, Organic Rankine cycle (ORC), and Kalina cycle (KC). Several definitions of the term low-grade heat source have been reported in the literature like that ranging between ambient temperature and 250 °C [2], however, in this thesis, this term covers the heat source temperature ranging between 80 and 160 °C.

2.3 Sorption cooling systems

Sorption phenomena can be classified into absorption and adsorption processes, where, in the absorption process, an absorbate fluid is dissolved by an absorbent which is usually a liquid so it is a bulk phenomenon [33]. In the adsorption process, the surface of an adsorbent which is usually solid such as Silica-gel has a strong affinity to the atoms that become in contact with it so the adsorption is a surface phenomenon. There are two types of adsorption; the first one is called physical adsorption which is controlled by physical forces called van der Waals forces. The second type of adsorption is the chemical adsorption, which is controlled by the

so-called covalent forces [34]. The absorption phenomenon is utilised in the absorption cooling technology by replacing the electrically driven mechanical compressor used in the traditional vapour compression cooling systems with a thermal compressor consisting of absorber, generator, and solution pump [35]. Although, many researchers reported a number of absorption working pairs lithium-bromide/water and ammonia/water are still the dominant working pairs that are used in absorption cooling systems [36]. Adsorption cooling systems depend on circulating an adsorbate (refrigerant) like water between adsorber bed, condenser, and evaporator and the working fluid can be cycled without any power consumption, because of the adsorption phenomenon [37]. To achieve a continuous and steady cooling output, two or more of adsorber beds are usually used.

2.3.1 Absorption cooling system

LiBr/water and ammonia/water are the most common absorption pairs used in the absorption cooling chillers. LiBr/water systems can be utilized for air conditioning of buildings and offices because it can generate effective cooling at a temperature higher than 0 °C, while ammonia/water systems can be used for refrigeration applications with cooling temperatures below the water freezing point [38]. Figure 2-2 illustrates a schematic diagram of a single effect absorption cooling system utilising LiBr/water. The system consists of generator, absorber, evaporator, condenser and pump, besides the precooler and the solution heat exchanger [39]. An external heat is added to the generator, while the precooler is used to reject the absorption heat. The absorber and evaporator are integrated into one component, and the cooling is generated in the evaporator [35, 39].

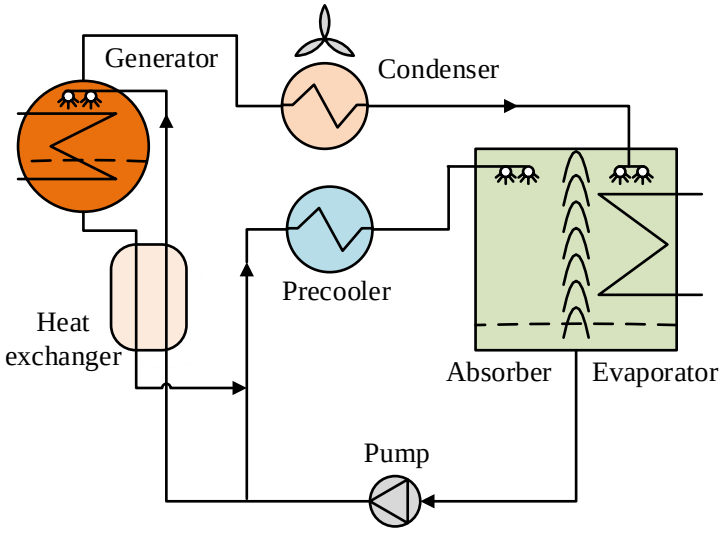

Figure 2-2: Single effect absorption system [39]

Yin et al. [40] investigated experimentally a small solar absorption chiller integrated with a ceiling cooling system, where the indoor thermal comfort index of the tested building is calculated. The system utilises driving temperature ranging between 74.8 and 89.1 °C, while the average temperature of the produced chilled water was 12.8 °C. Results showed that a cooling capacity of 4.6 kW was achieved during continuous 9 hours of working with an average COP of 0.31. Compared to that of fan coil units, the cooling capacity increased by 23.5%, also with using two cooling stages, the energy saving was 43.5%.

Bellos et al. [41] numerically examined a new absorption pair (LiCl/water) and compared results to LiBr/water commonly used in absorption cooling applications. The system consists of a set of flat plate collectors, storage tank, and absorption unit which generates 250 kW with a chilled temperature of 10 °C. The two pairs are studied using two different driving temperatures and three different values of ambient temperature. Results showed that LiCl/water achieved greater exergy efficiency and lower collector area by 8% for the same cooling capacity, and the best driving temperature for LiCl/water is lower.

Domínguez-Inzunza [42] experimentally evaluated the performance of an ammonia/lithium nitrate absorption chiller utilising driving temperature ranging from 80 to 100 °C and cooling temperature ranging from 20 to 34 °C. The chiller produced a maximum cooling output of 4.5 kW with chilled water temperature lower than 4 °C and COP values ranging from 0.3 to 0.62. Results also showed that as driving temperature increases the COP increases, while as cooling temperature decreases the COP increases. In addition, the study showed that the solution recirculation can enhance the system performance, particularly at high driving temperatures. Table 2-1 reviews a number of the published work on the absorption cooling system and it is noticed that this technology can work utilising driving temperature ranging between 50 to 200 °C with a maximum COP of 0.7 using ethylene glycol/water [43] and ammonia/lithium nitrate [44], however the double effect absorption chiller can show higher COP value of up to 2 [45].

Table 2-1: Absorption cooling systems [20]

Working pair	Driving temp. (°C)	Application	Evaporator temp. (°C)	COP	Ref.
Ammonia/water	100	Air conditioning	6	0.441	[46]
Ethylene glycol/water	88	Chilled water	7	0.7	[43]
Lithium bromide/water	100	Chilled water	3.6	0.69	[35]
Ammonia/water	140	Ice storage	-10	0.47	[47]
Lithium bromide/water	84.9	Chilled water	12.8	0.31	[40]
Ammonia/lithium nitrate/water	85-105	Chilled water	1	0.45-0.70	[44]
Ammonia/lithium nitrate	80-100	Chilled water	4	0.3-0.62	[42]
Lithium bromide/water	75-95	Air conditioning	10-15	0.6-0.68	[39]
Ammonia/water	120	Chilled water	2	0.61	[48]
Ammonia/water	200	Ice storage	-12-0	0.6	[49]
Lithium bromide/water	90	Air conditioning	7	0.37	[50]
Lithium bromide/water	50-90	Air conditioning	15-22	0.11-0.27	[51]

2.3.2 Adsorption cooling systems

Adsorption cooling systems can be driven using a range of heating temperatures from 50 to 500 °C without any serious problems like corrosion, while in absorption cooling systems, corrosion may occur with a heating temperature higher than 200°C [11]. Also, they can be good alternative to the conventional vapour compression systems, which consume large amount of electric energy, and this leads to more environmental problems.

2.3.2.1 Two-bed adsorption cooling system

Figure 2-3 illustrates a schematic diagram of a basic two-bed adsorption cooling system, which contains two adsorber beds (bed 1 and bed 2), condenser and evaporator [20]. The adsorber beds are packed with an adsorbent material like Silica-gel, and the system is charged with a working fluid like water. Figure 2-3 shows also that, bed 1 undergoes a heating process using an external heat source and this phase is called desorption process and during this phase, the valve V1 is open so that bed 1 is connected to the condenser and the high temperature and pressure fluid vapour generated through the desorption process enters the condenser. Meanwhile, bed 2 undergoes a cooling process and this phase is called adsorption process and during this process V4 is open and bed 2 is connected to the evaporator so that bed 2 adsorbs the vapour from the evaporator which allows further evaporation generating cooling effect [52]. In adsorption cooling systems, two adsorber beds are typically used and preheating and precooling processes are carried out in the switching phase where all valves are closed. Also, during this phase, the pressure of the desorber bed (hot bed) increases until reaching the condenser pressure, while the pressure of the adsorber bed (cold bed) decreases until reaching the evaporator pressure.

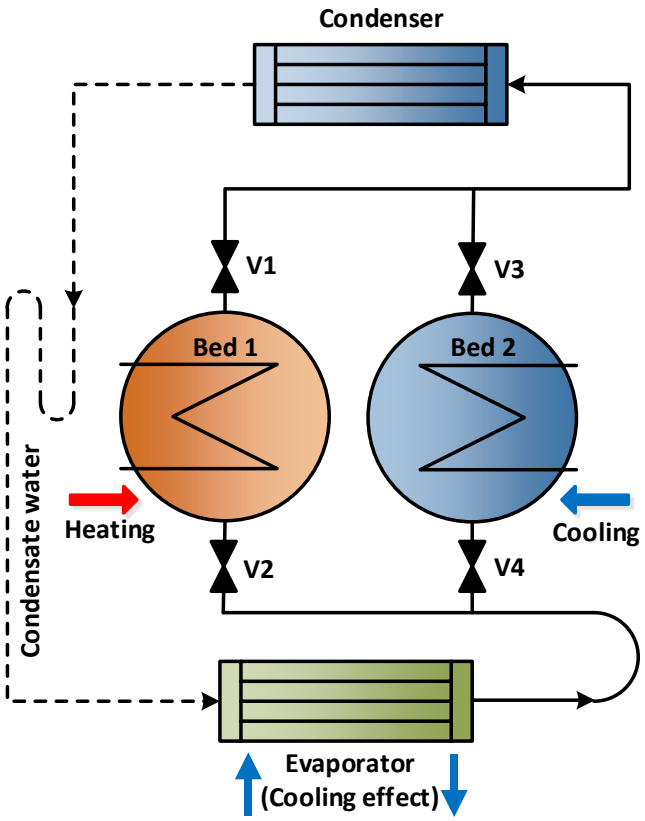

Figure 2-3: Basic adsorption cooling system [20, 52]

Tso et al. [53] studied the potential of improving the performance of adsorption cooling system driven by low-grade heat using activated carbon-based composite adsorbent material. The influence of driving temperature, cooling water temperature, evaporator temperature and adsorption and desorption time on the COP and SCP were investigated. It was found that COP of 0.65 and SCP of 380 W/kg_{ads} can be produced. Results also showed that the best half-cycle time was 360 s depending on COP and SCP optimization with a chilled water temperature of 9 °C. Results also showed that this composite material has better COP, SCP and evaporator outlet temperature than those of the traditional Silica-gel/water.

In typical two-bed adsorption cooling systems, adsorption time is equal to desorption time and this is called the half-cycle time. Many researchers studied the effect of using various adsorption and desorption times on the performance of various adsorption systems [54, 55]. Glaznev and Aristov [56] concluded that desorption is faster than adsorption by 2.2 to 3.5 times. Sapienza et al. [54] concluded that optimum performance can be obtained when the adsorption time is 7 times the desorption time. El-Sharkawy et al. [55] theoretically studied the effect of adsorption/desorption (ads/des) time ratios on the performance of a silica gel/water adsorption cooling system. Results showed that the system performance is enhanced when ads/des time ratio is less than one. Results also showed that utilising two-beds only with a half-cycle time of 350 s, switching time of 35 s and ads/des time ratio of 0.8, can generate continuous cooling with less fluctuation. Moreover, the study showed that maximum cooling of 14.63 kW can be achieved using half-cycle time ranging from 300 to 350 s.

2.3.2.2 Integrated adsorption cooling systems

Integrated adsorption cooling systems consist of two or three vacuum chambers, where two or three of the main components are integrated into one unit to produce more compact and reliable systems with no need for vacuum valves. Xia et al [57] built an innovative two-bed adsorption cooling system utilising Silica-gel/water. A condenser, evaporator and two adsorber beds have been integrated into one unit so that no vacuum valves were needed. The system consists mainly of three vacuum chambers including two adsorption beds with heat pipe as shown in Figure 2-4. It was found that the proposed system can produce COP and cooling output of 0.388 and 8.69 kW respectively with chilled water temperature of 11.9 °C utilising driving temperature and condenser cooling temperature of 82.5 °C and 30.4 °C respectively. Also, it was concluded that when the outlet chilled water temperature set to 16.5 °C the system can achieve COP and cooling capacity of 0.432 and 11 kW respectively. The

suggested experimental system can achieve an improvement in the COP of about 12% compared to that of the earlier adsorption cooling systems.

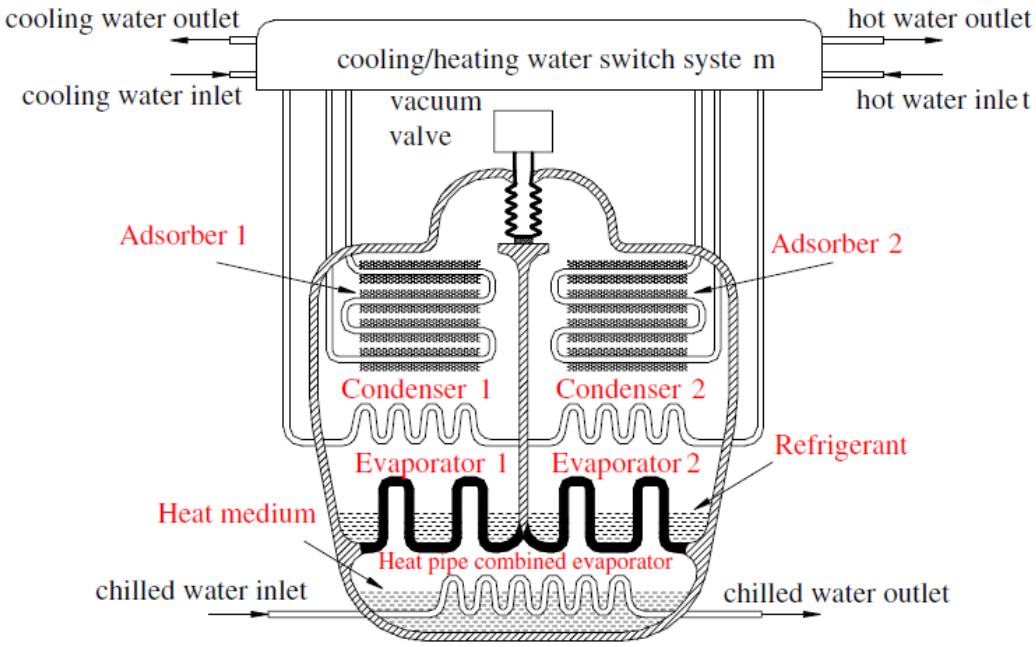

Figure 2-4: Improved adsorption cooling system adopted by reference [57]

He et al [58] studied the performance of a compact prototype adsorption cooling system for vehicles applications. The proposed chiller is designed to meet the vehicle requirements, especially the size where only 40 L volume is available to install the suggested chiller. The prototype consists of two adsorber beds, condenser and evaporator, besides four vapour valves to be used as alternative to the vacuum valves as shown in Figure 2-5. It was found that, the chiller can produce cooling output of about 1500 W utilising heating temperature of about 95 °C and adsorption cycle time of 3 minutes. Results also showed that, the system achieved a maximum cooling output of 436 W/kg_{ads} and COP of 0.31 using heat source temperature of 80 °C.

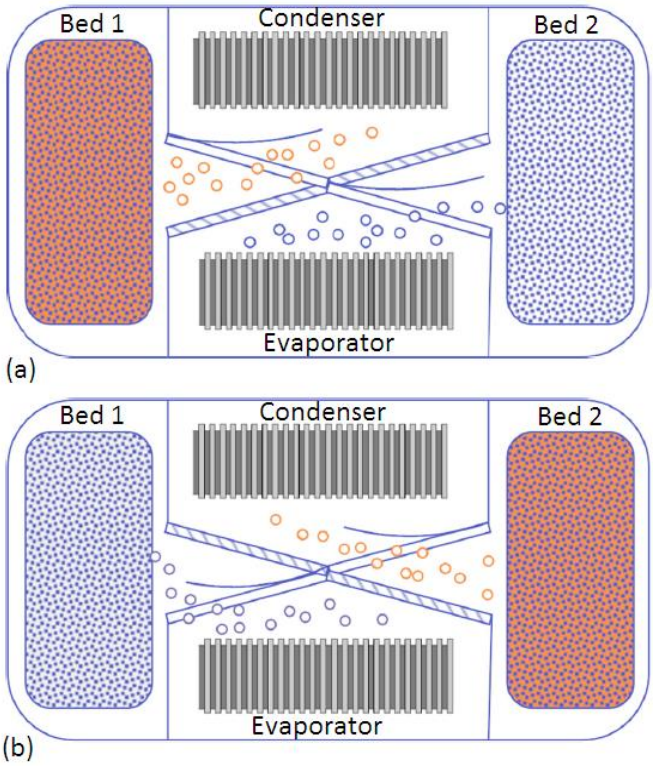

Figure 2-5: Compact adsorption chiller utilised by [58] (a) bed 1 in desorption process, (b) bed 2 in desorption process

2.3.2.3 Multi-bed and multi-stage adsorption cooling systems

Aiming to generate continuous cooling, the multi-bed adsorption cooling systems are used in many advanced adsorption systems. Also, multi-stage adsorption systems are another example of the advanced adsorption systems and the aim of using such systems is to utilize effectively the heat sources with low temperatures [59]. Chorowski and Pyrka [60] numerically and experimentally investigated the performance of a three-bed adsorption cooling system utilising Silica-gel/water at a heating temperature ranging between 45 and 70 °C. The numerical model was developed for 90 kW cooling capacity adsorption chiller with two cases of outlet chilled water temperature of 8 °C and 13 °C. A number of key parameters like adsorption and desorption rates, switching time, driving temperature, and cooling condenser temperature were studied. Maximum COP of 0.642 was achieved using switching time of 900

s, condenser cooling temperature of 25 °C, and driving temperature of 60 °C. Also, they reported that a maximum cooling capacity of 90.4 kW was achieved using switching time of 900 s, condenser cooling temperature of 25 °C, and heat source temperature of 64 °C [60].

Khan et al. [61] presented a new multi-stage Silica-gel/water, utilising six-bed adsorption system with reheat utilising driving temperature ranging from 50 to 70 °C and cooling temperature of 30 °C. It was concluded that cooling output and system COP with reheat can achieve higher values than those of the system without reheating process. In addition, the proposed chiller with reheating process can generate lower chilled water temperature compared to that without reheating in the case of using driving temperature higher than 52 °C. Moreover, the highest COP can be achieved with the cycle time ranging from 4000 to 4600 s and mass recovery time of 600 s, also the predicted results are validated with experimental data.

Farid et al [62] investigated a two-stage Silica-gel/water adsorption chiller with four beds utilising various mass ratios with re-heat scheme utilising heating temperature ranging from 50 °C to 90 °C, with cooling water temperature of 30 °C. It was concluded that using the two-stage adsorption system with re-heat and mass allocation of 3:2 topping/bottoming generate higher cooling than that of the two-stage system with re-heat and mass allocation of 1:1 topping/bottoming. Wang et al. [63] have proposed an enhanced lumped-parameter model to study the performance of a Silica-gel/water chiller with four beds. The model is validated against an experimental data where the model can predict the value of cooling capacity and COP with an accuracy of 10% and 12% respectively. Authors concluded that the improved model can effectively define the multi-bed adsorption system and offer useful data for designers and users. Table 2-2 summarizes a number of literature on the adsorption chillers including the driving temperature, minimum chilled temperature achieved by the system,

cooling capacity and maximum COP. A maximum COP of 0.64 can be achieved utilising Silica-gel/water at driving temperature of 60 °C.

Table 2-2: Adsorption cooling systems [20-22, 64, 65]

Working pair	Driving temp. (°C)	System description	Evaporator temp. (°C)	Max COP	Cooling capacity W/kg or kW*	Ref.
AQSOA-Z01/ AQSOA-Z02/ AQSOA-Z05 and water	55-90	2 bed chiller	14.8	0.42	350	[66]
AQSOA-Z02 /water	80	2 bed automobile compact chiller prototype	15	0.31	436	[58]
Silica gel/water	80	2 bed simulation using TRANSYS	15	0.467 - 0.491	8.46-10.3*	[67]
Silica gel/water	60	3 bed chiller with two evaporators	5/15	0.642	90*	[60]
Silica gel/water	40-95	4 bed 2 stage and 4 stage dual-mode chiller	14	0.2/0.45	2/5*	[68]
AQSOA-Z02/water Silica gel/water	90	3 beds chiller prototype with des-/adsorption allocation	18	0.35	4.4*	[69]
CPO-27(Ni)/water SAPO-34/water	90-170	2 bed automotive air conditioning	15	0.456	440	[70]
Zeolite FAM Z01/water	65-85	2 bed chiller	12 ± 2	0.44	12.13*	[71]
Maxsorb III/CO2	95	4 bed chiller	15	0.1	2*	[72]
Zeolite 13X-CaCl2/water	80	2 bed chiller	15	0.5	517	[73]
Maxsorb III/ R1234ze(E)	85	4 bed chiller	15	0.17	2.5*	[74]

2.4 Low-grade heat driven power generation cycles

Power generation is one of the main challenging issues that face our world today, where the fast increase in the global population which might reach 9 billion by 2050 and the continuous development of electrically powered systems may add more commitments for the governments and societies to secure this highly increasing power demand [75]. In addition, the negative impact of using more fossil fuel motivated researchers to develop more efficient and clean power generation technologies and energy resources [76]. Recently, generating electric power utilising low-grade heat sources, received significant interest, and many researchers suggested new system configurations to use low-grade heat sources to generate electricity like Organic Rankine Cycle (ORC) and Kalina Cycle (KC) [77].

2.4.1 Organic Rankine Cycle (ORC)

ORC is similar to the steam Rankine Cycle, but with the steam replaced by an organic refrigerant (hydrocarbon fluids) [78]. Figure 2-6 shows a simple Organic Rankine cycle which consists mainly of evaporator, condenser, turbine and pump. The superheated refrigerant generated in the evaporator expands through the turbine to produce a mechanical work, while the low-pressure fluid passes through the condenser then to a circulating pump to be pumped to the evaporator [79].

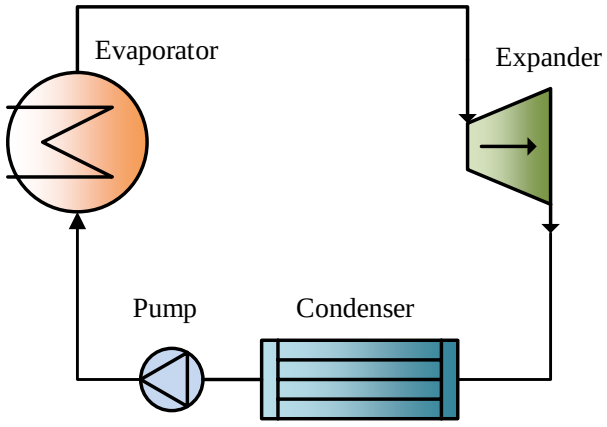

Figure 2-6: Basic Organic Rankine Cycle [79]

Usman et al [80] studied the part-load performance of water and air-cooled ORC utilising low to medium grade geothermal heat sources at different locations around the world. They compared R245fa with R1233zde in terms of thermo economic performance, environment-friendly and high system efficiency. Weather data of Ulsan, London, Vegas and Kuala Lumpur have been used to simulate the ambient temperature, while experimental validation and mathematical simulation were investigated for the condenser using wet cooling tower. They also optimized the ORC system for maximum power generation at different ambient (off-design) conditions. In addition, they made an economic analysis of the capital investment/kW and levelized cost of electricity (LCOE) during system lifespan. Results showed that R1233zde can outperform R245fa at driving temperature higher than 145 °C.

Le et al [81] used a number of low global warming potential fluids to optimize the performance of basic and regenerative supercritical organic Rankine cycles utilizing 150 °C pressurised hot water as a heating fluid. Maximum efficiencies of the basic and regenerative configurations were 11.6 % and 13.1 % respectively using R152a, while the maximum power generated was 4.1 kW using R1234ze. Depending on the ranking method and considering low Global Warming Potential (GWP) criterion, R152a and R32 were found to be the best refrigerants in terms of efficiency, while for the basic cycle R1234ze was the best in terms of power generation.

Xu et al. [82] tested a small-scale ORC system including the performance of a diaphragm pump, utilising R245fa, R123, R152a and R600a as working fluids under various operating conditions. The effect of volume flow rate, pressure difference and physical properties of refrigerants on the isentropic efficiency of the pump were investigated. Results showed that as the pressure difference and flow rate increase, the isentropic efficiency of the pump increases.

In addition, results showed that using R245fa, R123, R152a and R600a can achieve an isentropic efficiency between 57.22 to 93.51% where $\eta_{R245fa} > \eta_{R123} > \eta_{R600a} > \eta_{R152a}$. The ratio $\alpha/\rho Cp$ (the ratio of the thermal expansion coefficient to the density times specific heat) has shown a significant influence on the pump's isentropic efficiency, as the isentropic efficiency decreases when $\alpha/\rho Cp$ increases for the different fluids.

Ziviani et al. [83] developed an 11 kW industrial small-scale ORC system to be used as a test facility utilising R245fa and Solkatherm (SES36) as working fluids. The system consists mainly of a screw compressor used as an expander, centrifugal pump and three plate heat exchangers. The effect of the expander on the ORC performance at different operating conditions was investigated. The system performance achieved the maximum values using SES36 and the maximum expander efficiency when using R25fa was 17 % lower than that of SES36.

2.4.2 Kalina Cycle (KC)

Alexander I. Kalina proposed a novel power cycle that utilises low-grade heat sources using ammonia/water as a working fluid [84]. Many designs of Kalina cycle (KC) have been suggested in the literature utilising various heat sources [85]. Figure 2-7 illustrates a schematic diagram of a simple form of an ammonia/water KC which consists of a boiler, separator, two condensers, two pumps, two recuperators, throttle valve and a turbine [85]. The mixture of the ammonia/water expands through the turbine to generate mechanical power, while the first recuperator recovers heat from the fluid mixture leaving the turbine. The ammonia/water is split in the separator into strong and weak solutions, where the strong solution goes directly to the second condenser before being pumped to the boiler again [85].

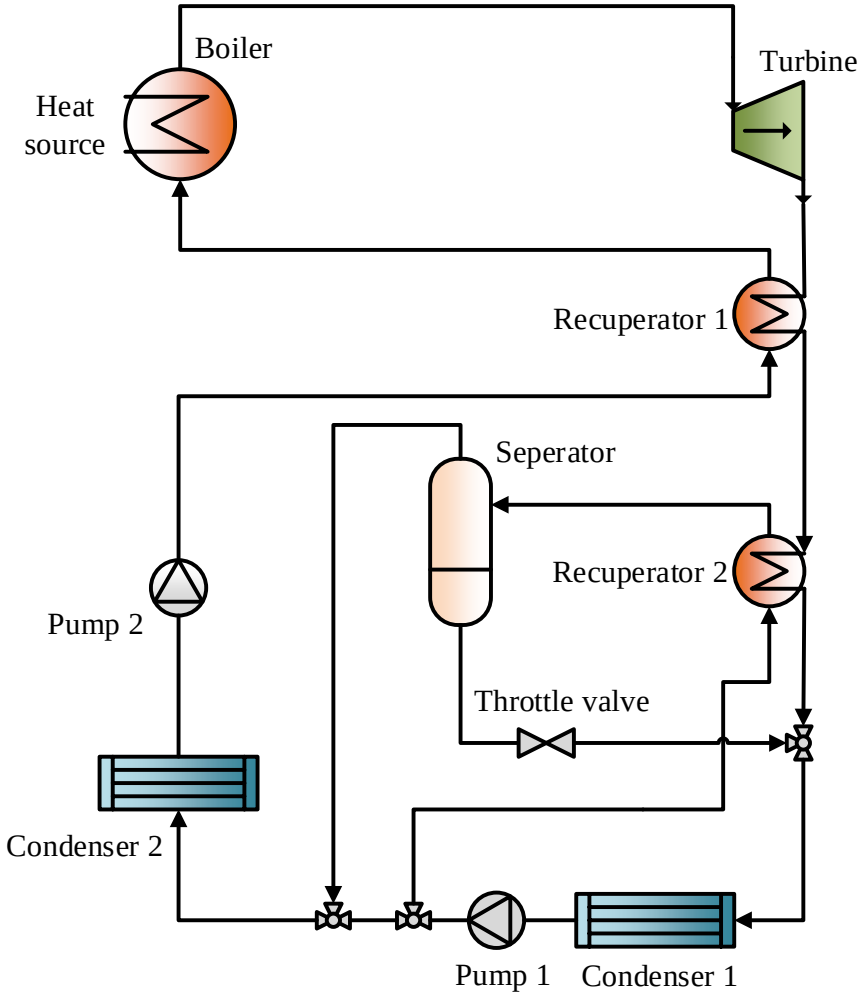

Figure 2-7: Kalina Cycle [85]

Wang and Yu [86] numerically studied and analysed a composition-adjustable KC system for geothermal applications under various climate conditions. The effect of the yearly ambient temperature variation on the KC performance is predicted using a numerical model. Results showed that the suggested KC can produce higher annual-average thermal efficiency compared to that of the system uses a fixed mixture composition. The study also concluded that, the economic feasibility of a composition-adjustable KC by balancing between cost and the efficiency enhancement.

Cao et al [87] presented a numerical investigation to explore the main thermodynamic parameters effects on the performance of a biomass KC. They also conducted a parametric optimization using genetic algorithm approach to highlight the optimum performance of the system with and without using a regenerative heater. It was found that maximum power output and cycle efficiency of 583.944 kW and 28.43% (with regeneration) can be achieved respectively. Results also showed that, as the inlet temperature or pressure increase, cycle efficiency and the power output increase.

2.4.3 Comparison of ORC and KC

ORC and KC are promising power generation cycles for producing electricity utilising low-grade heat sources. A number of researchers compared the performance of the ORC to the KC using various working fluids and operating conditions [88, 89]. Walraven et al [88] compared the performance of a number of ORC types with KC utilising geothermal heat source temperature ranging from 100 to 150 °C. Optimisation results showed that transcritical and multi-pressure subcritical ORCs outperformed the KC and they can achieve an exergy efficiency of more than 50%. Eller et al [89] compared between KC (version KCS-34) with zeotropic mixtures and ORC Cycle utilising heat source temperature ranging from 200 to 400 °C. Results showed that subcritical and supercritical ORCs with zeotropic mixtures can outperform KC and an exergy efficiency of 13% higher than that of KC can be achieved. Also, maximum exergy efficiency of 59.2% was obtained using supercritical ORC utilising benzene/toluene 36/64. The exergy efficiency of KC can be increased using alcohol/alcohol mixtures, however, it was still lower than those of subcritical and supercritical ORC with binary zeotropic mixtures.

2.4.4 Resorption power generation cycle

Resorption power generation cycle can employ a similar configuration of the pumpless ORC system which contains two vessels, one works as a desorber/adsorber bed, while the other works as an evaporator/condenser. An expander is located between the two vessels and valves are used to allow the refrigerant passing through the expander in the two-way direction as shown in Figure 2-8 [90].

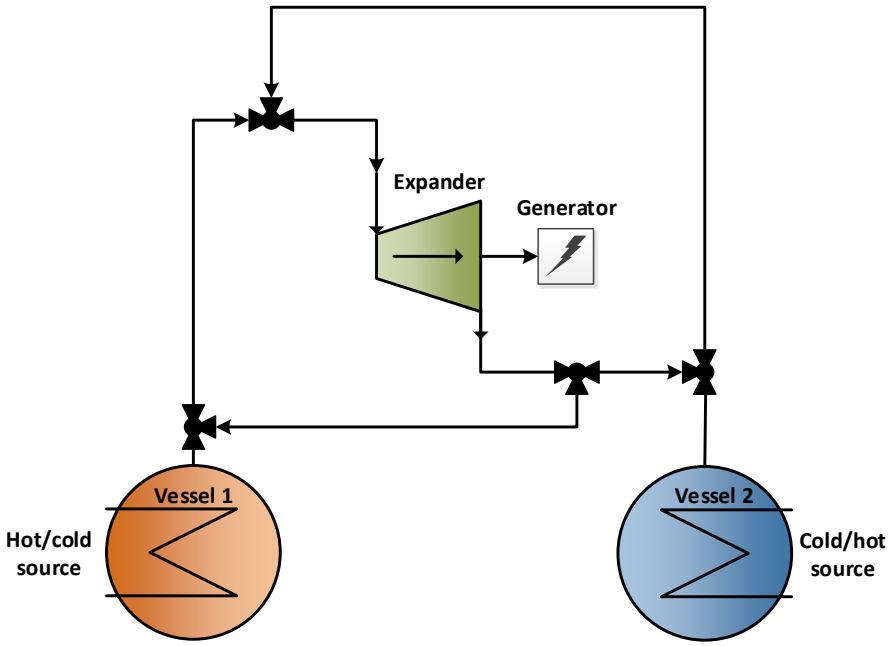

Figure 2-8: Resorption power generation cycle, and pumpless ORC system [90]

Bao et al [90] numerically analysed a resorption power generation cycle as shown in Figure 2-8 utilising heating fluid temperature ranging from 60 to 180 °C and using four metallic salts namely; manganese chloride, strontium chloride, barium chloride and sodium bromide. Performance criteria like efficiency, energy density and power capacity are compared to that of the pumpless ORC system (which has a similar arrangement of the resorption power generation system) using pentane, R123 and R245fa under the same driving temperature range. Results showed that pumpless ORC can achieve higher thermal efficiency,

while resorption power generation system can generate higher energy density which is almost twice the amount generated by the pumpless ORC.

Bao et al [91] also studied a new resorption power generation system with reheating scheme utilising driving temperature ranging from 70 to 200 °C. The system consists of two sorbent beds namely low temperature salt (LTS) and high temperature salt (HTS), and an expander which is placed between the HTS sorbent bed and the LTS sorbent bed. In the first half cycle, heat is added to generate the ammonia vapour from HTS bed which then expands through the expander to generate electric power as shown Figure 2-9 (a). In the second half cycle, the heat is added to the LTS bed and the ammonia vapour is directed again through the expander as shown Figure 2-9 (b). Three different salts, including $MnCl_2$, $SrCl_2$ and NaBr were investigated while ammonia was used as a refrigerant. The reheating process can increase the power generated by 10–600%, while the thermal efficiency can be enhanced by 1.4 to 4.5 times while the exergy efficiency can be improved by up to 2.0–8.3 times.

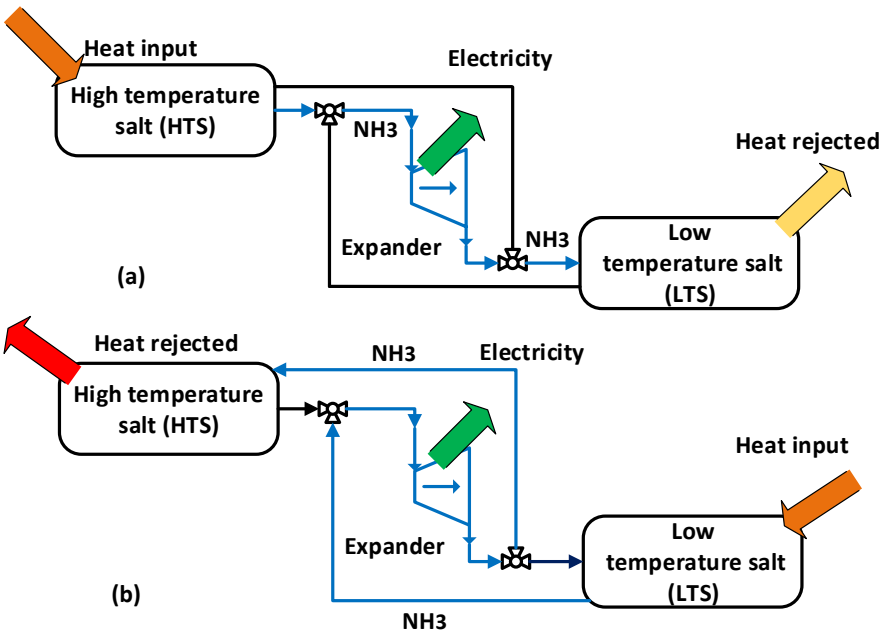

Figure 2-9: Basic resorption power generation cycle reported by [91]

Also Bao et al. [92] proposed an innovative multi-stage resorption power generation cycle that utilises multi expanders as shown in Figure 2-10. Each expansion process is combined with a re-heater to prevent the ammonia getting wet and produce the maximum amount of work output. Three resorption salt pairs were used namely; NaBr-$MnCl_2$, NaBr-$SrCl_2$, and $SrCl_2$-MnCl2 with ammonia. Results showed that work output of 100-600 kJ/kg can be achieved using NaBr-$MnCl_2$ and NaBr-$SrCl_2$ and utilising driving temperature ranging from 30 to 150 °C.

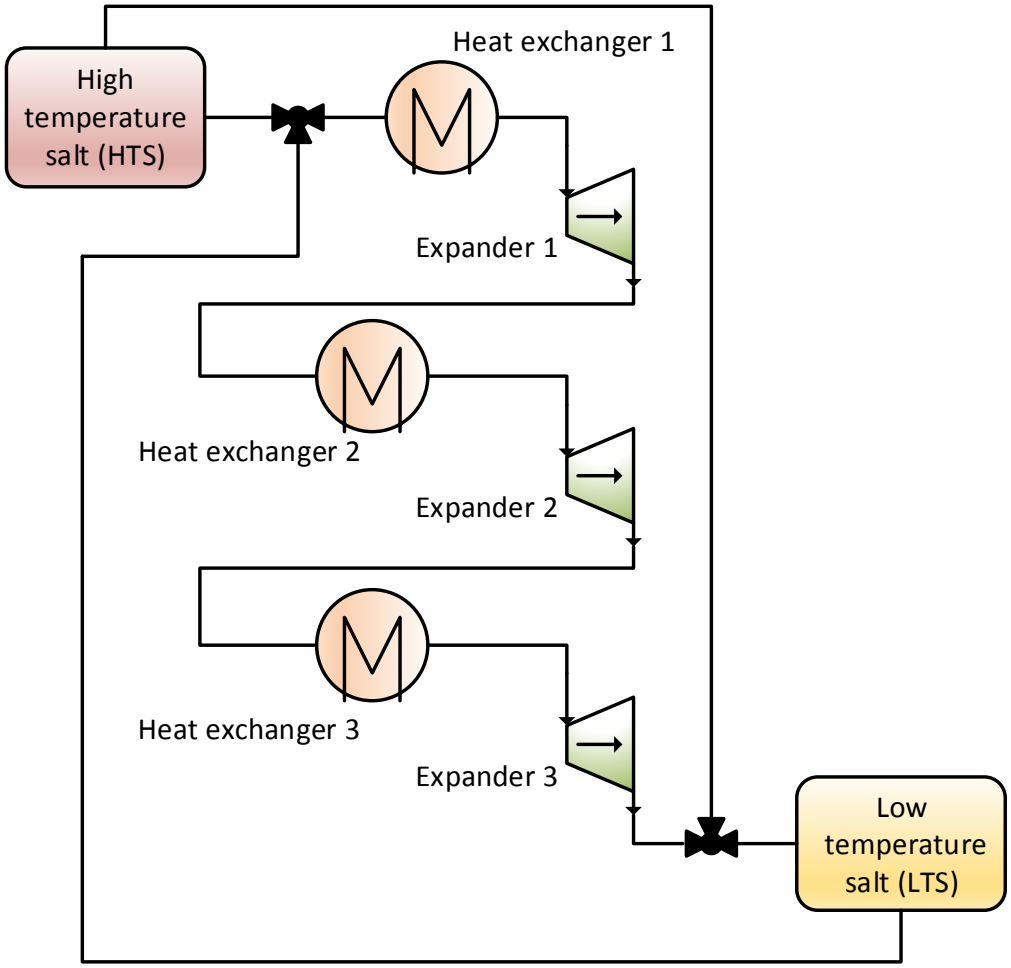

Figure 2-10: Multi-stage resorption power generation system [92]

Lu et al. [93] proposed an innovative chemisorption power generation system utilising two heat sources. The cycle consists mainly of two scroll expanders, four cascading resorption

beds and valves. Nine Metal Chlorides salts and ammonia were examined in this investigation to find the appropriate operating conditions for this system. Results showed that, $SrCl_2$ is the best salt in terms of the thermal efficiency that can be used in the LTS with an efficiency of up to 11%, while $MnCl_2$-$SrCl_2$ is suitable for HTS with the first heating fluid temperature ranging from 200 to 250°C, and for the second heating fluid temperature of 100 °C with an overall efficiency of about 10%. Results also showed that the topping cycle can generate an average electric power of 300 W within 30 minutes time with driving temperature of 220 °C, while the bottoming cycle can generate an average electric power of 500 W within 22.5 minutes time and utilising driving temperature of 160 °C.

Dutta et al. [29] suggested replacing the compressor of the Brayton Cycle, with a sorption thermal compression process using four adsorber beds to increase the fluid pressure from the minimum cycle pressure to the maximum cycle pressure. The proposed system was powered by low-grade heat source and utilised activated carbon as adsorbent and R507a, R134a, R410a, propane, R32, and CO_2 as working fluids. Results showed that, maximum thermal efficiency of 8% can be achieved and that the system performance using R32 can exceed that of the CO_2 and R410a.

Table 2-3 summarizes the literature review on the latest technologies and advanced working fluids used to generate electricity utlising low and medium grade heat sources. Three main cycles are included in this table namely Kalina Cycle (KC), Organic Rankine Cycle (ORC), and resorption power generation cycle (RPG). A maximum thermal efficiency of about 32% is achieved with ORC using toluene and heating temperature ranging from 150 to 400 °C, while a maximum thermal efficiency of about 31% is achieved using Kalina cycle utlisnig ammonia/water and heating fluid temperature of 500 °C.

Table 2-3: Power generation cycles utilising a number of different technologies [20-22, 64, 65]

System type	Working fluid	Driving temp. ^{o}C	System performance	Ref.
A two-parallel-step ORC for ICE waste heat	R-123, R-134a, and water	470	R-123 is the best fluid. Output power of 468 kW and exergy efficiency of 21%.	[94]
Basic ORC combined with a naval ship	7 different ORC fluids	150-400	Toluene is the best fluid. Electric power output of 92 kW. Efficiency of up to 32% with toluene.	[95]
Basic ORC	R-1234ze(E), R-600a, R-236fa and R-245fa	135	Maximum thermal efficiency of 10.5% and net power of 1kW.	[96]
Partial evaporating ORC (PEORC)	R245fa/R227ea mixture	120	PEORC generate 24.7% more power than the traditional subcritical ORC using R227ea. Power output of 6.19 kw and efficiency of 7.40%.	[97]
Basic ORC	R245fa	100	Maximum electrical power and thermal efficiency are 1.89 kW and 5.92%.	[98]
Basic ORC with heat exchanger	12 different ORC fluids	50–140	Output power of 100 kW and thermal efficiency of about 19% using neo-pentane.	[99]
Kalina cycle	Ammonia/water	116–128	Maximum power output of 1573.5 kW with the corresponding thermal efficiency of 9.94%.	[100]
Kalina cycle	Ammonia/water	150-300	Thermal efficiency, recovery efficiency and exergy efficiency of 21.6%, 18.32% and 48.32% respectively.	[101]
Different Kalina cycle layouts including KC12, KC123, KC234 and KC1234	Ammonia/water	500	Output design power of 20 MW. KC1234 gave the highest cycle efficiency of 31.47 %. KC123 had the second maximum efficiency of 31.46 %. KC234 had the lowest efficiency of 27.35 %.	[102]
A solar-driven Kalina cycle	Ammonia/water	98-108	Net power output of 10.94 kW. Thermal efficiency was 7.55% and the optimized modified system efficiency was 8.54%.	[103]
Kalina cycle (KCS-34) and supercritical ORC	Alcohol/alcohol mixtures	200-400	Maximum exergy efficiency of 55.8% achieved using methanol/heptanol 60/40. A maximum exergy efficiency of 59.2% achieved for supercritical ORC using benzene/toluene 36.	[89]

Non-regenerative ORC	R12, HCFC-123, HFC-134a, and R717	277	Maximum thermal efficiency of about 25% and output power of about 2000 kW using R123.	[104]
Pumpless organic Rankine /resorption power generation	Manganese chloride, strontium chloride, barium chloride and sodium bromide/ammonia and pentane, R123 and R245fa for ORC	60-180	Maximum thermal efficiency of about 25% for pumpless ORC using Pentane. Maximum thermal efficiency of about 17% for resorption power generation cycle using $MnCl_2$- $MnCl_2$/ammonia.	[90]
Advanced absorption power generation (APG) double-effect, half-effect and one ejector-combined APG cycles based on Kalina KCS-11	Ammonia/water	70-140	Maximum energy and exergy efficiencies were 9%–14% and 65%–72% using driving temperature of 70–100 °C. Double-effect APG cycle could improve the energy and exergy efficiencies by 3.6–12.6%, 10.7–28.2% and 19–900% using driving temperature of 100,120, and 140 °C, however power was 43–63% lower.	[6]
Multi-stage expansion chemisorption power generation	Ammonia/$MnCl_2$, $SrCl_2$, and NaBr	30–150	$SrCl_2$-$MnCl_2$ can generate output work of 550 kJ/kg using driving temperature of 150 °C. Energy efficiency of 6% -15% using 2–4 expansions and driving temperature between 80-150 °C.	[92]

2.5 Absorption systems for cooling and electricity

Many researchers investigated the potential of producing electricity and cooling simultaneously using the absorption technology. A number of thermodynamic cycles with binary fluids mixtures were suggested in the literature and one of these well-known cycles is Goswami cycle which is an integration of an ammonia/water absorption cooling system and an ammonia organic Rankine cycle [105]. Other studies combined absorption cooling system with Kalina cycle, to produce cooling and electricity at the same time. Liu, and Zhang [106]

proposed a new absorption system for cooling and electricity utilising low-grade heat as shown in Figure 2-11.

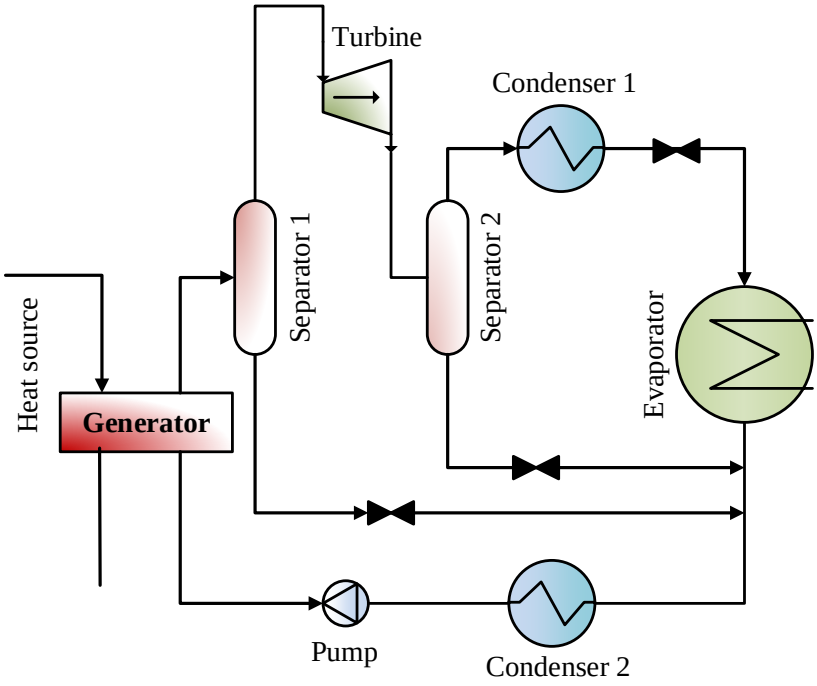

Figure 2-11: Ammonia/water absorption system for cooling and electricity [106]

The new system integrates an ammonia/water absorption cooling system and Kalina cycle and the system consists mainly of generator, turbine, evaporator, pump, two separators and two condensers. The ammonia/water is pumped to the generator pressure, while the vaporised mixture produced from the generator is separated in the first separation process into weak and strong mixtures. The strong mixture passes through a turbine to produce power, and after another separation process, the rich mixture is delivered to the first condenser to generate the liquid ammonia required to achieve cooling in the evaporator. Another condenser is used to condense the mixture of the weak solution while ammonia vapour leaving the condenser is pumped again to the generator.

Muye et al. [107] modelled and studied the annual performance of an ammonia/water absorption system for cooling and electricity. Solar thermal energy is used to power the

system as the main heat source while biomass energy is used as an auxiliary heat source and the study includes Seville in Spain and Chennai in India. A scroll expander is used for the power generation which is located between the super heater and the condenser. Also, the effects of using various driving temperatures, cooling temperatures, and evaporator temperatures on the system performance were studied. It was concluded that the annual system efficiency varied between 6 to 8% and the annual solar contribution achieved values ranging from 23% to 30%, depending on the location and the designed evaporator temperature, while the annual expander efficiency achieved was ranging from 59% to 63% [107].

Mohammadi et al. [108] suggested a hybrid combined system for heating, cooling, and power generation for domestic applications. This system comprises mainly of a gas turbine, an ORC system, and an absorption chiller. A numerical study was carried out to examine the effect of various factors on the performance, power generation, heating capacity and cooling capacity. Results showed that the system can achieve an overall efficiency of 67.6% and generate 30 kW of power, 8 kW of cooling and COP of 0.6196. The parametric investigation showed that the turbine inlet temperature has an important impact on the electric power generated and the overall system efficiency. Liu and Zhang [8] have suggested a cogeneration of ammonia/water Rankine cycle and an absorption cooling system utilizing a driving temperature of around 450 °C to generate cooling and electricity simultaneously. Splitting of absorption unit was used to keep the desired levels of ammonia concentration in the different processes of the cycle. It was concluded that maximum exergy efficiency of 58% can be achieved and that the suggested system can reduce the power consumption by 18.2% compared to traditional cooling and power generation systems that are working individually.

Zhang and Lior [10] investigated an ammonia/water cogeneration system to generate cooling and electricity simultaneously. Energy and exergy efficiencies were evaluated with the values

of 27.7% and 55.7%, respectively achieved using driving temperature of 450 °C. They also studied the main parameters that can affect the cycle performance. Results showed that the cogeneration system has higher energy and exergy efficiencies compared to that of the generation of cooling and electricity separately for the same capacities. Table 2-4 summarises the literature work on the absorption system for cooling and electricity utilising a number of different configurations which depend mainly on Kalina Cycle, absorption cooling system, and ORC. A maximum thermal efficiency of 35-45% can be achieved in [109] using heat source temperature ranging between 120 to 160 °C. Also, a maximum exergy efficiency of 72% can be noticed in [110] utilising heat source temperature of 90-170 °C.

Table 2-4: Absorption system for cooling and electricity [20-22, 64, 65]

System type	Driving temp. ˚C	Evaporator temp. ˚C	System performance	Ref.
Absorption refrigeration cycle and Kalina extraction turbine cycle	133	8	For cooling only, cooling of 34.26 kW and COP of 0.57. For combined generation, cooling of 15.26 kW and power of 2.21 kW. Effective first-law and exergy efficiencies were 13% and 48%	[111]
Integration of absorption refrigeration cycle and Kalina cycle	200	15	Net power output of 35.88, kW, net refrigeration output of 75.12 kW. Thermal efficiency of 13.72% and exergy efficiency of 5.40%.	[106]
Absorption combined Power/Cooling cycle based on Kalina cycle	350	-10	Thermal and exergy efficiencies of 24.2% and 37.3%. Power of 774.7 kW and refrigeration of 298.8 kW.	[9]
Novel integrated ammonia/water Rankine cycle and an ammonia refrigeration cycle	450	-15	Reduction in energy consumption by 18.2%. Power of 737.3 kW and refrigeration of 203.8 kW. Exergy efficiency of 57.6%.	[8]
Novel combined cooling and power cycle	170	0	Net power output of 1379 kW, cooling output of 1736 kW, first-law efficiency 43.25%,	[112]

(based on Kalina cycle)			second-law efficiency of 22.51%.	
Combined ammonia refrigeration system and ammonia/water Rankine cycle	450	-25	Thermal efficiency and exergy efficiency of 27.7%, and 55.7%. Power of 733.4 kW and refrigeration of 241.9 kW.	[10]
Combined Rankine power and absorption cooling cycles	257-347	-15 to -5	Net power output of 614.3 kW, net refrigeration output of 839.8 kW. Heat efficiency of 20.35 and exergy efficiency of 35.68%.	[113]
Combined Rankine power and absorption cooling cycles	90-170	20	Effective first-law and exergy efficiencies were 20% and 72%.	[110]
A combination of a gas turbine, ammonia/water turbine and LiBr-H_2O absorption refrigerator	80/150	4	Power output of 2575 kW, Cooling output of 2902 kW, and heating output of 730 kw. Energy saving ratio of 31.70% and exergy efficiency of 37.89%.	[114]
An ammonia-water combined power and cooling system	90/500	-15	Equivalent heat-to-power efficiency of 19.76%. Refrigeration output of 225.72 kW and net power output of 14.76 kW. Exergy efficiency of 33.69%.	[115]
GAX (generator absorber heat exchange) based combined power and absorption cooling system	120-160	-10 to 10	Overall thermal efficiency of 35-45% and COP of 0.35. Power output and cooling capacity were 225 kW and 80 kW at evaporator temperature of 0 C.	[109]
Two systems, Kalina power-cooling cycle (KPCC) using ammonia/water, and Kalina lithium bromide absorption chiller cycle (KLACC)	370	-	Kalina Cycle generated 1722 kW power with thermal efficiency of 16.1%. KLACC and KPCC generated 277 and 393 kW cooling besides 1550 and 1722 kW power. KPCC and KLACC had a thermal efficiency of 15.2 and 16.9% and power-cooling efficiency of 18.8 and 20.2%	[116]

2.6 Adsorption systems for cooling and electricity

Integrating electricity generation with adsorption cooling system using low-grade heat sources has the advantage of the dual power and cooling generation simultaneously and increasing the overall system performance [15, 16]. Figure 2-12 shows a resorption cogeneration system (resorption system is an adoption system but without condenser or evaporator [14]) for cooling and electricity that developed by [13], the system consists of two adsorbent beds, super heater, precooler and a turbine. The turbine is placed between the HTS sorbent bed and the LTS sorbent bed to produce electricity. The proposed system works in two phases; during the first phase superheated ammonia is generated and expands through the turbine generating electric power. In the second phase, cooling is generated due to decomposition heat and the internal energy difference of ammoniate LTS in bed 2 as shown in Figure 2-12. The proposed cycle archives an electricity generation exergy efficiency of up to 69% and cooling COP of up to 0.77. Results also showed utilising heat source temperature greater than 100 °C can produce maximum overall exergy efficiency of 90% and COP of 0.77 and when heat source temperature of 200 °C is used, electric power and cooling of 1.42 kW and 5-6 kW can be obtained utilizing 10 kW of heat [13].

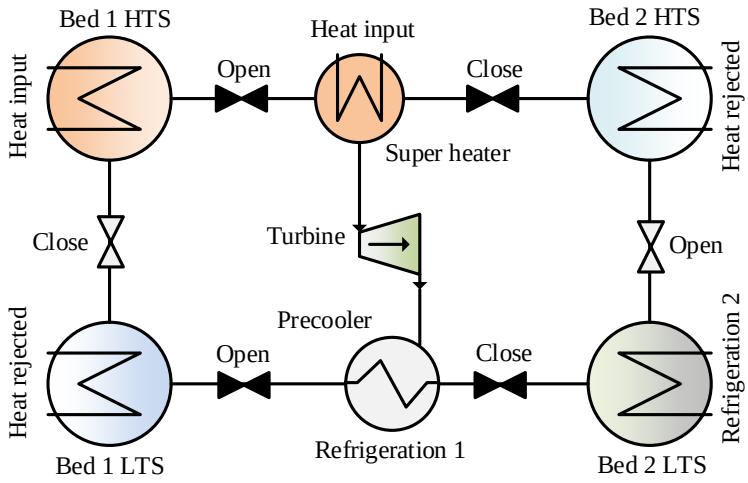

Figure 2-12: Resorption cogeneration system for cooling and electricity [13]

Jiang et al [14] have presented a resorption cogeneration system for cooling and electricity with similar electrical efficiency and considerably higher cooling performance than Goswami cycle. The cycle comprises of two adsorber beds, precooler, super heater and an expander. Results showed that the cycle has efficiency and COP of 7.2–12.6% and 0.33–0.53 respectively, without heat recovery, while when using heat recovery it has thermal efficiency and COP of 9.5–15.8% and 0.416–0.691 respectively. A maximum exergy efficiency of 82% was achieved, which is 50% higher compared to Goswami cycle. Results also showed that the proposed system can outperform the Rankine cycle and the Goswami cycle in terms of the exergy efficiency.

Bao et al. [16] introduced a new adsorption system for cooling and electricity by integrating a scroll expander with a chemisorption cooling system. Experimental facility of such system utilising chemical adsorbents has been built using $CaCl_2$/activated carbon and ammonia with a scroll expander. The system consists of two adsorption units, two evaporators, two condensers and an expander. An external heat source is used to power the adsorber bed which generates high temperature and pressure flow of ammonia that expands through the expander generating a mechanical work. Results showed that the system can generate maximum electricity of 490 W and minimum cooling temperature of about 5.4 °C. The study also discussed the main challenges that may face such system, where the flow generated from desorption process was varying between a minimum and maximum values in a periodic manner. A number of solutions have been recommended to fix the problem of incompatibility between the expansion process and the desorption process.

Jiong et al [17] have designed and studied a new resorption cogeneration system for electricity, cooling and energy storage using $MnCl_2$-$CaCl_2$ and ammonia as working pair with

a scroll expander. To assess the performance of the scroll expander, an air pressure of 0.6 to 1 MPa was applied and an isentropic efficiency of about 60% was achieved. Results revealed that the suggested system can generate an electric power of 300 W and a maximum cooling capacity of 2 kW, also results showed that using the cogeneration system increases the overall system efficiency from 31.6% to 37.6% when utilising driving temperature of 130 °C and chilled temperature ranging between -10 to 20 °C, while the exergy efficiency decreases from 40.2% to 39.1%.

Yiji Lu et al [18] have used a computer software to improve the ammonia resorption cogeneration cycle using mass and heat recovery. They used twelve different working pairs with heating temperature ranging from 100 to 300 °C. Results showed that the system COP has been increased by 38% and 35% utilising $NiCl_2$ and $MnCl_2$ respectively. The electrical efficiency was enhanced by up to 12% and the exergy efficiency reached 41% using $BaCl_2$–$MnCl_2$ utilising heating temperature of 110 °C. It was concluded that the proposed system can be applied for various scale applications with the advantage of producing cooling and electricity simultaneously with high performance.

Bao et al [15] proposed two chemical adsorption system prototypes for cooling and electricity utilising heating fluid temperature ranging from 85 to 255°C. The study aimed to examine the feasibility of integrating a solid-gas chemisorption adsorption system with a scroll expander to produce electricity and cooling simultaneously utilising a number of adsorption salts including $NiCl_2$, $MnCl_2$, $CaCl_2$, and $BaCl_2$ and ammonia. The proposed system consists mainly of two adsorber beds, evaporator, condenser and a scroll expander. An external heat source is used to heat bed 1 and hence the desorption process is started in this bed, so the high pressure and temperature ammonia leaves bed 1 to the expander to generate an electric power

as shown in Figure 2-13 (a), while the evaporated ammonia leaves the evaporator to bed 2 which is cooled (under adoption process) and cooling is generated in the evaporator. To achieve continuous generation of cooling and electricity, after a half cycle time, bed 1 switches to cooling, while bed 2 switches to heating and the same procedure is repeated as shown in Figure 2-13 (b). It was found that an electricity of 320 W was generated instead of 1kW that was predicted and this was because of common constraints between the adsorption cooling system and the expansion system, also results showed that exergy efficiency of 62% and COP of 0.57 can be achieved.

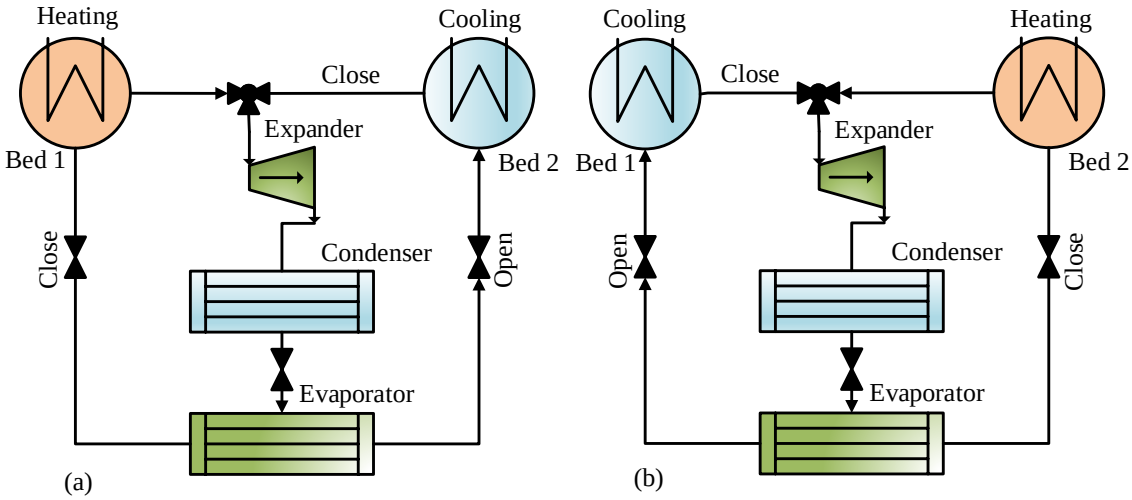

Figure 2-13: Adsorption system for cooling and electricity adopted by [15], (a) bed 1 in desorption and bed 2 in adsorption, (b) bed 2 in desorption and bed 1 in adsorption

Jiang et al [19] presented a novel resorption system for cooling and electricity utilising $MnCl_2$-$CaCl_2$/ammonia and driving temperature ranging from 120 to 170 °C. As shown in Figure 2-14, it consists of HTS bed, LTS bed, oil tanks, an expander (turbine) and valves. During the desorption process of HTS, the valves V1, V2, V3, V4, V10 and V11 are open, while the valve V9 is close and the HTS bed is heated using the hot oil tank, while the LTS bed is cooled using the cold tank. The high temperature and pressure ammonia generated from

the HTS expands through the turbine generating electricity [19]. During the desorption process of LTS, the valves V5, V6, V7, V8, and V9 are open, while valves V1, V2, V3, V4, V10 and V11 are close, while the HTS bed is cooled and the desorption process in the LTS generates cooling in the chilled tank. Experimental results revealed that the cogeneration system can generate maximum electric power and cooling of 253 W and 2980 W respectively. Also, results showed that the suggested cogeneration system can increase the overall efficiency from 29.3% to 41.7% and the exergy efficiency from 12% to 16% [19].

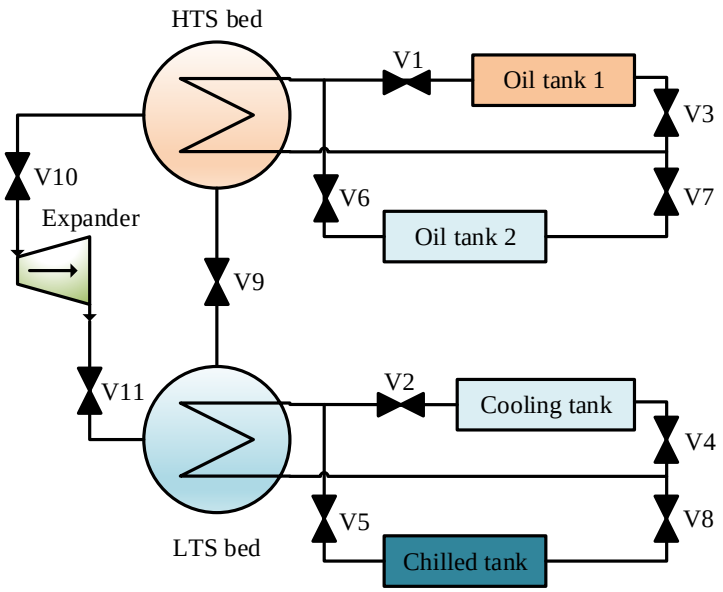

Figure 2-14: Cogeneration system for cooling and electricity proposed by [19]

2.7 Integrated adsorption-ORC systems for cooling and electricity

A number of researchers studied the possibility of combing adsorption cooling system with ORC system to generate electricity and cooling simultaneously. Jiang et al. [117] studied the feasibility of cascading a two stage adsorption cooling system with an ORC to produce cooling and electricity concurrently utilising heat source of 78-98 °C. $CaCl_2$-$BaCl_2$ and ammonia were used as an adsorption working pair, while R245fa is used as an ORC working fluid. The two systems were connected to the heating source, such that the heating fluid drives

the ORC and then the adsorption chiller. It was concluded that, the proposed system can produce cooling of about 1.92 to 2.7 kW and electric power of about 390 to 560 W. Results also showed that the cascading system can enhance the heat utilization exergy efficiency by 20.4-29.1%. Wang et al. [118] studied the possibility of combining an ORC with a water adsorption chiller to generate cooling and electricity simultaneously utilising heat source temperature of 70-100 °C. Silica-gel and R600 are used as adsorbent material and ORC working fluid respectively. The two systems were integrated using the heating fluid line. The ORC is set up as a topping system, while the adsorption chiller is set up as a bottoming system. Results revealed that an electric power of 1 kW and cooling of 6.3 kW can be achieved. The integrated system can achieve maximum exergy efficiency of 74% compared to that of 89% and 46% for a single ORC and a single adsorption chiller respectively.

Lu et al. [119] presented a newly combined resorption chiller and ORC system to enhance the overall performance of an internal combustion engine (ICE) by generating cooling and electricity as a result of recovering the coolant heat and the exhaust heat from the ICE. The proposed system as shown in Figure 2-15 consists mainly of an ORC cycle which has regenerator, expander, condenser, and two evaporators and a resorption chiller which has two HTS beds, and two LTS beds. To achieve continuous cooling switching between the two phases of the resorption chiller was used as illustrated in Figure 2-15 (a) and (b). It was concluded that the cogeneration system can produce cooling of 16.58 kW and electric power of 13.88 kW. Jiang et al. [120] investigated a new cascading system for cooling and electricity utilising heat source temperature of 75-95 °C. The proposed system comprises mainly of a pumpless ORC cycle and an adsorption cooling system (utilises Silica-gel/LiCl and methanol) which were connected using the heating and cooling fluids. The ORC cycle contains two heat

exchangers that can work as condenser or evaporator, an expander, and 4-way valve and it utilises R245fa as a working fluid.

It was found that the integrated system can produce cooling of 4.94 kW and electricity of 232 W utilising heating fluid temperature of 95 °C and cooling water temperature of 25 °C [120]. Also, the system can achieve an exergy efficiency ranging from 30.1% to 41.8% which is 60% and 144% higher than the single adsorption cooling system and the single pumpless ORC.

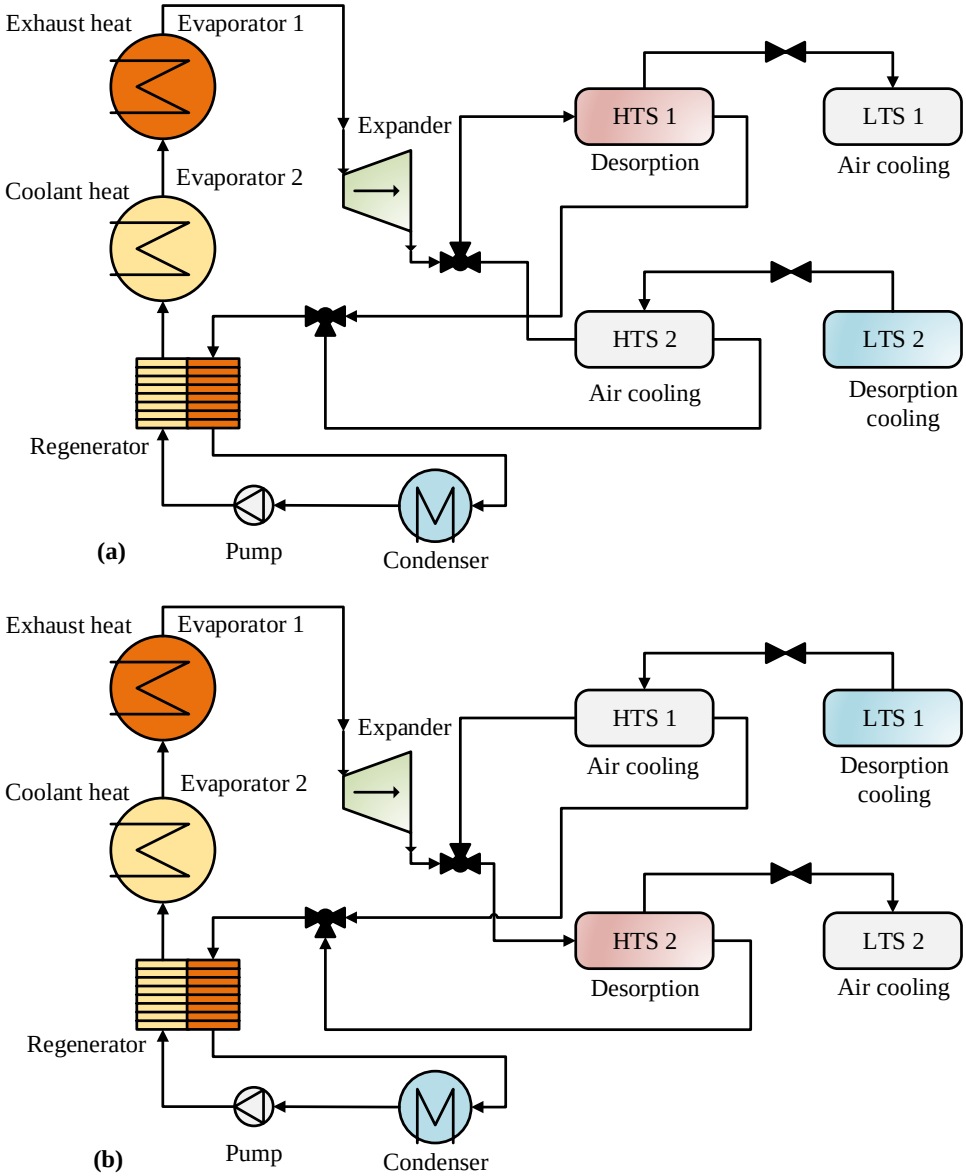

Figure 2-15: Combined ORC and resorption chiller for cooling and electricity (a) HTS 1 and LTS 2 in desorption process (b) HTS 2 in adsorption and LTS 1 in desorption process [119]

Table 2-5 summarizes the literature review on the adsorption systems for cooling and electricity generation that utilising low and medium grade heat sources. The first part of the table presents the adsorption systems integrated with expanders. It can be noticed that maximum COP of 0.77 and maximum exergy efficiency of 90% can be achieved in [13] utilising driving temperature ranging from 100 to 400 °C. The second part of the table presents the adsorption systems that integrated with ORC systems and it can be noticed that maximum exergy efficiency of 89% can be accomplished in [118] with the corresponding COP of 0.8.

Table 2-5: Adsorption systems for cooling and electricity [20-22, 64, 65]

Working pair/fluid	Driving temp. °C	System performance	Ref.
$FeCl_2$, $MnCl_2$, $SrCl_2$, $NiCl_2$, $BaCl_2$, and ammonia	100-400	For the combined system, the thermal efficiency of 9.5–15.8%, COP of 0.416 –0.691 and maximum exergy efficiency of 82% using heat recovery. For a single tube of adsorber bed (for different adsorbents), SCP and COP range from 74.9 –79.4 W/kg, 0.16 –0.21.	[14]
$PbCl_2$, $BaCl_2$ $CaCl_2$, and ammonia	100-400	Electricity generation exergy efficiency of 69% and refrigeration COP of 0.77. Optimum overall exergy efficiency of about 90%.	[13]
$NiCl_2$, $MnCl_2$, $CaCl_2$, and $BaCl_2$ and ammonia	85-255	Exergy efficiency of 62% and COP of 0.57. Power output was increased by 10–600%, while thermal and exergy efficiencies were improved by 1.4–4.5 and 2.0–8.3 times respectively.	[15]
$CaCl_2$/ammonia	120-130	Generated electricity of 490 W and minimum evaporator temperature of 5.4 °C.	[16]
$MnCl_2$-$CaCl_2$/ ammonia	130	Cooling of 2 kW and electricity of 300 W. Energy efficiency increases from 31.6% to 37.6% and exergy efficiency decreased from 40.2 to 39.1% when the evaporator temperature increased from -10 to 20 °C.	[17]

12 different salts/ammonia	100-300	COP increased by 38% using high temperature salt $NiCl_2$, and 35% using $MnCl_2$. Efficiency increased by up to 12% and exergy efficiency achieved 41% using resorption working pair $BaCl_2$–$MnCl_2$ and driving temperature of 110 °C.	[18]
$MnCl_2$-$CaCl_2$/ammonia	120-170	Maximum total efficiency of 41% and Maximum exergy efficiency of 16%. Maximum cooling of 2.98 kW and average shaft power of 82.3W.	[19]
$MnCl_2$–NaBr, $MnCl_2$–$SrCl_2$, and $SrCl_2$–NaBr and ammonia	110-250	Thermal efficiency of about 17% using driving temperature of between 250 °C. COP of 0.4–0.6 and cooling output at a temperature from -28 to 9 °C.	[91]
Adsorption and ORC			
$CaCl_2$/$BaCl_2$ and R245fa	78 -98	Electric power of 390-560W and cooling of 1.92-2.7 kW. Energy and exergy efficiencies were 10.1% to 13.1% and 18.5% to 20.3%, respectively. The integrated system improved the exergy efficiency by 20.4% to 29.1%.	[117]
Silica-gel/water and R600	78 -97	Electric power of 1 kW and cooling of 6.3 kW from 15 kW of heat. Cooling COP of 0.8, exergy efficiency between 84% and 89% and between 0.32 and 0.46 for the single ORC and adsorption refrigeration cycle, respectively.	[118]
$SrCl_2$- $MnCl_2$/ammonia and R245fa	200-700	Electric power of 13.88 kW and cooling of 16.58 kW.	[119]
Silica-gel-LiCl/methanol and R245fa	75-95	Cooling of 4.94 kW and electricity of 232 W. Exergy efficiency of 30.1% to 41.8%.	[120]

2.8 Adsorbent materials

Adsorption cooling systems are based mainly on the phenomenon of adsorption to produce the evaporation/condensation process required to generate cooling [121]. Adsorber bed is the key component of each adsorption cycle, which packed with a solid adsorbent material like

Silica-gel to achieve adsorbing and desorbing processes. Recently, many researchers reported a number of new adsorption pairs either for cooling or other applications [122]. Adsorbent materials can be classified into physical adsorbent materials, chemical adsorbent materials or a composite of both.

2.8.1 Physical adsorbent materials

Physical adsorbents are porous materials and the adsorption process depends on Van der Waals force. They are more stable than chemical adsorbents and they can retain their original properties after releasing the working fluid by using desorption process, as a result, these materials are widely used in commercial systems. Physical adsorbents can be classified into silicates, metal aluminophosphates, zeolites, activated carbons and Metal Organic Frameworks [123].

2.8.2 Chemical adsorbent materials

The adsorption/desorption process in the chemical adsorbents is based on the reaction between the adsorbate molecules and the chemical adsorbent material. Calcium-chloride and ammonia is the most frequently used working pair of the chemisorption cooling systems because it is cheap and has low desorption temperature. The main problems of such adsorbents are the dissolution, agglomeration, and swelling, however, these problems can be solved by mixing these materials with some additives like expanded graphite to produce composite adsorbents [124]. Chemical adsorbents can be classified into metal chloride salt and metal hydrides, metal oxides, and composite adsorbents (chemical and physical mixtures).

2.8.3 Composite adsorbent materials

The main purpose of using composite adsorbent materials is to enhance the adsorption characteristics of the physical adsorbent materials as chemical adsorbents have higher heat of adsorption and then higher kinetics rate than that of the physical adsorbents. Also, they used to avoid the disadvantages of the chemical adsorbent materials like agglomeration, swelling and low thermal conductivity [34]. For example, adding hygroscopic salts to Silica-gel can enhance its adsorption characteristics and increase the water uptake and avoids the aforementioned problem of the chemical adsorbent materials [125].

2.8.4 Advanced physical adsorbent materials

Enhancing adsorption technology requires advanced adsorbent materials with high adsorption capabilities. During the last decade, many researchers and companies developed new adsorbent materials to enhance the performance of the adsorption systems [126]. MOFs materials are new adsorbent materials with superior water uptake and high surface area. Also, AQSAO-Z02 produced by Mitsubishi Plastic is an advanced adsorbent material that received significant interest during the last few years, because of its high water uptake.

Ali and Chakraborty [127] have numerically examined Silica-gel and AQSOA-Z02 to be used in a two-stage water adsorption system for desalination and cooling. Results showed that AQSOA-Z02 can generate more cooling capacity, while Silica-gel produces more specific daily water production (SDWP). They used a heat recovery scheme between the evaporators and the condenser of the two stages to enhance the overall system performance showing that the proposed system has increased cooling capacity by 45% and fresh water by 26% compared to those of the traditional systems.

Ilis [128] numerically studied the effect of using new adsorbent materials for refrigeration applications using Comsol software utilising evaporator and driving temperatures of 2 °C and 77 °C respectively. The constants of the isotherms equations for AQSOA-Z01, AQSOA-Z02, NH_2-MIL-125(Ti) and MIL101@GO5 were calculated and used in the modelling. It was concluded that MIL101 (Cr)@GO5 has the maximum SCP of 21.13 kJ/kg_{ads} and the minimum COP of 1.20, while AQSOA-Z01 has the maximum cooling capacity of 53.85 kJ/h. Also, it is found that AQSOA-Z01 and NH_2-MI-125(Ti) are promising materials for refrigeration applications.

Elsayed et al [129] numerically studied the feasibility of using CPO-27(Ni), Al-Fumarate (Aluminium-Fumarate), and MIL101(Cr) in an adsorption desalination system with two adsorbent beds utilising heating fluid temperature ranging from 70 to 150 °C with various operating conditions. Results showed that, MIL101(Cr) produced the maximum amount of fresh water generated of 11 $m^3/(ton_{ads}.day)$ at evaporator temperature of 20 °C, compared to 6 $m^3/(ton_{ads}.day)$ generated using Al-Fumarate at evaporator temperature of 20 °C and 4.3 $m^3/(ton_{ads}.day)$ generated using CPO-27(Ni) at 5 °C . Results also showed that CPO-27(Ni) is more appropriate for cooling and desalination systems. It is concluded that CPO-27(Ni) is appropriate for heat source temperature higher than 110 °C, while Al-Fumarate needs low heat source temperature of about 70 °C.

Youssef et al [130] experimentally investigated CPO-27(Ni) in one-bed adsorption test facility for desalination and cooling. The effects of operating parameters on the generated cooling and water were studied and results showed that a freshwater generation of about 22.8 $m^3/(ton_{ads}.day)$ was obtained utilising heating fluid temperature of 95 °C, cooling water temperature of 5 °C and evaporation temperature of 40 °C [130]. Also, cooling with chilled

water less than 20 °C of about 65 Rton/ton_{ads} was achieved. In addition, the experimental results were validated against the values predicted by a numerical model. Du et al [131] investigated ZSM-5 zeolite and AQSAOA-Z02 (SAPO-34 zeolite) as adsorbent materials and water as a working fluid in a novel adsorption refrigeration system using solar thermal collectors as a heat source. Experimental results showed that AQSAOA-Z02 was superior in terms of the mass transfer, while ZSM-5 zeolite was superior in terms of heat transfer. Also, cooling capacity and desorption speed of AQSAOA-Z02 are considerably higher than that of ZSM-5 zeolite.

Table 2-6 summarizes the latest literature review on the new and commonly used adsorbent materials and working fluids utilised in the adsorption technology for a number of applications at a range of heat source temperatures. Metal Organic Framework MOF materials showed superior adsorption characteristics with a maximum water uptake of 1.47 kg/kg_{ads} achieved by MIL101(Cr).

Table 2-6: Adsorbent materials and refrigerants utilised in various adsorption applications

Adsorbent	Refrigerant	Uptake	Desorption temp. (°C)	Application	Ref.
Silica-gel (physical adsorbent materials)					
Silica-gel	water	0.2 kg/kg_{ads}	80	cooling	[132]
Silica-gel	water	0.592 kg/kg_{ads}	85	cooling/ desalination	[133]
Silica-gel	water	-	50-70	cooling	[61]
Type RD Silica-gel	water	0.4465 kg/kg_{ads}	-	cooling	[134]
Type A Silica-gel	water	0.3948 kg/kg_{ads}	-	cooling	[134]
Zeolite-based adsorbent materials (physical adsorbents)					
AQSOA-Z01	water	0.1 kg/kg_{ads}	-	cooling	[135]
Zeolite 13X	water	0.23 kg/kg_{ads}	90 - 150	cooling	[136]
AQSOA-Z02	water	0.31 kg/kg_{ads}	85	cooling/ desalination	[127]
Activated carbon AC (physical adsorbent materials)					
AC	R134a	1.649 E-3 m^3/ kg_{ads}	-	cooling	[137]
AC	R507A	1.175 E-3 m^3/ kg_{ads}		cooling	[137]

AC 207EA	Methanol	0.33 kg/kg_{ads}	-	cooling/ heating	[138]
AC WS-480	Methanol	0.49 kg/kg_{ads}	-	cooling/ heating	[138]
Metal Organic Framework MOF (physical adsorbent materials)					
MIL101(Cr)	Ethanol	1.1 kg/kg_{ads}	-	cooling	[139]
MIL101	Isobutene	0.45 kg/kg_{ads}	95	cooling	[140]
MIL-101(Cr)	water	1.47 kg/kg_{ads}	70-150	desalination	[129]
CPO-27(Ni)	water	0.462 kg/kg_{ads}	70-150	desalination	[129]
Al-Fumarate	water	0.53 kg/kg_{ads}	70-150	desalination	[129]
CPO-27(Ni)	water	-	95	ice making/ desalination	[141]
Salts (chemical adsorbent materials)					
NaBr-$MnCl_2$	ammonia	-	30 -150	power generation	[92]
NaBr-$SrCl_2$	ammonia	-	30 -150	power generation	[92]
$MnCl_2$-$CaCl_2$	ammonia	-	130	cooling/electricity	[17]
$MnCl_2$	ammonia	40% weight	170	cooling	[142]
Composite adsorbent materials					
AC,/Silica-gel/$CaCl_2$	water	0.805 kg/kg_{ads}	115	cooling/ dehumidification	[143]
$CaCl_2$/AC	ammonia	-	120-130	cooling/electricity	[16]

2.9 Expanders and turbines

Expanders are the key parts of any power generation systems like ORC, Kalina and for the cycles with multiple outputs such as the adsorption system for cooling and electricity. They can be classified according to the fluid passing through their blades like steam, gas, water, or ORC expanders [20]. Also, they can be classified as velocity type expanders like axial and radial turbines, or volumetric expanders like scroll, and screw expanders [144, 145].

Volumetric expanders are positive displacement machines that convert the energy of the expanding fluid into a useful power by means of changing the volume of closed spaces between the moving parts and the expander casing. In the literature, scroll expanders are used widely within the power generation cycles like ORC. Such expanders are mostly modified from existing scroll compressors, and not designed to meet the cycle operating conditions nor the specific aerodynamics properties of the fluid, and as a result, they have relatively low

efficiencies. On the other hand, velocity type expanders like axial and radial turbine are widely used in various power generation systems, because they are simple, and compact with light weight compared to the volumetric expanders. Axial turbine is usually used for applications with high mass flow rate and low-pressure ratio [146], while the radial turbine is used for systems that have relatively low mass flow rate [147].

Clemente et al. [148] studied and compared a number of expanders for ORCs in order to design a bottoming cycle powered by the exhaust heat of 100 kWe regenerative gas turbine. Six different refrigerants were utilized and adjusted to increase the electric power generated. A scroll expander (commonly used as a compressor in refrigeration systems) and a piston expander were used as an alternative to turbines.

Mendoza, et al [149] presented a scroll expander for a combined absorption system for cooling and electricity utilising ammonia/lithium nitrate, ammonia/sodium thiocyanate and ammonia/water. In this study, a scroll compressor from Sanden Company was developed to work as an expander because it is cheap and compatible with ammonia. The expander was designed for inlet pressure and volume ratio of 3500 kPa and 1.9 respectively and was tested experimentally using ammonia to study the impact of operating conditions and lubrication level on the expander performance. Using an inlet pressure of 1400 kPa and rotational speed of 50 Hz, the expander generated about 958 W.

Maurizio et al [150] converted a scroll compressor to be used as a scroll expander in non-regenerative ORC system. R410A was used to test the expander within an ORC system. Results showed that using commercial scroll expander is feasible, however, the system performance was low because of using such expander and the high pump consumption. In

addition, four different fluids namely; R245fa, R134a, R1234yf, and R1234ze were simulated using heating temperature of 100 °C and it was concluded that R245fa is the best fluid.

2.9.1 Turbines modelling

2.9.1.1 Preliminary design

Many preliminary design methods for predicting the performance of a radial inflow turbine (RIT) were reported in the literature using the losses correlations which based on experimental work. The one-dimensional mean-line modelling is the most famous method and it is assumed that the parameters at the mean radius of the flow can represent the flow in the entire turbine stage [151]. Rahbar et al. [151] developed a 1D mean-line model to design a small-scale RIT for distributed power generation using heating temperature of up to 200 °C. The effect of various turbine parameters like rotational speed, velocity ratio, flow angles, on the turbine performance and the inlet diameter were studied. Mean-line method results showed that to increase the power output, mass flow rate, pressure ratio, and inlet temperature should be increased.

Nithesh et al. [152] designed a 2 kWe RIT utilising R-22 as a refrigerant for Ocean thermal energy conversion applications. The turbine has rotational speed, mass flow rate and inlet temperature of 34000 rpm, 0.46 kg/s, and 24.5 °C respectively. A numerical study with 1D design was carried out to find the best geometry of the RIT including the stagger angle, and the number of blades [152]. It was concluded that maximum efficiency of 74% and output electricity of 2.5 kW were achieved utilising 15 blades for the rotor and 12 blades for the stator.

Ventura et al. [153] established a programming code to determine the preliminary design of RITs including losses calculations along with selection criteria. The model can predict the efficiency of RITs, and it was validated against previous codes. The authors claimed that the model can be integrated with the thermodynamic cycle design and 3D blade design analysis.

2.9.1.2 Three dimensional CFD modelling

The actual flow in the RIT is a 3D turbulent and viscous flow with secondary flow regions. Therefore the mean-line method which assumes one-dimensional flow cannot capture all the effects of the three-dimensional parameters like supersonic/transonic flow, the interaction between the stator and the rotor and tip clearance. As a result, a more powerful tool is required to facilitate the study of the three-dimensional flow in the RITs. CFD modelling can capture the influence of the three-dimensional parameters on the turbine performance, also save the time and the cost of the prototype manufacturing.

Sauret and Gu [154] developed an RIT for ORC applications with power of 400 kW utilising R143a as working fluid. They used mean-line analysis and detailed 3D CFD simulations using the commercial software ANSYS CFX. Wide ranges of operating conditions were applied and the 3D CFD and the mean-line results were compared showing a good agreement. However the CFD modelling was shown to enable enhancing the performance of the turbine to achieve maximum efficiency of 88.45% corresponding to power output of 400 kW compared to maximum efficiency of 79.8% and power output of 393.6 kW obtained by the mean-line method.

Fiaschi et al. [155] developed a small-scale expander for the ORC applications using the preliminary design and the three dimensional CFD simulations utilising R134a. The three dimensional CFD modelling depended on the preliminary design point with updating some other key factors using ANSYS Fluent. The three-dimensional rotor analysis leads to improving the blade profile of the rotor and selecting the right number of blades, which improved the blade loading.

Rahbar et al [156] carried out a parametric investigation and optimization for a small-scale RIT for ORC applications. The preliminary design method was combined with 3D CFD simulation using genetic algorithm optimization scheme provided by ANSYS to investigate the main parameters that affect the turbine performance. Eight different ORC fluids were examined using the designed turbine. Optimization results showed that the studied turbine can reach a maximum efficiency of 84% utilising R152a with 7 K superheat, however, if the superheated degree is excluded, isobutane can show better features with a rotor diameter of 66.3 mm and efficiency of 83.82% at inlet driving temperature of 89.2 °C.

2.9.2 Turbines working fluid selection

The selection of the appropriate fluid of any power generation cycle in terms of the thermodynamic properties and the environmental requirement is an important issue. Many researchers investigated many working fluids to highlight their influence on the performance of the power generation cycles. Costall et al. [157] established a design method to design and select the working fluid for three different small-scale ORC radial turbo expanders utilising Siloxanes and Toluene as working fluids for integration with diesel engines. Three different sizes (small, medium, and large) turbines were designed and studied. The small turbine can generate power capacity of 15.5 kW with 1.6 mm inlet blade height and 20 mm diameter. The

medium turbine can generate power of 34.1 kW with efficiency of 51.5% and a diameter of 62.9 mm while the large turbine can generate power of 45.6 kW with efficiency of 56.1% and a diameter of 83.0 mm. Results showed that Toluene is the preferable working fluid.

Li and Ren [158] investigated a thermodynamic study of an ORC system using a number of working fluids, they also developed an aerodynamic model of an organic RIT using R123. Results showed that, as the driving temperature increases, the thermal efficiency increases for all refrigerants used and maximum cycle thermal efficiency of 17% (at an evaporator temperature of about 430 K) was achieved using R141b, while the lowest thermal efficiency value was obtained using R601a. Under the design condition, R123 can generate power output of 534 kW and cycle efficiency of 13.5%. Also, results showed that the waste heat utilization ratio of about 42% was achieved using R245fa and R600, while the designed RIT can achieve a maximum isentropic efficiency of 84%.

2.9.3 Evaluation of expanders and turbines for small-scale applications

Velocity type expanders like axial and radial turbines are more suitable to the small-scale power systems because of their compactness and simplicity compared to the volumetric expanders which have a number of disadvantages like complicity, and high cost. On the other hand, RITs have a number of advantages compared to the axial turbines in terms of their compactness and high performance at a low mass flow rate. However, the axial turbines have the advantages of their compatibility for the multi-stage applications and they can work efficiently at low rotational speed. Al Jubori et al. [159] carried out with optimization of a small-scale axial turbine utilising ANSYS CFX for ORC systems using heating temperature of less than 100 °C. A number of ORC fluids including R123, R141b, R152a, R134a, isobutane and R245fa were investigated and a number of optimization parameters including

throat width, stagger angle, tip clearance and number of blades for the stator and the rotor were included. It was concluded that a shaft power of 6.3 kW and an efficiency of 88% can be achieved, the ORC thermal efficiency can be increased by up to 14% compared to that of the preliminary design.

Al Jubori et al. [160] developed three dimensional CFD designs using ANSYS CFX for small-scale radial inflow and axial turbines for ORC systems utilising low-grade heat sources. Both turbines were examined using R245fa, R141b, n-pentane, n-butane, and R1234yf using a mass flow rate ranging from 0.1 to 0.5 kg/s. CFD results showed that n-pentane produced the maximum power and efficiency for all the studied cases. For the RIT, maximum power and efficiency of about 8.9 kW and 84% were achieved while for the axial turbine, maximum power and efficiency of about 8.5 kW and 83.5% were achieved. Also, the ORC thermal efficiency can achieve 10.6% and 10.14% utilising radial inflow and axial turbines respectively. Daabo et al [161] designed two small-scale radial inflow and axial turbines for Brayton cycle application. The effects of inlet temperature, inlet pressure, mass flow rate, and rotational speed on the power output and the efficiency have been investigated. The 3D CFD simulations of the two turbines were carried out and it was concluded that the radial turbine was superior with low mass flow rate, while the axial turbine was better with low rotational speed. Table 2-7 summarizes a number of the latest literature on the development of expanders and turbines for electricity generation systems powered by low-grade heat sources. A maximum isentropic efficiency of 88% is achieved using RIT with R123 utilising driving temperature of less than 100°C.

Table 2-7: Small-scale expanders and turbines used in a number of power cycles

Expander type	Working fluid	Driving temp. °C	Efficiency %	Power kW	Speed RPM	Ref.
Axial turbine	R141b,R152a R123,,R134a,iso butane and R245fa	100	88	6.3	10000-30000	[159]
Axial and radial turbines	R141b, n pentane,R245fa, n-butane, and R1234yf	67-92	84	8.9	40000-50000	[160]
RIT	R245fa		79	33	63000	[162]
RIT	R123		65	1.36	24000	[163]
Axial turbine/ radial-outflow turbine	R141b, R245fa, R365mfc, isobutane and n–pentane	87	82.5/79.05	15.15/13.625	18000–20000	[164]
RIT	15 working fluids	117	80	7.23	40700-105982	[165]
RIT	R134a	24.5	70	2	22000	[166]
Radial turboexpander	R134a	122.5	68	5	87645	[155]
Radial turbine	8 working fluids	89.2	84	15	35000-65000	[156]
Scroll expander	R134a, R245fa, R1234yf, and R1234ze	100	53.3	10	5830	[150]
Scroll expander	Ammonia	90-120	-	6	-	[149]
RIT	Air	20-40	84.5	4.343	55000	[167]

2.10 Summary

This chapter reviewed the latest literature on the main technologies that utilises low-grade heat sources to produce cooling, electricity and both cooling and electricity simultaneously. For cooling applications, the literature review covered absorption and adsorption cooling systems. For power generation, the literature covered Organic Rankine Cycle (ORC), Kalina Cycle (KC), and resorption power generation cycle. The aforementioned review is important to understand the next part of the literature review which includes the latest work on the main

technologies used to produce electricity and cooling simultaneously utilising low-grade heat sources. From this detailed review the following conclusions can be made:

1. The first technology for producing cooling and power simultaneously was based on absorption system utilising ammonia/water as working pair [8, 10, 106]. More recently, research on using adsorption system for cooling and power generation particularly using chemical sorption with metal salts/ammonia as the main working pairs. Very limited literature was found regarding the use of physical adsorption systems for cooling and power production.

2. Also, it is concluded that there is no previous work on the use of water adsorption system for cooling and power generation that utilises physical adsorbent materials. These materials are more stable than the chemical adsorbent materials where the latter has practical problems like swelling and agglomeration which limits the development of such technology [34]. Furthermore, water is an environmentally friendly fluid compared to ammonia which is poisonous fluid and does not meet the health and safety requirements.
3. This review identified advanced adsorbent materials with superior adsorption characteristics which have not been used before to generate cooling and electricity, including Metal Organic Framework MOF materials that have water adsorption uptake reaching about 1.5 kg/kg_{ads}.
4. In addition, this chapter reviewed the latest technologies used in the expanders and turbines that generate electricity. It is noticed that there is no previous work that has a detailed CFD turbine design to meet the operating conditions of the adsorption system for cooling and electricity particularly at a very low mass flow rate of about 0.01 kg/s with vacuum pressures in the inlet and outlet of the turbine.

CHAPTER THREE
ADSORBENT MATERIALS

3.1 Introduction

Choosing adsorbent/refrigerant working pair is essential for any adsorption system. Water is an environmentally friendly and safe fluid with the advantage of the high latent heat of evaporation and thermal properties [168]. New adsorbent materials with high water adsorption capacities have been reported in the literature. However, those adsorbents were not investigated for simultaneous production of cooling and power. This chapter aims to experimentally predict the water adsorption characteristics of two advanced adsorbent materials namely MIL101(Cr) MOFs, and AQSOA-Z02 zeolite where these materials with additional two advanced MOFs materials namely Al-Fumarate and CPO-27(Ni) are compared to the commonly used Silica-gel in terms of water adsorption characteristics.

3.2 Adsorption pairs

Adsorbent materials are classified into physical, chemical and composite adsorbent materials. In this study, all the adsorbent materials used are of the physical type. Physical adsorbent materials are porous adsorbents like zeolite, Silica-gel, and Metal Organic Frameworks MOFs with different pore sizes. The adsorption process in these materials is driven by Van der Waals force (an intermolecular force). They have the advantage of keeping their original properties during the adsorption/desorption process, which leads to being commonly used in the practical applications.

Silica-gel/water has relatively low adsorption uptake of about 0.2 kg/kg_{ads} [132], however, some types of Silica-gel/water showed higher water uptake with a value of 0.4465 kg/kg_{ads} for type RD silica gel, and 0.3948 kg/kg_{ads} for type A silica gel [27, 169]. Zeolites are micro-porous crystalline alumina silicate minerals and many types of zeolite frameworks are available with different uptake values [170]. AQSOA-Z02 (SAPO-34) is an advanced synthetic zeolite with a unique adsorbent performance that has been developed by MITSUBISHI PLASTIC Company using inorganic material design technology.

MOFs materials are advanced adsorbents with high porosity, superior adsorption characteristics, uniform pore size, and large surface area (up to 5500m^2/g) [171, 172]. Particularly MIL101(Cr) is a remarkable adsorbent material that shows very high water uptake by up to 1.47 kg/kg_{ads} [20]. Also, MOFs Al-Fumarate and CPO-27(Ni) are commercialised materials and they have a maximum water uptake of about 0.53 kg/kg_{ads} and 0.47 kg/kg_{ads} respectively [129]. Therefore, MIL101(Cr), CPO-27(Ni), in addition to AQSOA-Z02 will be used in this study to investigate their performance in adsorption system for cooling and power generation compared to Silica-gel. Table 3-1 lists the main physical properties of the adsorbent materials used in this study.

Table 3-1: Physical properties of the adsorbent materials used in this study

Property	Silica-gel	AQSOA-Z02	MIL101(Cr)	CPO-27(Cr)	Al-Fumarate
BET surface area m^2/g	840 [173]	590 [135]	3460 [174]	469.777 [175]	893.965 [175]
Max uptake kg/kg_{ads}	0.5092[55]	0.2901[a]	1.4773[a]	0.4711[a]	0.5591[a]
Bulk density kg/m^3	820 [176]	715.3[b]	620 [177]	599.3[b]	577.8[b]
Pore volume cm^3/g	0.4477 [178]	0.2769 [135]	1.753 [174]	0.5 [129]	0.436 [129]
Heat of adsorption (kJ/kg)	2430 [179]	3420 [135]	2557 [180]	2626 [181]	2483 [182]
Particle radius (m)	0.16E-3[168]	0.19E-9 [183]	0.46E−6 [174]	0.65E−6 [175]	53.75E-6 [175]

a: measured using the DVS analyser, b: measured using a scaled container and an accurate electronic balance.

Figure 3-1 shows the SEM images of Silica-gel, AQSOA-Z02, MIL101(Cr), CPO-27(Ni) and Al-Fumarate (Aluminium-Fumarate). AQSOA-Z02 has solid regular cubic particles and it has smaller particle size [184] compared to Silica-gel.

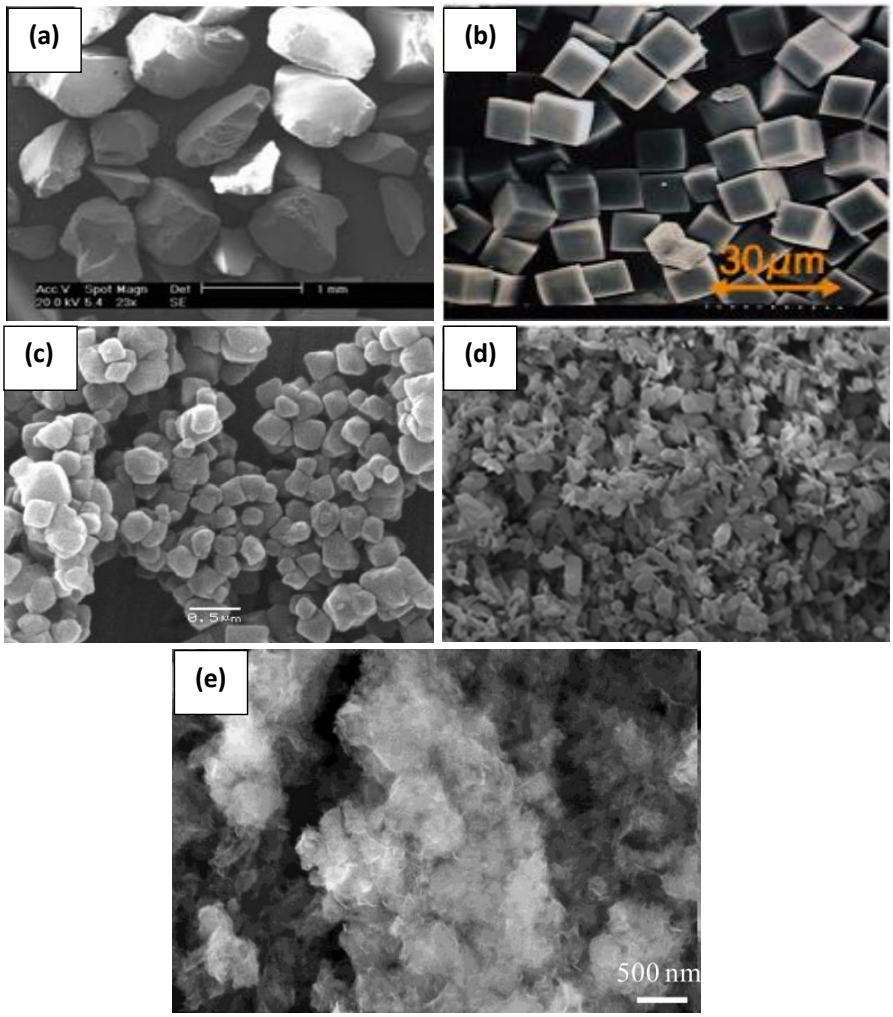

Figure 3-1: SEM image (a) Silica-gel [185], (b) AQSOA-Z02 [184], (c) MIL101(Cr) [186], (d) CPO-27(Ni)[130], and (e) Al-Fumarate [187]

3.3 DVS analyser

A DVS (Dynamic Vapour Sorption) analyser from Surface Measurement System Ltd as shown in Figure 3-2 is utilised to test the adsorption characteristics of two adsorbent materials utilized in this study. Figure 3-3 shows the fully automated analyser which comprises a temperature controller with an ultra-sensitive microbalance to measure the weight of the

adsorbent. It works with a range of temperature between 5 - 60 °C while the microbalance has a sensitivity of 0.1µg. The microbalance and stand are accommodated in a well-controlled temperature oven, which provides a high stability and precise vapour generation control. The microbalance mechanism is very sensitive to the adsorption/desorption processes, consequently, a continuous flow rate of nitrogen is used.

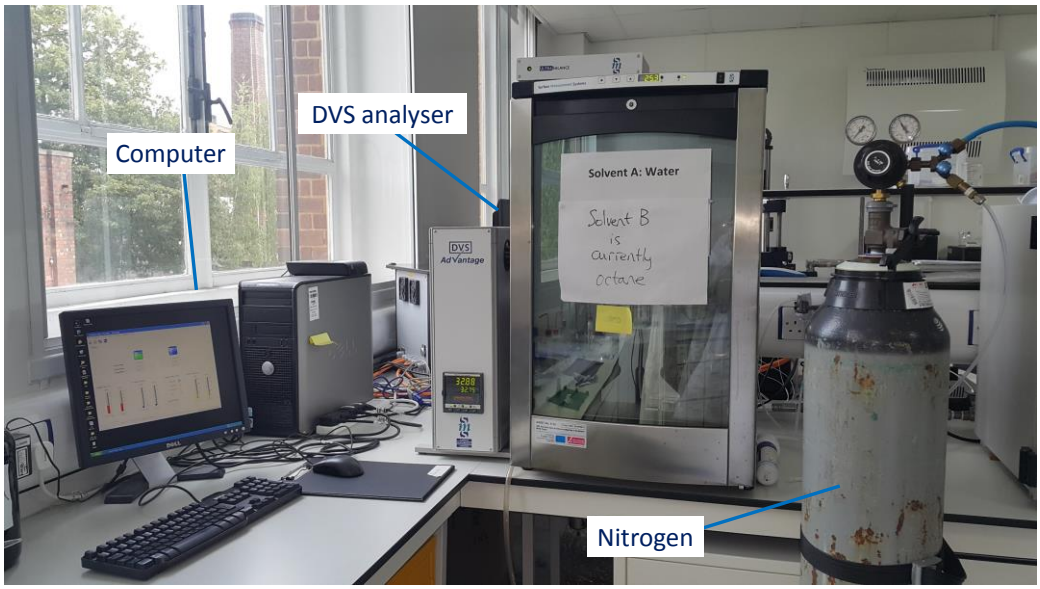

Figure 3-2: DVS analyser test facility

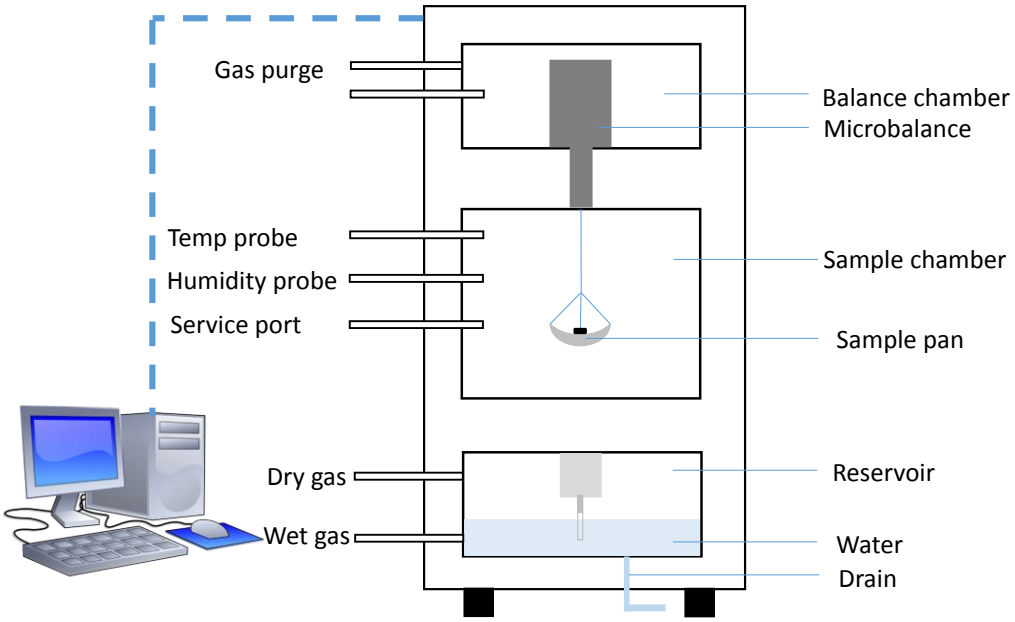

Figure 3-3: DVS analyser schematic diagram

A PC microcomputer is interfaced to the balance and the oven control units. An advanced microprocessor system is used to control a number of sub-component systems including, sample pre-heater, mass flow controller, optical sensor, temperature RTD probes, and isolation valves as shown in Figure 3-4.

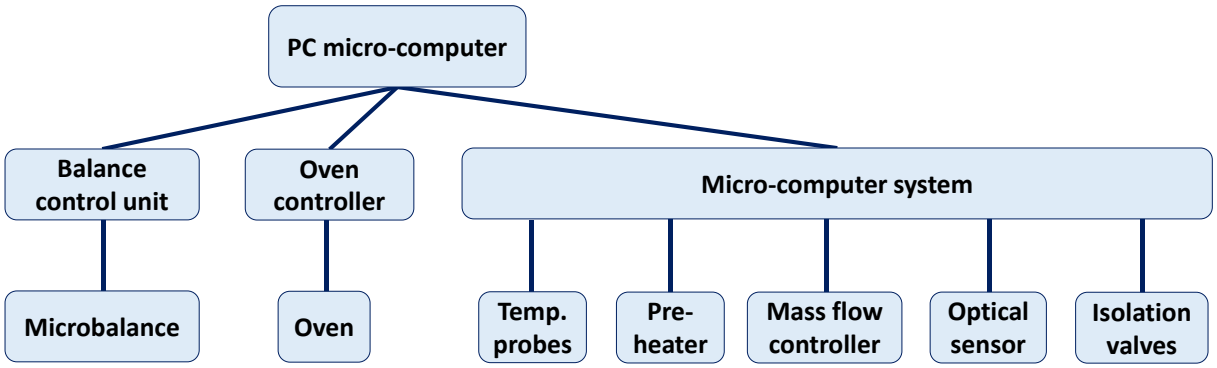

Figure 3-4: DVS instrument's sub-systems

A convenient and flexible software package (DVS analysis suite) as shown in Figure 3-5 is provided with the DVS analyser to set up and run the experiments easily. Furthermore, the DVS Analysis Suite can be linked to Microsoft Excel, which provides powerful tools for plotting and data analysis.

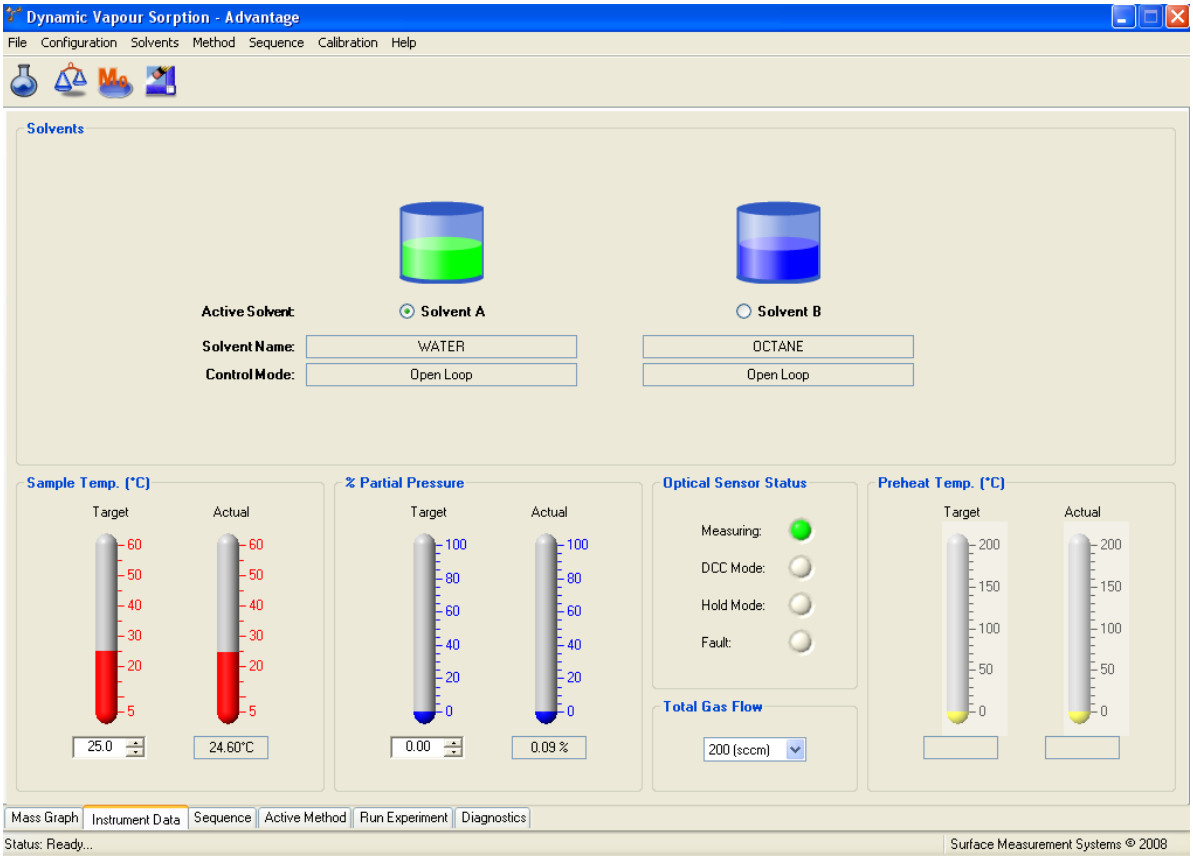

Figure 3-5: DVS analysis suite

3.4 DVS experimental procedure [20]

To have accurate readings from the DVS analyser it is important to ensure that the sample pan is clean. Figure 3-6 shows how to load the sample into the sample pan outside the DVS analyser and then hung the pan in the right place. At the beginning of the testing process, a dry nitrogen gas is used with a stable flow before packing the sample to the analyser. A built-in high accuracy and high stability microbalance is used to read the mass change every 4 seconds, while the other experimental conditions can be recorded using RTD sensors and pressure transducers [20]. Once, the material sample of about 10 mg is placed in the sample pan, the analyser starts to dry the sample until no mass change is noticed. After that, the adsorption process will be started, at a constant temperature, while the partial pressure (the

ratio between the supplied and the saturation pressures) [188] is varied gradually in a step of 10% from 0% to 95% where it is kept constant during each partial pressure ratio step [20]. During this process, the microbalance measures the adsorption/desorption process by recording the mass change in the adsorption sample [20].

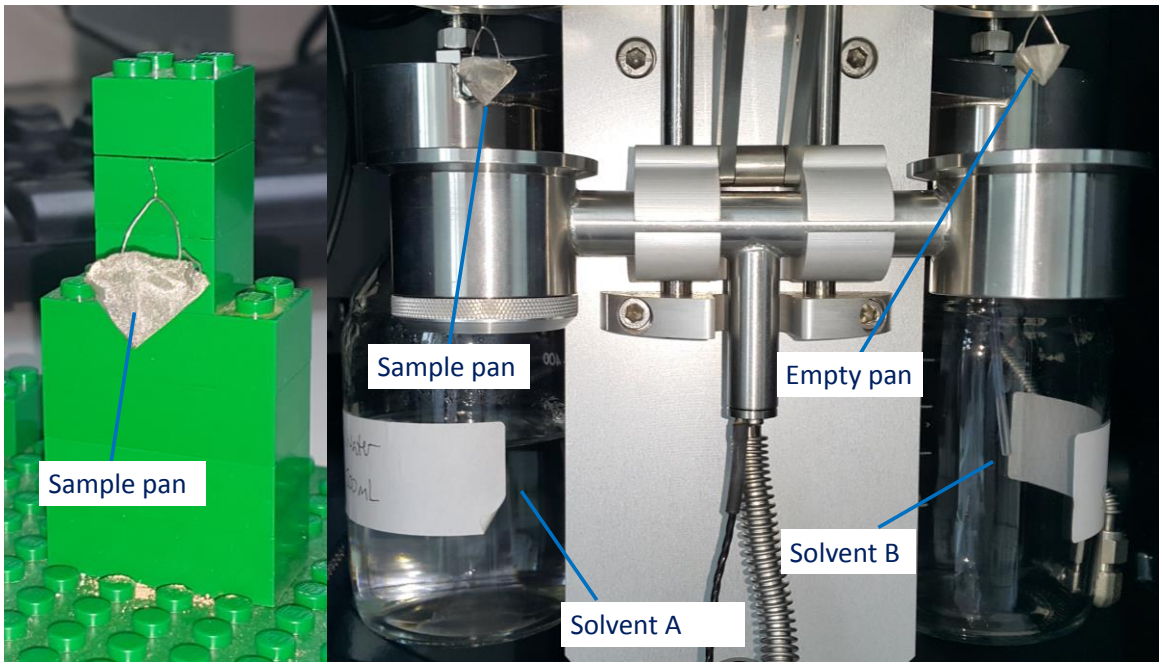

Figure 3-6: Loading the sample outside the DVS analyser (left), loading the sample inside the DVS analyser (right)

Figure 3-7 shows a sample of the raw data obtained from the DVS analyser for CPO-27(Ni)/water at 25 °C, which shows the change in the mass of the sample and the partial pressure during the experiment.

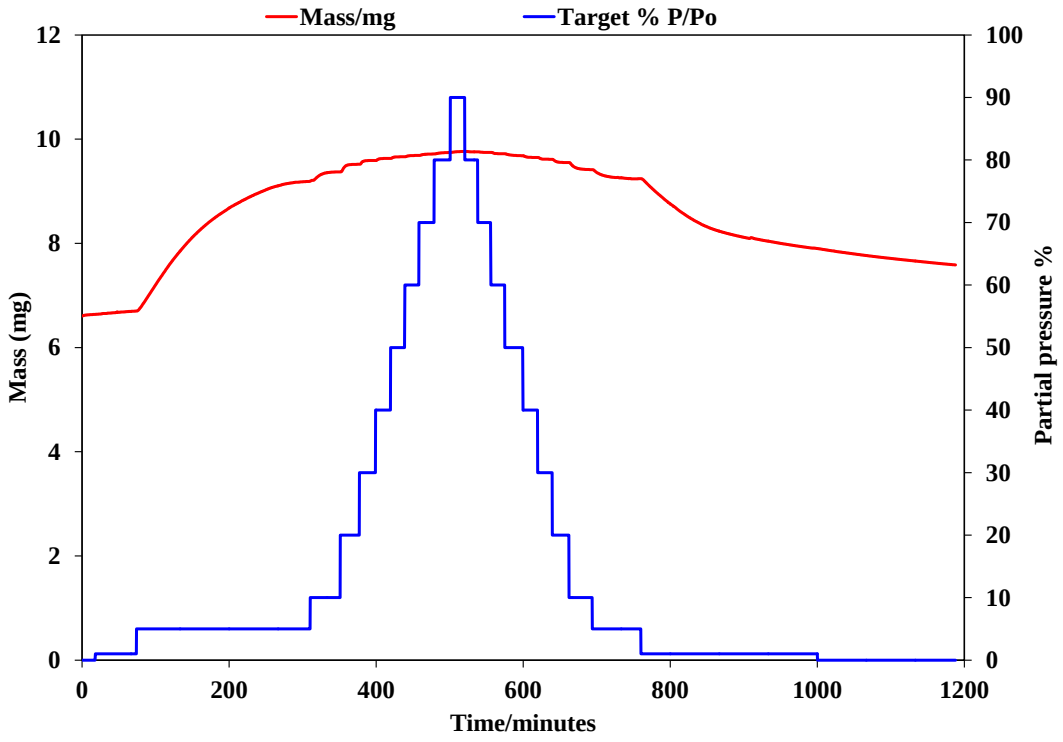

Figure 3-7: Change in mass and partial pressure during a DVS analyser test for CPO-27(Ni)/water at 25 °C [189]

3.5 Adsorbent materials characteristics [20]

The performance of adsorbent materials is measured mainly by the two well-known terms ‘isotherms’ and ‘kinetics’. Adsorption isotherms are defined by the maximum adsorbate amount (working fluid) that can be adsorbed per one dry kilogram of the adsorbent, while kinetics is defined as the rate at which the adsorbent can adsorb or desorb the adsorbate (working fluid) at a certain partial pressure. The DVS analyser is used to characterize AQSOA-Z02/water and MIL101(Cr)/water at various partial pressures between 0% and 95%, with temperatures of 25°C, 35°C, and 45°C [20]. For the remaining adsorbent materials, their water adsorption characteristics are taken from the literature and this is detailed in the next two sections.

3.5.1 Adsorption isotherms [20]

Adsorption isotherms define how much refrigerant (water) can be contained in the pores of the adsorbent material under equilibrium conditions. Many adsorption isotherms models like modified Freundlich and Dubinin–Astakhov are reported in the literature to define the adsorption equilibrium [190]. In this study, the DVS experiment starts with adsorption process and then desorption process using constant temperature. However, adsorption results are used to fit the isotherms model as the curves of the adsorption and desorption processes are assumed to be symmetric [20, 132, 191]. For AQSOA-Z02/water, the readings from the DVS analyser are fitted to the model of Sun and Chakraborty [192] in the form of equation 3-1 as shown in Figure 3-8 [20].

$$x_{eq} = x_o \left[\frac{k\left(\frac{P_s(T_w)}{P_s(T_a)}\right)^n}{1+(k-1)\left(\frac{P_s(T_w)}{P_s(T_a)}\right)^n} \right] \quad 3\text{-}1$$

Where, $P_s(T_w)$ is the saturation pressure at the working fluid vapour temperature, and $P_s(T_a)$ is the saturation pressure at adsorbent material temperature [52].

$$k = \alpha \exp\left[n(Q_{st} - h_{fg})/(R_w T_{bed})\right] \quad 3\text{-}2$$

x_o is the maximum uptake (kg/kg_{ads}), Q_{st} refers to the adsorption isosteric heat (J/kg), h_{fg} is the evaporation latent heat (J/kg), R_w refers to the gas constant (J/kg K), and T_{bed} is the bed temperature (K). Results show that good agreements can be noticed between experimental and numerical data, while the constants of equations 3-1 and 3-2 obtained from this fitting are listed in Table 3-2 [20].

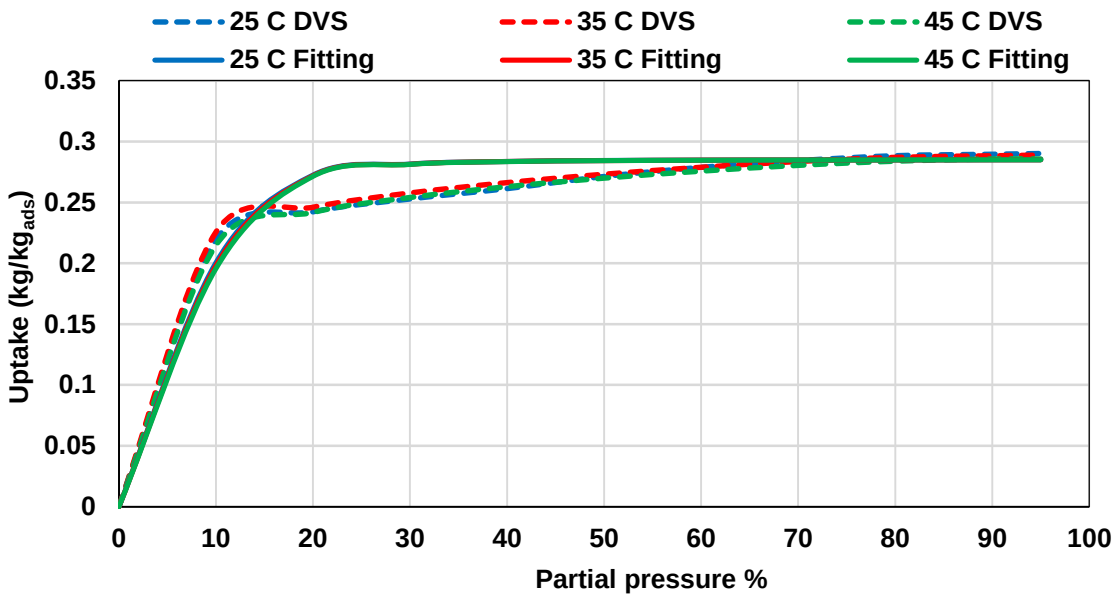

Figure 3-8: AQSOA Z02/water isotherms fitting of the experimental and the predicted uptake

Table 3-2: Parameters used in equations 3-1 and 3-2 [20]

x_o	0.285	kg/kg$_{ads}$	[20]
α	1032	-	[20]
n	3.18	-	[20]
Q_{st}	3420	kJ/kg	[135]

For MIL101(Cr)/water, the experimental isotherms data from the DVS analyser are fitted to equation 3-3 as shown in Figure 3-9 which has three parts as shown in Table 3-3 due to the S-shape isotherms of this adsorption pair. This three-part isotherms model can be achieved using the function Polyfit in MATLAB software [20].

$$x_{eq}=\mathrm{f}(\mathbf{A}) \qquad 3\text{-}3$$

A is the adsorption potential which can be calculated as:

$$\mathbf{A} = -\mathrm{R_w T_{bed}} \ln\left(\frac{\mathrm{P_s(T_w)}}{\mathrm{P_s(T_a)}}\right) \qquad 3\text{-}4$$

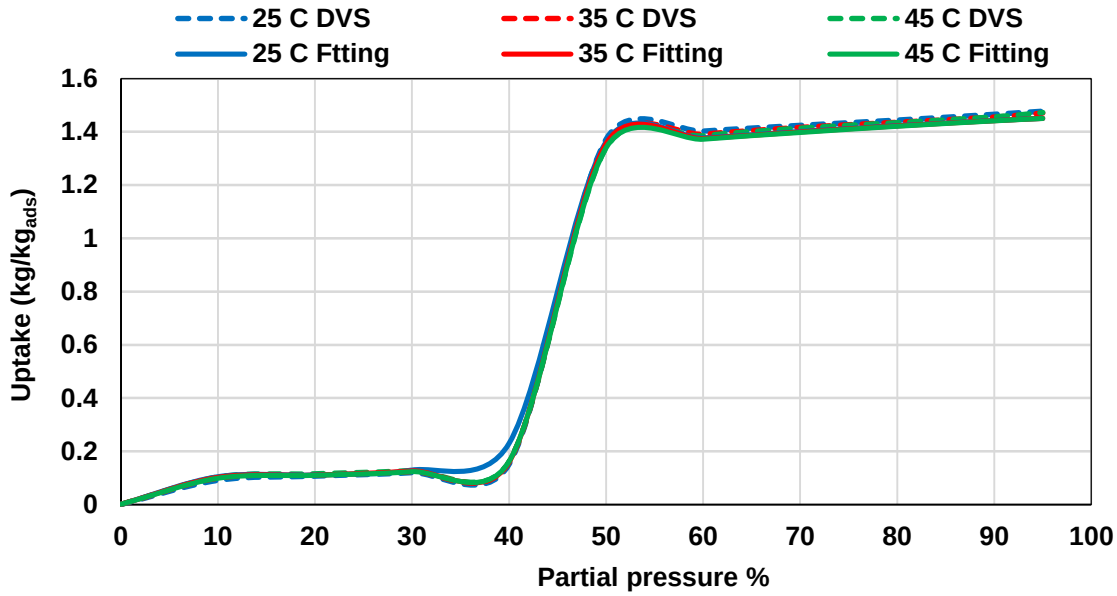

Figure 3-9: MIL101(Cr)/water isotherms fitting of experimental and predicted uptake

Table 3-3: MIL 101(Cr)/water isotherms of equation 3-3 [20]

A<1774.9	x_{eq} =1.46-5.76E-5**A** - 1.34E-08**A**^{2} + 6.65E-12**A**^{3}
A>2498.7	x_{eq} =0.475-2.29E-04**A**+4.79E-08**A**^{2} +3.36E-12**A**^{3}
1774.9≤**A**≤2498.7	x_{eq} =2252.774-5.567**A**+0.0055**A**^{2} -2.66E-06**A**^{3} + 6.42E-10**A**^{4} -6.14E-14**A**^{5}

For Al-Fumarate/water, the adsorption isotherms model was obtained from Elsayed et al. [175] who used equation 3-3 with the empirical constants listed in Table 3-4 [20].

Table 3-4: Al-Fumarate/water isotherms of equation 3-3 [20, 175]

A< 2900	x_{eq} = 0.5948-3.12E-4**A** +1.68302E-7 **A**^{2}-3.124455E-11**A**^{3}
A> 3987	x_{eq} = 0.111993EXP(-0.000258797**A**)
2900≤**A**≤3987	x_{eq} = 2.36129-9.93768E-4**A**+ 1.05709E-7**A**^{2}

For CPO-27(Ni)/water, the adsorption isotherms were reported by Shi et al. [70] using the Dubinin–Astakhov (D–A) equation 3-5:

$$x_{eq} = x_o \, Exp\left\{-\left[\frac{-R_w T_{bed} \ln\left[\frac{P_S(T_w)}{P_S(T_a)}\right]}{E}\right]^n\right\} \quad 3\text{-}5$$

E is characteristic adsorption work (J/mole) and has the value of 10088.7, while the constants x_o=0.468, n=6 and they are taken from [70].

For Silica-gel/water, the modified Freundlich model is applied to define the adsorption isotherms [20, 52, 55, 193] as below:

$$x_{eq} = A(T_s)\left[\frac{P_s(T_w)}{P_s(T_a)}\right]^{B(T_s)} \quad 3\text{-}6$$

Where

$$A(T_s) = A_o + A_1 T_s + A_2 T_s^2 + A_3 T_s^3 \quad 3\text{-}7$$

$$B(T_s) = B_o + B_1 T_s + B_2 T_s^2 + B_3 T_s^3 \quad 3\text{-}8$$

T_s is the saturation temperature (K), while the constants of equations 3-7 and 3-8 are taken from [20, 55, 190] and listed in Table 3-5.

Table 3-5: Values of parameters used in equations 3-7 and 3-8 [20, 55, 190]

A_o	-6.5314
A_1	0.072452
A_2	-0.23951×10-3
A_3	0.25493×10-6
B_o	-15.587
B_1	0.15915
B_2	-0.50612×10-3
B_3	0.5329×10-6

3.5.2 Adsorption kinetics [20]

Adsorption and desorption are time-dependent processes and the LDF model (linear driving force model) is commonly used to define adsorption and desorption rates as [20, 52, 73, 193]:

$$\frac{dx}{dt} = k_o \exp(-E_a/R_w T_{bed})(x_{eq} - x) \quad 3\text{-}9$$

$$k_o = \frac{FD_{so}}{R_p^2} \quad 3\text{-}10$$

F is a shape factor, R_p is the radius of the adsorbent particle, D_{so} is pre-exponential constant (m^2/s). The kinetics constants of Equation 3-9 for the case of AQSOA-Z02 were reported by Youssef et al. [173] and listed in Table 3-6.

Table 3-6: LDF equation constants of AQSOA-Z02/water [20, 173]

Parameter	$PP > 0.1$	$PP \leq 0.1$	Unit
E_a	17709.8	44423.5	J/mole
k_o	3.23E+04	1.85E+04	1/s

PP: partial pressure

For CPO-27(Ni) the constants of equation 3-9 are taken from [70] and listed in Table 3-7.

Table 3-7: LDF equation constants of CPO-27(Ni)/water [70]

Parameter	PP<0.2	PP>0.2
R_P	0.12×10^{-3}	0.12×10^{-3}
D_{so}	7.83×10^{-8}	7.467×10^{-10}
E_a	3.2×10^{4}	1.48×10^{4}
F	15	15

PP: partial pressure

For MIL101(Cr) the kinetics constants are obtained by fitting, the experimental data with a range of partial pressure between 0% to 95% and three isotherms temperatures at 25, 35, and 45 °C to the LDF equation as shown in Figure 3-10, Figure 3-11, and Figure 3-12. Good agreements between the experimental and the numerical uptake (with a maximum deviation of 13%) are achieved while the constants are obtained from the fittings and are listed in Table 3-8. For Al-Fumarate the constants of equation 3-9 are taken from [175], where k_o=1.29 1/s and E_a=18026 J/mole [20].

Table 3-8: Fitted LDF equation constants of MIL101(Cr)/water [20]

Parameter	0.5 ≥ PP ≥ 0.4	Else	Unit
E_a	27612	19610	J/mole
k_o	10	3.25	1/s

PP: partial pressure

For Silica-gel the constants of equation 3-9 are: k_o= 1.3183 E+05 1/s, and E_a= 42000 J/mole, and they are taken from [20, 21, 52, 55].

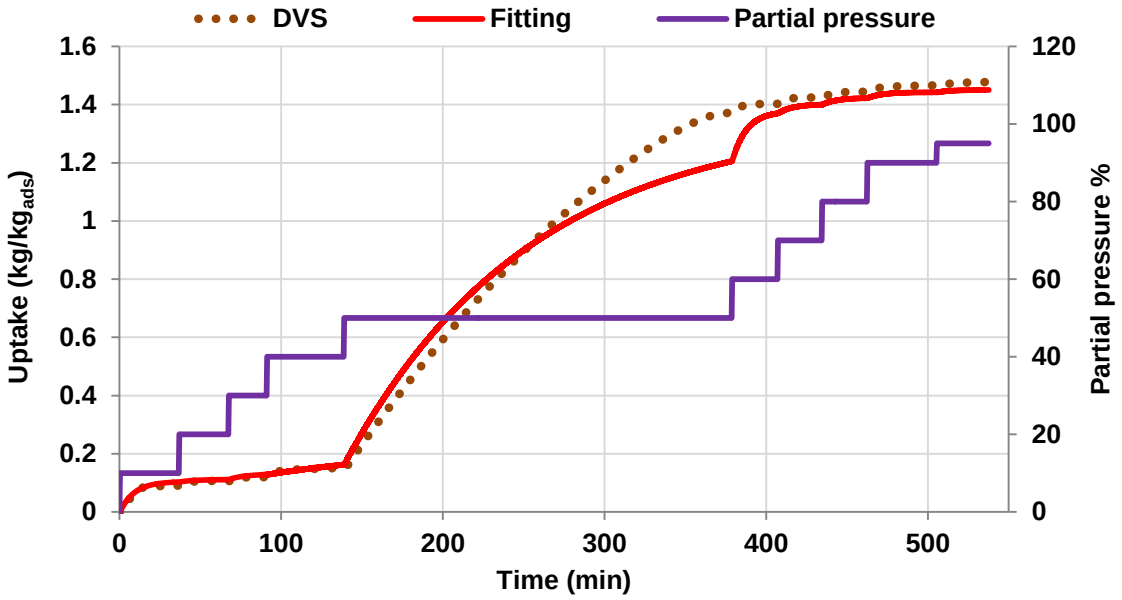

Figure 3-10: Kinetics fitting of MIL101(Cr)/water for the experimental and predicted uptake at 25 °C

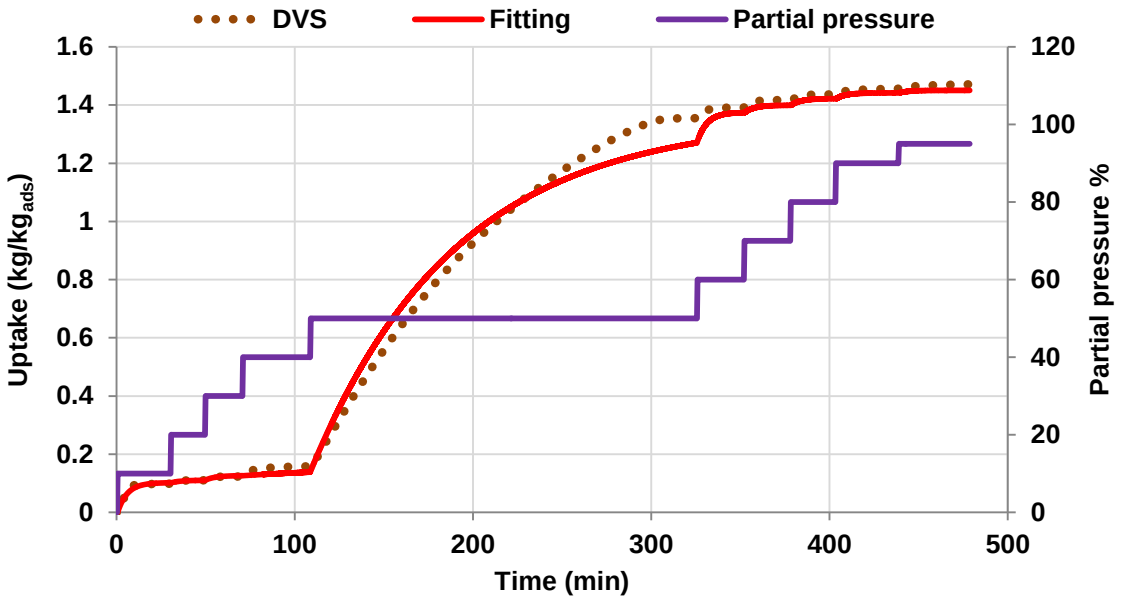

Figure 3-11: Kinetics fitting of MIL101(Cr)/water for the experimental and predicted uptake at 35 °C

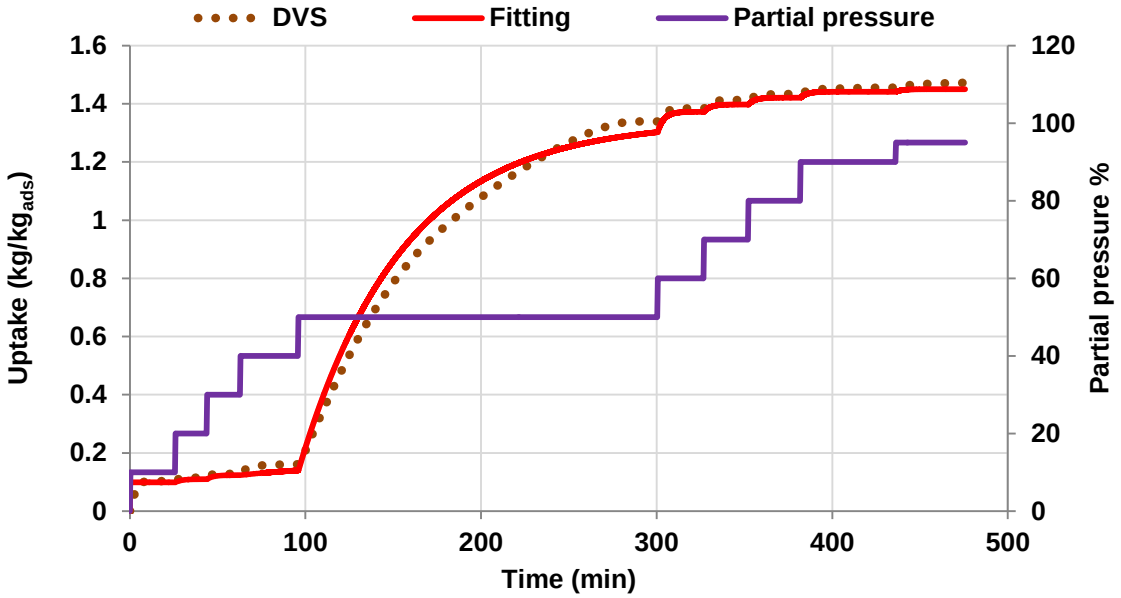

Figure 3-12: Kinetics fitting of MIL101(Cr)/water for the experimental and predicted uptake at 45 °C

3.6 Experimental results discussions

In this study, the characteristics of two advanced adsorption pairs namely AQSOA-Z02/water (adsorption isotherms), and MIL101(Cr)/water (adsorption isotherms and kinetics) is carried out using experimental data taken from the DVS analyser [20]. The predicted data and the experimental results from the DVS analyser showed good agreements as shown in Figure 3-8 for the isotherms of AQSOA-Z02/water and in Figure 3-9, Figure 3-10, Figure 3-11, and Figure 3-12 for the isotherms and kinetics of MIL101(Cr)/water [20].

Figure 3-13 and Figure 3-14 compare the experimental adsorption isotherms of the four advanced adsorption pairs to those of Silica-gel at two different temperatures of 25 °C and 35 °C. MOFs MIL101(Cr)/water showed a superior water uptake of about 1.47 kg/kg_{ads} due to its high porosity and internal surface area compared to other materials [20]. However, in this pair, the maximum uptake happened at a partial pressure of around 50%, which does not meet the requirements of the adsorption cooling systems that need low partial pressure between 30% and 40% for adsorption process [20]. On the other hand, the remaining adsorption pairs reach their maximum uptake at a partial pressure less than 40%. Adsorption systems (either for cooling, power or desalination) are dynamic systems, hence the adsorption isotherms analysis is not enough and the kinetics analysis is important as in such systems, the adsorption uptake is a time-dependent variable.

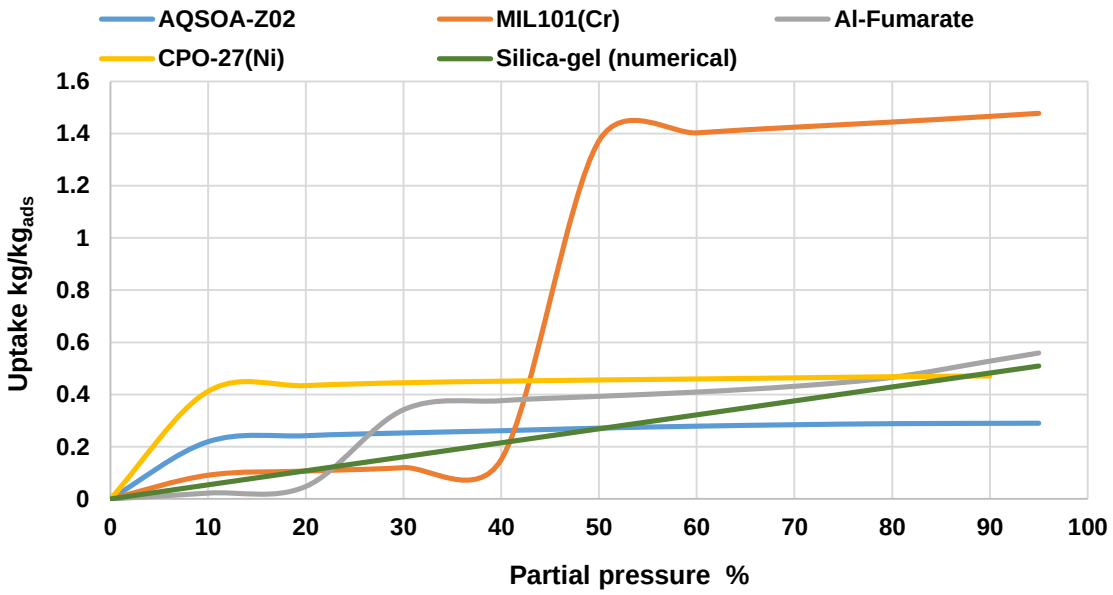

Figure 3-13: Experimental water adsorption isotherms for different adsorbent materials compared to Silica-gel (from simulation) at 25 °C

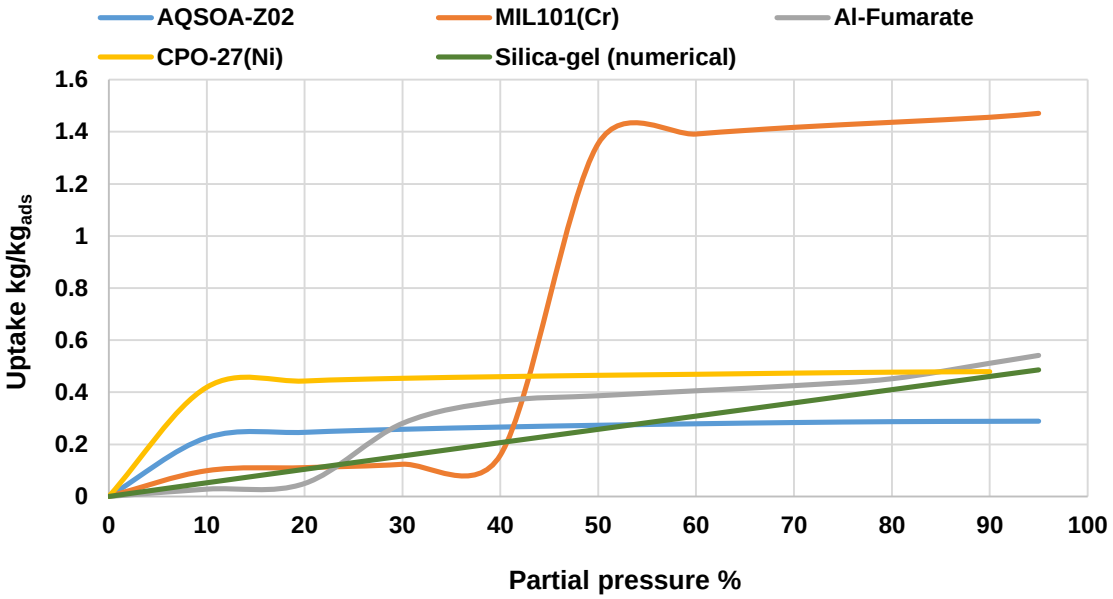

Figure 3-14: Experimental water adsorption isotherms for different adsorbent materials compared to Silica-gel (from simulation) at 35 °C

Figure 3-15 and Figure 3-16 show the experimental kinetics for AQSOA-Z02, MIL01(Cr), CPO-27(Ni) and Al-Fumarate with water at 25 °C and 35 °C respectively. It can be seen that

Al-Fumarate is very slow compared to the other materials and it takes about 6000 minutes to reach about 80% of its maximum value.

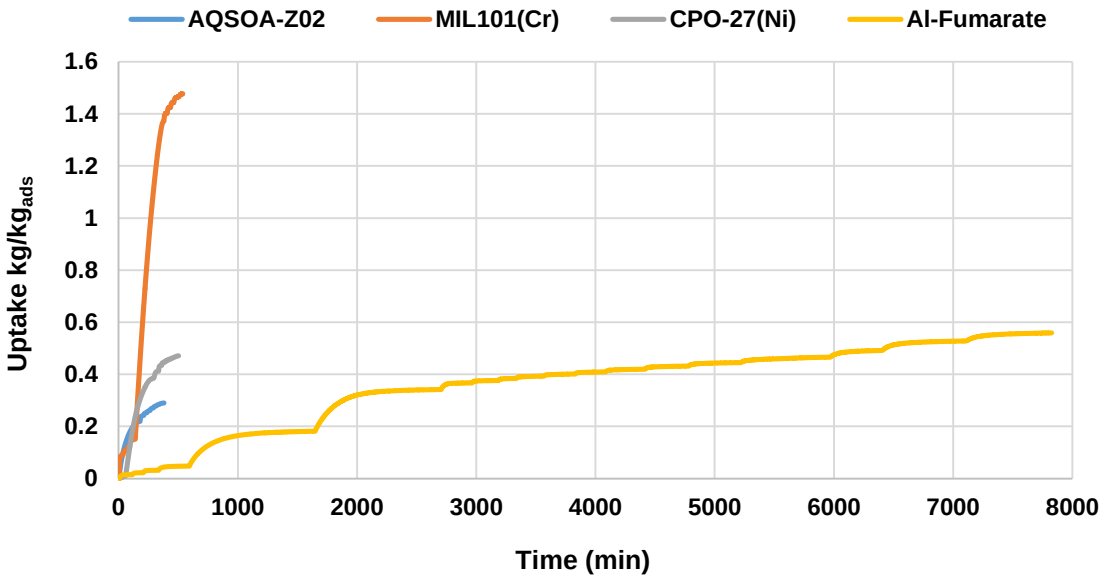

Figure 3-15: Experimental water adsorption kinetics for different adsorbent materials at 25 °C

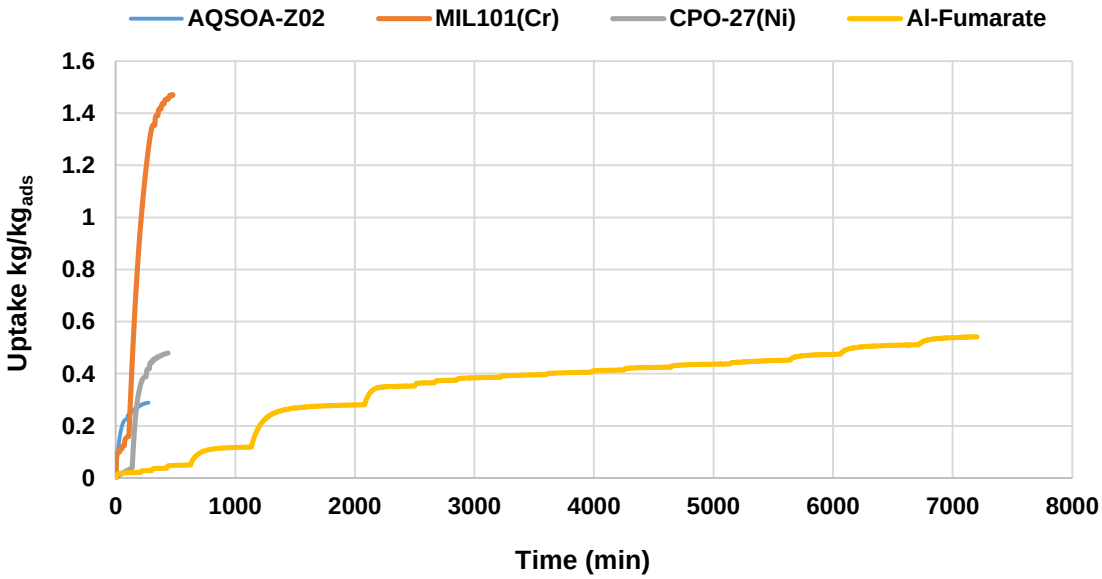

Figure 3-16: Experimental water adsorption kinetics for different adsorbent materials at 35 °C

Figure 3-17 compares the kinetics uptake of the AQSOA-Z02, MIL01(Cr) and CPO-27(Ni) at 35 °C. Although MIL01(Cr) and CPO-27(Ni) show higher maximum uptake compared to AQSOA-Z02, this material has faster kinetics than MIL01(Cr), and CPO-27(Ni). AQSOA-Z02 takes about 100 minutes to reach its maximum value of water uptake compared to MIL01(Cr), and CPO-27(Ni) which take about 250 and 200 minutes respectively to reach about 80% of their maximum water uptake. As there is a certain time for the adsorption/desorption process in the dynamic adsorption system, faster materials like AQSOA-Z02 has more chance to achieve higher uptake compared to the other materials.

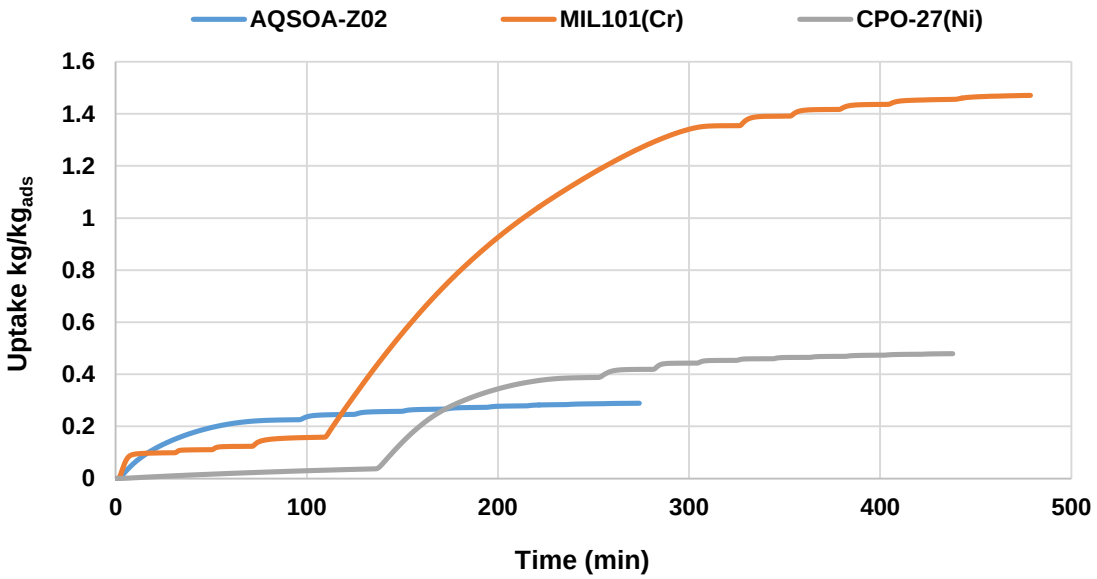

Figure 3-17: Experimental water adsorption kinetics for AQSOA-Z02/water, MIL101(Cr) and CPO-27(Ni) at 35 °C

However, in typical adsorption cooling systems, the partial pressure does not reach very low values like 0% or high values like 50%, but it changes from the partial pressure of the adsorption process (around 30% to 40%) to the partial pressure of the desorption process (around 10% or less). Figure 3-18 compares kinetics and partial pressure for AQSOA-Z02/water and CPO-27(Ni)/water at 35 °C. CPO-27(Ni) can outperform AQSOA-Z02 if the

desorption partial pressure reaches the value of 5% which is more likely to happen at high desorption temperature and the water uptake difference is between Max and Min 1 (grey). If the desorption partial pressure cannot reach 5%, which is likely to happen at low desorption temperatures, then the uptake difference is between Max and Min 2 (grey), which is low compared to the previous case. As a result, CPO-27(Ni) can outperform AQSOA-Z02 at a high driving temperature and the opposite is true at low driving temperature.

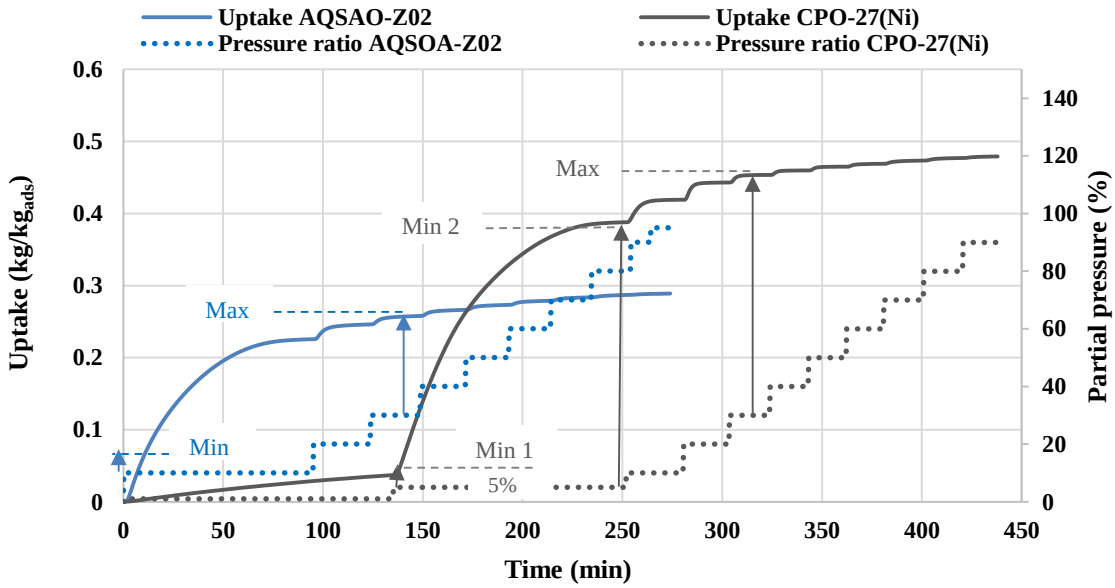

Figure 3-18: Experimental water adsorption kinetics and partial pressure for AQSOA-Z02 and CPO-27(Ni) at 35 °C

3.7 Summary

In this chapter, the water adsorption characteristics of four advanced physical adsorbent materials including MIL101(Cr), Al-Fumarate and CPO-27(Ni) MOFs, and AQSAOA-Z02 zeolite are presented and compared to Silica-gel. The experimental data from the DVS analyser is utilised to express the isotherms of the AQSOA-Z02/water, and isotherms and kinetics of the MIL101(Cr)/water. The results of the two characterized materials showed good agreements between the experimental and the predicted data. For the remaining adsorbent

materials, the adsorption isotherms and kinetics are available in the literature. Also, the experimental water uptake of the studied adsorbent materials was compared to Silica-gel and results showed that AQSOA-Z02 and CPO-27(Ni) are promising materials and CPO-27(Ni) can outperform AQSOA-Z02 at high heat source temperatures.

CHAPTER FOUR

SIMULATION OF ADSORPTION SYSTEM FOR COOLING AND ELECTRICITY (FIRST CONFIGURATION)

4.1 Introduction

Low-grade heat sources like solar thermal energy, industrial waste heat and geothermal energy can be an alternative to the traditional fossil fuel for producing electricity and cooling thus reducing the CO_2 emissions and global warming [20]. Such sources can be converted directly to produce cooling by means of clean technologies like absorption [194-196], and adsorption [126, 197, 198], or to generate electricity by using Kalina cycle and Organic Rankine cycle (ORC) [199-201]. In hot climate countries cooling and air conditioning consume a large proportion of the total electricity required for houses and offices, so it would be more practical to convert the heat energy into cooling and electricity directly (instead of converting heat to electricity and then to cooling) and simultaneously to enhance the overall system performance and reduce the energy conversion losses. This chapter aims to investigate the feasibility of producing electricity in addition to the cooling produced by basic adsorption cooling system (BACS) through integrating an expander between the desorber bed and the condenser (ASCE) [20]. In addition, ASCE is investigated using multiple beds and hybrid system with four cascaded adsorber beds. Advanced water adsorbent materials with superior adsorption characteristics like CPO-27(Ni) and AQSOA-Z02 are used and compared to the

commonly used Silica-gel. Figure 4-1 shows the main arrangements of the adsorption system for cooling and electricity (ASCE) [20, 21, 65] used in this chapter.

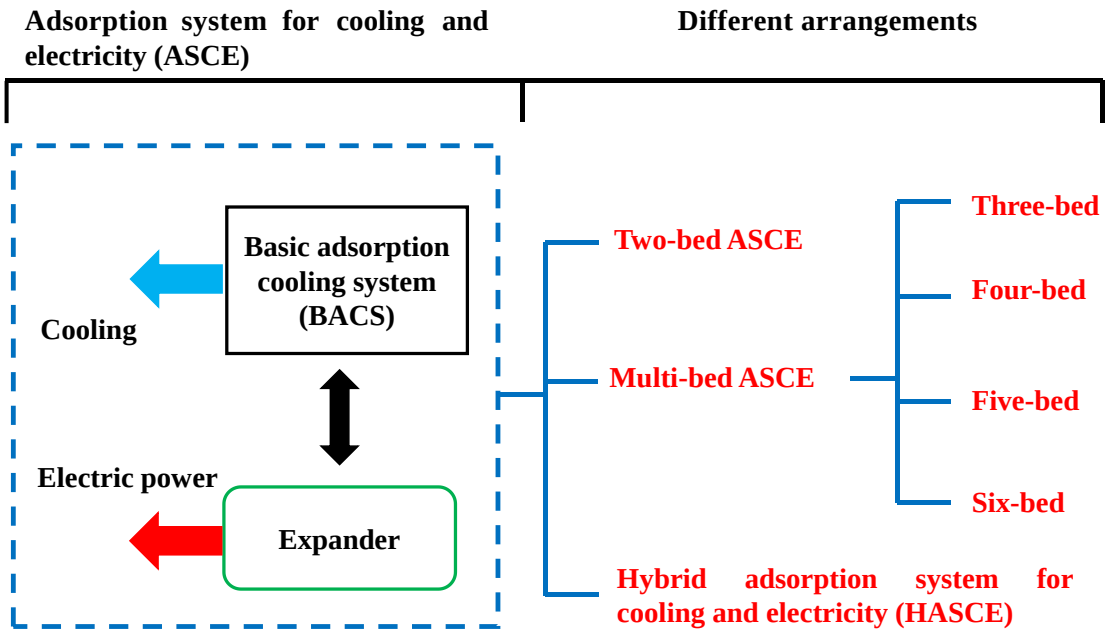

Figure 4-1: Adsorption system for cooling and electricity (ASCE) layout

4.2 Basic adsorption cooling system (BACS) [20, 21]

The basic adsorption cooling system (BACS) consists mainly of four components namely: adsorber (cold bed), desorber (hot bed), evaporator, and condenser [202]. Figure 4-2 (left) shows a schematic diagram of the BACS where cooling is needed to cool the adsorber through the adsorption process which is obtained from an external cooling sink CS, while heating is needed during the desorption process which is obtained from an external heat source HS [20, 21]. Subsequently, the condenser cools the hot water vapour coming from the desorber to provide the evaporator with the liquid refrigerant. Figure 4-2 (right) shows the BACS system on an isosteric diagram, where the system works in sequence through four processes [20, 21]. Process 1-2 is an isosteric heating (preheating process) and during this process, the heat is added to the desorber while all valves are closed. Process 2-3’ is a

constant pressure heating and during this process, the heating continues in the desorber (bed 1) meanwhile valve 1 is opened. Process 3'-4' is an isosteric cooling (precooling process) and through this process, the heat is rejected from the adsorber (bed 2) while all valves are closed [20, 21]. Finally, process 4'-1 is a constant pressure cooling and the cooling process continues in the adsorber while valve 4 is opened [20, 21]. Through the preheating process, the bed pressure increases from the pressure of the evaporator to the pressure of the condenser, while through the precooling process the bed pressure decreases from the pressure of the condenser to the pressure of the evaporator [20, 21]. Also, during the constant pressure heating process, the desorber bed is connected to the condenser to discharge the hot vapour refrigerant so that it can be cooled and condensed, while through the constant pressure cooling process, the adsorber bed is connected to the evaporator so that the vapour refrigerant can be sucked by the adsorbent material [20, 21]. These processes are repeated by switching between the two beds so that a continuous cooling effect can be achieved in the evaporator [20, 21, 65].

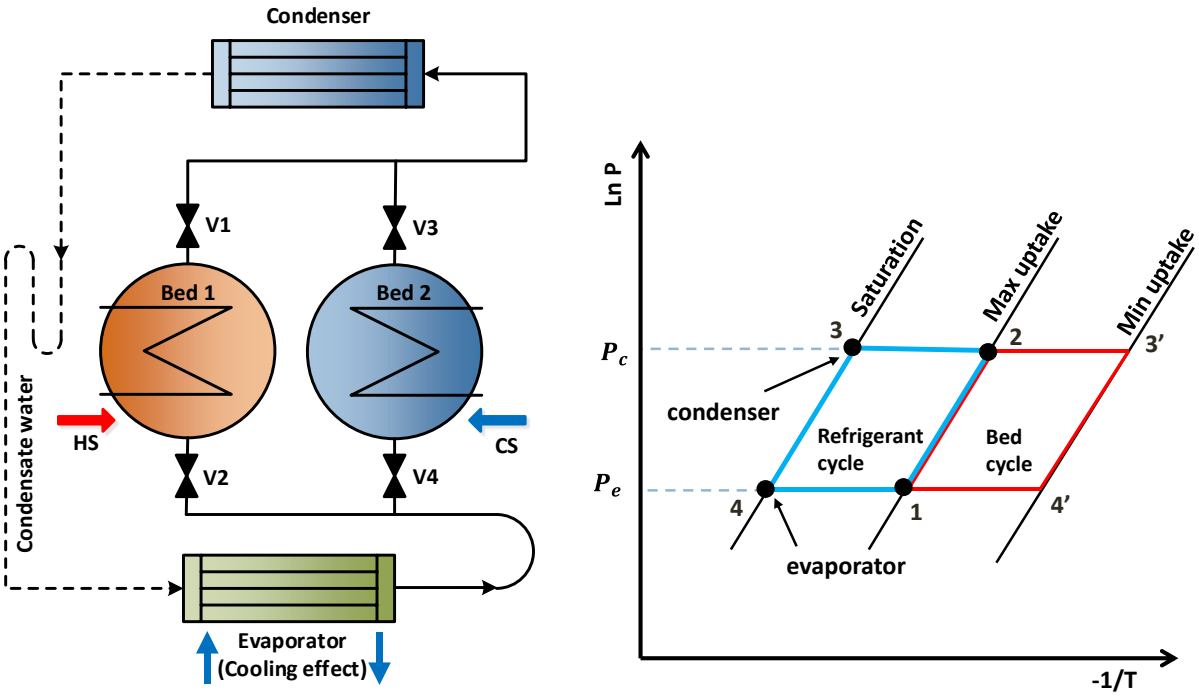

Figure 4-2: Basic two-bed adsorption cooling system (left) schematic diagram (right) isosteric diagram

4.3 Adsorption system for cooling and electricity (ASCE) [20, 21]

The basic adsorption cooling system BACS can be modified to generate cooling and electricity (electric power) simultaneously by incorporating an expander within the cycle [20, 21]. However, adding the expander is not sufficient to produce the electricity without producing a significant pressure difference between the desorber (hot bed) and the condenser and this can be obtained by making the pressure of the condenser lower than the pressure of the desorber (hot bed) [20, 21]. Figure 4-3 (left) illustrates a schematic diagram of the ASCE (modified two-bed cooling adsorption system) which contains adsorber, desorber, evaporator condenser, and expander (turbine) integrated between the desorber and the condenser. The modified system can work as BACS as shown in Figure 4-3 (right) to produce cooling only (1-2-x-4-5-1) and as ASCE (1-2-3-4-5-1) to generate electricity as well as cooling [20, 21, 28].

In the ASCE cycle, the process 1-2 is an isosteric heating (preheating process) and during this process, the heat is added to the desorber until reaching P_{max} at point 2 and during this process, all valves are closed [20, 21]. Process 2-x' is a constant pressure heating and during this process, the heating continues in the desorber meanwhile valve 1 is opened and desorption process is started in bed 1 which generates the cycle maximum pressure P_{max} while, bed 2 undertakes an adsorption process [20, 21]. Power can be generated, when the superheated refrigerant at point 2 (with pressure P_2) passes through the expander and leaves it at point 3 (with pressure P_3) as shown in Figure 4-3 (right) [20, 21]. The evaporator is always provided by the condensate refrigerant (water) coming from the condenser to absorb heat during the evaporation process as a result cooling effect can be generated. During switching time, all valves are closed and bed 1 undertakes an isosteric heating process (preheating),

while bed 2 undertakes an isosteric cooling process (precooling). The other ASCE cycle processes are similar to that of BACS processes shown in Figure 4-3 (left) [20, 21, 65].

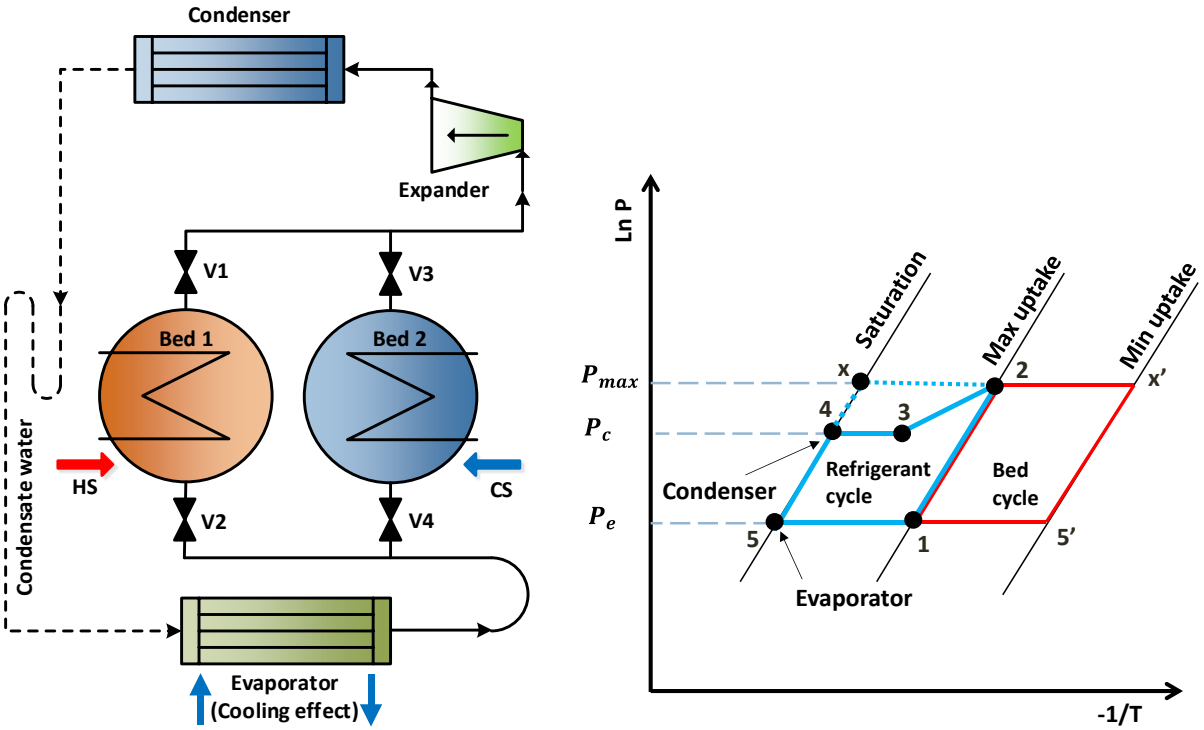

Figure 4-3: Two-bed adsorption system for cooling and electricity (ASCE), (left) schematic diagram, and (right) isosteric diagram

Figure 4-4 shows the expander expansion process on a T-s diagram where the process 2-3 is the actual expansion process, while the process 2-3s is an isentropic process [20, 21]. The maximum pressure at point 2 (P_2) as shown in Figure 4-3 (right) varies depending on the bed temperature during desorption process and the condenser temperature. As in Figure 4-4, the entropy at point 3s can be determined using steam tables corresponding to the condenser temperature. So, as the entropy at point 2 is equal to the entropy at point 3s ($s_2=s_{3s}$), the maximum pressure (P2) can be obtained [20, 21].

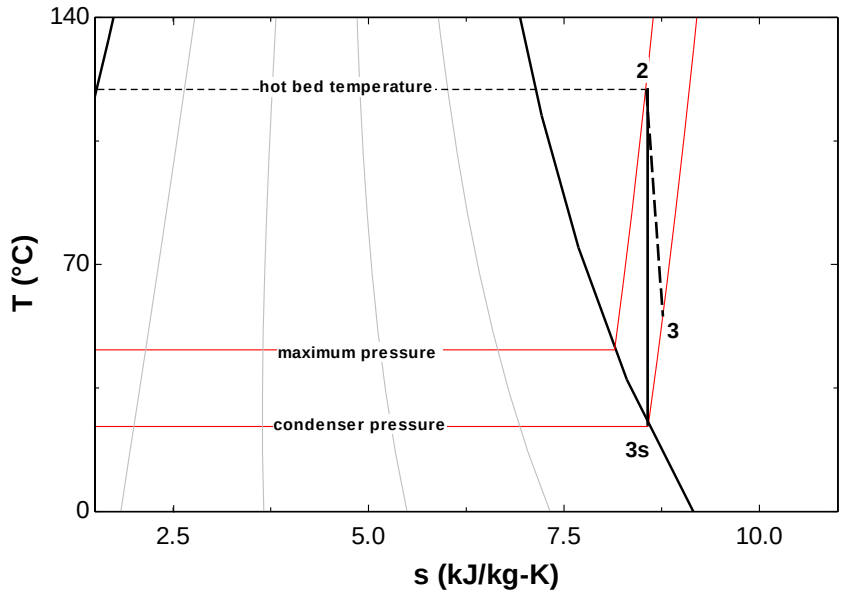

Figure 4-4: The expansion process on a T-s diagram utilising desorption temperature of 120 °C

4.4 Multi-bed adsorption system for cooling and electricity [20, 65]

Multi-bed adsorption system for cooling and electricity (Multi-bed ASCE) [65] has the same working principle of the two-bed ASCE as discussed in section 4.3. Instead of using two adsorber beds, a number of adsorber beds can be used in the same system as shown in Figure 4-5 [28, 65]. Usually in two-bed systems, adsorption time equals to desorption time .i.e. the adsorption/desorption (ads/des) time ratio R=1, (R = total switching and adsorption time /the total switching and desorption time) [65].

This section aims to investigate the effect of using multi-bed arrangements with a number of ads/des time ratio (R) on the overall system performance. For example, In the three-bed adsorption system with R=1/2 shown in Figure 4-5 (a), one bed is in adsorption process while the other two beds are in desorption process (with different starting time), also the opposite case is possible i.e. when the first bed is in desorption process and the other two beds can undertake an adsorption process [65]. The same concept can be used for the four-bed, five-

bed and six-bed systems as shown in Figure 4-5 (b), (c) and (d) with R of 1/3, 1/4 and 1/5 respectively [65].

Besides using two-beds (2B), three beds (3B), four beds (4B), five beds (5B) and six beds (6B) systems another two arrangements are investigated in this study. The first one is the four-bed system arrangement in parallel with R=1 as shown in Figure 4-5 (e), while the other one uses six-bed arrangement in parallel with R=1/2 as shown in Figure 4-5 (f) [65]. Thus, 9 different cases including 7 different bed arrangements and 7 ads/des time ratios are investigated to find the best bed arrangement and ads/des time ratio in terms of coefficient of performance, specific cooling power and specific power output [65].

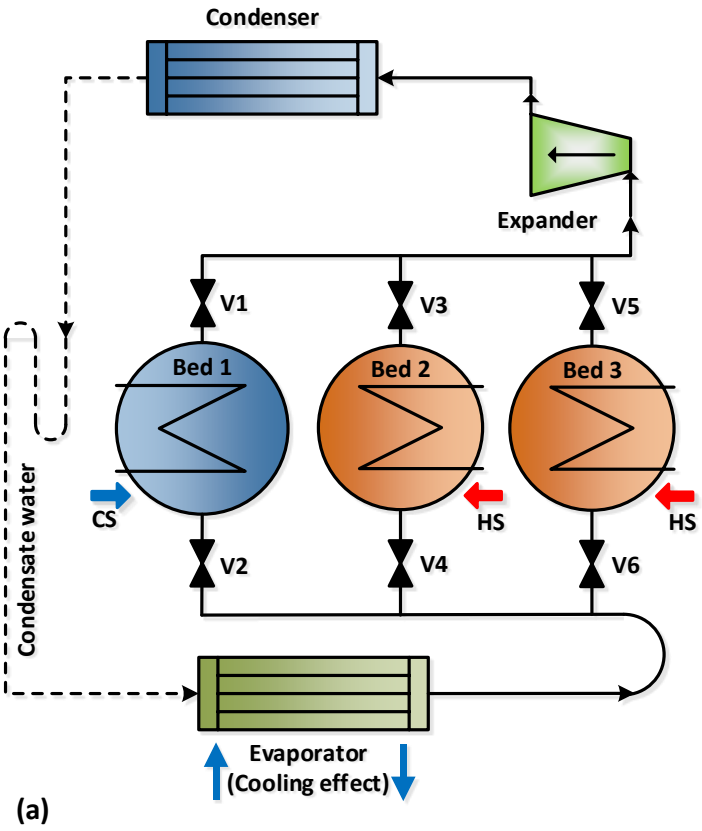

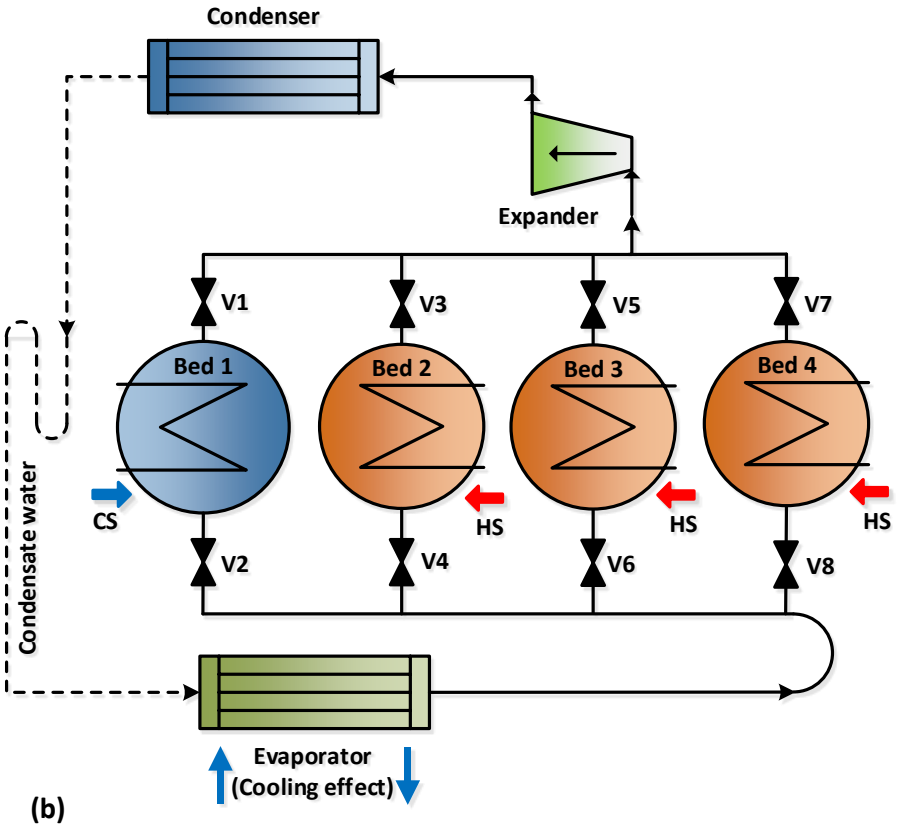
Condenser
Expander
V1
V3
V5
V7
Bed 1
Bed 2
Bed 3
Bed 4
CS
HS
HS
HS
V2
V4
V6
V8
Condensate water
Evaporator
(Cooling effect)

(b)

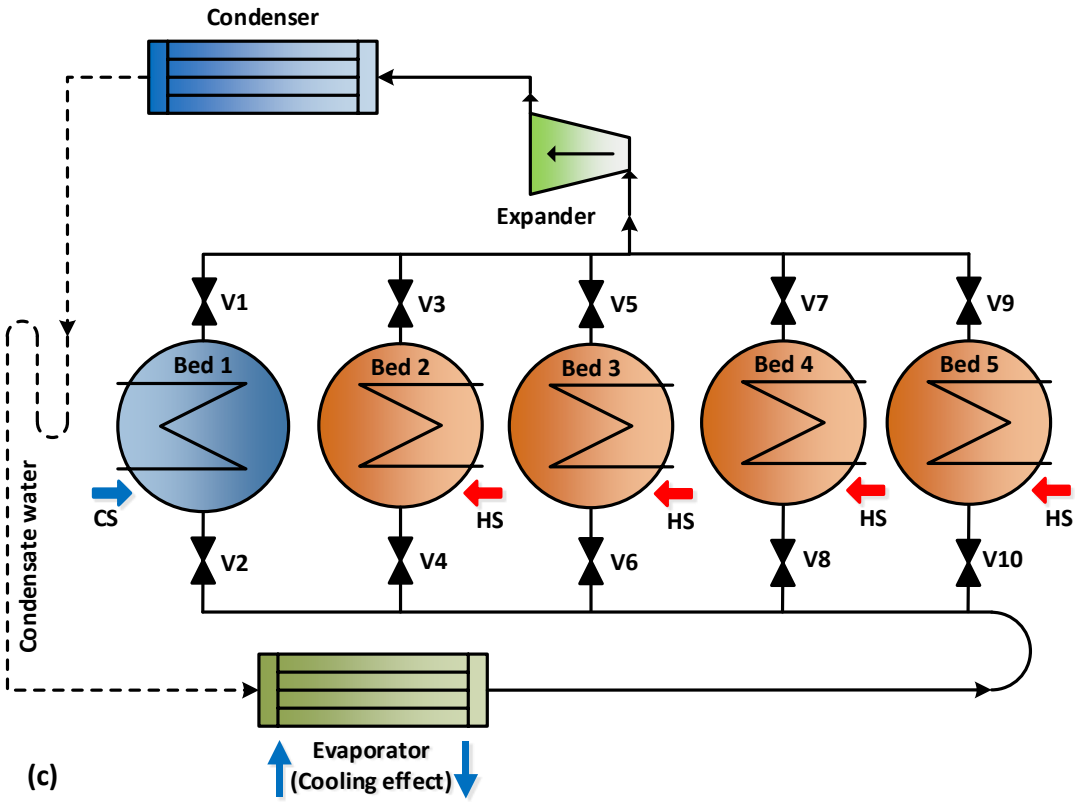
Condenser
Expander
V1
V3
V5
V7
V9
Bed 1
Bed 2
Bed 3
Bed 4
Bed 5
CS
HS
HS
HS
HS
V2
V4
V6
V8
V10
Condensate water
Evaporator
(Cooling effect)

(c)

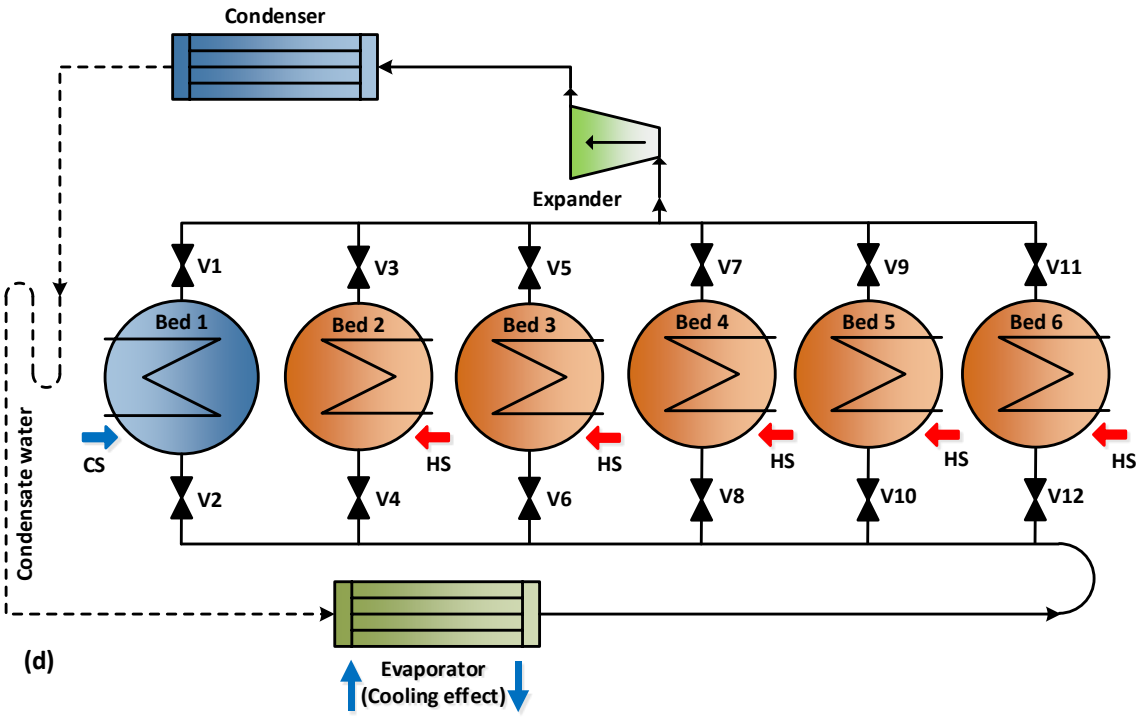
Condenser
Expander
V1
V3
V5
V7
V9
V11
Bed 1
Bed 2
Bed 3
Bed 4
Bed 5
Bed 6
CS
HS
HS
HS
HS
HS
V2
V4
V6
V8
V10
V12
Condensate water
Evaporator
(Cooling effect)

(d)

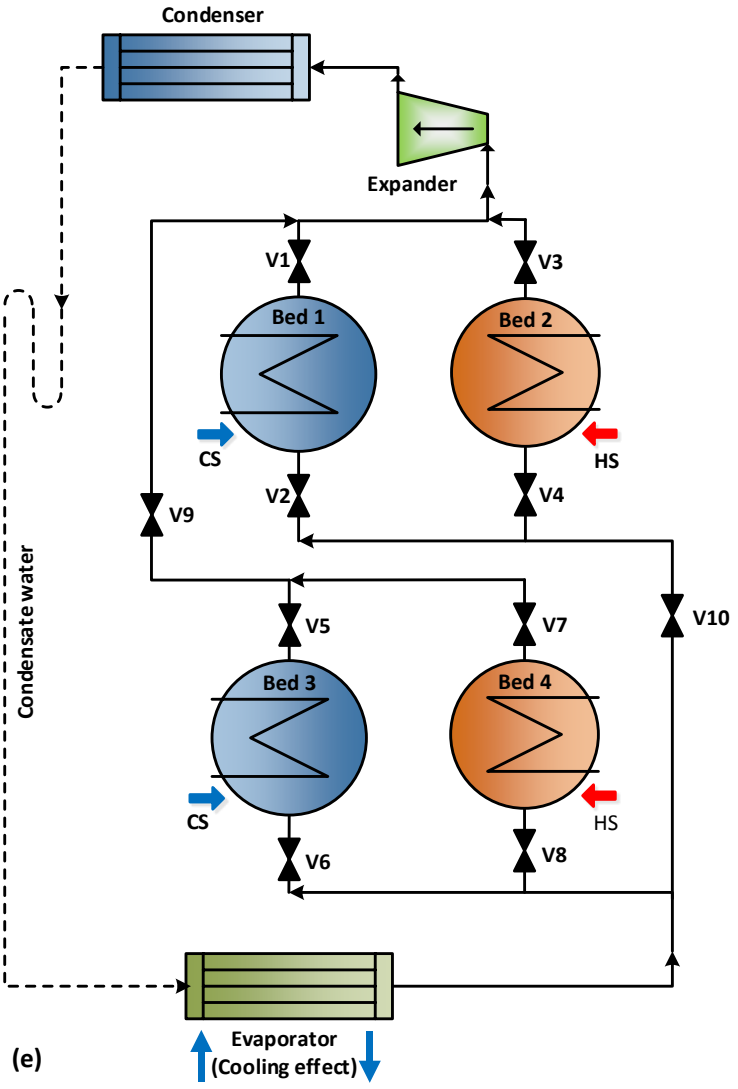
Condenser
Expander
V1
V3
Bed 1
Bed 2
CS
HS
V2
V4
V9
V5
V7
V10
Bed 3
Bed 4
CS
HS
V6
V8
Condensate water
Evaporator
(Cooling effect)

(e)

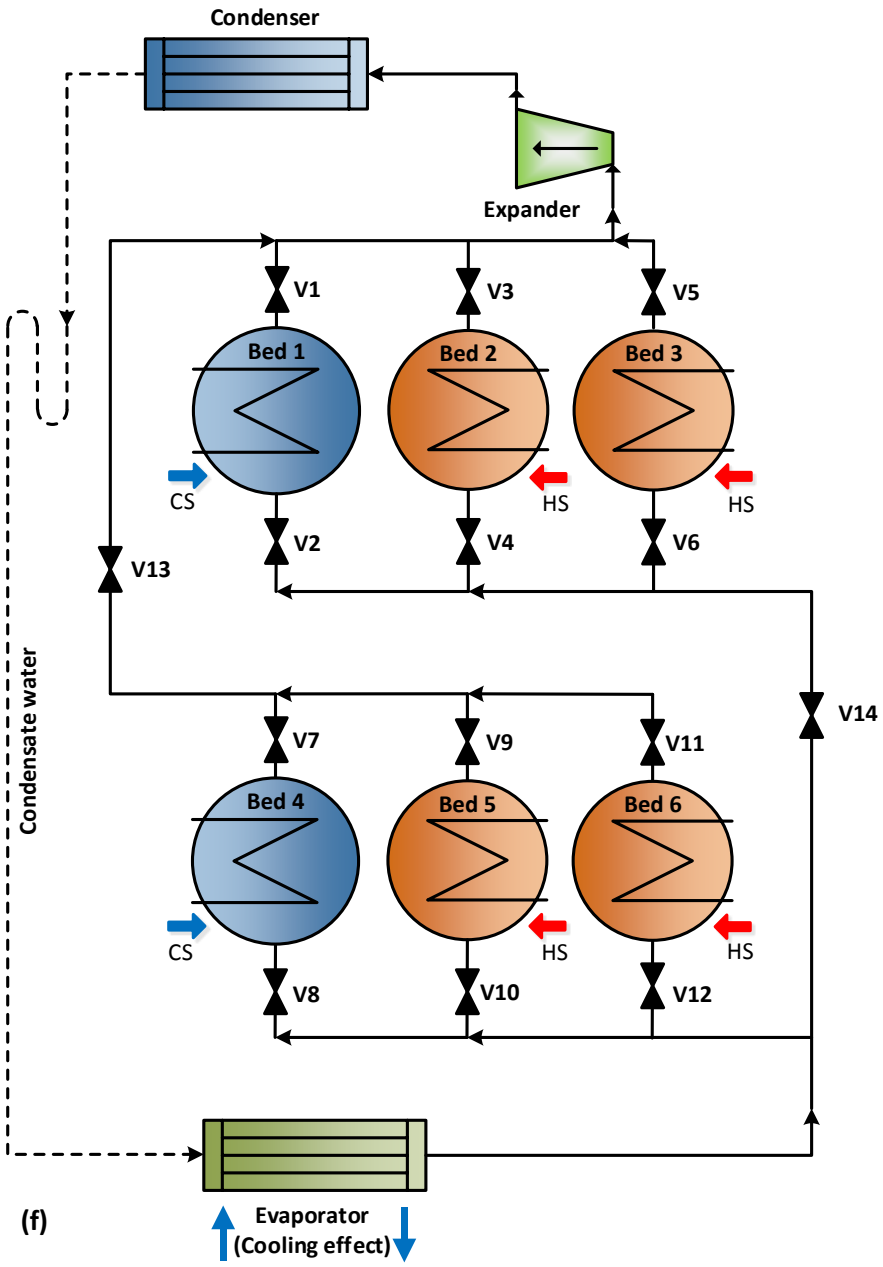

Figure 4-5: Multi-bed ASCE schematic diagram (a) three-bed (b) four-bed in series (c) five-bed (d) six-bed in series (e) four-bed in parallel and (f) six-bed in parallel

4.5 Mathematical model

4.5.1 Adsorbent material characteristics [20, 65]

Four advanced water adsorbents namely Al-Fumarate, CPO-27(Ni), MIL101(Cr) MOFs, and AQSOA-Z02 zeolite are investigated and their performance are compared to that of the conventional Silica-gel [20, 65]. The experimental data from the DVS analyser is utilised to define the water adsorption characteristics of the AQSOA-Z02, and MIL101(Cr). For Silica-gel, Al-Fumarate, and CPO-27(Ni), the adsorption isotherms and kinetics are obtained from the literature as described in details in Chapter 3 [20, 65].

4.5.2 System energy balance [20, 65]

Lumped parameter modelling method is used to define the energy balance in adsorber beds, where the bed is assumed to be at constant temperature [20, 52, 65, 73, 203, 204].

$$(MC_p)_{bed,eff}\frac{dT_{bed}}{dt} + (M_a x c_p)\frac{dT_{bed}}{dt} = \varphi M_a \left(\frac{dx}{dt}\right)(Q_{st}) - (\dot{m}C_p)_j(T_{j,o} - T_{j,in}) \quad 4\text{-}1$$

Symbols T, M, C_p and t refer to temperature (K), mass (kg), specific heat capacity (J/kg.K), and time (s) respectively. The symbol φ is a flag that has the value of zero at switching process and it has the value of one at adsorption/desorption process. Also, $\dot{m}$ refers to the mass flow rate (kg/s), Q_{st} is the isosteric heat of adsorption (J/kg), while x is the water uptake (kg/kg_{ads}). Subscript (j) refers to cooling/heating process during adsorption/desorption process. Also, subscripts (in) and (o) refer to the fluid inlet and outlet respectively and the subscript (eff) represents the effective value [20, 65].

The first term of the equation 4-1 (left side) denotes the energy capacity of the bed heat exchanger including the heat exchanger materials and the adsorbent material, while the second term of the left side represents the water energy capacity. Also, in the right side of equation 4-1, the first term shows the heat of adsorption [20, 65]. The second term represents the rejected heat to the cooling fluid during the adsorption process or the added heat from the heating fluid during the desorption process [20, 65]. The bed outlet temperature can be expressed as [20, 65, 73, 203].

$$T_{j,o} = T_{bed} + \left(T_{j,in} - T_{bed}\right)\exp\left[\frac{-(UA)_{bed}}{(\dot{m}c_p)_j}\right] \quad 4\text{-}2$$

U refers to the overall heat transfer coefficient (W/m^2/K), while A refers to the surface area of the adsorber bed (m^2) [20, 65].

The evaporator energy balance can be written as [20, 53, 55, 62, 65].

$$\left(MC_p\right)_{evap,eff}\frac{dT_{evap}}{dt} = \varphi h_{fg} M_a \frac{dx_{ads}}{dt} - (\dot{m}c_p)_{evap}\left(T_{chill,o} - T_{chill,in}\right) - (c_p)_w(T_{cond} - T_{evap})M_a\frac{dx_{des}}{dt} \quad 4\text{-}3$$

The symbol h_{fg} is the heat of vaporization and it has a negative value as heat is released by the system during vaporization process (J/kg), M_a refers to the adsorbent material mass (kg), and the subscripts (evap), (chill), (ads), (des) and (w) refer to the evaporator, chilled water, adsorption process, desorption process and water respectively.

The outlet chilled water temperature is expressed as [20, 53, 62, 65, 193].

$$T_{chill,o} = T_{evap} + \left(T_{chill,in} - T_{evap}\right)\exp\left[\frac{-(UA)_{evap}}{(\dot{m}c_p)_{evap}}\right] \quad 4\text{-}4$$

The mass balance in the evaporator is expressed as [20, 53, 65, 73, 193, 203].

$$\frac{dM_{ref}}{dt} = -M_a\left[\frac{dx_{des}}{dt} + \frac{dx_{ads}}{dt}\right] \quad 4\text{-}5$$

The subscript (ref) refers to the adsorption refrigerant (water).

The condenser energy balance equations are given as [20, 53, 55, 62, 65, 205].

$$(MC_p)_{cond,eff}\frac{dT_{cond}}{dt} = \varphi h_{fg} M_a \frac{dx_{des}}{dt} - (\dot{m}c_p)_{cond}\left(T_{w,o} - T_{w,in}\right) - \left(c_p\right)_w (T_{exp} - T_{cond}) M_a \frac{dx_{des}}{dt} \quad 4\text{-}6$$

The subscripts (des), and (cond), refer to desorption process, and condenser respectively.

The condenser cooling water outlet temperature can be written as [20, 53, 62, 65].

$$T_{w,o} = T_{cond} + \left(T_{w,in} - T_{cond}\right)\exp\left[\frac{-(UA)_{cond}}{(\dot{m}c_p)_{cond}}\right] \quad 4\text{-}7$$

The mechanical power produced in the expander (turbine), can be written as below [65]:

$$W_{exp,ads} = \frac{\int_0^{t_{cycle}} \dot{m}_{ads}\Delta h dt}{t_{cycle}} \quad 4\text{-}8$$

Where, h refers to the enthalpy through the expander and $\dot{m}_{ads}$ is the expander mass flow rate, the expansion process is assumed to be ideal in this thermodynamic study. The overall performance of the ASCE can be defined using the terms specific cooling power (SCP), specific power (SP), coefficient of performance (COP), adsorption power efficiency (η_{ads}),

equivalent coefficient of performance (COPe) and equivalent specific cooling power (SCPe) as written in equations 4-9 to 4-17 [20, 21, 65].

$$COP = \frac{(\dot{m}c_p)_{evap}\int_0^{t_{cycle}}(T_{chill,in}-T_{chill,o})dt}{(\dot{m}c_p)_h\int_0^{t_{cycle}}(T_{h,in}-T_{h,o})dt} \quad 4\text{-}9$$

The subscript (h) refers to the heat source.

$$SCP = \frac{(\dot{m}c_p)_{evap}\int_0^{t_{cycle}}(T_{chill,in}-T_{chill,o})dt}{M_a t_{cycle}} \quad 4\text{-}10$$

$$SP = \frac{\int_0^{t_{cycle}}\dot{m}_{ads}\Delta h dt}{M_a t_{cycle}} \quad 4\text{-}11$$

The symbol Δh refers to the enthalpy difference through the adsorption expander (J/kg).

Adsorption power efficiency (η_{ads}) is defined as the ratio of the mechanical power output generated in the adsorption expander to the total heat added to adsorber bed during heating process during the cycle time and it can be written as:

$$\eta_{ads} = \frac{\int_0^{t_{cycle}}\dot{m}_{ads}\Delta h dt}{(\dot{m}c_p)_h\int_0^{t_{cycle}}(T_{h,in}-T_{h,o})dt} \quad 4\text{-}12$$

The symbol $\dot{m}_{ads}$ refers to the adsorption refrigerant mass flow rate passing through the expander.

$$COPe = \frac{(\dot{m}c_p)_{evap} \int_0^{t_{cycle}} (T_{chill,in} - T_{chill,o})dt + F[\int_0^{t_{cycle}} \dot{m}_{ads}\, \Delta h dt]}{(\dot{m}c_p)_h \int_0^{t_{cycle}} (T_{h,in} - T_{h,o})dt} \quad 4\text{-}13$$

$$SCPe = \frac{(\dot{m}c_p)_{evap} \int_0^{t_{cycle}} (T_{chill,in} - T_{chill,o})dt + F[\int_0^{t_{cycle}} \dot{m}_{ads} \Delta h dt]}{M_a t_{cycle}} \quad 4\text{-}14$$

The term (η_{ads}) in equation 4-12 is used to represent the power generation efficiency of the adsorption system i.e. the ratio of the amount of mechanical power output generated by the expander incorporated within the adsorption system to the total heat consumed by the adsorber beds [65]. The term COPe and SCPe are used to compare the performance of ASCE to the two-bed basic adsorption cooling system (BACS) [65]. F is a factor equivalent to the typical COP of vapour compression refrigeration system, assumed to be 3 [64, 65] in this work. This factor is used to convert the power generated by adsorption system into cooling energy in order to compare between ASCE system and the basic adsorption cooling system (BACS). Using the second law of thermodynamics, exergy efficiency is the ratio between the output exergy to the input exergy and it is used to highlight the grade difference between cooling and power generated by the ASCE used in this study [65]. The exergy efficiency can be defined as [10, 65, 106]:

$$\eta_{ex=} \frac{W_{exp,ads} + E_{evap}}{E_{in}} \quad 4\text{-}15$$

Where E_{evap} is the cooling exergy through the evaporator and can be defined as [65, 206-208]:

$$E_{evap}=\frac{(\dot{m}c_p)_{evap}\int_0^{t_{cycle}}(T_{chill,in}-T_{chill,o})dt}{t_{cycle}}\left[\frac{T_{amb}}{T_{evap}}-1\right] \quad 4\text{-}16$$

The subscript (amb) refers to ambient temperature. While, E_{in} is the exergy input to the system and can be defined as [10, 65, 106]:

$$E_{in}=\frac{\dot{m}_h\int_0^{t_{cycle}}[(h_{h,in}-h_{h,o})-T_{amb}(s_{h,in}-s_{h,o})]dt}{t_{cycle}} \quad 4\text{-}17$$

The symbol s refers to the entropy (J/kg.K).

Adsorption system for cooling and electricity (ASCE) proposed in this chapter is simulated using MATLAB Simulink software in order to study the possibility of generating cooling and electricity simultaneously [20, 65]. A number of MATLAB Simulink models are developed to investigate the effect of using various adsorber bed arrangements and operating parameters on the overall system performance of ASCE [20, 65]. Figure 4-6 shows the flowchart of the adsorbent bed which is a key component of the adsorption system for cooling and electricity (ASCE). Figure 4-7 shows the key steps used to solve the numerical model of ASCE which includes the energy balance equations of the main components of the system.

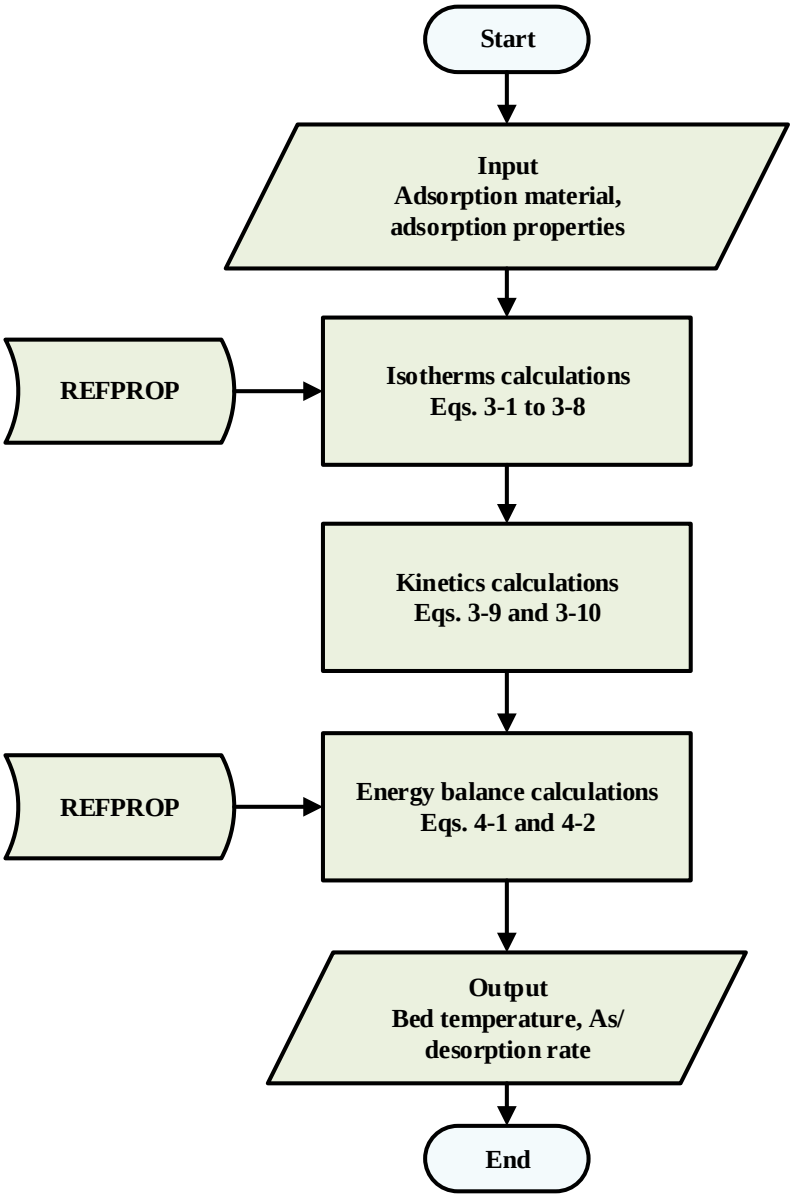

Figure 4-6: Flowchart of the absorbent bed model

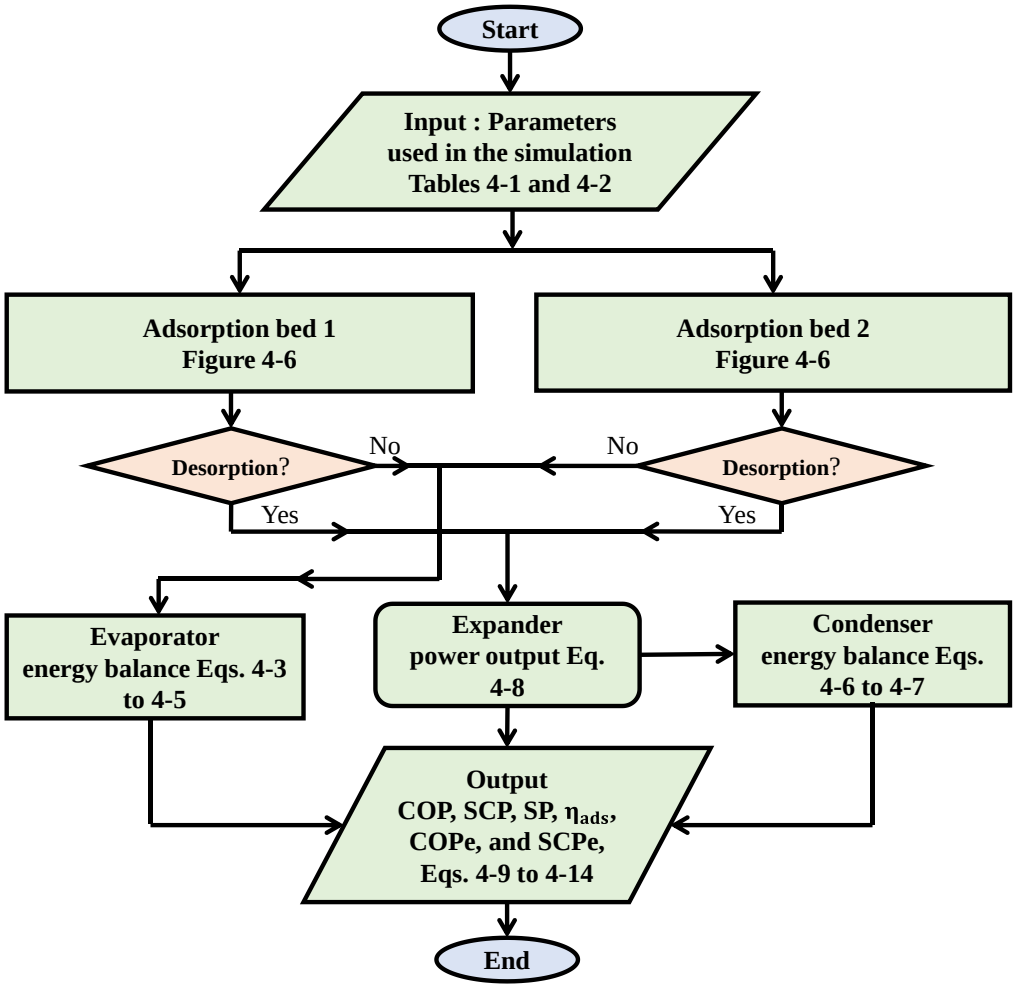

Figure 4-7: Flowchart of adsorption system for cooling and electricity ASCE model

4.6 Performance of ASCE [20, 65]

Table 4-1 shows the main operating conditions, and Table 4-2 shows the main characteristics of the bed heat exchanger, evaporator, and condenser used in this work. The data of Table 4-2 are taken from [20, 21, 65, 70, 209], but some parameters like number of tubes and module length are updated to meet the requirement of ASCE, where large bed size is required to increase the steam mass flow rate passing through the expander and the UA values of the three heat exchangers (bed, condenser and evaporator) are calculated within the numerical models.

Table 4-1: Parameters used in the simulation [20, 21, 65]

Heat source temperature ^{o}C	80-160
Bed cooling water temperature ^{o}C	28
Condenser cooling water temperature ^{o}C	28
Inlet chilled water temperature ^{o}C	18
Bed hot water mass flow rate kg/s	1.85
Bed cold water mass flow rate kg/s	1.85
Condenser water mass flow rate kg/s	0.85
Evaporator mass flow rate kg/s	0.85
Adsorption/desorption (half cycle) time s	324
Switching time s	20

Table 4-2: Adsorption system characteristics [20, 21, 70, 209]

Bed heat exchanger characteristics	
Fins length m	172E-3
Fins width m	30E-3
Fins pitch m	1.2E-3
Module length m	800E-3
Number of module	4
Number of pipes per module	6
Number of bypass	2
Pipe outside diameter m	15.875E-3
Pipe thickness m	0.8E-3
Condenser characteristics	
Pipe length m	5.5
Number of pipes	4
Pipe outside diameter m	15.875E-3
Pipe thickness m	0.8E-3
Evaporator characteristics	
Pipe length m	10
Number of pipes	4
Pipe outside diameter m	15.875E-3
Pipe thickness m	0.8E-3
Fins length m	40E-3
Fins thickness m	0.12E-3
Fins pitch m	1.2E-3

Four advanced adsorbent materials namely; Al-Fumarate, CPO-27(Ni), MIL101(Cr) and AQSOA-Z02, are studied and compared to the commonly used Silica-gel utilising heating

water temperature ranging from 80 to 160 °C [20, 65]. Silica-gel was not investigated at 140 and 160 °C as many researchers reported that Silica-gel can show high performance at a regeneration temperature of below 95 °C [210, 211] and Silica-gel can be damaged by heating the material above 120°C [212]. Also, high temperature heating is provided using pressurised water with properties evaluated using REFPROP database [20]. Figure 4-8 shows the output of the ASCE utilising AQSOA-Z02 with heat source temperature ($T_{heating}$) of 160 ºC, cooling temperature ($T_{cooling}$) of 28 ºC, and inlet chilled water temperature ($T_{chilled}$) of 18 ºC [20, 21]. The system can generate average power and cooling of about 1.06 kW and 10.58 kW respectively. Figure 4-9 shows the cooling and power that can be generated using CPO-27(Ni) with average power and cooling of about 1.1 kW and 11 kW respectively utilising heat source temperature of 160 ºC, cooling temperature of 28 ºC, and inlet chilled water temperature of 18 ºC [20, 21].

Figure 4-10 compares COP, SCP, and SP of the ASCE utilising Al-Fumarate/water, MIL101(Cr)/water, AQSOA-Z02/water, and CPO-27(Ni)/water at heat source temperature of 160 °C to that using chemical adsorption pairs like $CaCl_2$/ammonia reported in [16] and $FeCl_2$-$BaCl_2$/ammonia reported in [14]. Results show that the advanced physical adsorbent materials adopted in this study are more efficient than the chemical adsorbent materials adopted in [14, 16]. The cooling COP achieved by CPO-27(Ni) is more than two times that of the chemical materials, also CPO-27(Ni) achieved SCP and SP of 800 W/kg_{ads} and 80 W/kg_{ads} respectively compared to 182 W/kg_{ads} and 28 W/kg_{ads} of the chemical adsorbent materials reported in [14, 16].

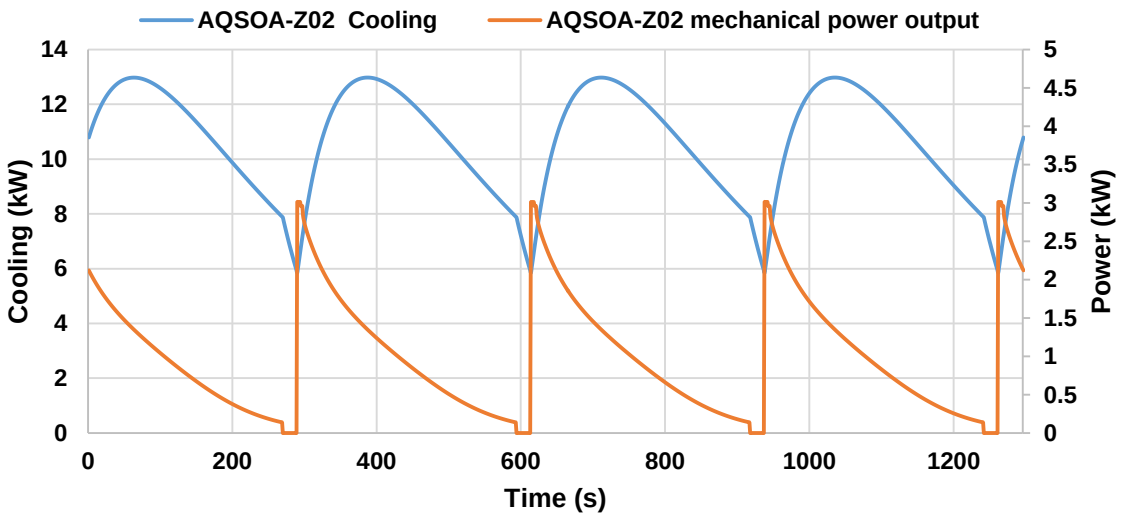

Figure 4-8: Two-bed AQSOA-Z02/water ASCE utilising $T_{heating}$=160 ºC, $T_{cooling}$=28 ºC and $T_{chilled}$=18 ºC using 8.24 kg of adsorbent per bed

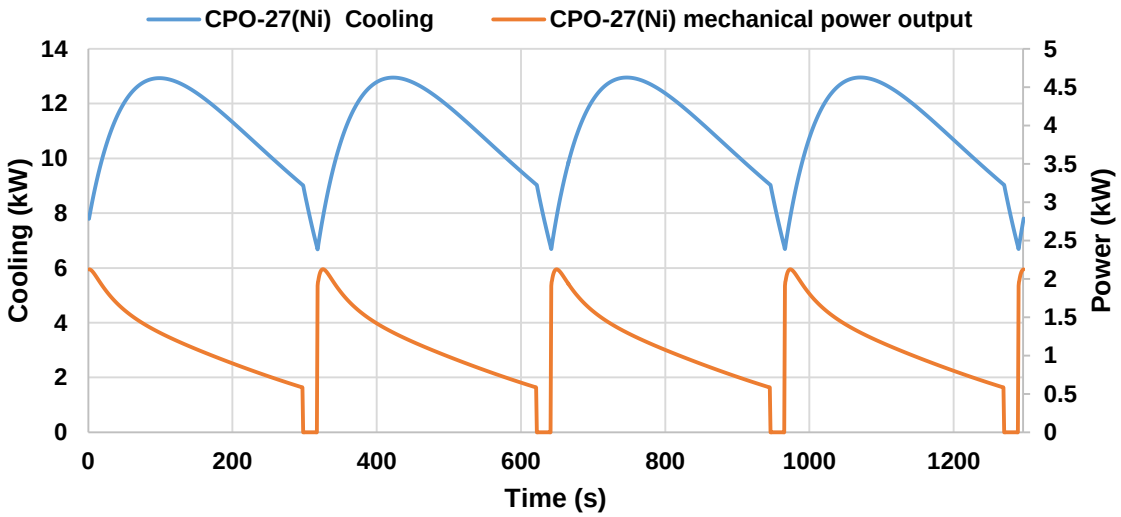

Figure 4-9: Two-bed CPO-27(Ni)/water ASCE utilising $T_{heating}$=160 ºC, $T_{cooling}$=28 ºC and $T_{chilled}$=18 ºC using 6.9 kg of adsorbent per bed

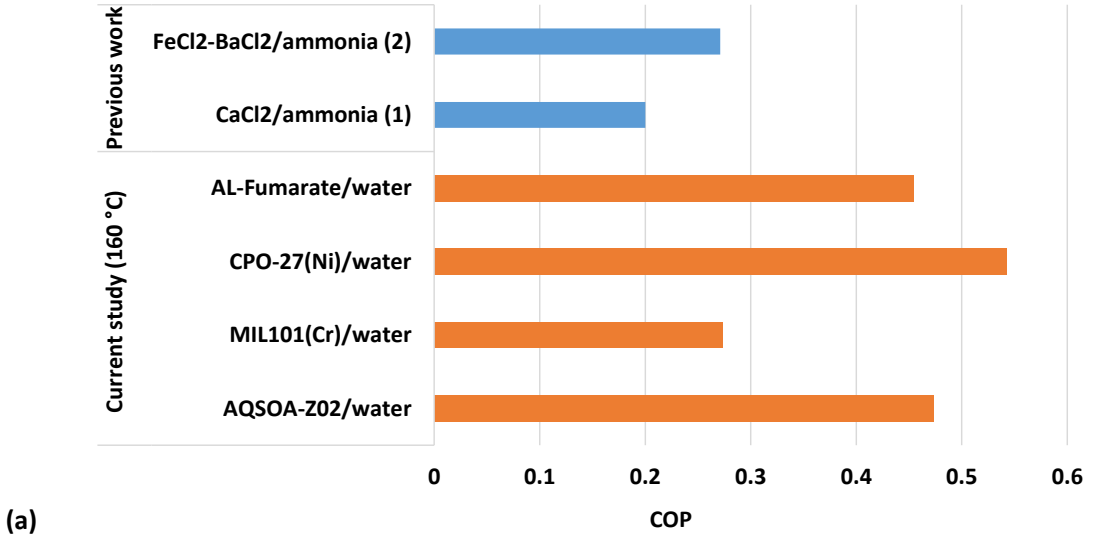

(a)

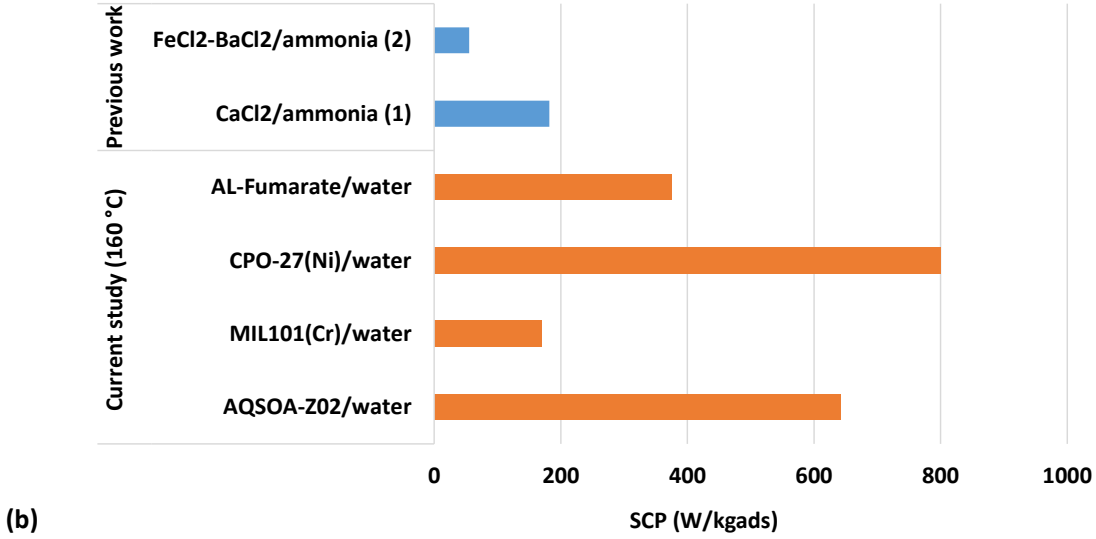

(b)

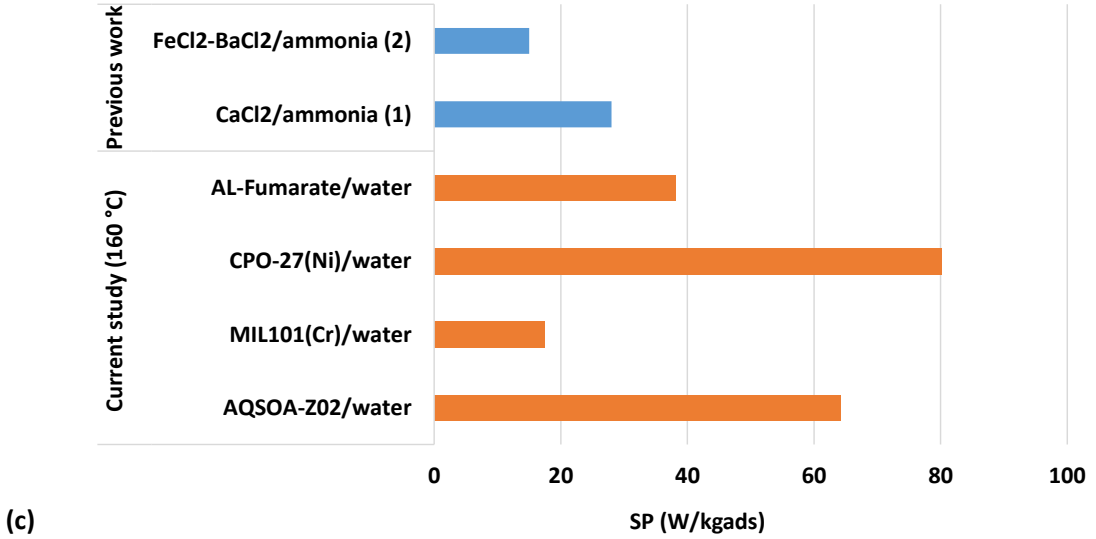

(c)

Figure 4-10: Comparison of (a) cooling COP (b) SCP (c) SP between the current study (ASCE) utilising $T_{heating}$=160 ºC and previous work (1) [16] and (2) [14]

Figure 4-11, Figure 4-12, and Figure 4-13 show a comparison between the ASCE and the BACS (using the same operating conditions including condenser temperature) in terms of COP/COPe, SCP/SCPe, and exergy efficiency for Silica-gel, AQSOA-Z02, MIL101(Cr), CPO-27(Ni), and Al-Fumarate with a range of heat source temperature. For cases of Silica-gel, MIL101(Cr), and Al-Fumarate COPe achieved by the ASCE is higher than the COP of BACS.

For AQSOA-Z02 and CPO-27(Ni), COPe of ASCE is higher than those of BACS at heating temperature higher than 120 °C and this is because of the additional power generated in ASCE. However, for AQSOA-Z02, and CPO-27(Ni) with heating temperature of 120 °C (or less), the COP of BACS is higher than COPe of ASCE and this is due to AQSOA-Z02, and CPO-27(Ni) show low performance with ASCE at low heat source temperatures. COPe of AQSOA-Z02, and CPO-27(Ni) achieved by ASCE at heat source temperature of 160 °C is about 28% and 24% higher than the COP of BACS respectively. Also, for Silica-gel, Al-Fumarate, and MIL101(Cr) SCPe achieved by the ASCE is higher than the SCP of BACS, while for AQSOA-Z02 and CPO-27(Ni), it is higher than the SCP of BACS at heating temperature higher than 140 °C. The SCPe achieved by AQSOA-Z02 at heat source temperature of 160 °C is 24% higher than the SCP of BACS [65]. For heating temperature ranging from 100 to 160 °C, ASCE has a maximum COPe of 0.8 utilising Silica-gel compared to maximum COP of 0.7 achieved by the BACS.

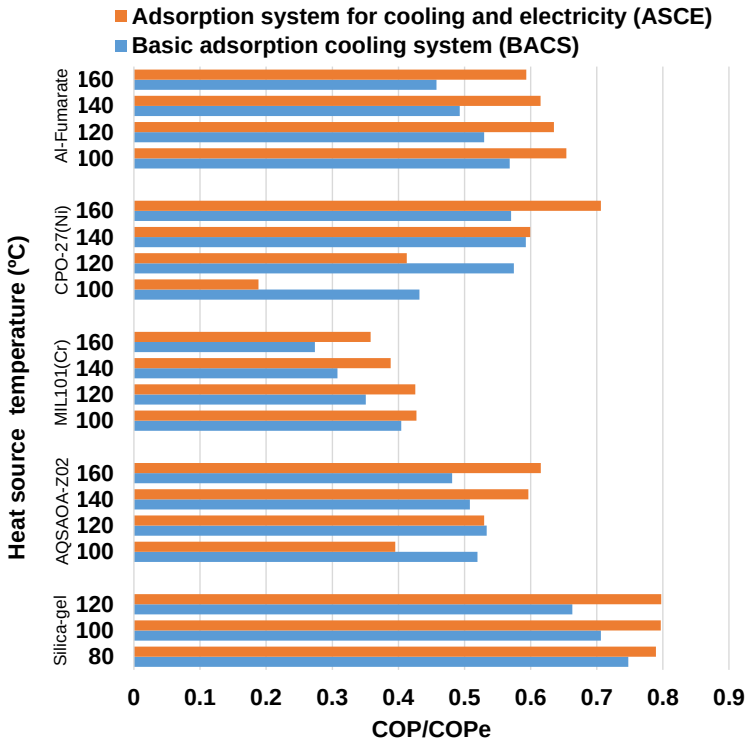

Figure 4-11: COP/COPe of BACS and ASCE (with two-bed) for a range of heat source temperatures utilizing Silica-gel, AQSOA-Z02, MIL101(Cr), CPO-27(Ni) and Al-Fumarate

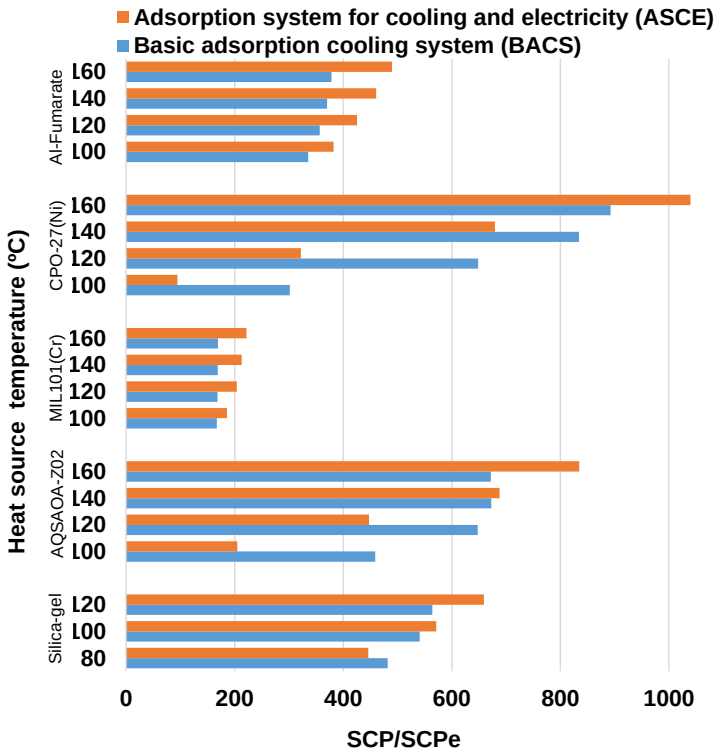

Figure 4-12: SCP/SCPe of basic adsorption cooling system (BACS) and ASCE (with two-bed) for a range of heat source temperatures utilizing Silica-gel, AQSOA-Z02, MIL101(Cr), CPO-27(Ni) and Al-Fumarate

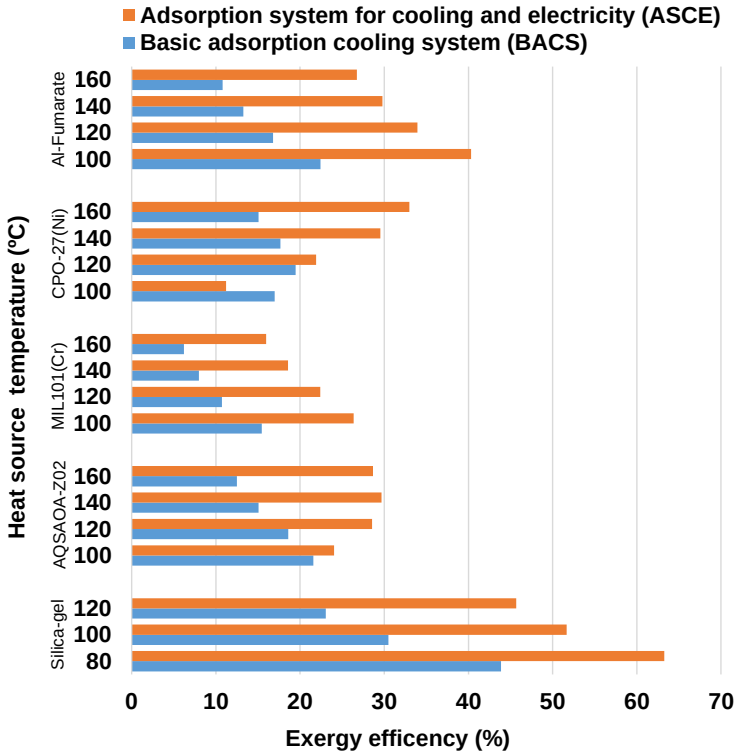

Figure 4-13: Exergy efficiency of BACS and ASCE (with two-bed) for a range of heat source temperatures utilizing Silica-gel, AQSOA-Z02, MIL101(Cr), CPO-27(Ni) and Al-Fumarate

For all adsorbent materials and heat source temperatures used (except for CPO-27(Ni) at 100°C) as shown in Figure 4-13, the exergy efficiency achieved by ASCE is higher than that of BACS and this is because the power generated by the former has higher grade than cooling. The maximum exergy efficiency of 63.26% is achieved using Silica-gel at heat source temperature of 80 °C [65]. Results also show that using ASCE can enhance the exergy efficiency of BACS by up to 2.5 times when using Al-Fumarate at heat source temperature of 160 °C [65]. Also, results show that different adsorbent materials presented different values of COP/COPe, SCP/SCPe, and exergy efficiency. For example, Silica-gel showed the highest COP and exergy efficiency, while AQSOA-Z02 and CPO-27(Ni) showed the highest SCP with heat source temperature of 140 °C or higher. COP is an important coefficient for determining the effectiveness of any heat pump because high COP values mean less energy used. Though, if the energy used is an infinite or semi-infinite source in terms of availability

at no cost like solar energy, SCP can be a more important criterion, because high SCP means more cooling generated using the same system size.

Moreover, for all cases, SCPe achieved by the ASCE is always higher than that produced by BACS as shown in Figure 4-12 except for Silica-gel at 80 °C, AQSOA-Z02 at 120 °C or less and CPO-27(Ni) at 140 °C or less and this is because less power is generated at low heating temperatures. At high heating temperatures, the mass flow rate of refrigerant (water) is higher because of high adsorption/desorption rate. In addition, at high heat source temperatures, high-pressure ratio can be obtained through the expander (turbine) which means more power can be generated. As the grade of electricity is higher than cooling (i.e. each 1 kW of power produces about 3 kW of cooling depending on the typical COP of compression refrigeration systems, which is assumed to be 3 in this study), SCPe of ASCE is higher than that of BACS at heat source temperature higher than 140 °C [28, 65].

Figure 4-14 shows the effect of heat source temperature on the COP of the ASCE and for AQSOA-Z02 and CPO-27(Ni) as the heat source temperature increases COP increases, while for MIL101(Cr), Al-Fumarate, and Silica-gel COP decreases due to higher heat consumption at high temperatures with limited increase in the cooling output [20]. Figure 4-15 shows that COPe has similar behaviour to the COP but with higher values because of the additional power generated.

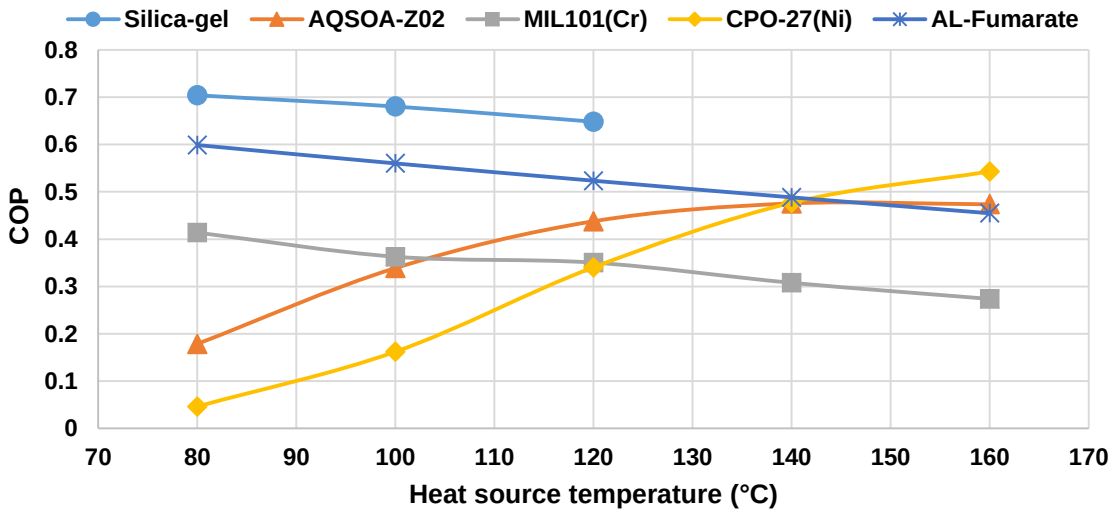

Figure 4-14: Effect of heat source temperature on the COP of the ASCE utilising $T_{cooling}$=28 ºC and $T_{chilled}$=18 ºC

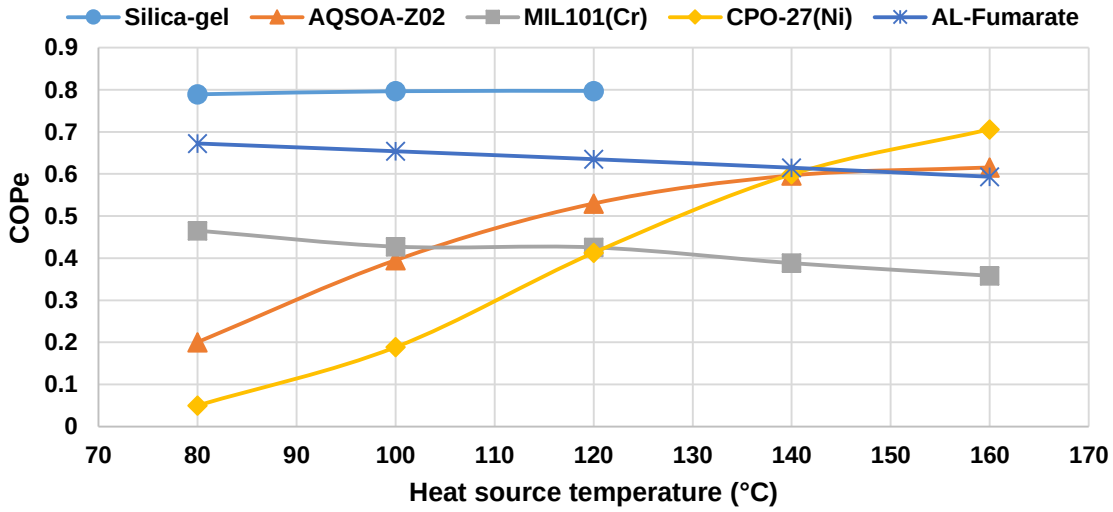

Figure 4-15: Effect of heat source temperature on the COPe of the ASCE utilising $T_{cooling}$=28 ºC and $T_{chilled}$=18 ºC

Figure 4-16 and Figure 4-17 show the effect of heat source temperature on SCP and SCPe of the ASCE and for all adsorbent materials used in this work, as heat source temperature increases SCP and SCPe increase and this is because of the water uptake increase leading to the increase in the water mass flow rate passing through the evaporator[20], however the rate of change is different, where AQSOA-Z02 and CPO-27(Ni) have higher rate of change than

that of Silica-gel, MIL101(Cr) and Al-Fumarate [20, 21]. For all cases, SCPe has a higher value than that of SCP and this is because additional power is generated which was converted to the equivalent cooling. Maximum SCP of 800 and 642 W/kg_{ads} were achieved by CPO-27(Ni) and AQSOA-Z02 respectively at heat source temperature of 160 °C.

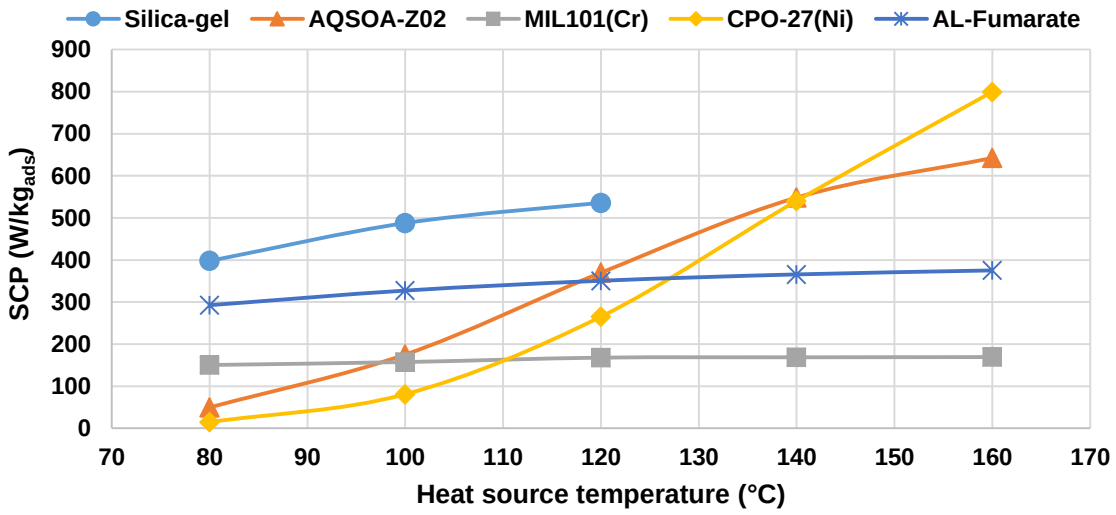

Figure 4-16: Effect of heat source temperature on SCP of the ASCE utilising $T_{cooling}$=28 ºC and $T_{chilled}$=18 ºC

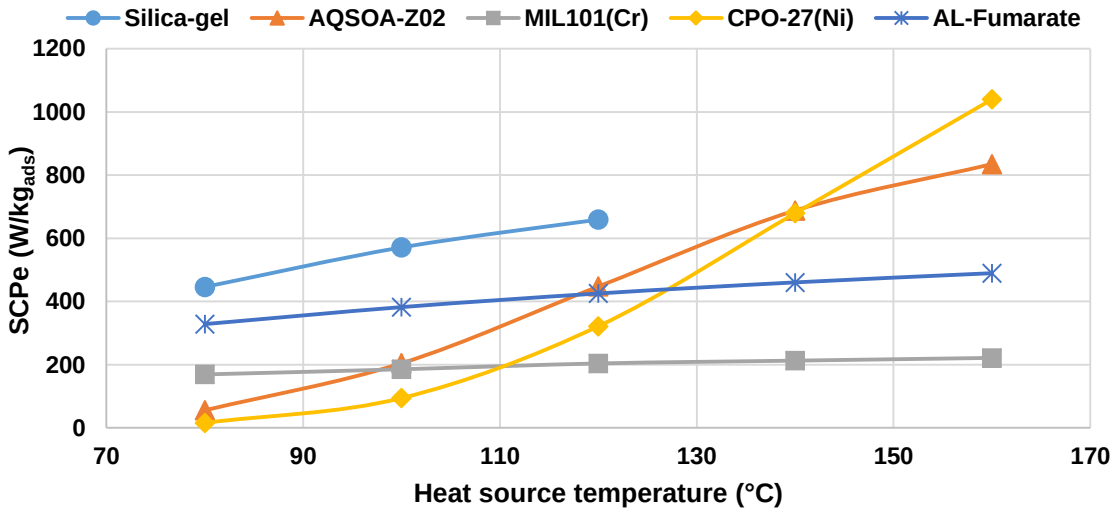

Figure 4-17: Effect of heat source temperature on SCPe of the ASCE utilising $T_{cooling}$=28 ºC and $T_{chilled}$=18 ºC

Figure 4-18 shows the effect of heat source temperature on SP whereas as the heating fluid temperature increases the SP increases and this is due to increasing the water uptake which leads to higher mass flow rate besides the increase in the enthalpy difference [20, 21]. Figure 4-19 shows the effect of heating temperature on the adsorption power efficiency and as the heating fluid temperature increases the adsorption power efficiency increases for all adsorbent materials and this is due to more power generated at high heat source temperature [20, 21].

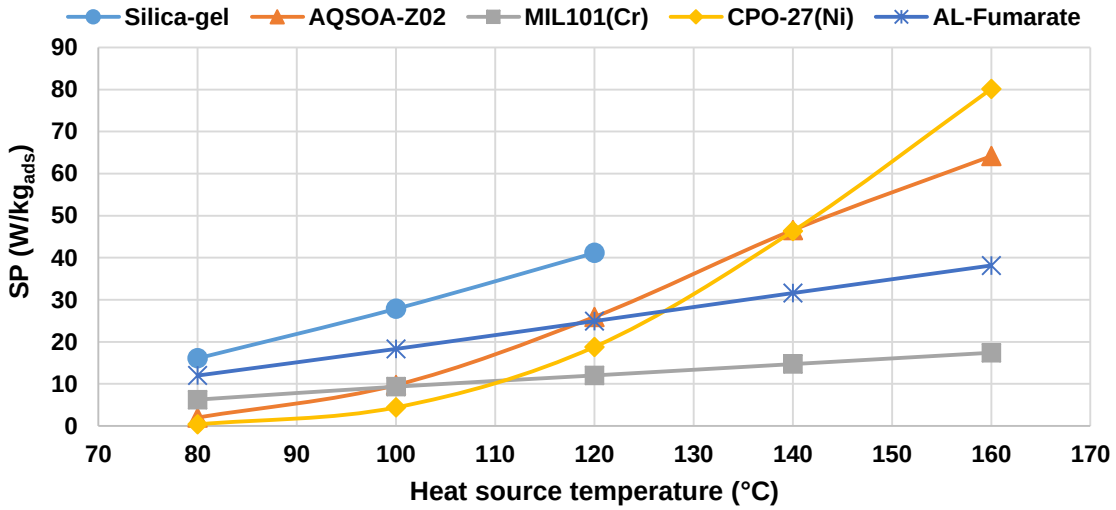

Figure 4-18: Effect of heat source temperature on SP of the ASCE utilising Tcooling=28 ºC and Tchilled=18 ºC

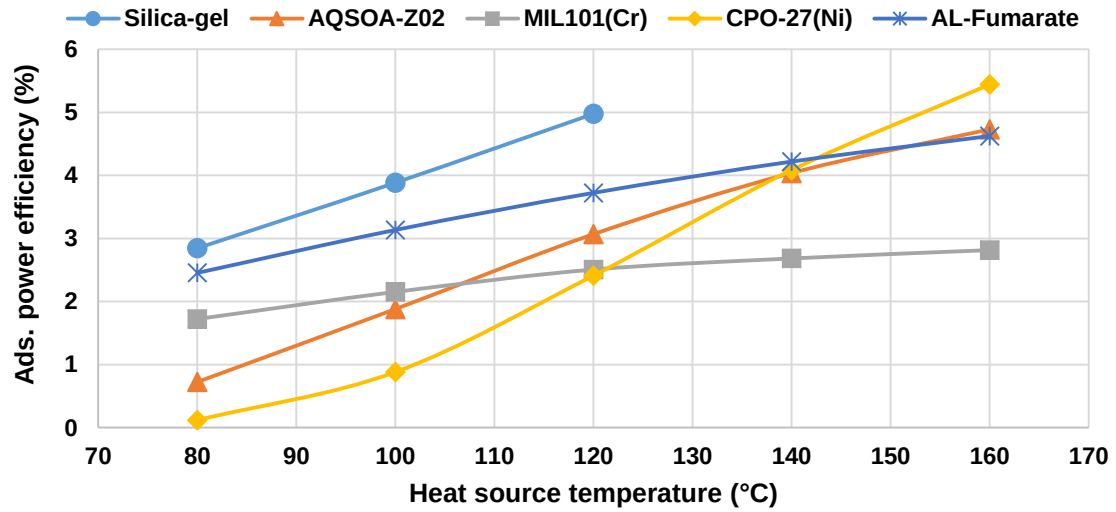

Figure 4-19: Effect of heat source temperature on the adsorption power efficiency of the ASCE utilising $T_{cooling}$=28 ºC and $T_{chilled}$=18 ºC

Figure 4-20 and Figure 4-21 show the effect of condensation temperature on the COP and COPe using the five different adsorbent materials utilising cooling temperature and inlet chilled water temperature of 28 °C, and 18 °C respectively [20, 21]. Generally, as the condenser temperature increases, the COP and COPe decrease and it is clear that AQSOA-Z02 and CPO-27(Ni) are more affected by the condenser temperature, while MIL101(Cr) is not affected [20, 21].

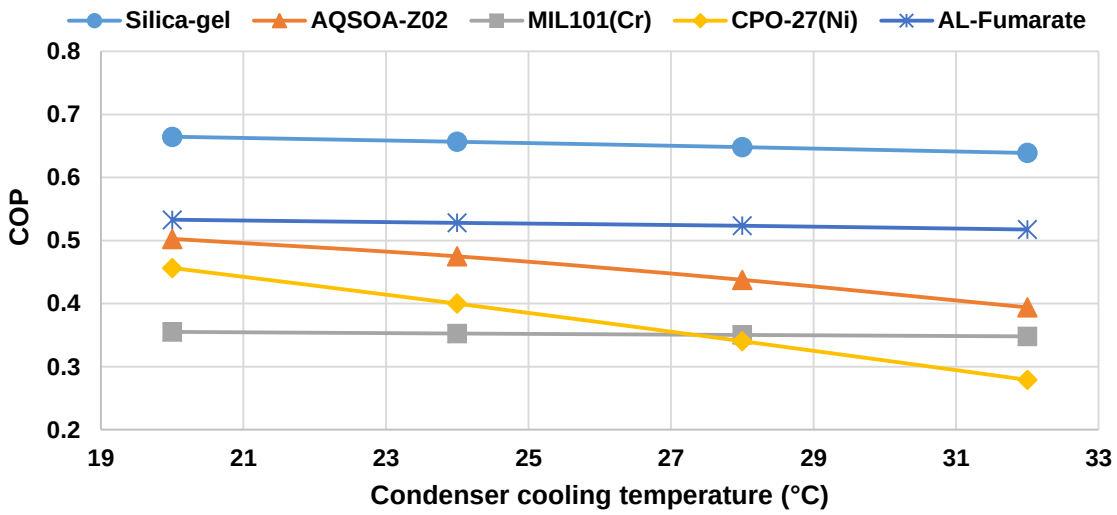

Figure 4-20: Effect of condenser temperature on the COP of the ASCE utilising $T_{heating}$=120 ºC, $T_{cooling}$=28 ºC and $T_{chilled}$=18 ºC

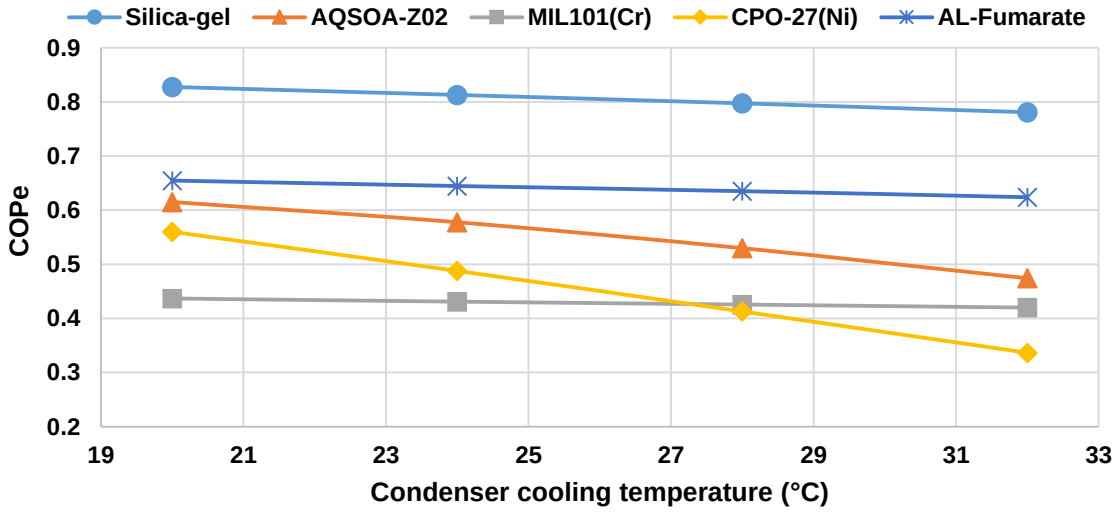

Figure 4-21: Effect of condenser temperature on the COPe of the ASCE utilising $T_{heating}$=120 ºC, $T_{cooling}$=28 ºC and $T_{chilled}$=18 ºC

Figure 4-22 and Figure 4-23 show the effect of the condensation temperature on SCP, and SCPe, respectively. Again as the condensation temperature increases SCP, SCPe, decrease except for MIL101(Cr). SCP, and SCPe, are affected by the condenser temperature, because it affects directly the water uptake, while for MIL101(Cr), SCP and SCPe are not affected because of the S-shape isotherms of this material as described in Chapter 3 [20].

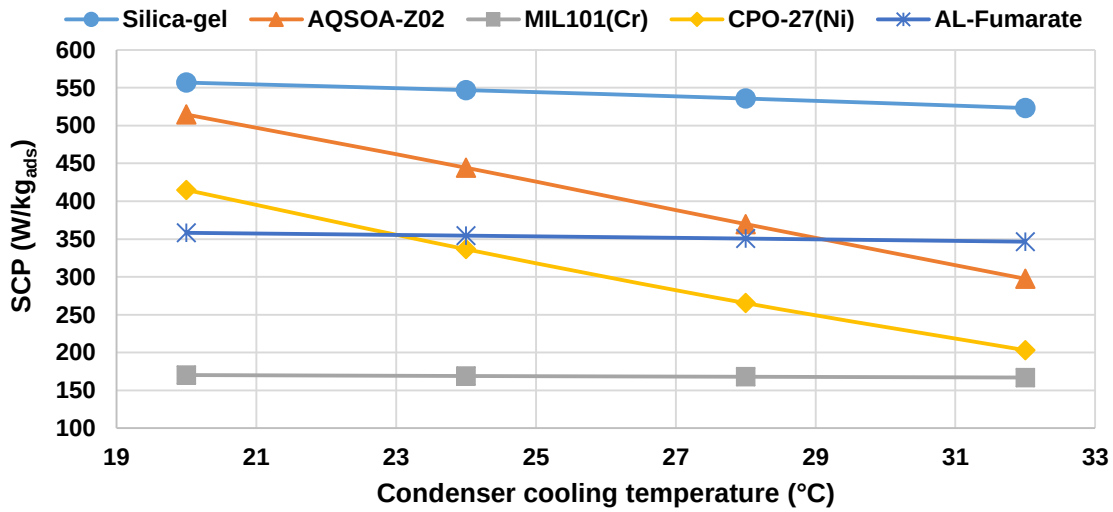

Figure 4-22: Effect of condenser temperature on SCP of the ASCE utilising $T_{heating}$=120 ºC, $T_{cooling}$=28 ºC and $T_{chilled}$=18 ºC

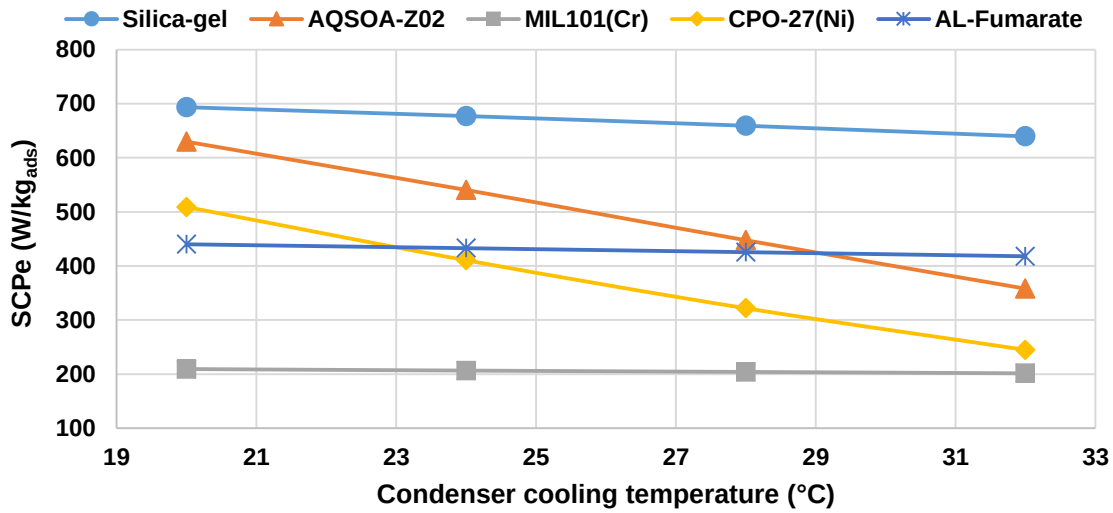

Figure 4-23: Effect of condenser temperature on SCPe of the ASCE utilising $T_{heating}$=120 ºC, $T_{cooling}$=28 ºC and $T_{chilled}$=18 ºC

Figure 4-24 and Figure 4-25 show the effect of condenser temperature on SP and adsorption power efficiency respectively and results show that for all materials as the condenser temperature increases the SP, and the adsorption power efficiency decrease and this is because of its effect on the water uptake and the pressure ratio of the turbine [20, 21].

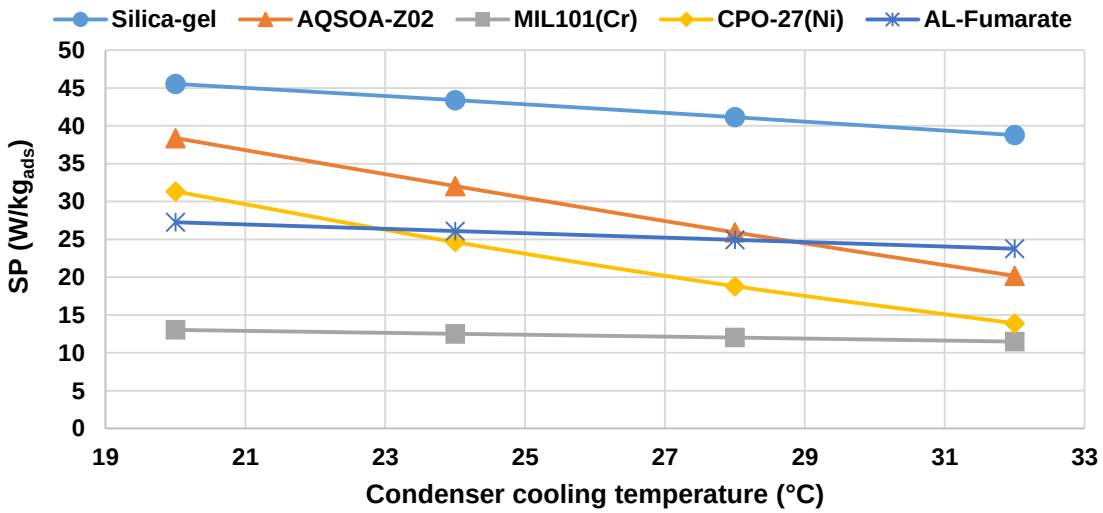

Figure 4-24: Effect of condenser temperature on SP of the ASCE utilising $T_{heating}$=120 ºC, $T_{cooling}$=28 ºC and $T_{chilled}$=18 ºC

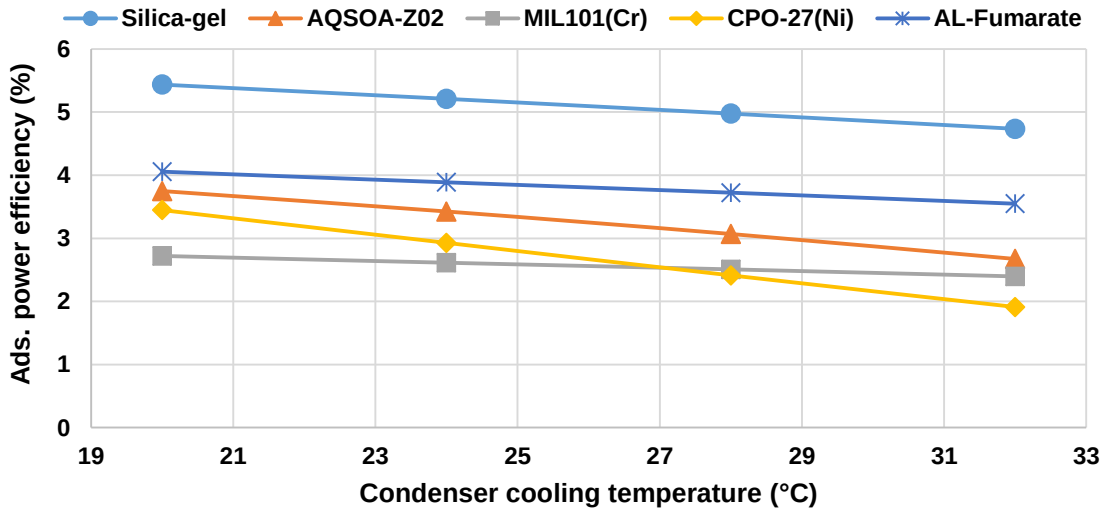

Figure 4-25: Effect of condenser temperature on the adsorption efficiency of the ASCE utilising $T_{heating}$=120 ºC, $T_{cooling}$=28 ºC and $T_{chilled}$=18 ºC

Increasing the condenser temperature decreases the pressure ratio and reduces the power output [20]. However, the rate of the decrease is different from material to the other, where SP, and adsorption power efficiency of AQSOA-Z02 and CPO-27(Ni) are the most affected by the increase in the condenser temperature. Figure 4-26 and Figure 4-27 show the effect of chilled water temperature on the COP and COPe of the ASCE utilising heat source temperature and cooling temperature of 120 °C and 28 °C respectively [20, 21]. For Silica-gel and MIL101(Cr) as the chilled water temperature increases, COP and COPe increase, while the other materials are not affected. MIL101(Cr) has good water adsorption characteristics with a maximum water uptake of 1.47 kg/kg$_{ads}$, but this high uptake happens only at partial pressure higher than 0.5 as described in Chapter 3 and this high partial pressure can be achieved when high chilled water temperature or low bed cooling water temperature are used and this explains why MIL101(Cr) has higher performance at high chilled water temperature [20, 21].

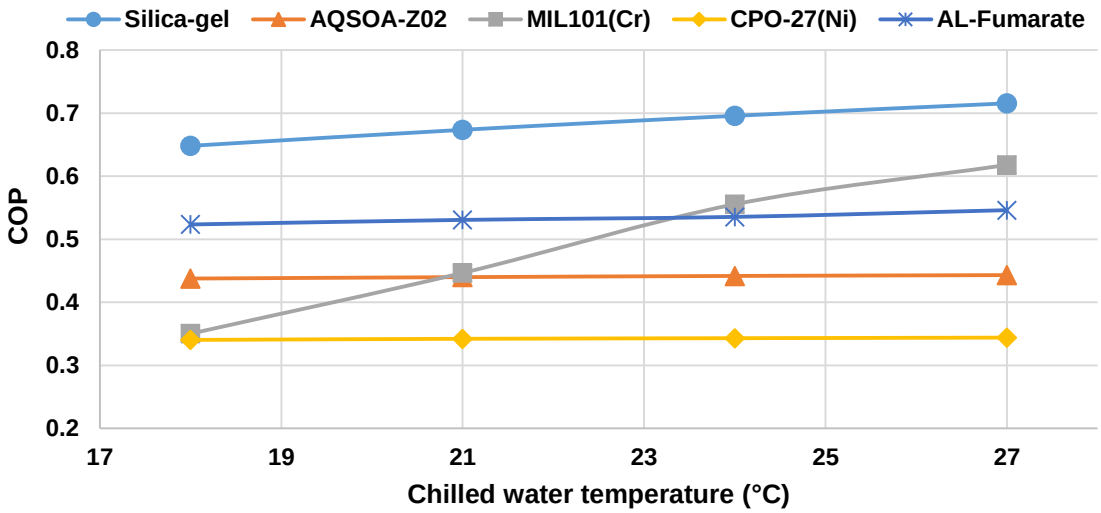

Figure 4-26: Effect of chilled water temperature on the COP of the ASCE utilising $T_{heating}$=120 ºC, and $T_{cooling}$=28 ºC

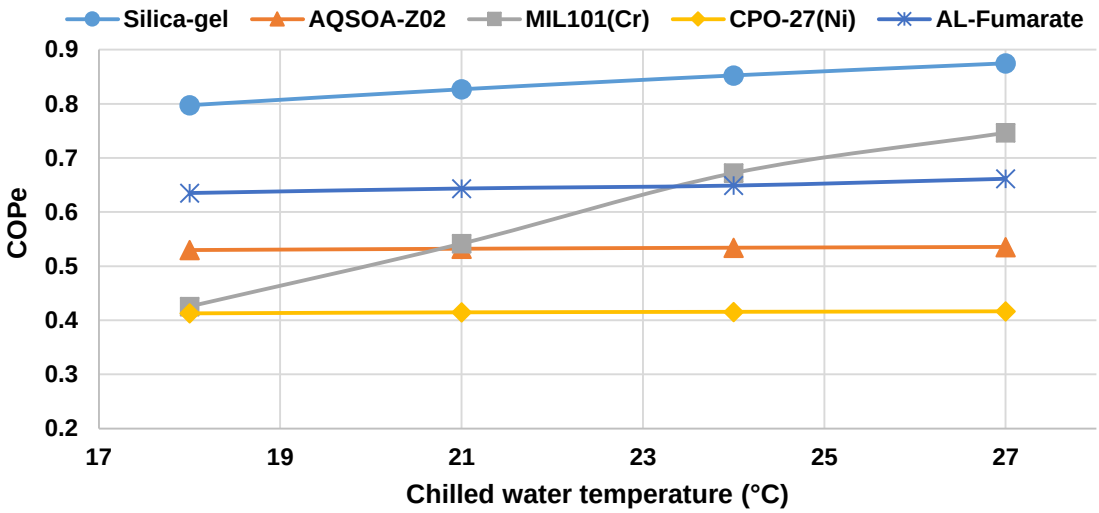

Figure 4-27: Effect of chilled water temperature on the COPe of the ASCE utilising $T_{heating}$=120 ºC, and $T_{cooling}$=28 ºC

Figure 4-28, Figure 4-29, Figure 4-30 and Figure 4-31 show the effect of chilled water temperature on SCP, SCPe, SP, and adsorption power efficiency respectively. For Silica-gel and MIL101(Cr) as the chilled water temperature increases, SCP, SCPe, SP and adsorption power efficiency increase. SCP, SCPe of MIL101(Cr) have relatively high values at high chilled temperature, but this is not suitable for the cooling applications nevertheless, MIL101(Cr) still has the potential of producing electricity [20].

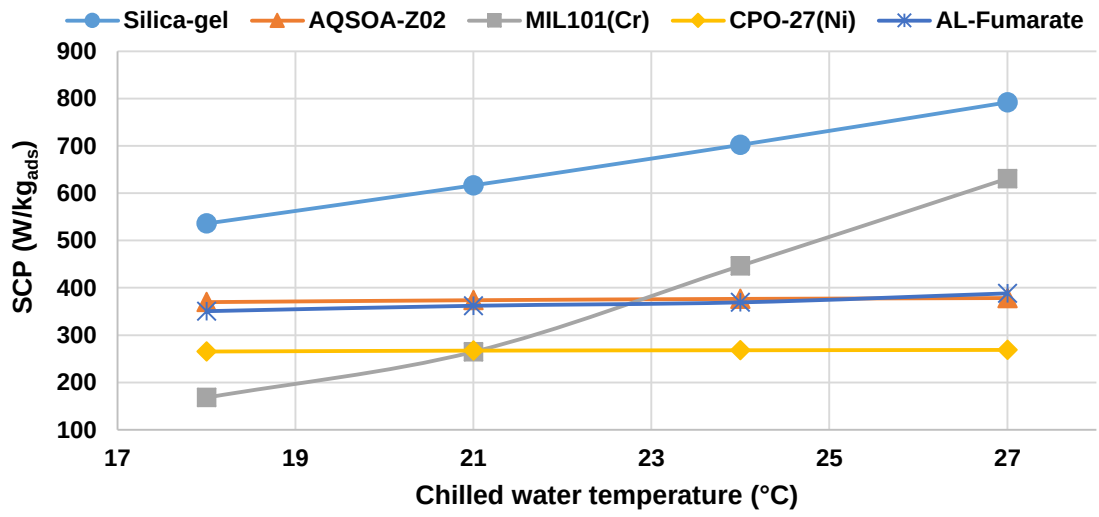

Figure 4-28: Effect of chilled water temperature on SCP of the ASCE utilising $T_{heating}$=120 ºC, and $T_{cooling}$=28 ºC

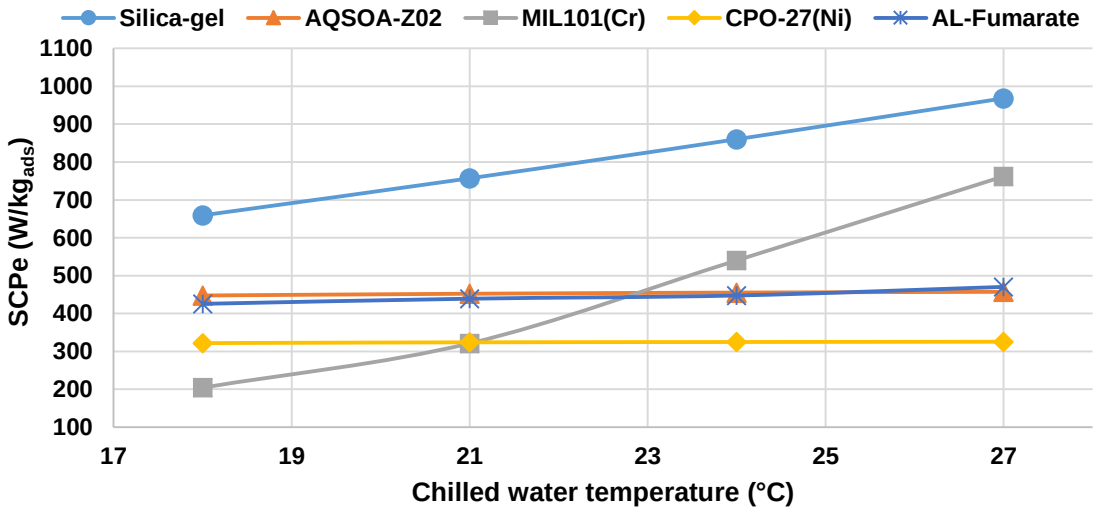

Figure 4-29: Effect of chilled water temperature on SCPe of the ASCE utilising $T_{heating}$=120 ºC, and $T_{cooling}$=28 ºC

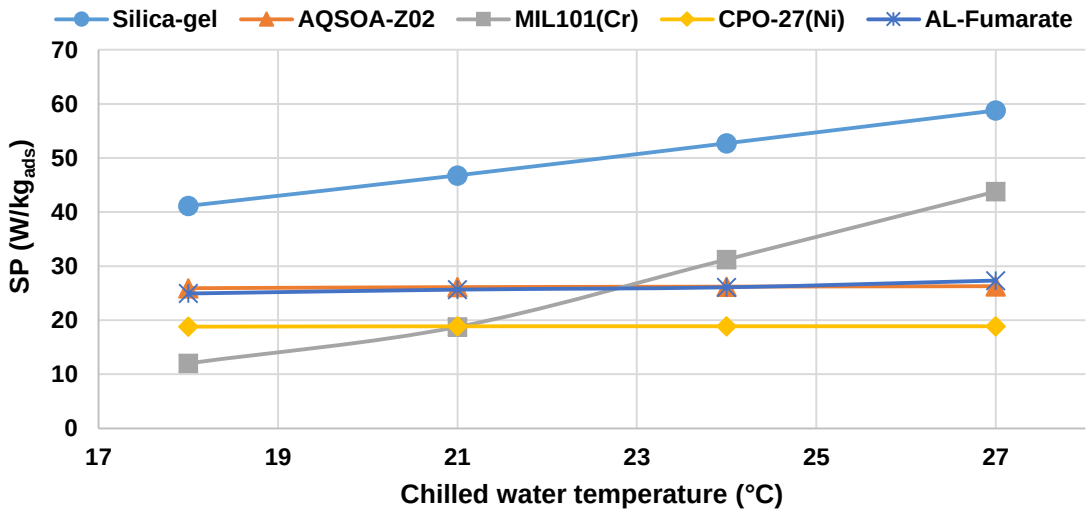

Figure 4-30: Effect of chilled water temperature on SP of the ASCE utilising $T_{heating}$=120 ºC, and $T_{cooling}$=28 ºC

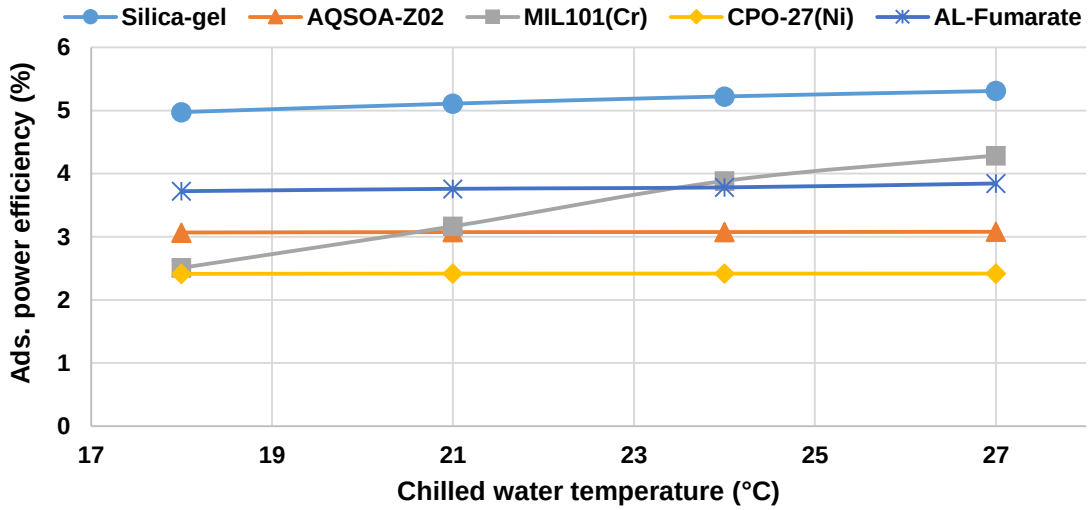

Figure 4-31: Effect of chilled water temperature on the adsorption efficiency of the ASCE utilising $T_{heating}$=120 ºC, and $T_{cooling}$=28 ºC

Figure 4-32, Figure 4-33, and Figure 4-34 show the effect of using different bed size (number of modules per bed, which is 4 for the normal size 1X, and 8 for 2X and 12 for 3X) on expander mass flow rate, cooling output and power generated by the ASCE for AQSOA-Z02 and CPO-27(Ni) utilising heating temperature of 140 and 160 ºC, cooling temperature of 28 °C and inlet chilled water temperature of 18 ºC. Maximum steam mass flow rate, cooling capacity and power of about 0.012 kg/s, 26.2 kW and 2.6 kW respectively are achieved using the bed size of 3X and AQSOA-Z02 with heat source temperature of 160 ºC.

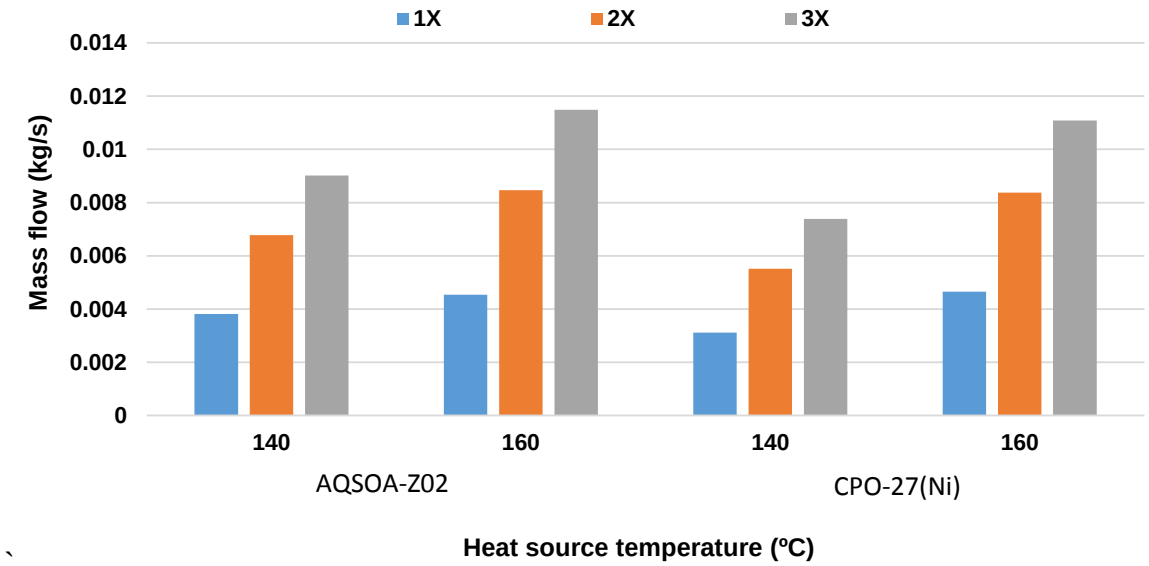

Figure 4-32: Effect of using different bed size on the steam mass flow rate generated by the ASCE utilising AQSOA-Z02 and CPO-27(Ni) with two heat source temperatures, $T_{cooling}$=28 ºC, and $T_{chilled}$=18 ºC

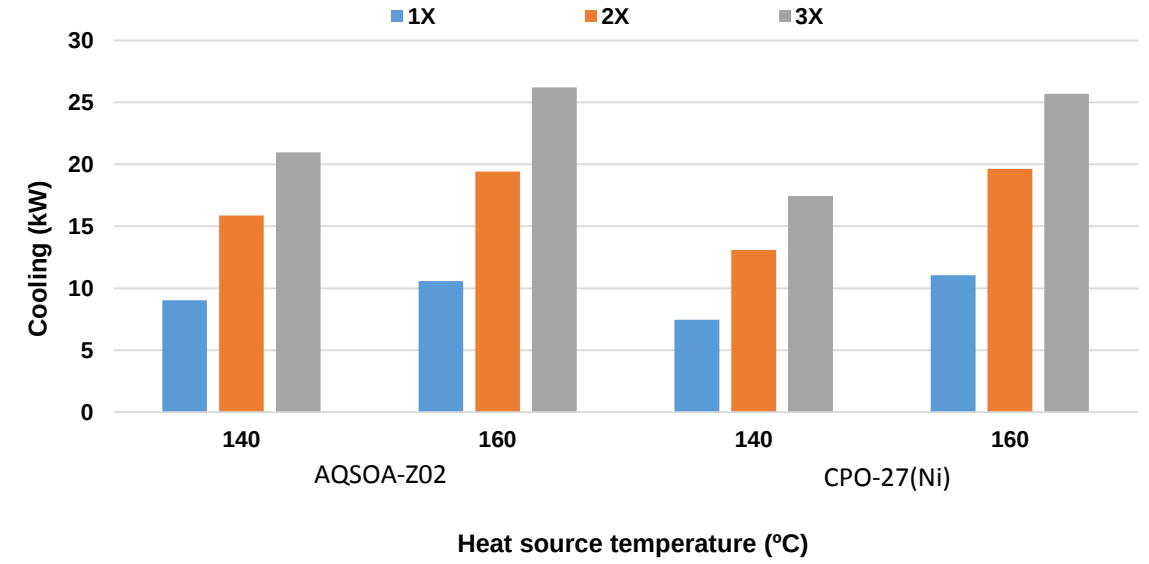

Figure 4-33: Effect of using different bed size on the cooling generated by the ASCE utilising AQSOA-Z02 and CPO-27(Ni) with two heat source temperatures, $T_{cooling}$=28 ºC, and $T_{chilled}$=18 ºC

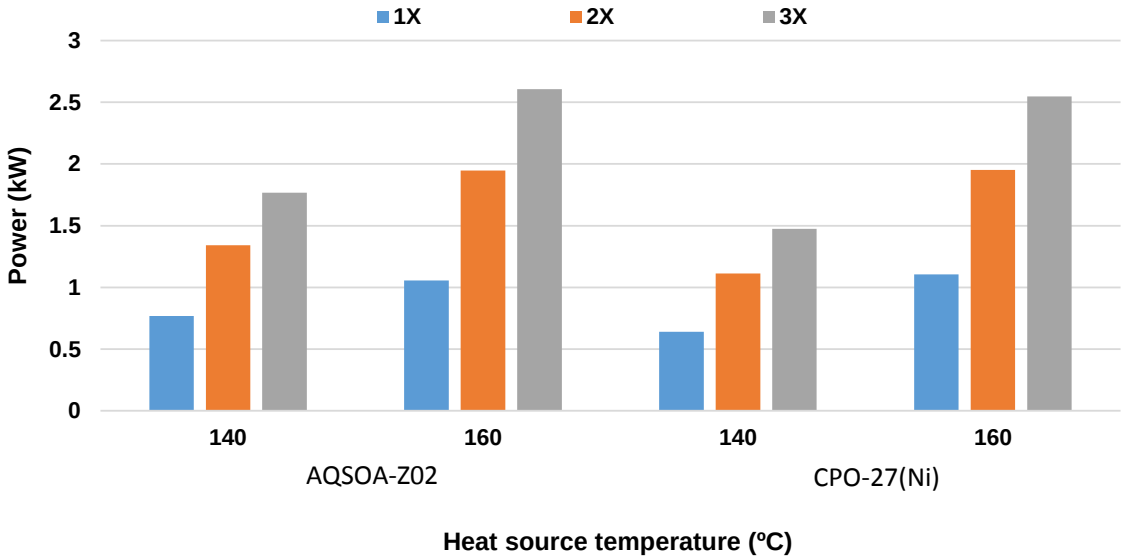

Figure 4-34: Effect of using different bed size on the power generated by the ASCE utilising AQSOA-Z02 and CPO-27(Ni) with two heat source temperatures, $T_{cooling}$=28 ºC, and $T_{chilled}$=18 ºC

Utilising multi-bed adsorption arrangement can help to improve the performance of the ASCE by improving the cooling and power generated. The main advantage of using multi-bed ASCE is to increase the values of SCP and SP generated [65]. Also, it improves the quality of the cooling and power generated so that they have less fluctuation. Figure 4-35, Figure 4-36, Figure 4-37, and Figure 4-38 show cooling and power generated using 7 different arrangements including two-bed, three-bed, four-bed, five-bed, and six-bed in addition to four-bed in parallel and six-bed in parallel utilizing CPO-27(Ni) with heating temperature of 160℃, cooling temperature of 28 ºC and inlet chilled water temperature of 18 ºC [65]. Results show that cooling and power can be generated at the same time however, the amount of cooling and power generated differs from one arrangement to another. As the number of beds increases the amounts of cooling and power increase because of more adsorbent materials are added to the system and more uptake and mass flow rate can be generated [65]. In addition, as the number of beds increases, more continuity in cooling and power can be noticed i.e. the cooling and power have less fluctuation which is preferable. A significant gain in cooling and

power can be noticed between 2B (two-bed) and 3B (three-bed) arrangements where more cooling and power can be generated with the arrangement of three-bed. Using the six-bed arrangement in parallel with R=1/2 gives the highest average cooling and power generated of 24.93 kW and 2.43 kW respectively [65].

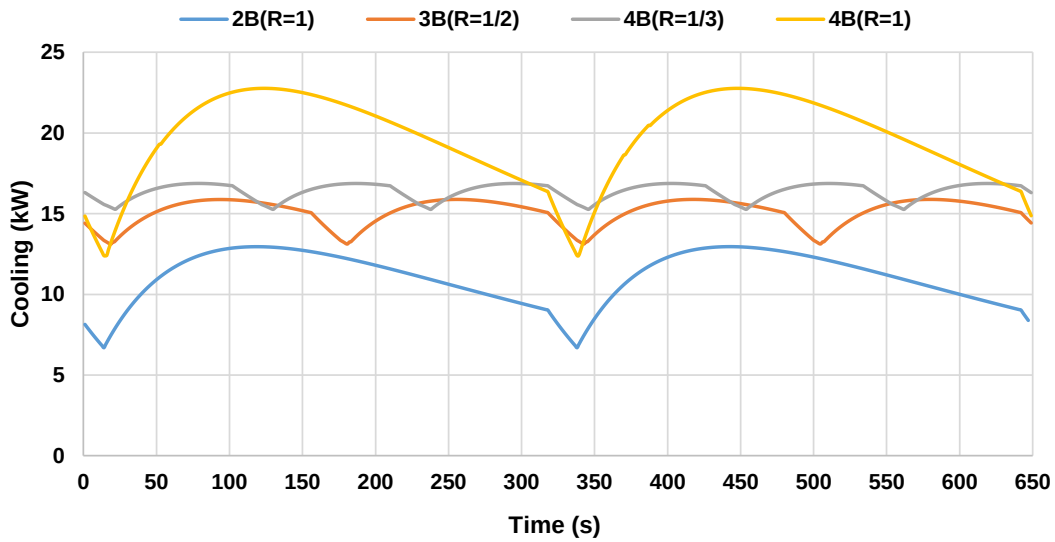

Figure 4-35: Cooling generated from multi-bed ASCE utilizing CPO-27(Ni) and using two, three and four beds utilising $T_{heating}$=160 ºC, $T_{cooling}$=28 ºC and $T_{chilled}$=18 ºC

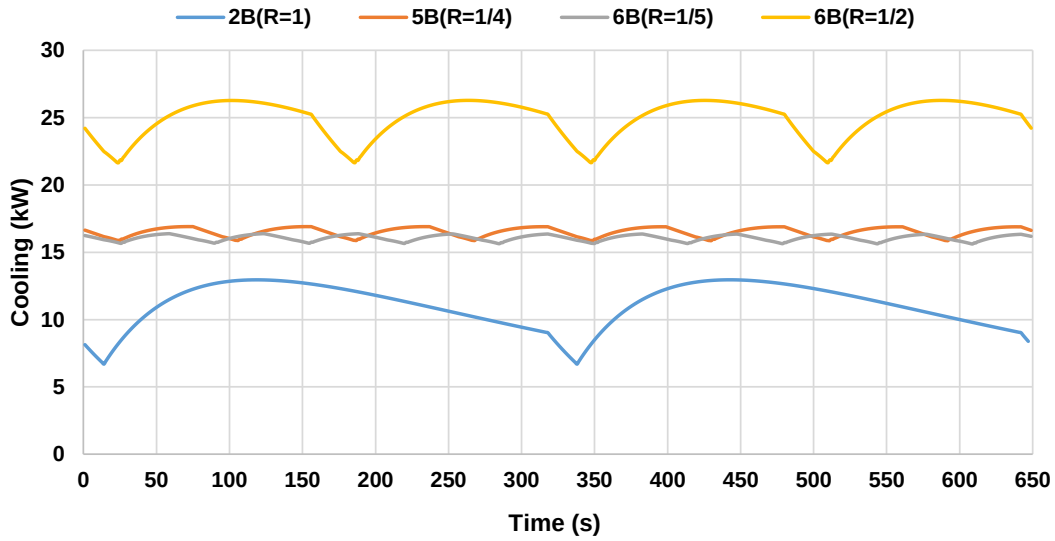

Figure 4-36: Cooling generated from multi-bed ASCE utilizing CPO-27(Ni) and using two, five and six beds utilising $T_{heating}$=160 ºC, $T_{cooling}$=28 ºC and $T_{chilled}$=18 ºC

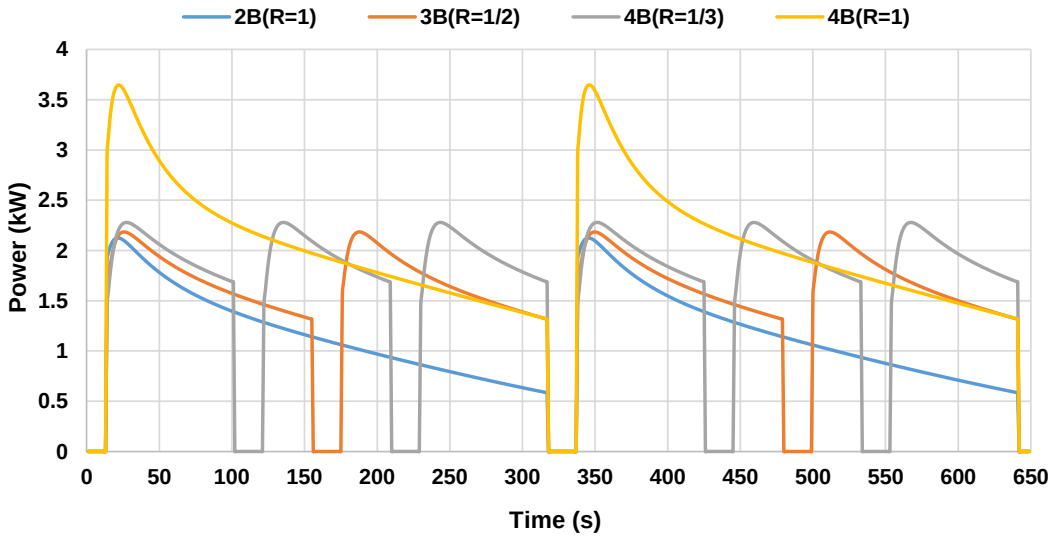

Figure 4-37: Power generated from multi-bed ASCE utilizing CPO-27(Ni) and using two, three and four beds utilising $T_{heating}$=160 ºC, $T_{cooling}$=28 ºC and $T_{chilled}$=18 ºC

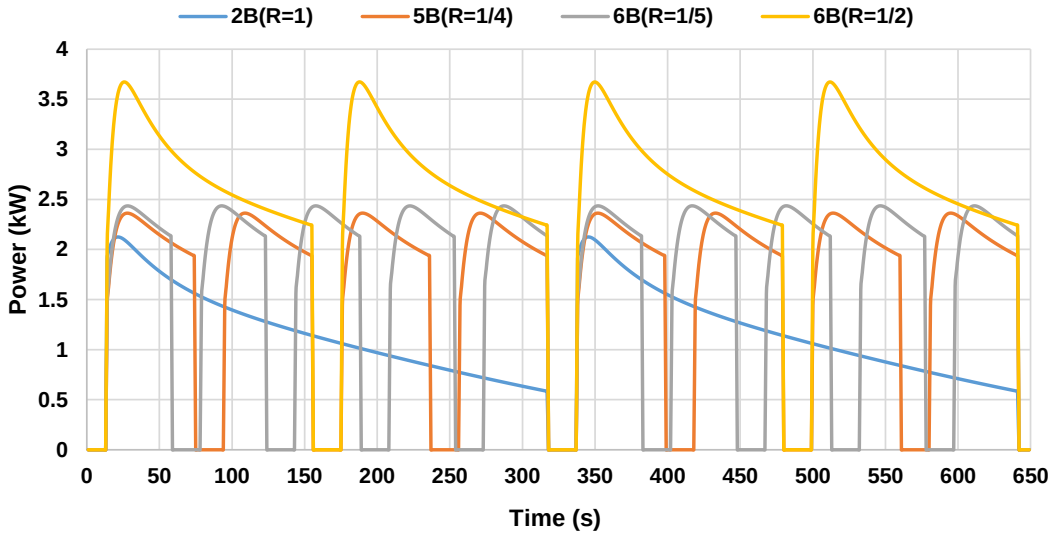

Figure 4-38: Power generated from multi-bed ASCE utilizing CPO-27(Ni) and using two, five and six beds utilising $T_{heating}$=160 ºC, $T_{cooling}$=28 ºC and $T_{chilled}$=18 ºC

Figure 4-39, Figure 4-40, Figure 4-41 and Figure 4-42 show cooling and power generated using 7 different arrangements utilizing Al-Fumarate at heating fluid temperature of 160 ºC, cooling temperature of 28 ºC, and inlet chilled water temperature of 18 ºC [65]. Similar results are obtained using Al-Fumarate, where a good improvement in cooling and power can be noticed in three-bed arrangement compared to the two-bed arrangement (2B) where more

cooling and power can be generated with the three-bed arrangement (3B), while using the six-bed arrangement (6B) in parallel with R=1/2 gives the highest average cooling and power generated of 16.2 kW and 1.61 kW respectively [65].

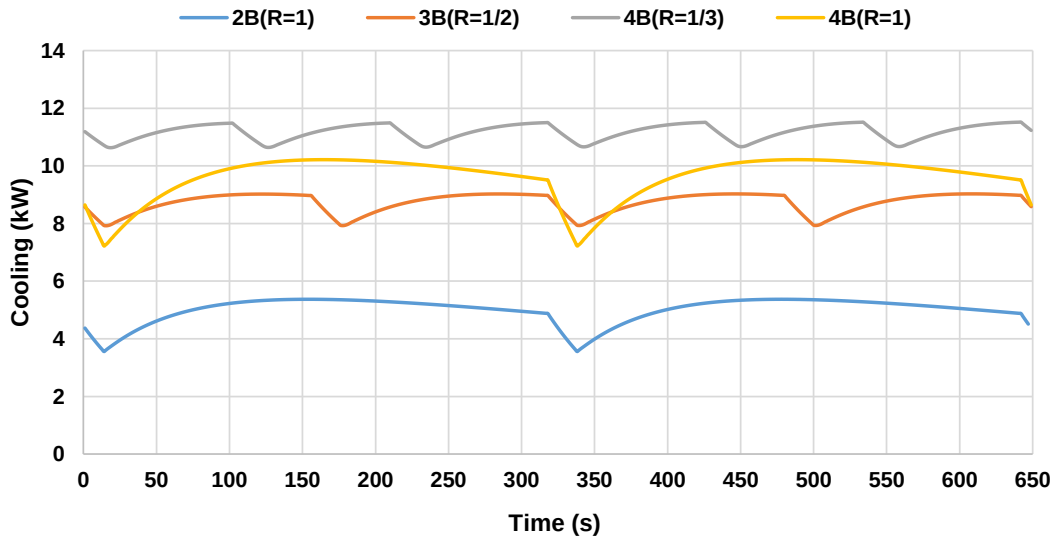

Figure 4-39: Cooling generated from multi-bed ASCE utilizing Al-Fumarate and using two, three, and four beds utilising $T_{heating}$=160 ºC, $T_{cooling}$=28 ºC and $T_{chilled}$=18 ºC

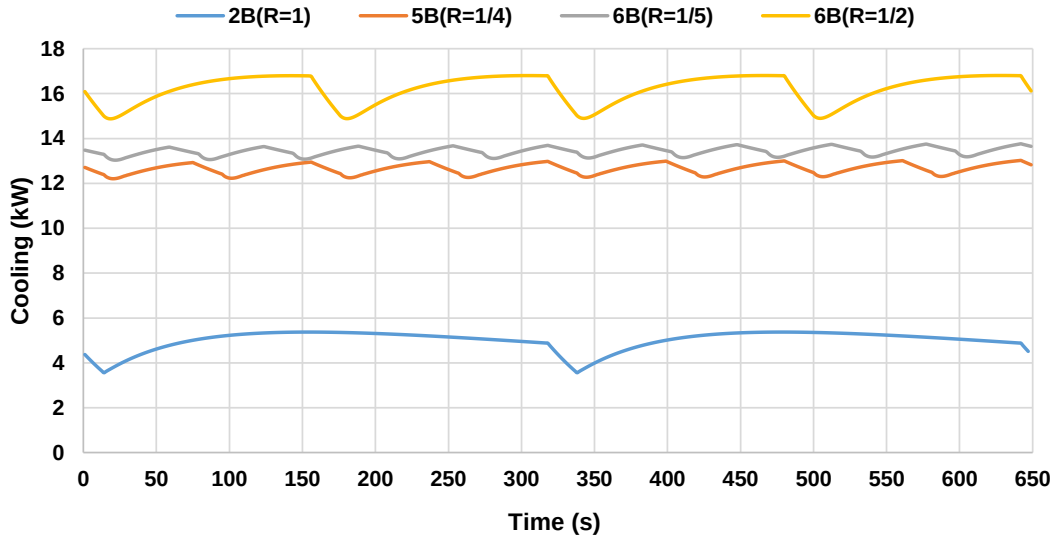

Figure 4-40: Cooling generated from multi-bed ASCE utilizing Al-Fumarate and using two, five, and six beds utilising $T_{heating}$=160 ºC, $T_{cooling}$=28 ºC and $T_{chilled}$=18 ºC

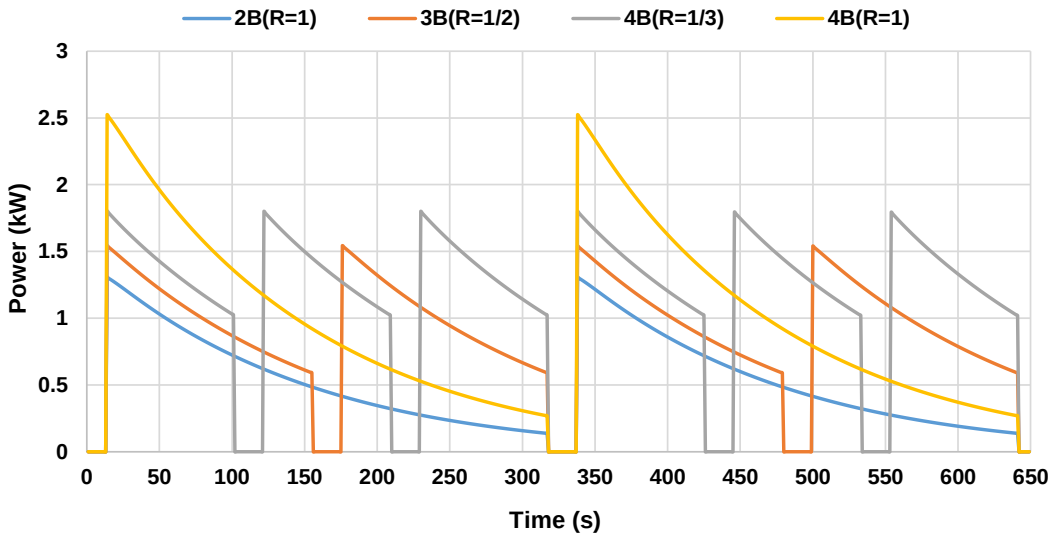

Figure 4-41: Power generated from multi-bed ASCE utilizing Al-Fumarate and using two, three, and four beds utilising $T_{heating}$=160 ºC, $T_{cooling}$=28 ºC and $T_{chilled}$=18 ºC

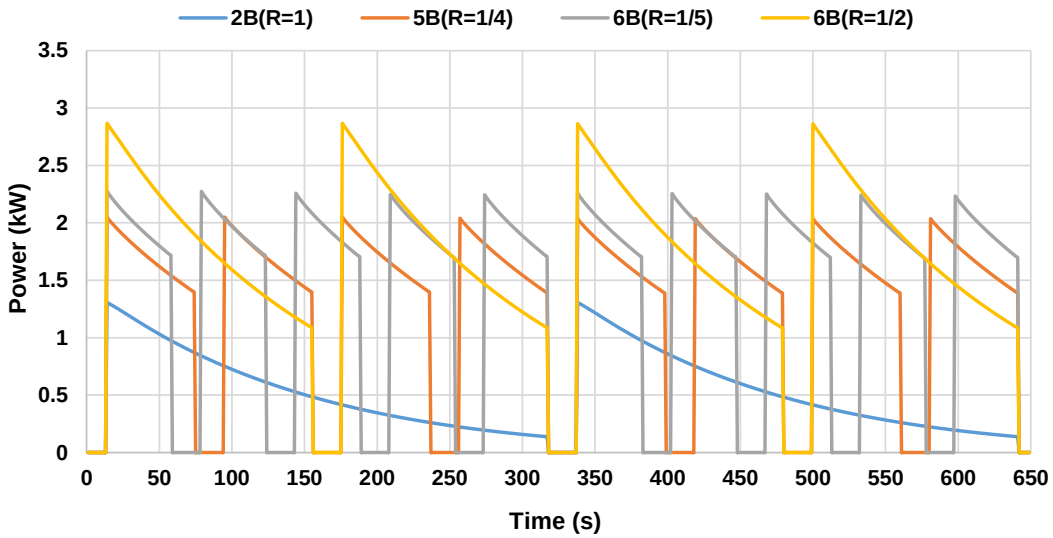

Figure 4-42: Power generated from multi-bed ASCE utilizing Al-Fumarate and using two, five, and six beds utilising $T_{heating}$=160 ºC, $T_{cooling}$=28 ºC and $T_{chilled}$=18 ºC

Figure 4-43, and Figure 4-44 show the COP and COPe of different bed arrangements and R ratios utilizing Al-Fumarate, CPO-27(Ni), AQSOA-Z02 and Silica-gel with a range of heat source temperature between 80 and 160 °C and cooling water temperature of 28 °C and inlet chilled water temperature of 18 °C [65]. The maximum COP achieved in this investigation is

0.7 using Silica-gel at heating fluid temperature of 80 °C with the two-bed arrangement and the maximum COPe achieved is 0.8 using Silica-gel at heating fluid temperature of 120 °C with the two-bed arrangement. Compared to other materials at heat source temperature between 80-120 °C, Silica-gel shows the highest COP and this is due to the high cooling capacity achieved with this material as a result of high water uptake (high adsorption/desorption rate). Silica-gel's isotherms which has a linear and uniform shape, besides its good kinetics which helps to generate such high uptake rate and this can explain the high water uptake and the high cooling capacity produced by this material. At heating fluid temperature of 80 °C the amount of heat consumed is the lowest which leads to highest COP, while at 120 ºC the power generated is the maximum for Silica-gel which leads to highest COPe. In terms of the number of beds and R ratio used, the two-bed arrangement with R=1 shows the maximum COP and COPe and this is due to using less amount of heat with this arrangement [65].

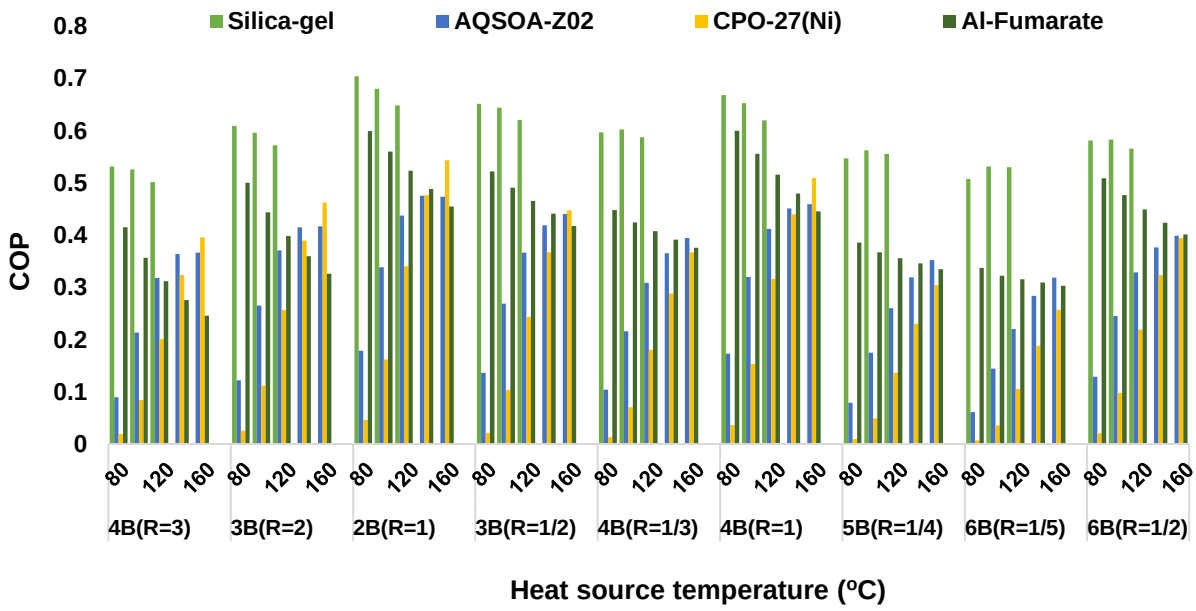

Figure 4-43: COP of different bed arrangements and ads/des ratio (R) of multi-bed ASCE utilizing four different adsorbent materials with $T_{cooling}$=28 ºC and $T_{chilled}$=18 ºC

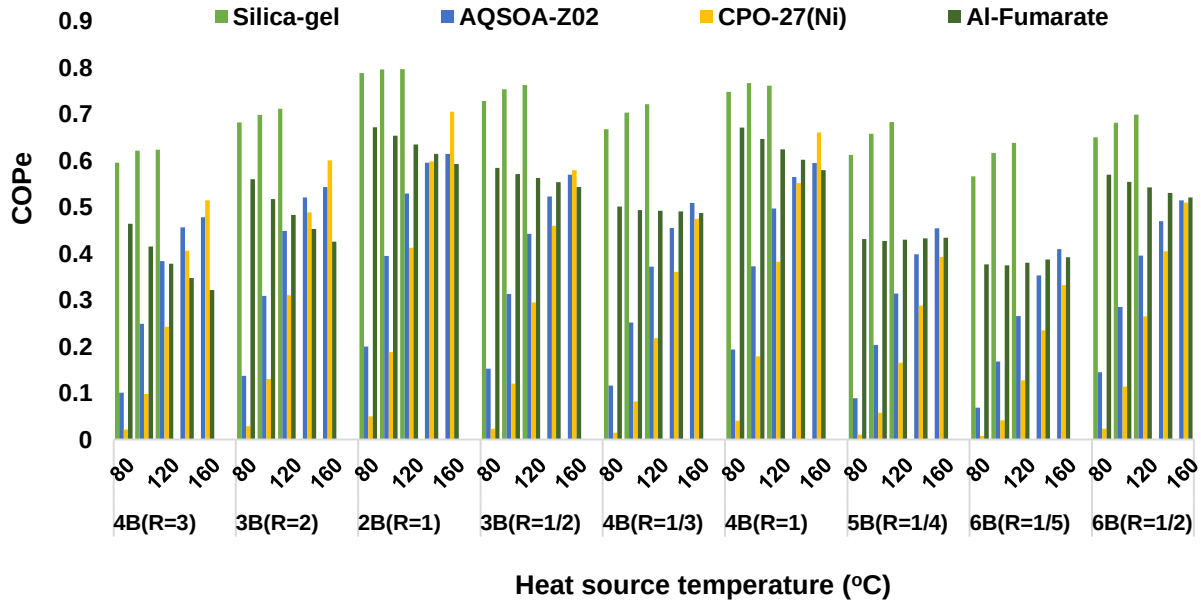

Figure 4-44: COPe of different bed arrangements and ads/des ratio (R) of multi-bed ASCE utilizing four different adsorbent materials with $T_{cooling}$=28 ºC and $T_{chilled}$=18 ºC

Figure 4-45, and Figure 4-46 show SCP and SCPe of different bed arrangements and R ratios utilizing the four different adsorbent materials with heating temperature ranging from 80 to 160 °C and cooling temperature of 28 °C and inlet chilled water temperature of 18 °C. The maximum SCP achieved is around 800 W/kg_{ads} using CPO-27(Ni) at heat source temperature of 160 °C using two-bed arrangement. For AQSOA-Z02 the maximum SCP achieved is about 678 W/kg_{ads} at heat source temperature of 160 °C using three-bed arrangement and R=1/2 compared to 642 W/kg_{ads} using two-bed arrangement. The maximum SCPe achieved is about 1040 W/kg_{ads} using CPO-27(Ni) at heat source temperature of 160 °C using two-bed arrangement. For AQSOA-Z02 the maximum SCPe achieved is around 878 W/kg_{ads} at 160 °C using three-bed arrangement. For Silica-gel and Al-Fumarate, the maximum SCP and SCPe happen when using three-bed arrangement. At heat source temperature below 120 °C, AQSOA-Z02 and CPO-27(Ni) showed poor performance due to their adsorption characteristics as discussed in Chapter 3.

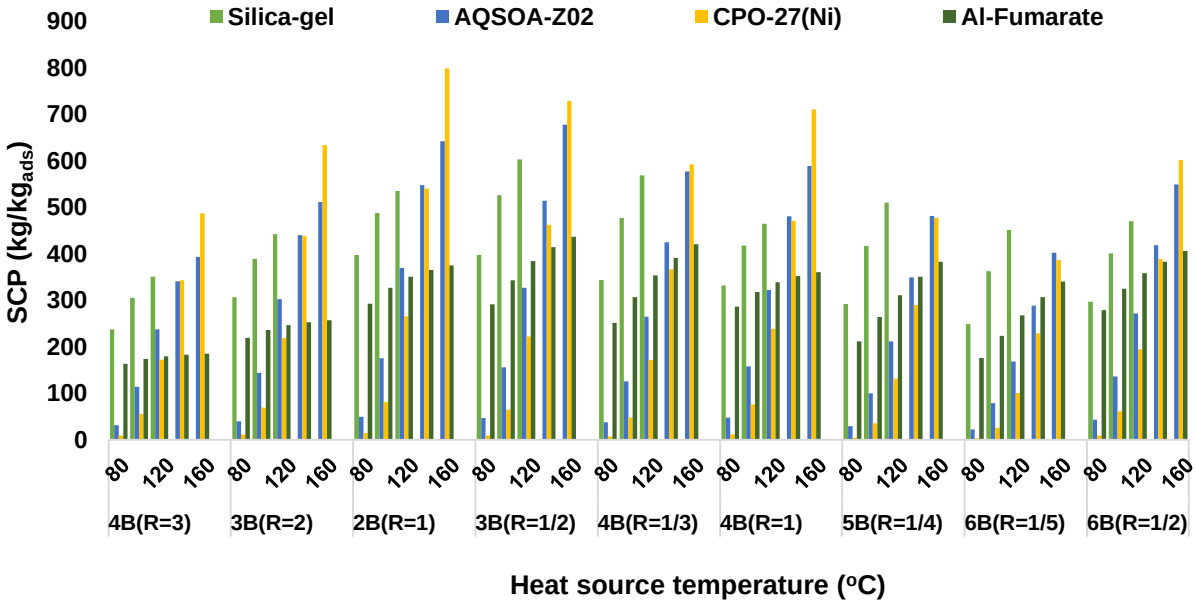

Figure 4-45: SCP of different bed arrangements and ads/des ratio (R) of multi-bed ASCE utilizing four different adsorbent materials with $T_{cooling}$=28 ºC and $T_{chilled}$=18 ºC

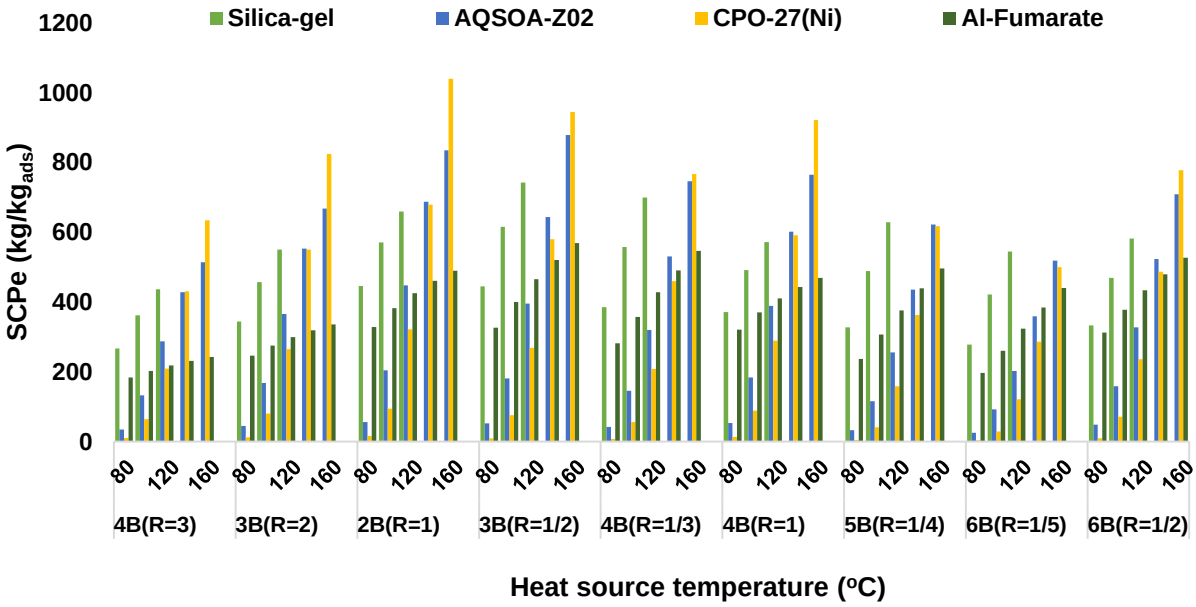

Figure 4-46: SCPe of different bed arrangements and ads/des ratio (R) of multi-bed ASCE utilizing four different adsorbent materials with $T_{cooling}$=28 ºC and $T_{chilled}$=18 ºC

Figure 4-47 shows the effect of using different bed arrangements and R ratios using four different adsorbent materials and heat source temperature between 80-160 °C on SP generated by the system. Maximum SP generated in this study is about 80 W/kg$_{ads}$ utilizing CPO-27(Ni)

at 160 °C with the two-bed arrangement and R=1. For AQSOA-Z02 the maximum SP achieved is around 67 W/kg_{ads} at 160 °C using the three-bed arrangement and R=1/2. In terms of the number of beds and R ratio used, the three-bed arrangement with R=1/2 has the maximum SP for Silica-gel and Al-Fumarate for all the range of heat source temperatures used, while for AQSOA-Z02 this occurred only with heating temperature of 160 °C and for CPO-27(Ni), the maximum SP was always achieved when using two-bed arraignment. This may reveal that for some materials there is a specific limit of heat source temperature, where after such limit the three-bed arrangement can be the best. The arrangements with R>1 have low SP compared to other arrangements, as the time of adsorption is more than that of desorption. SP of 80 W/kg_{ads} is not large value compared to SCP of 800 W/kg_{ads} (about only 10%), however the grade of power is higher than that of cooling because ideally each 1 kW of power can generate 3 kW of cooling when the typical COP for compression refrigeration system is assumed to be 3 [64, 65].

It is known that desorption rate is faster than adsorption rate [56] and this is because the later occurs at a relatively low temperature, so discharging the adsorption refrigerant (water) from the adsorbent material can be faster than charging the adsorbent materials with the refrigerant. Figure 4-48 shows the effect of using different bed arrangements and R ratios using four different adsorbent materials and heat source temperature between 80-160 °C on the adsorption power efficiency of the system. Maximum adsorption power efficiency achieved is around 5.4% utilising CPO-27(Ni) and heat source temperature of 160 °C and 2B arrangement.

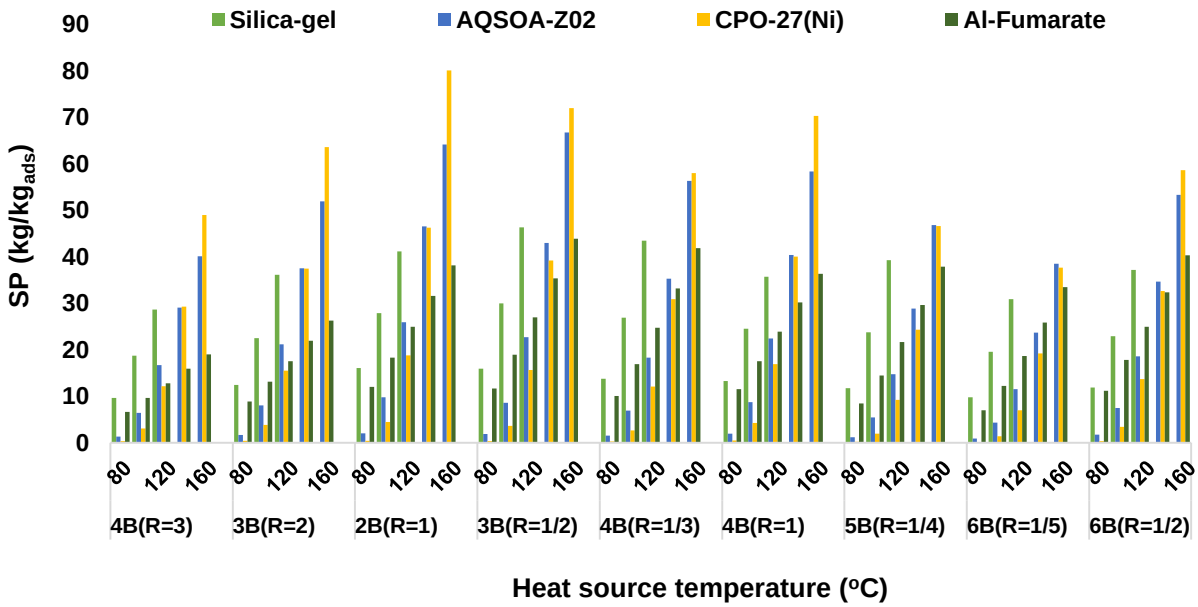

Figure 4-47: SP of different bed arrangements and ads/des ratio (R) of multi-bed ASCE utilizing four different adsorbent materials with $T_{cooling}$=28 °C and $T_{chilled}$=18 °C

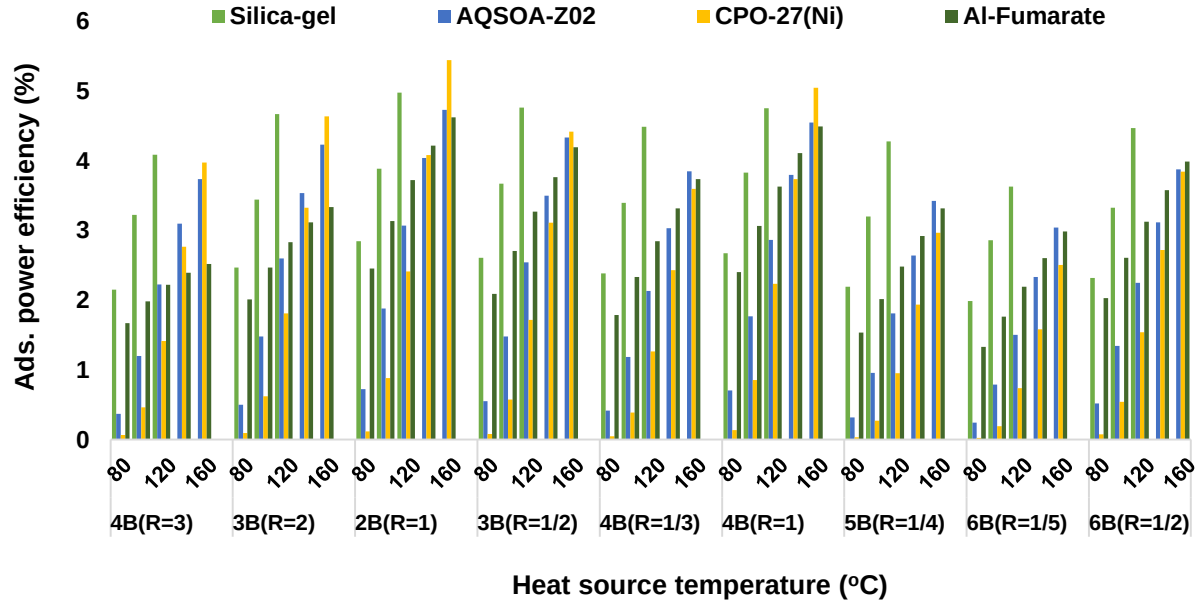

Figure 4-48: Adsorption power efficiency of different bed arrangements and ads/des ratio (R) of multi-bed ASCE utilizing four different adsorbent materials with $T_{cooling}$=28 °C and $T_{chilled}$=18 °C

4.7 Hybrid adsorption system for cooling and electricity (HASCE) [28]

The two-bed ASCE can be modified so that, four hybrid adsorber beds can be used, besides two evaporators, condenser and expander as shown in Figure 4-49 [28]. The topping beds (bed 1 and bed 2) use a high temperature adsorbent material (adsorbent material with high performance at high heat source temperature like CPO-27(Ni) and AQSOA-Z02) and they are powered using an external heat source, while the bottoming beds (bed 3 and bed 4) use low temperature adsorbent materials (adsorbent with high performance at low heat source temperature like Silica-gel) and they are powered using the heat recovered from the topping beds during adsorption process, so no more heat is added to the bottoming beds [28].

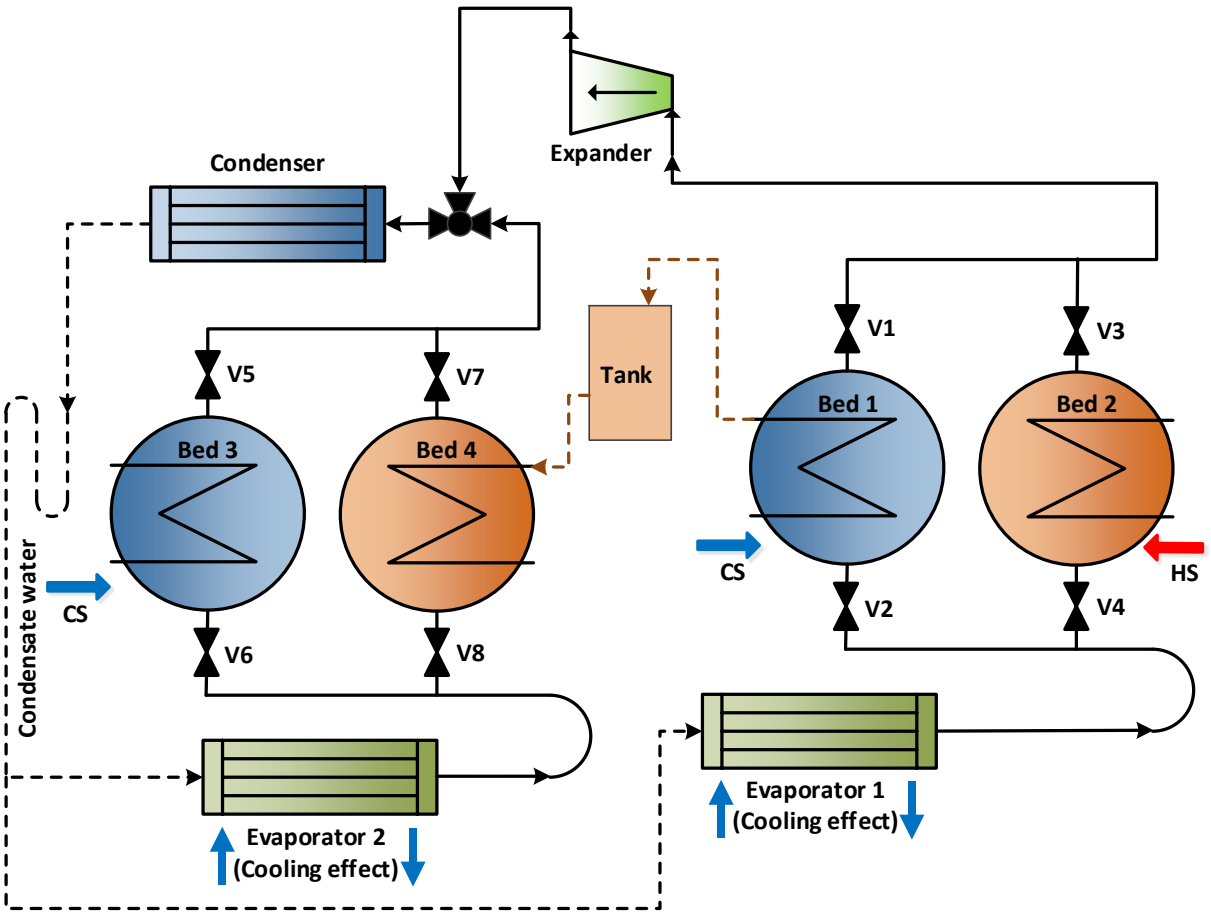

Figure 4-49: Hybrid adsorption system for cooling and electricity (HASCE)

In this design, the bed cooling water temperature of the topping beds is set to be at a relatively high value (46-48 ºC) so that the cooling water leaving the topping bed can be in the range of 50-55 ºC which can power the bottoming beds [28]. During adsorption process, the cooling water recovers additional heat so it leaves the topping beds to the tank in order to reduce the fluctuating in temperature when powering the bottoming beds [28].

The overall performance of the HASCE can be defined using the terms COP, SCP, COPe, SCPe, SP and adsorption power efficiency (η_{ads}). COP, SCP, COPe, SCPe can be calculated using [20, 28, 65]:

$$COP = \frac{(\dot{m}c_p)_{evap,1}\int_0^{t_{cycle}}(T_{chill,in,1}-T_{chill,o,1})dt+(\dot{m}c_p)_{evap,2}\int_0^{t_{cycle}}(T_{chill,in,2}-T_{chill,o,2})dt}{(\dot{m}c_p)_h\int_0^{t_{cycle}}(T_{h,in}-T_{h,o})dt} \quad 4\text{-}18$$

$$SCP = \frac{(\dot{m}c_p)_{evap,1}\int_0^{t_{cycle}}(T_{chill,in,1}-T_{chill,o,1})dt+(\dot{m}c_p)_{evap,2}\int_0^{t_{cycle}}(T_{chill,in,2}-T_{chill,o,2})dt}{M_a t_{cycle}} \quad 4\text{-}19$$

$$COPe = \frac{(\dot{m}c_p)_{evap,1}\int_0^{t_{cycle}}(T_{chill,in,1}-T_{chill,o,1})dt+(\dot{m}c_p)_{evap,2}\int_0^{t_{cycle}}(T_{chill,in,2}-T_{chill,o,2})dt\ +F[\int_0^{t_{cycle}}\dot{m}_{ads}\,\Delta h dt]}{(\dot{m}c_p)_h\int_0^{t_{cycle}}(T_{h,in}-T_{h,o})dt} \quad 4\text{-}20$$

$$SCPe = \frac{(\dot{m}c_p)_{evap,1}\int_0^{t_{cycle}}(T_{chill,in,1}-T_{chill,o,1})dt+(\dot{m}c_p)_{evap,2}\int_0^{t_{cycle}}(T_{chill,in,2}-T_{chill,o,2})dt\ +F[\int_0^{t_{cycle}}\dot{m}_{ads}\,\Delta h dt]}{M_a t_{cycle}} \quad 4\text{-}21$$

SP and η_{ads} can be calculated as in equations 4-11 and 4-12. Also the exergy efficiency is used to evaluate the HASCE and it can be defined as [65, 206-208]:

$$\eta_{ex=}\frac{W_{exp,ads}+E_{evap,1+}E_{evap,2}}{E_{in}} \quad 4\text{-}22$$

Where E_{evap} is the cooling exergy through the evaporator and can be defined as [65, 206-208]:

$$E_{evap,1=}\frac{(\dot{m}c_p)_{evap,1}\int_0^{t_{cycle}}(T_{chill,in,1}-T_{chill,o,1})dt}{t_{cycle}}\left[\frac{T_{amb}}{T_{evap,1}}-1\right] \quad 4\text{-}23$$

$$E_{evap,2=}\frac{(\dot{m}c_p)_{evap,2}\int_0^{t_{cycle}}(T_{chill,in,2}-T_{chill,o,2})dt}{t_{cycle}}\left[\frac{T_{amb}}{T_{evap,2}}-1\right] \quad 4\text{-}24$$

The exergy input to the system (E_{in}) can be defined as [10, 65, 106]:

$$E_{in=}\frac{\dot{m}_h\int_0^{t_{cycle}}[(h_{h,in}-h_{h,o})-T_{amb}(s_{h,in}-s_{h,o})]dt}{t_{cycle}} \quad 4\text{-}25$$

4.8 Performance of HASCE [28]

Figure 4-50 shows COPe/COP of the hybrid adsorption system for cooling and electricity (HASCE) compared to that of ASCE and BACS systems utilising AQSOA-Z02/Silica-gel and CPO-27(Ni)/Silica-gel [28]. For all cases, COPe of HASCE is higher than that of ASCE and BACS with maximum value of 0.97 achieved by AQSOA-Z02/Silica-gel at 100 ºC. Figure 4-51 shows SCPe/SCP of HASCE compared to that of ASCE and BACS systems utilising AQSOA-Z02/Silica-gel and CPO-27(Ni)/Silica-gel. Results show that the SCPe of

HASCE is always lower than that of ASCE and BACS and this due to using relatively high cooling temperature at the toping beds and relatively low heat source temperature that powering the bottoming beds. Figure 4-52 shows the exergy efficiency of HASCE compared to that of ASCE and BACS systems utilising AQSOA-Z02/Silica-gel and CPO-27(Ni)/Silica-gel. For all cases, exergy efficiency of HASCE is higher than that of ASCE and BACS (except for CPO-27(Ni)/Silica-gel at 160 ºC) with a maximum value of 48% utilizing AQSOA-Z02/Silica-gel at 100 ºC [28].

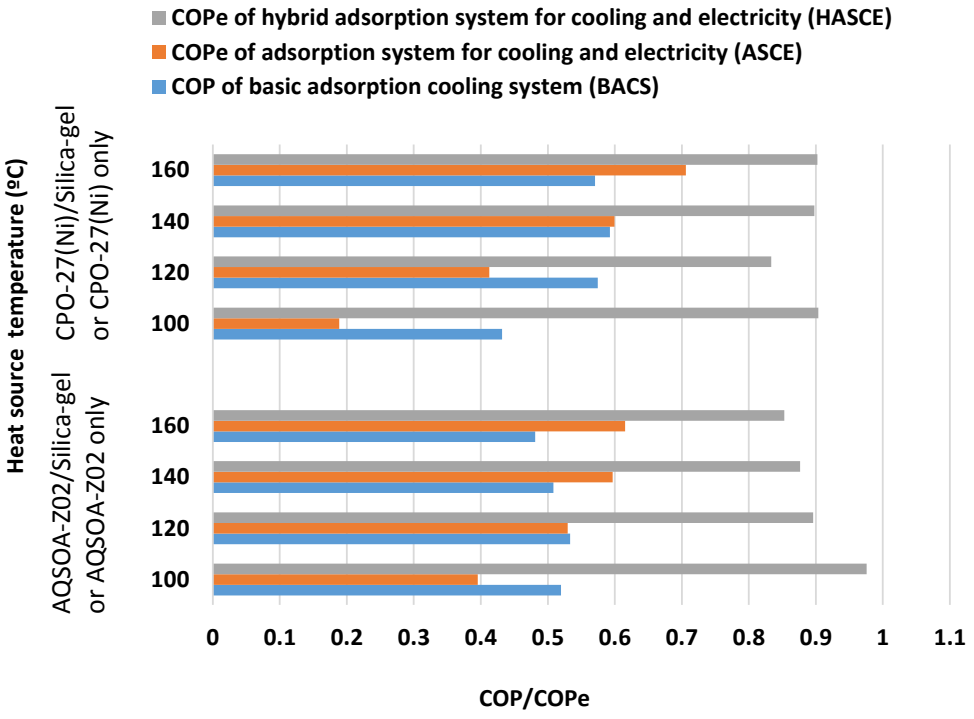

Figure 4-50: COP/COPe of HASCE compared to ASCE and BACS utilizing AQSOA-Z02/Silica-gel and CPO-27(Ni)/Silica-gel with $T_{cooling}$=28 ºC and $T_{chilled}$=18 ºC

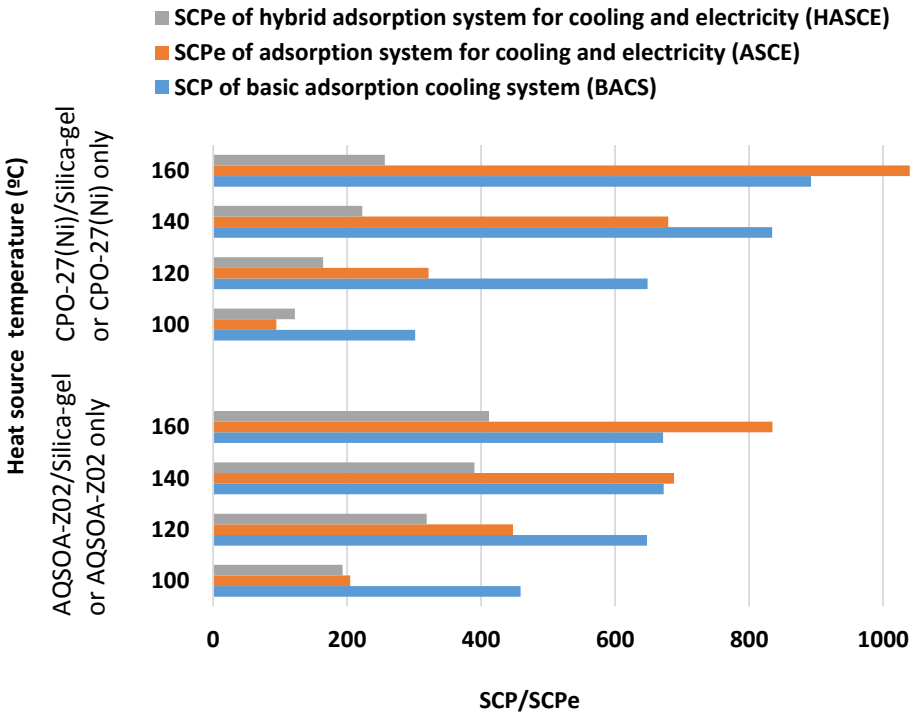

Figure 4-51: SCP/SCPe of HASCE compared to ASCE and BACS utilizing AQSOA-Z02/Silica-gel and CPO-27(Ni)/Silica-gel with $T_{cooling}$=28 ºC and $T_{chilled}$=18 ºC

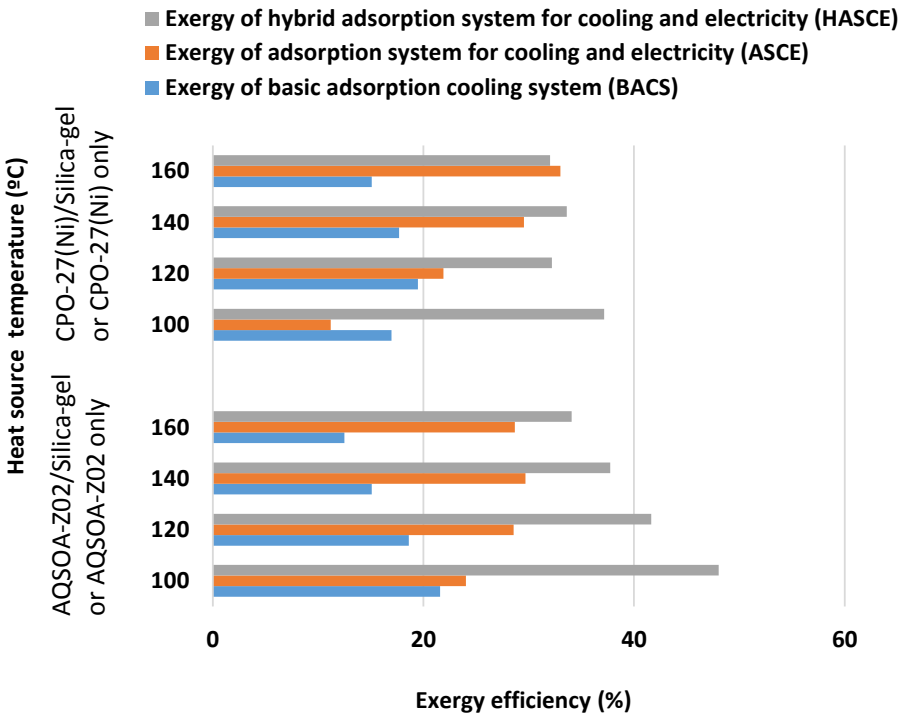

Figure 4-52: Exergy efficiency of HASCE compared to ASCE and BACS utilizing AQSOA-Z02/Silica-gel and CPO-27(Ni)/Silica-gel with $T_{cooling}$=28 ºC and $T_{chilled}$=18 ºC

Figure 4-53 and Figure 4-54 show the effect of using a range of heat source temperature between 100-160 °C (very low cooling with almost no power were achieved below 100 °C) on the COP and COPe of HASCE respectively. A maximum COP of 0.93 is achieved using AQSOA-Z02/Silica-gel (AQSOA-Z02 in the topping beds and Silica-gel in the bottoming beds) at heat source temperature of 100 ºC, while for CPO-27(Ni)/Silica-gel, the maximum COP of 0.89 is achieved at 100 ºC. Maximum COPe of 0.97 is achieved using AQSOA-Z02/Silica-gel at 100 ºC, while for CPO-27(Ni)/Silica-gel, maximum COPe of 0.9 is achieved using heat source temperature of 100 ºC. HASCE has significantly higher COP and COPe compared to the two-bed ASCE utilising AQSOA-Z02 and CPO-27(Ni) separately and this is mainly because HASCE has two evaporators producing cooling without any additional heat for powering the bottoming cycle.

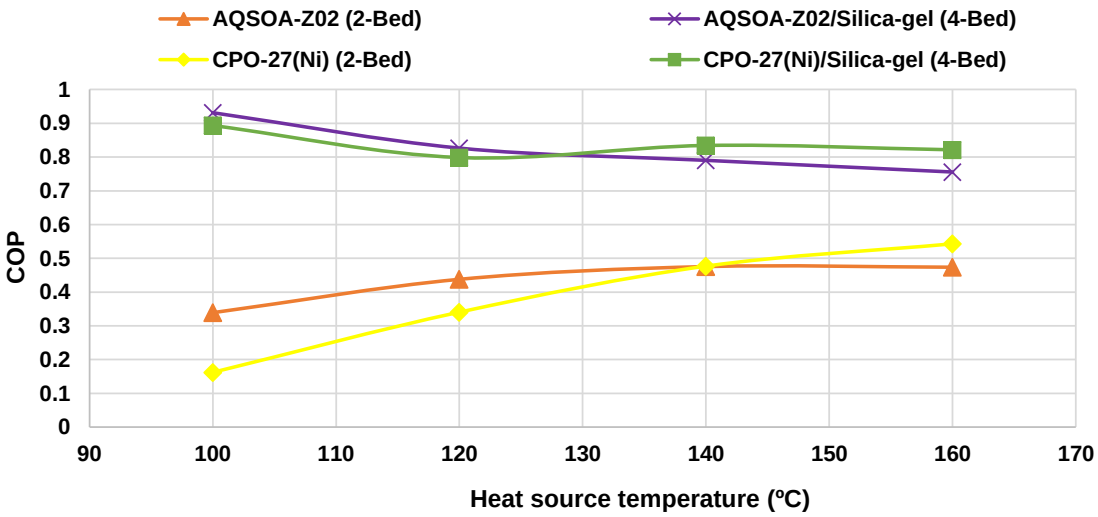

Figure 4-53: Effect of heat source temperature on COP of the HASCE utilizing CPO-27(Ni)/Silica-gel and AQSOA-Z02/Silica-gel utilising $T_{cooling}$=28 ºC and $T_{chilled}$=18 ºC

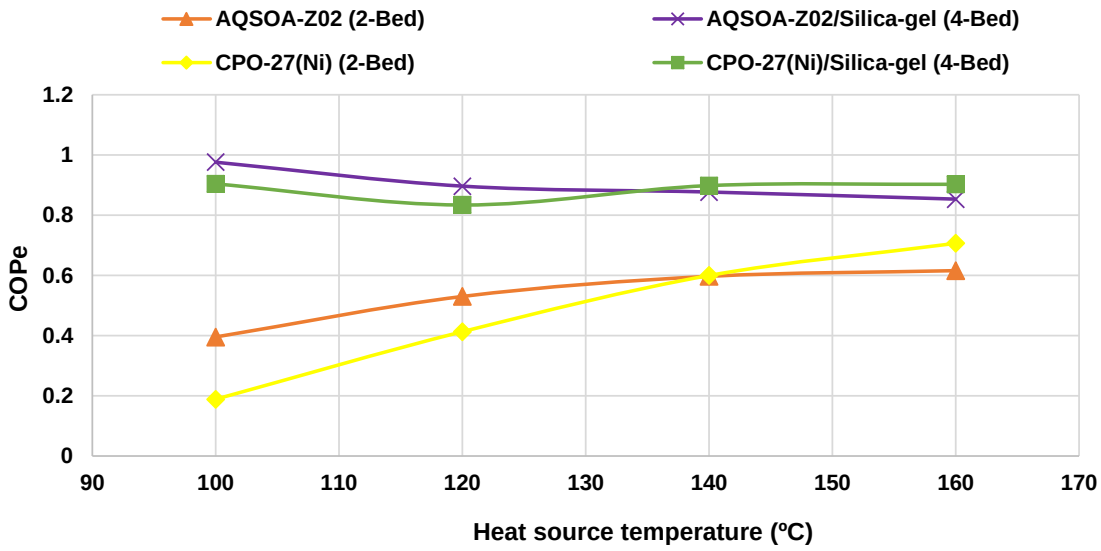

Figure 4-54: Effect of heat source temperature on COPe of the HASCE utilizing CPO-27(Ni)/Silica-gel and AQSOA-Z02/Silica-gel utilising $T_{cooling}$=28 ºC and $T_{chilled}$=18 ºC

Figure 4-55 and Figure 4-56 show the effect of using a range of heat source temperature with cooling water temperature of 28 °C and inlet chilled water temperature of 18 °C on SCP and SCPe of the HASCE [28]. Even though, HASCE shows higher COP and COPe compared to the two-bed adsorption system, unfortunately, this system shows relatively low SCP and SCPe and this is because of using relatively high bed cooling water temperature in the topping cycle, and relatively low heat source temperature in the bottoming cycle. Maximum SCP of 341 W/kg_{ads} is achieved using AQSOA-Z02/Silica-gel at heat source temperature of 160 ºC, while maximum SCPe of 412 W/kg_{ads} is achieved using AQSOA-Z02/Silica-gel at 160 ºC [28]. Figure 4-57 and Figure 4-58 show the effect of heating fluid temperature on SP and adsorption power efficiency of the HASCE. SP and adsorption power efficiency of this system are relatively low for the same reasons that discussed SCP and SCPe, however maximum amount of SP of 23.5 W/kg_{ads} and adsorption power efficiency of 4.9 % are achieved using AQSOA-Z02/Silica-gel at 160 ºC.

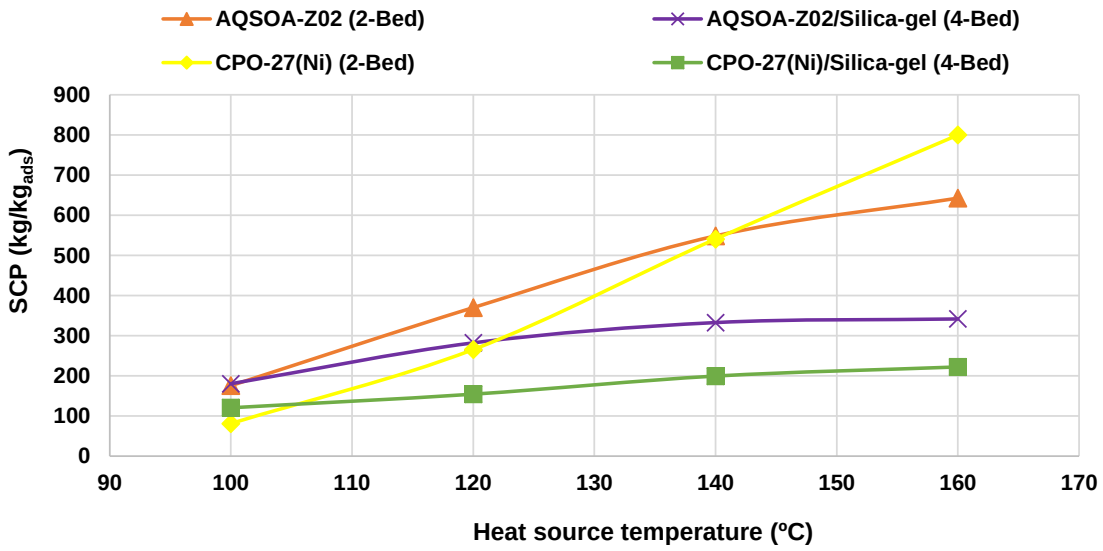

Figure 4-55: Effect of heat source temperature on SCP of the HASCE utilizing CPO-27(Ni)/Silica-gel and AQSOA-Z02/Silica-gel utilising $T_{cooling}$=28 ºC and $T_{chilled}$=18 ºC

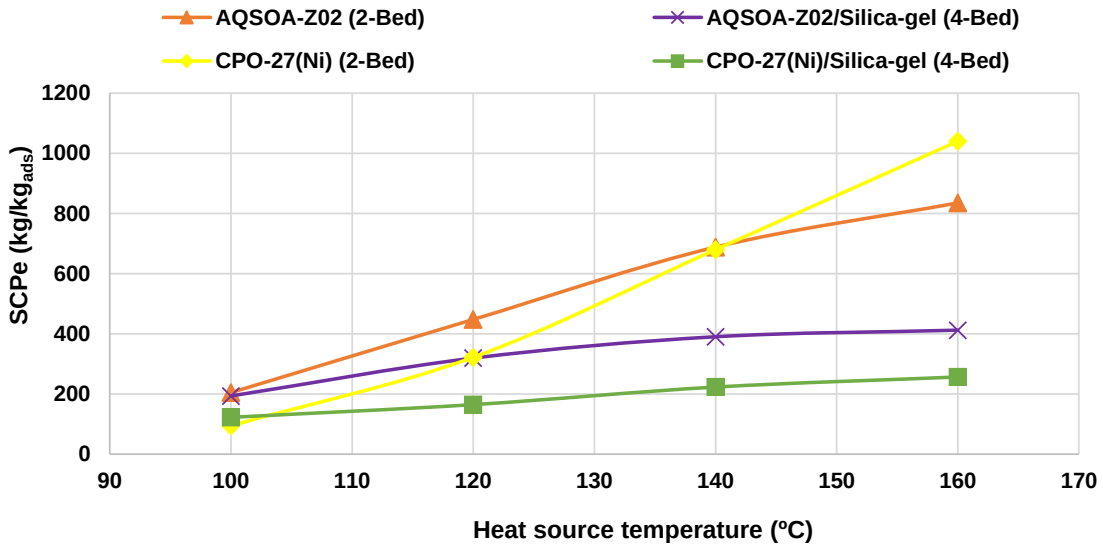

Figure 4-56: Effect of heat source temperature on SCPe of the HASCE utilizing CPO-27(Ni)/Silica-gel and AQSOA-Z02/Silica-gel utilising $T_{cooling}$=28 ºC and $T_{chilled}$=18 ºC

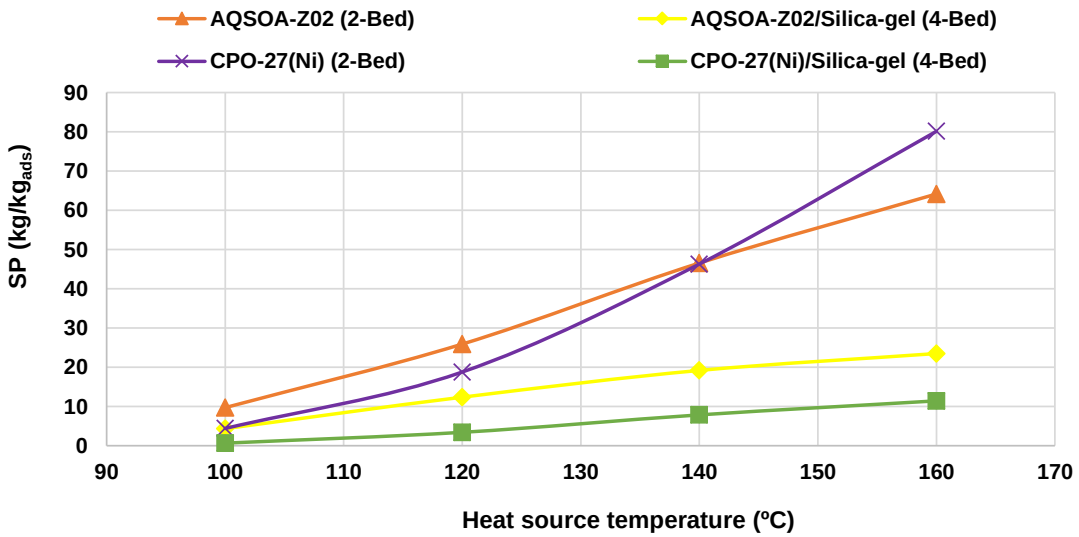

Figure 4-57: Effect of heat source temperature on SP of the HASCE utilizing CPO-27(Ni)/Silica-gel and AQSOA-Z02/Silica-gel utilising $T_{cooling}$=28 ºC and $T_{chilled}$=18 ºC

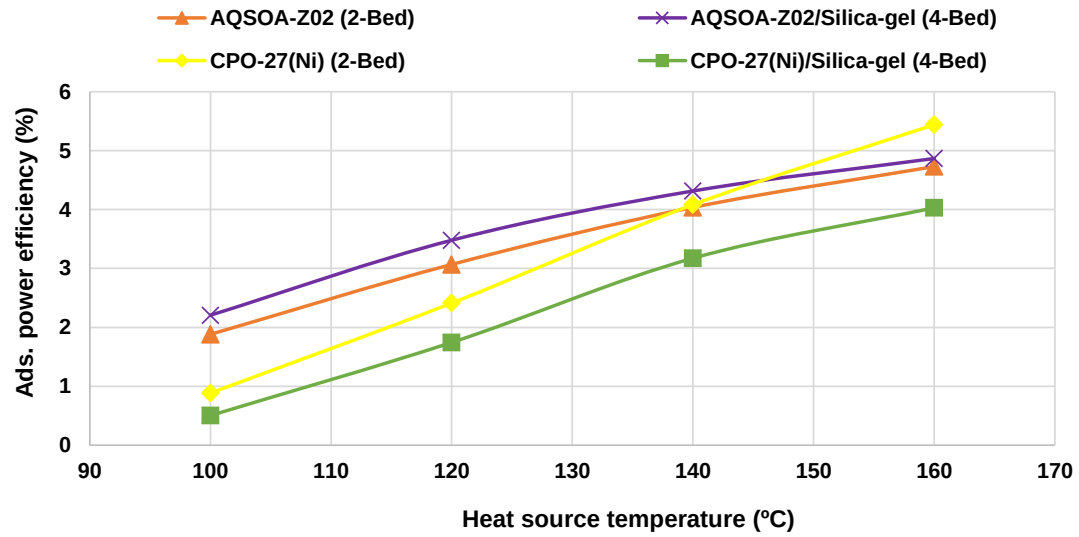

Figure 4-58: Effect of heat source temperature on the adsorption power efficiency of the HASCE utilizing CPO-27(Ni)/Silica-gel and AQSOA-Z02/Silica-gel utilising $T_{cooling}$=28 ºC and $T_{chilled}$=18 ºC

Hybrid adsorption system for cooling and electricity (HASCE) can generate cooling and electricity at the same time with relatively high COPe (with a maximum value of 0.97) compared to that of the ASCE (with a maximum value of 0.8) which can be useful especially when the amount of heat is limited. However, the SCPe generated by HASCE are low compared to the ASCE [28].

4.9 Summary

In this chapter, the basic adsorption cooling system (BACS) has been modified to study the feasibility of producing cooling and power simultaneously by combining an expander between the hot adsorber bed (desorber) and the condenser [20]. The modified system utilises advanced adsorbent materials like Metal Organic Framework MOF CPO-27(Ni), MIL101(Cr), Al-Fumarate, and AQSOA-Z02 zeolite and results are compared to Silica-gel. The main conclusions of this chapter can be listed as [20]:

1. Adsorption system for cooling and electricity (ASCE) is feasible and can generate cooling and power simultaneously. The system can generate maximum SCP of 800 W/kgads and SP of 80 W/kgads utilising CPO-27(Ni) with heat source temperature 160 ºC [20].

2. Generating cooling and power simultaneously is more effective at heat source temperature higher than 120 °C and generally as the heat source temperature increases, the specific cooling power (SCP) and specific power (SP) increase [20].

3. The ASCE has maximum equivalent coefficient of performance COPe of 0.8 utilising Silica-gel compared to maximum COP of 0.7 achieved by BACS utilising Silica-gel at heat source temperature of 100 °C. Also, the ASCE has maximum equivalent specific cooling power SCPe of 1040 W/kg_{ads} achieved by CPO-27(Ni) compared to maximum

SCP of 892 W/kg_{ads} achieved by BACS using the same material at heat source temperature of 160 °C.

4. For all adsorbent materials with heat source temperatures used in this study, the exergy efficiency of ASCE is higher than that of BACS [65] (except for CPO-27(Ni) at 100 °C), and maximum exergy efficiency of 63% is achieved utilising Silica-gel at 80 °C.
5. In terms of bed arrangement, the two-bed arrangement with R=1 has the maximum COP/COPe for all adsorbent materials and all range of temperatures used in this study. The three-bed arrangement with R=1/2 has the maximum SCP/SCPe and SP for Silica-gel and Al-Fumarate for all the range of heat source temperatures used, while for AQSOA-Z02 with heating fluid temperature of 160 °C.
6. As the number of bed increases, more continuity in cooling and power can be achieved. For most cases, four-bed and three-bed arrangements working in parallel produce higher COP, SCP and SP than those of the four-bed and six-bed arrangements working in series.
7. Hybrid adsorption system for cooling and electricity (HASCE) is another form of the ASCE utilising four cascaded adsorber beds. The system can generate cooling and power with higher COP/COPe compared to the ASCE, however, the amount of cooling and power generated are low compared to the ASCE.

CHAPTER FIVE

SIMULATION OF INTEGRATED ADSORPTION-ORC SYSTEM FOR COOLING AND ELECTRICITY (SECOND CONFIGURATION)

5.1 Introduction

In this chapter, a two-bed water adsorption cooling system has been integrated with an Organic Rankine Cycle (ORC) to simultaneously generate cooling and electricity (IAOSCE) [22]. CPO-27(Ni), and Al-Fumarate MOFs and AQSOA-ZO2 zeolite are used and compared to the commonly used Silica-gel while R245fa, R365mfc and R141b are used as ORC working fluids. Four different scenarios of the integrated adsorption-ORC system have been investigated for cooling and electricity (IAOSCE), where in the first three scenarios, the adsorption system is set up as a topping system, and ORC is set up as a bottoming system. In the fourth scenario, the ORC is used as a topping system, and the adsorption system is used as a bottoming one. Figure 5-1 shows that there are two main arrangements of the IAOSCE, the first one uses one expander (IAOSCE-1EXP), while the second one uses two expanders (IAOSCE-2EXP) so that more electric power can be generated, while the four scenarios of integration are applied to both cases of IAOSCE.

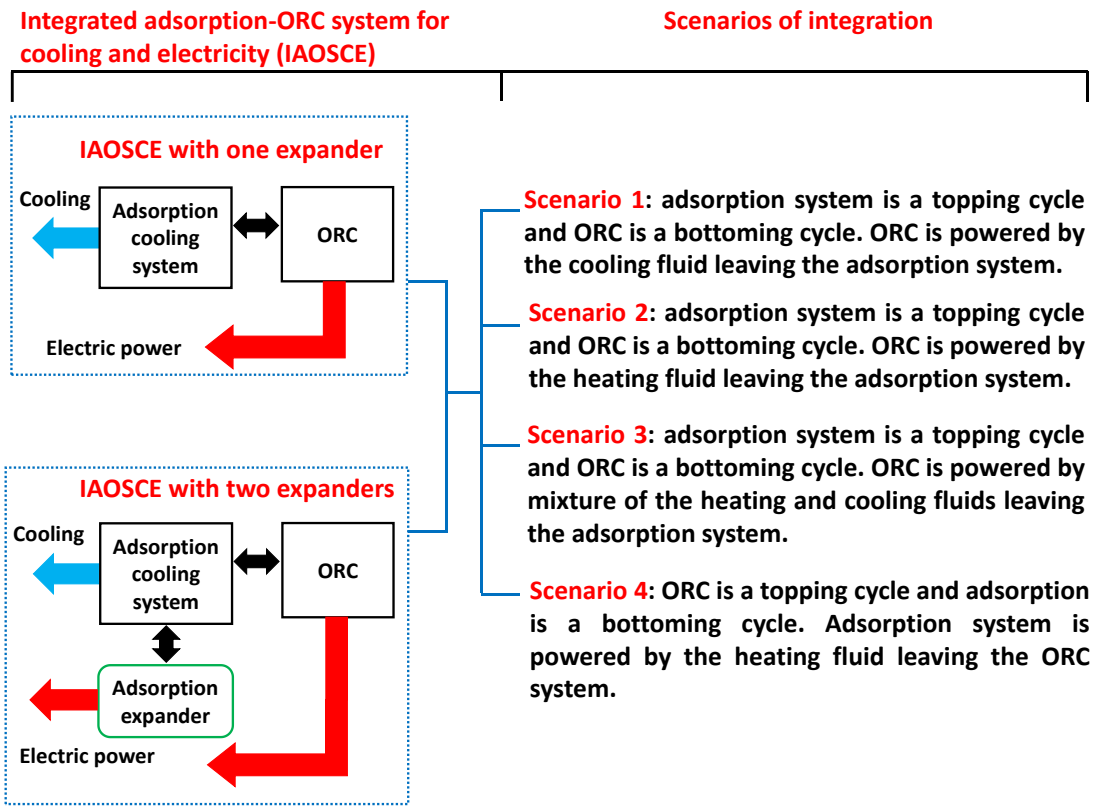

Figure 5-1: Integrated adsorption-ORC system for cooling and electricity (IAOSCE) with different scenarios

5.2 Integrated adsorption-ORC system for cooling and electricity [22]

The main purpose of using the integrated adsorption-ORC system for cooling and electricity (IAOSCE) is to investigate the possibility of producing electricity and cooling simultaneously by modifying the basic two-bed adsorption cooling system (BACS) to be integrated with an ORC system so that the heat utilization efficiency can be improved [22]. This study can be carried out using four scenarios:

Scenario 1 [22]: this scenario is shown in Figure 5-2 where the adsorption cooling system is used as a topping system while the ORC is used as a bottoming system. The two-bed adsorption cooling cycle is driven by an external heat source (HS) like waste heat or solar energy to sustain the desorption process in the desorber. As cooling is needed during

adsorption process, an external cooling fluid is used to absorb the heat of adsorption and sustain the adsorption process, which produces cooling effect in the evaporator [22], while ORC is powered using the same cooling fluid leaving the adsorption cooling system.

Scenario 2 [22]: this scenario is shown in Figure 5-3, where the adsorption cooling system is set up as a topping system and powered by an external heat source, while ORC is set up as a bottoming system and it is driven using the same heat source leaving the adsorption system.

Scenario 3 [22]: this scenario is shown in Figure 5-4, the adsorption cooling system is set up as topping system and it is powered by an external heat source. This scenario combines scenarios 1 and 2 where the recovered heat from the adsorption mixes with the return heating source to produce new heat source that can be used to power the ORC.

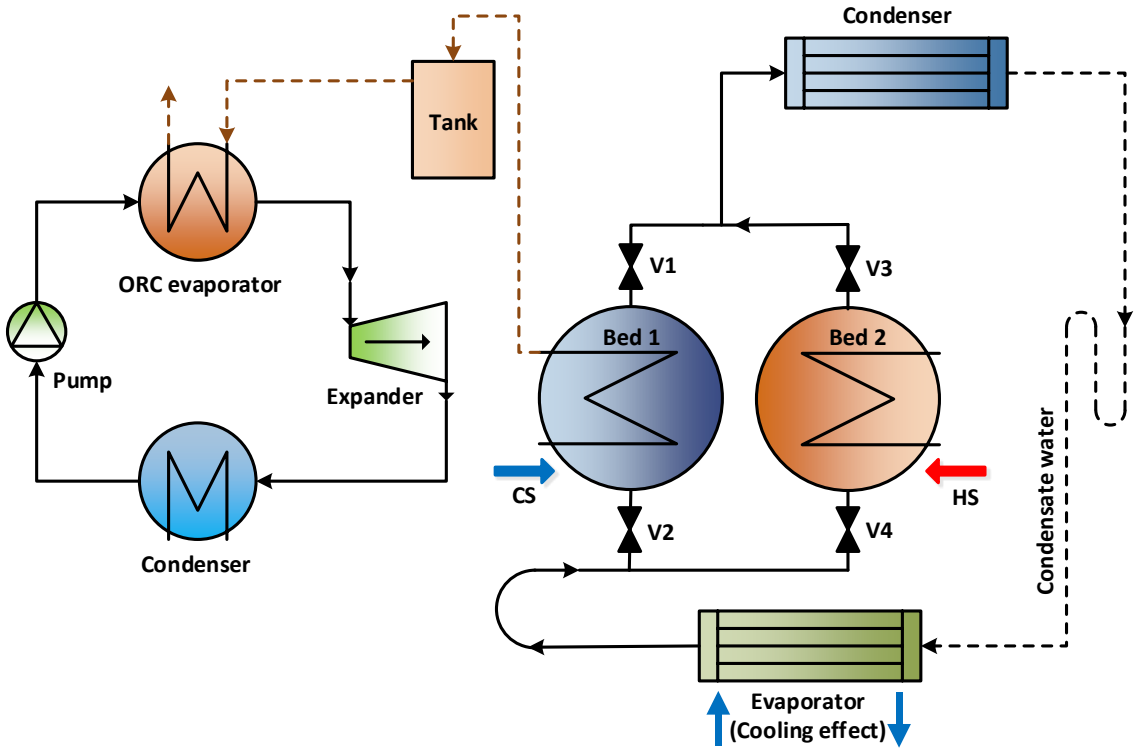

Figure 5-2: IAOSCE schematic diagram (scenario 1)

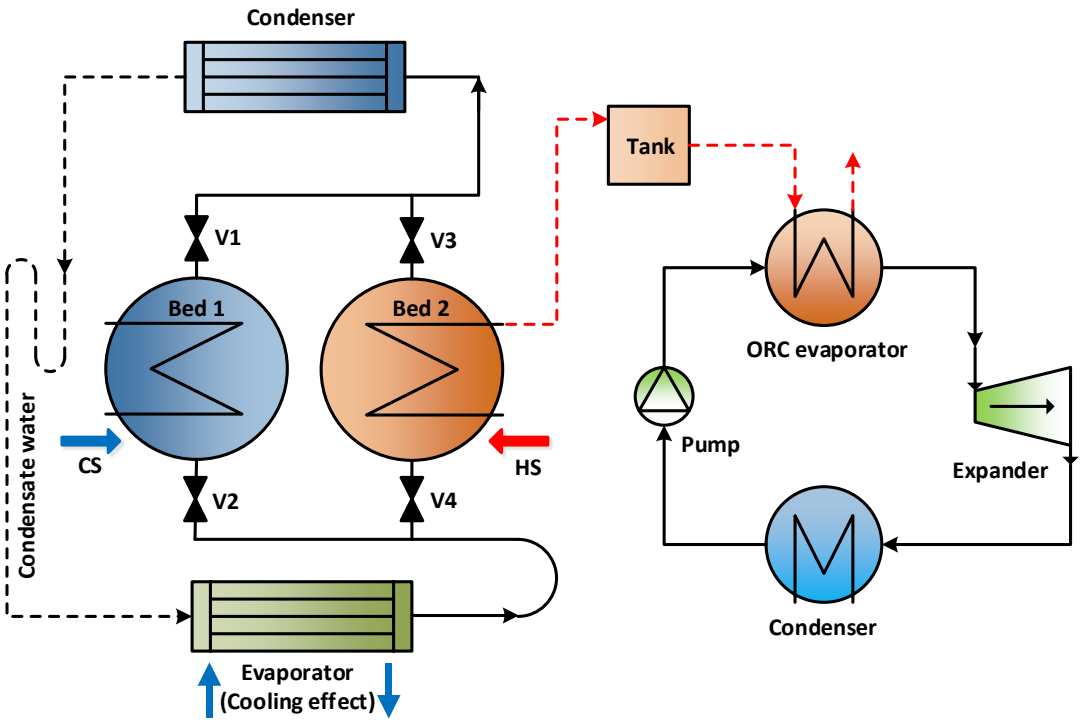

Figure 5-3: IAOSCE schematic diagram (scenario 2)

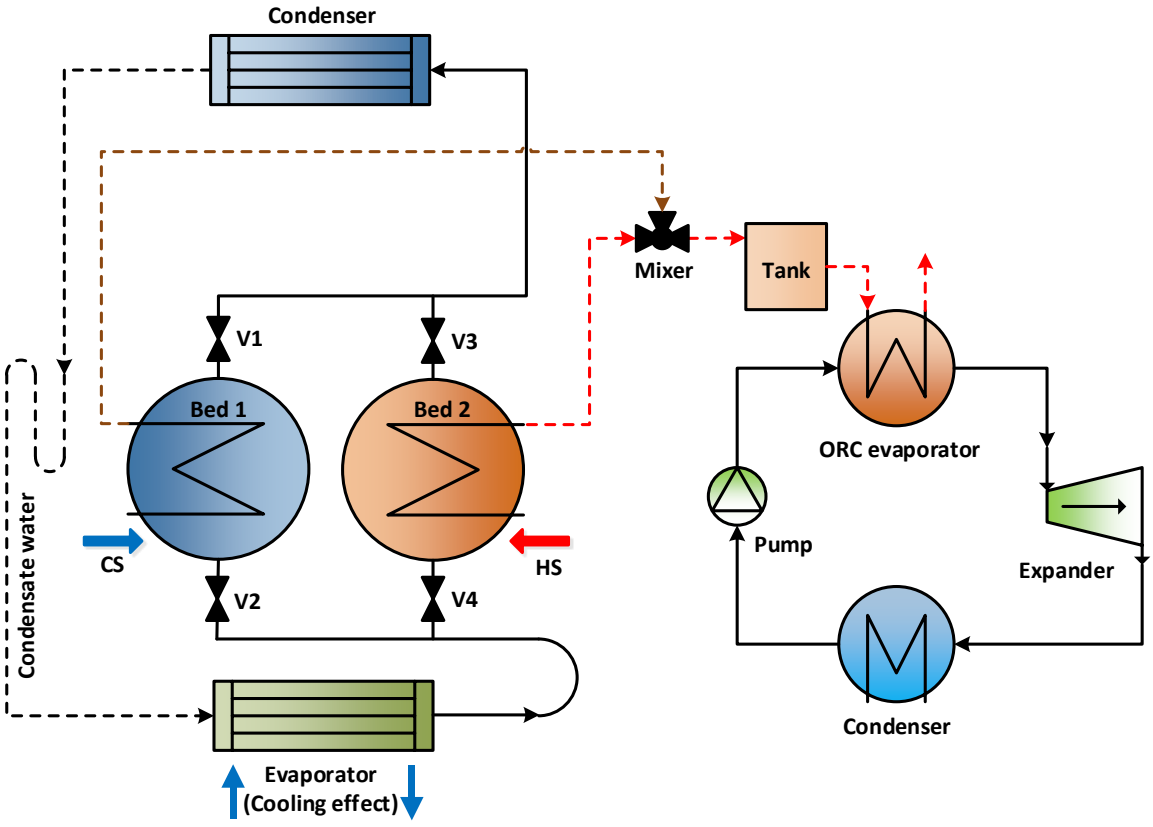

Figure 5-4: IAOSCE schematic diagram (scenario 3)

Scenario 4 [22]: this scenario, is shown in Figure 5-5, an external heat source is used to drive the ORC system, which is set up as topping system while the adsorption cooling system is set up as a bottoming system. The heating fluid leaving the ORC evaporator is used to power the adsorption cycle and cooling can be generated in the adsorption evaporator, while electricity can be generated by the ORC expander.

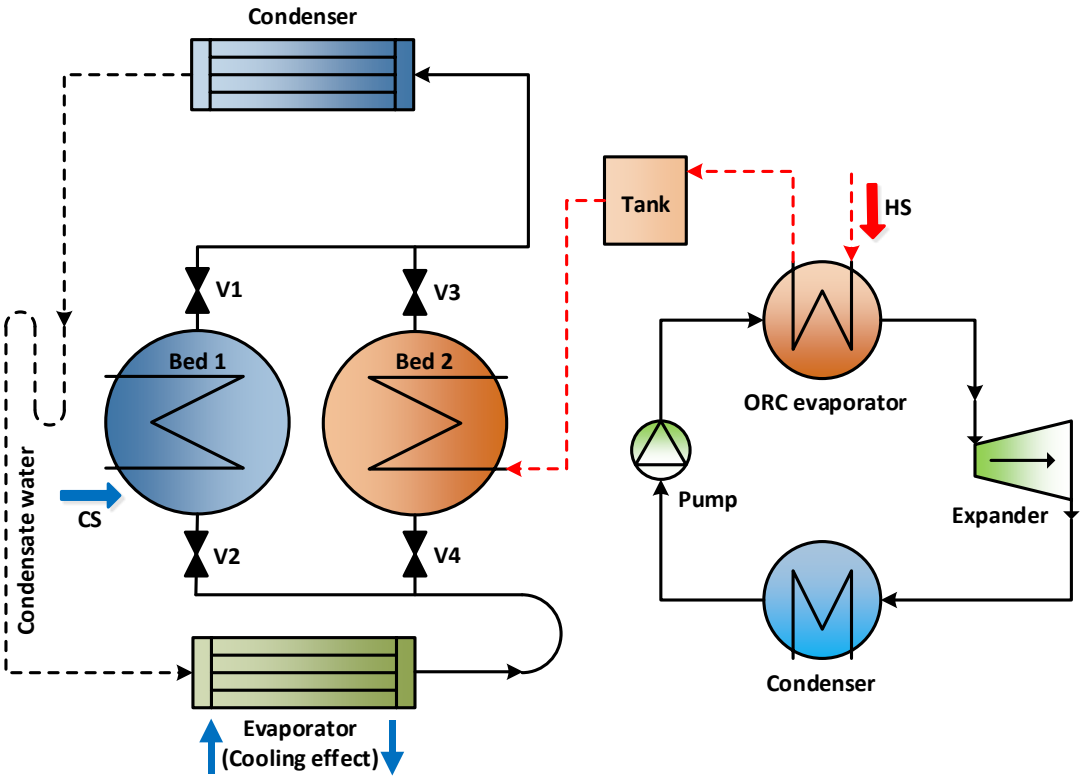

Figure 5-5: IAOSCE schematic diagram (scenario 4)

In scenarios 1 and 3, the cooling fluid (water) used has a relatively high temperature (48 °C) compared to the scenarios 2 and 4, so that the heat of adsorption can be recovered to produce hot fluid with temperature in the range of 50-55 °C which can be used to power the ORC without using the external heat source [22].

5.3 IAOSCE with two expanders [64]

This study examines the opportunity of producing electricity and cooling simultaneously by integrating a two-bed adsorption system for cooling and electricity (ASCE) described in Chapter 4 with an ORC system. As a result, cooling can be generated in the evaporator, while two expanders generate electricity (steam expander and ORC expander) [64]. Four scenarios similar to those used in the IAOSCE with one expander as discussed in section 5.2 are presented in Figure 5-6, Figure 5-7, Figure 5-8 and Figure 5-9 [64]. The steam expander (turbine) incorporated between the desorber and the condenser (in the adsorption cycle), while the ORC cycle already has an ORC expander (turbine).

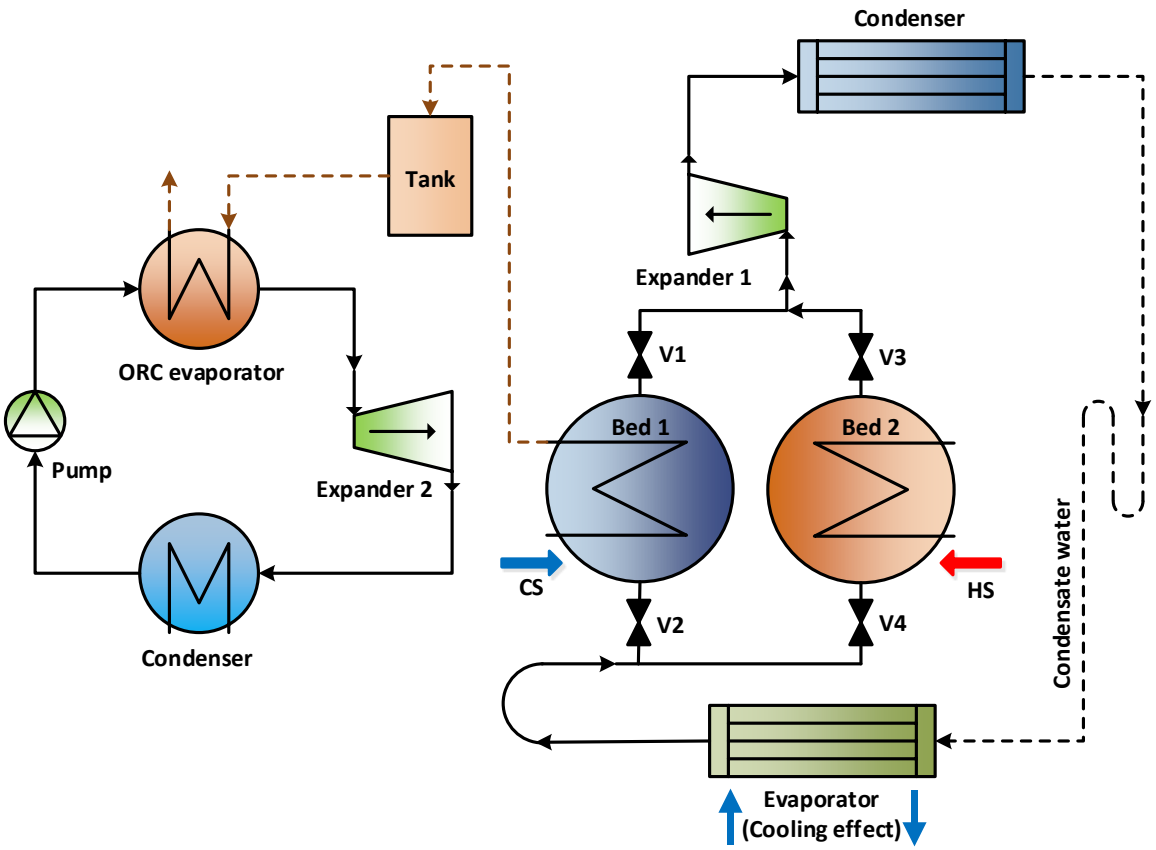

Figure 5-6: Schematic diagram of the IAOSCE with two expanders (scenario 1)

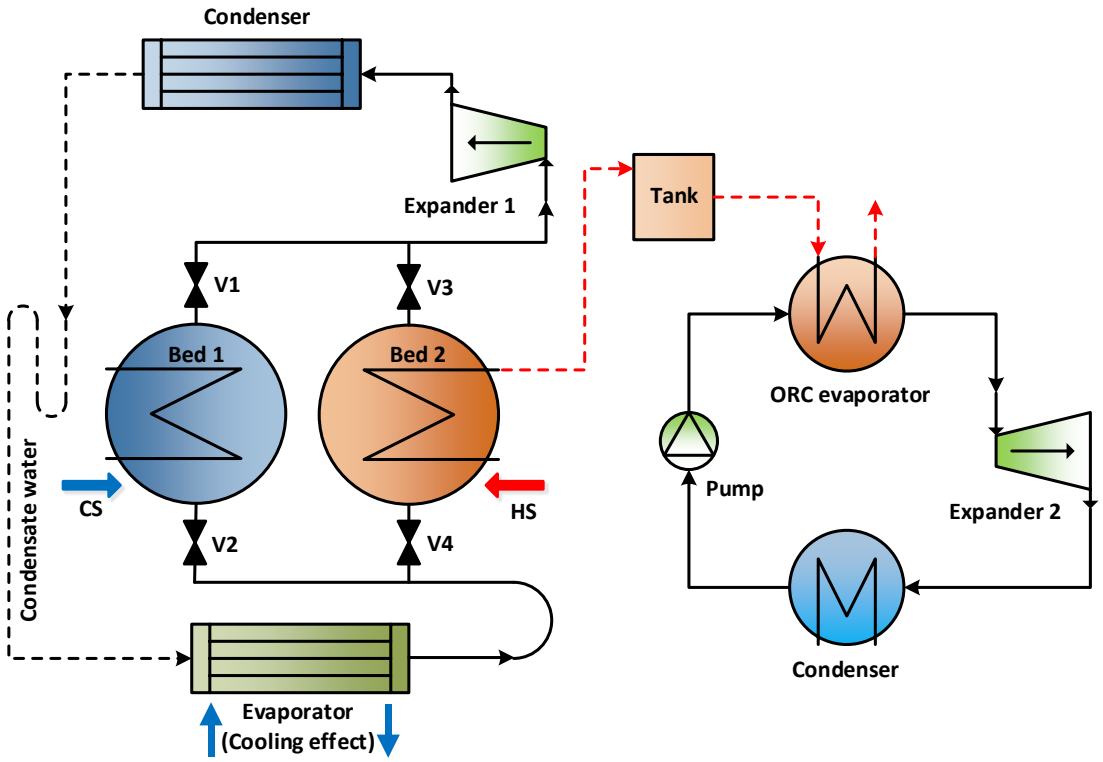

Figure 5-7: Schematic diagram of the IAOSCE with two expanders (scenario 2)

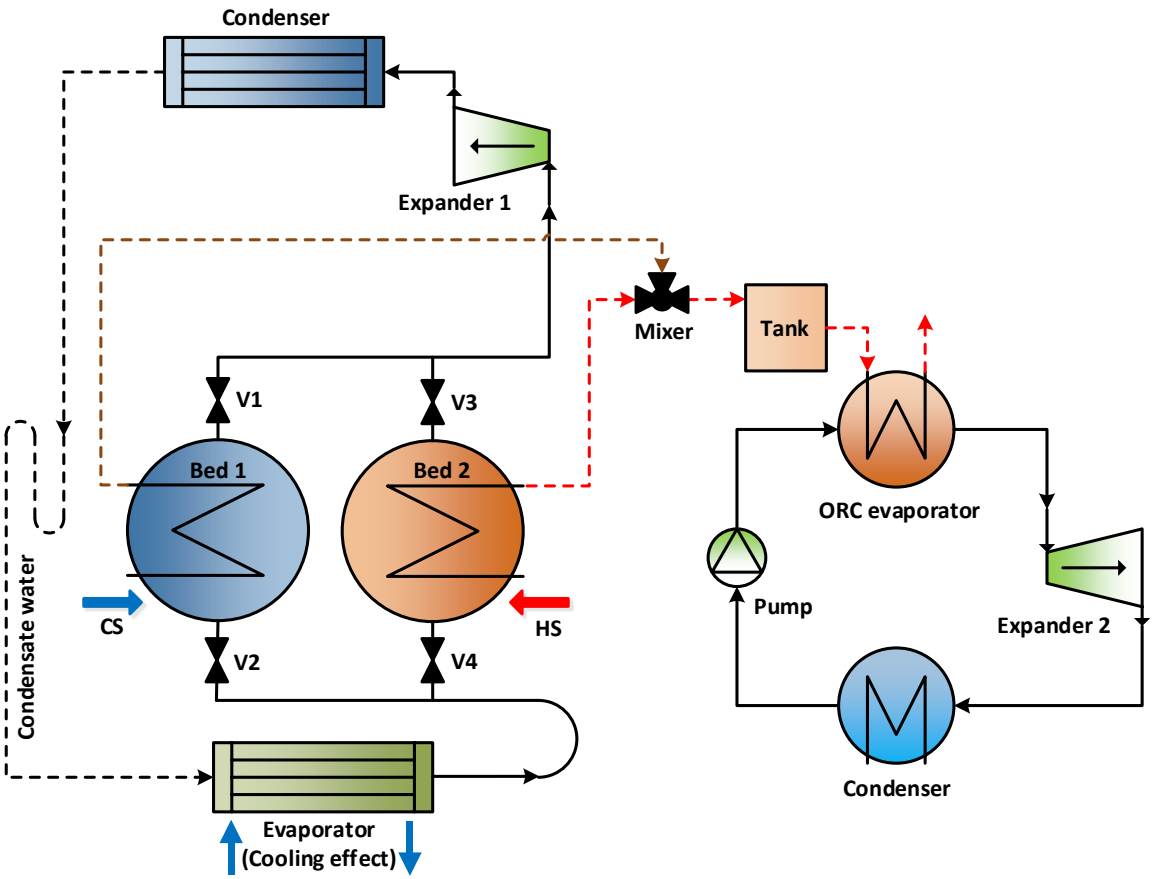

Figure 5-8: Schematic diagram of the IAOSCE with two expanders (scenario 3)

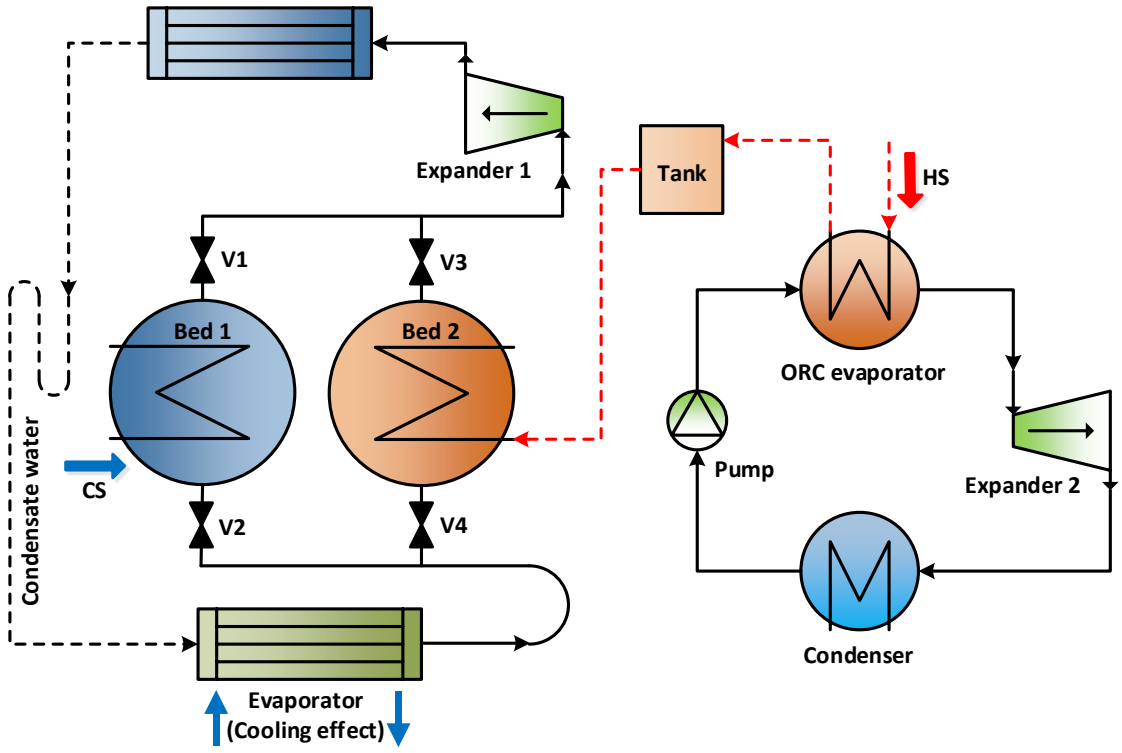

Figure 5-9: Schematic diagram of the IAOSCE with two expanders (scenario 4)

5.4 Mathematical modelling [22, 64]

Three advanced adsorbent materials including Al-Fumarate, and CPO-27(Ni) MOFs and AQSOA-Z02 zeolite are investigated and compared to the traditional Silica-gel [64]. The lumped parameter model method is used to define the energy balance equations of the adsorbent bed, as described in Chapter 4, where refrigerant (water), adsorbent material, and the heat exchanger materials are assumed to be at the same temperature during the adsorption/desorption cycle time [20, 22, 28]. In addition, the energy balance equations for the adsorption condenser and evaporator are similar to those used in Chapter 4 [20]. For the ORC cycle, heat added to the ORC evaporator (Q_{in}) and heat rejected in the ORC condenser (Q_{out}) can be written as [22, 64, 213-215]:

$$Q_{in} = \frac{\int_0^{t_{cycle}} \dot{m}_{e,ORC} c_p (T_{e,in} - T_{e,o}) dt}{t_{cycle}} \quad 5\text{-}1$$

$$Q_{out} = \frac{\int_0^{t_{cycle}} \dot{m}_{c,ORC} c_p (T_{c,in} - T_{c,o}) dt}{t_{cycle}} \quad 5\text{-}2$$

In equation 5-1, $\dot{m}_{e,ORC}$ is the heating fluid mass flow rate of the ORC evaporator which equals to the mass flow rate of cooling fluid of the adsorber bed in scenario 1 and it is the same as the mass flow rate of the adsorber bed heating fluid in scenario 2 [64]. Moreover, it represents the summation of the mass flow rates of the cooling and heating fluids (water) leaving the adsorption cycle after mixing them to produce new heating source in scenario 3, while it is the main heat source mass flow in scenario 4 [64]. $T_{e,in}$ is the heat source temperature of ORC, which equals to that of the cooling fluid leaving the adsorption cycle after recovering the heat of adsorption in scenario 1. Also, $T_{e,in}$ refers to the heating fluid leaving the adsorption cycle in scenario 2 and the mixture of hot and cold fluids temperature of the adsorption cycle in scenario 3 [64]. In addition, it represents the main heat source temperature in scenario 4. In all scenarios, $T_{e,o}$ is the temperature of the fluid leaving the ORC evaporator and it is used to power the adsorber beds in scenario 4. In equation 5-2, $\dot{m}_{c,ORC}$ represents the mass flow rate of the cooling fluid (water), used to cool the ORC condenser and it is assumed constant during this study [64]. $T_{c,in}$ and $T_{c,o}$ are the inlet and the outlet cooling fluid temperatures of the ORC condenser, and the outlet temperatures of the ORC condenser and evaporator are calculated as that used in Chapter 4. The power generated by the ORC expander can be calculated as [22, 64]:

$$W_{exp,ORC} = \frac{\int_0^{t_{cycle}} \dot{m}_{ORC} (\Delta h)_{ORC} dt}{t_{cycle}} \quad 5\text{-}3$$

$\dot{m}_{ORC}$ is the mass flow rate of the ORC fluid (kg/s) and $(\Delta h)_{ORC}$ is the enthalpy difference across the ORC expander. The power consumed in the pump can be calculated as [22, 64]:

$$W_{pump} = \frac{\int_0^{t_{cycle}} \dot{m}_{ORC}(\Delta P)dt}{t_{cycle}\,\rho\eta_{pump}} \quad 5\text{-}4$$

ΔP is the pressure difference across the pump (Pa), ρ is the density of the liquid refrigerant (kg/m^3), and η_{pump} is the pump efficiency. For the adsorption system, the equations of energy balance, evaporator mass balance, temperature outlet of the adsorbent beds, evaporator and condenser are used as listed in Chapter 4 (equations 4-1 to 4-7). The overall performance of IAOSCE with one expander can be evaluated using the terms COP, SCP, COPe, SCPe, SP and ORC efficiency (η_{ORC}) as written in equations 5-5 to 5-10 [64, 65]:

$$COP = \frac{(\dot{m}c_p)_{evap}\int_0^{t_{cycle}}(T_{chill,in}-T_{chill,o})dt}{(\dot{m}c_p)_h\int_0^{t_{cycle}}(T_{h,in}-T_{h,o})dt} \quad 5\text{-}5$$

$\dot{m}$ is the mass flow rate in kg/s and C_p is the specific heat at constant pressure in J/(kgK). $T_{chill,o}$ and $T_{chill,i}$ are the inlet and the outlet temperatures of the chilled water in °C. $T_{h,o}$ and $T_{h,in}$ are the inlet and the outlet temperatures of the hot water across the adsorbent bed in °C [22].

$$SCP = \frac{(\dot{m}c_p)_{evap}\int_0^{t_{cycle}}(T_{chill,in}-T_{chill,o})dt}{M_a t_{cycle}} \quad 5\text{-}6$$

$$COPe = \frac{(\dot{m}c_p)_{evap}\int_0^{t_{cycle}}(T_{chill,in}-T_{chill,o})dt+F\int_0^{t_{cycle}}[\dot{m}_{ORC}(\Delta h)_{ORC}-\dot{m}_{ORC}(\Delta P)/(\rho\eta_{pump})]dt}{(\dot{m}c_p)_h\int_0^{t_{cycle}}(T_{h,in}-T_{h,o})dt+\dot{m}_{e,ORC}c_p\int_0^{t_{cycle}}(T_{e,in}-T_{e,o})dt} \quad 5\text{-}7$$

$$SCPe = \frac{(\dot{m}c_p)_{evap}\int_0^{t_{cycle}}(T_{chill,in}-T_{chill,o})dt+F\int_0^{t_{cycle}}[\dot{m}_{ORC}(\Delta h)_{ORC}-\dot{m}_{ORC}(\Delta P)/(\rho\eta_{pump})]dt}{M_a t_{cycle}} \quad 5\text{-}8$$

$$SP = \frac{\int_0^{t_{cycle}}[\dot{m}_{ORC}(\Delta h)_{ORC}-\dot{m}_{ORC}(\Delta P)/(\rho\eta_{pump})]dt}{M_a t_{cycle}} \quad 5\text{-}9$$

$$\eta_{ORC} = \frac{\int_0^{t_{cycle}}[\dot{m}_{ORC}(\Delta h)_{ORC}-\dot{m}_{ORC}(\Delta P)/(\rho\eta_{pump})]dt}{\dot{m}_{e,ORC}c_p\int_0^{t_{cycle}}(T_{e,in}-T_{e,o})dt} \quad 5\text{-}10$$

The terms COPe (equivalent coefficient of performance) and SCPe (equivalent specific cooling power) are used to compare the performance of the four different scenarios of the proposed integrated system to the basic adsorption cooling system (BACS). F is a factor used to convert the power generated to cooling for comparison purpose. It is equal to the typical value of vapour compression refrigeration systems COP and assumed to be 3 in this study [64, 65]. In addition, in this thermodynamic study, the expansion process in the ORC expander is considered as an ideal isentropic process.

Also, the exergy efficiency is used to evaluate the IAOSCE which can be defined as [10, 106]:

$$\eta_{ex=}\frac{W_{exp,ORC}-W_{pump}+E_{evap}}{E_{in,1}+E_{in,2}} \quad 5\text{-}11$$

Where E_{evap} is the cooling exergy through the evaporator and can be defined as [206-208]:

$$E_{evap}=\frac{(\dot{m}c_p)_{evap}\int_0^{t_{cycle}}(T_{chill,in}-T_{chill,o})dt}{t_{cycle}}\left[\frac{T_{amb}}{T_{evap}}-1\right] \quad 5\text{-}12$$

While, $E_{in,1}$ $E_{in,2}$ are the input exergies to the adsorption system and the ORC system respectively and can be defined as [10, 106]:

$$E_{in,1}=\frac{\dot{m}_{h,1}\int_0^{t_{cycle}}[(h_{h,in,1}-h_{h,o,1})-T_{amb}(s_{h,in,1}-s_{h,o,1})]dt}{t_{cycle}} \quad 5\text{-}13$$

$$E_{in,2}=\frac{\dot{m}_{h,2}\int_0^{t_{cycle}}[(h_{h,in,2}-h_{h,o,2})-T_{amb}(s_{h,in,2}-s_{h,o,2})]dt}{t_{cycle}} \quad 5\text{-}14$$

The overall performance of IAOSCE with two expanders can be evaluated using the terms COP, SCP, COPe, SCPe, SP, and ORC efficiency (η_{ORC}) and adsorption power efficiency (η_{ads}) as written in equations 5-15 to 5-21 [64]:

$W_{exp,ads}$ can be calculated using equation 4-8 and $W_{exp,ORC}$ can be calculated using equation 5-3.

$$COP=\frac{(\dot{m}c_p)_{evap}\int_0^{t_{cycle}}(T_{chill,in}-T_{chill,o})dt}{(\dot{m}c_p)_h\int_0^{t_{cycle}}(T_{h,o}-T_{h,in})dt} \quad 5\text{-}15$$

$$SCP=\frac{(\dot{m}c_p)_{evap}\int_0^{t_{cycle}}(T_{chill,in}-T_{chill,o})dt}{M_a t_{cycle}} \quad 5\text{-}16$$

$$COPe = \frac{(\dot{m}c_p)_{evap}\int_0^{t_{cycle}}(T_{chill,in}-T_{chill,o})dt+F\int_0^{t_{cycle}}[\dot{m}_{ads}(\Delta h)_{ads}+\dot{m}_{ORC}(\Delta h)_{ORC}-\dot{m}_{ORC}(\Delta P)/(\rho\eta_{pump})]dt}{(\dot{m}c_p)_h\int_0^{t_{cycle}}(T_{h,in}-T_{h,o})dt+\dot{m}_{e,ORC}c_p\int_0^{t_{cycle}}(T_{e,in}-T_{e,o})dt} \quad 5\text{-}17$$

$$SCPe = \frac{(\dot{m}c_p)_{evap}\int_0^{t_{cycle}}(T_{chill,in}-T_{chill,o})dt+F\int_0^{t_{cycle}}[\dot{m}_{ads}(\Delta h)_{ads}+\dot{m}_{ORC}(\Delta h)_{ORC}-\dot{m}_{ORC}(\Delta P)/(\rho\eta_{pump})]dt}{M_a t_{cycle}} \quad 5\text{-}18$$

$$SP = \frac{\int_0^{t_{cycle}}[\dot{m}_{ads}(\Delta h)_{ads}+\dot{m}_{ORC}(\Delta h)_{ORC}-\dot{m}_{ORC}(\Delta P)/(\rho\eta_{pump})]dt}{M_a t_{cycle}} \quad 5\text{-}19$$

η_{ORC} can be calculated using equation 5-10 and adsorption power efficiency (η_{ads}) can be calculated as [65]:

$$\eta_{ads} = \frac{\int_0^{t_{cycle}}\dot{m}_{ads}(\Delta h)_{ads}dt}{(\dot{m}c_p)_h\int_0^{t_{cycle}}(T_{h,in}-T_{h,o})dt} \quad 5\text{-}20$$

Also, to evaluate the performance of IAOSCE with two expanders, the exergy efficiency is used as [10, 64, 106]:

$$\eta_{ex=}\frac{W_{exp,ORC}-W_{pump}+W_{exp,ads}+E_{evap}}{E_{in,1}+E_{in,2}} \quad 5\text{-}21$$

Table 5-1 and Table 5-2 show the main operating conditions used in this chapter and the characteristics of the adsorption system components like adsorber bed, condenser and evaporator in addition to the ORC components like evaporator and condenser [22, 64].

Table 5-1: Parameters used in the simulation [20, 22, 64]

Bed heating fluid temperature ^{o}C	80-160
Bed cooling fluid temperature ^{o}C	48*/28
Condenser cooling water temperature ^{o}C	28
Chilled water temperature ^{o}C	18
Bed hot fluid mass flow rate kg/s	1.85
Bed cold fluid mass flow rate kg/s	1.85
Condenser mass flow rate kg/s	0.8
Evaporator mass flow rate kg/s	0.8
Half cycle time s	324
Switching time s	20
ORC condenser temperature ^{o}C	25*/28
ORC condenser mass flow kg/s	0.8
ORC refrigerant mass flow kg/s	0.12

*: conditions used only in scenarios 1 and 3

Table 5-2: System physical characteristics [20-22, 64, 209]

Bed heat exchanger	
Fin length m	172E-3
Fin width m	30E-3
Fin pitch m	1.2E-3
Module length m	800E-3
Number of module	4
Number pipes/module	6
Number of bypass	2
Pipe OD m	15.875E-3
Pipe thickness m	0.8E-3
Adsorption condenser	
Pipe length m	5.5
Number pipes	4
Pipe OD m	15.875E-3
Pipe thickness m	0.8E-3
Adsorption evaporator	
Pipe length m	10
Number of pipes	4
Pipe outside diameter m	15.875E-3
Pipe thickness m	0.8E-3
Fins length m	40E-3
Fins thickness m	0.12E-3
Fins pitch m	1.2E-3
ORC condenser/evaporator	
Pipe length m	11
Number pipes	6
Pipe OD m	15.875E-3
Pipe thickness m	0.8E-3

The IAOSCE with one expander and two expanders proposed in this chapter is simulated using MATLAB Simulink software. Two MATLAB Simulink models have been developed to study the effect of using various integration scenarios, adsorbent materials, ORC fluids and operating parameters on the overall system performance of the IAOSCE. Figure 5-10 and Figure 5-11 show the flowcharts of the IAOSCE models with one expander and two expanders respectively.

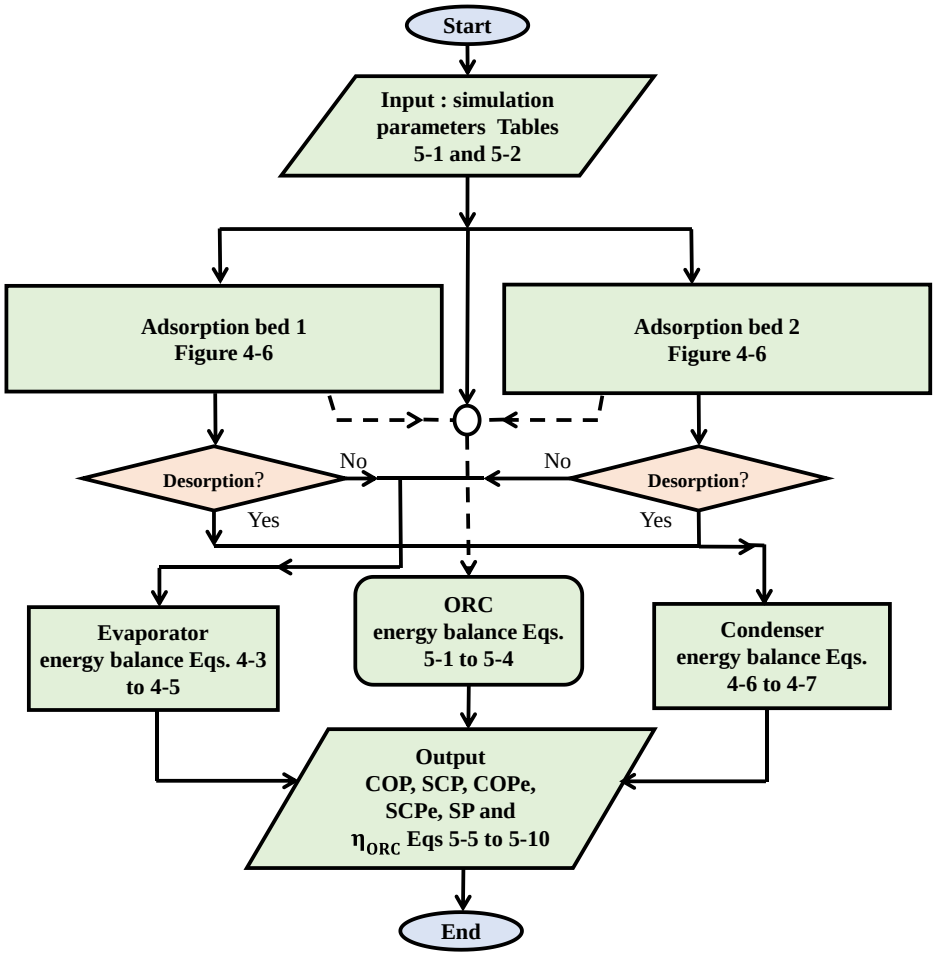

Figure 5-10: Flowchart of the IAOSCE model (with one expander)

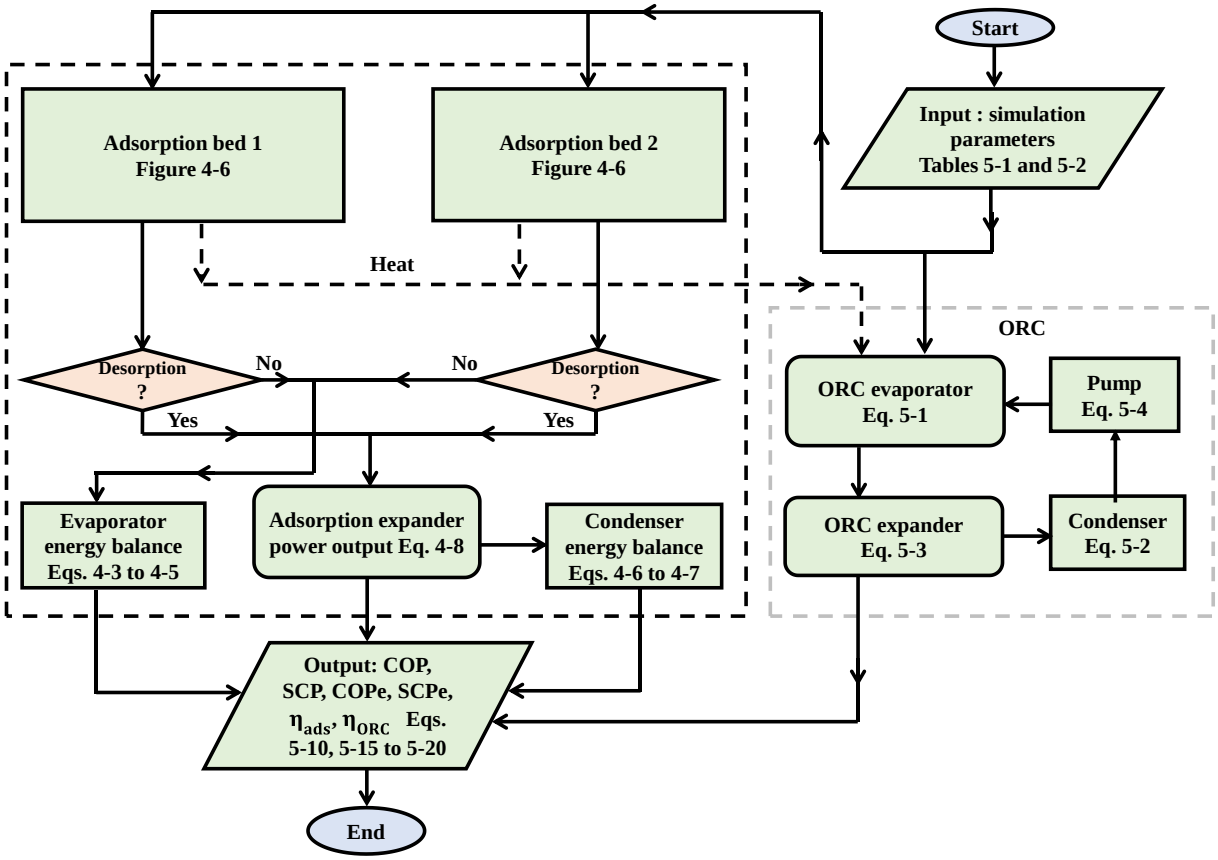

Figure 5-11: Flowchart of the IAOSCE model (with two expanders)

5.5 Performance of IAOSCE [22]

In this study, three advanced adsorbent materials were investigated namely; CPO-27(Ni), Al-Fumarate and AQSOA-Z02, and compared to the commonly used Silica-gel utilising heat source temperature ranging from 80 to 160 °C [22]. Silica-gel was not investigated at 140 and 160 °C as many researchers reported that Silica-gel can show high performance at regeneration temperature of below 95 °C [210, 211] and that Silica-gel can be damaged by heating the material above 120°C [212]. Also, to provide high temperature heating, water under pressure is used with properties evaluated using REFPROP database.

Figure 5-12, Figure 5-13, Figure 5-14, and Figure 5-15 show the cooling, and power generated by the IAOSCE using scenario 1, scenario 2, scenario 3, and scenario 4 respectively utilising Al-Fumarate, CPO-27(Ni), AQSOA-Z02, and Silica-gel as adsorbent materials and R141b as ORC fluids [22]. Results show that, this system can generate cooling and power simultaneously, however the amount of cooling and power generated is affected by the scenario used and the adsorbent materials [22]. For example, Silica-gel produces more cooling and power when using scenarios 2 and 4, while the value of cooling generated by CPO-27(Ni) varies from one scenario to another. Al-Fumarate produces lower cooling capacity than that of the other adsorbent materials for all scenarios as this material shows low performance with ASCE and this is due to its slow adsorption kinetics which leads to low water uptake as discussed in Chapters 3 and 4 and the situation becomes worse with scenarios 1 and 3 where the relatively high cooling water temperature again reduces the water uptake [22] so, Al-Fumarate is excluded from the remaining part of this study.

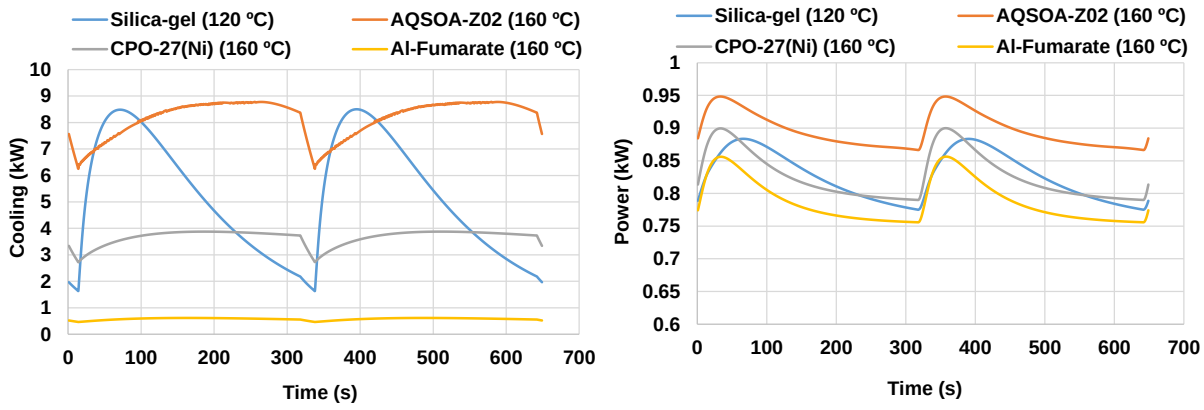

Figure 5-12: Cooling and power generated by IAOSCE using scenario 1 and R141b as ORC fluid

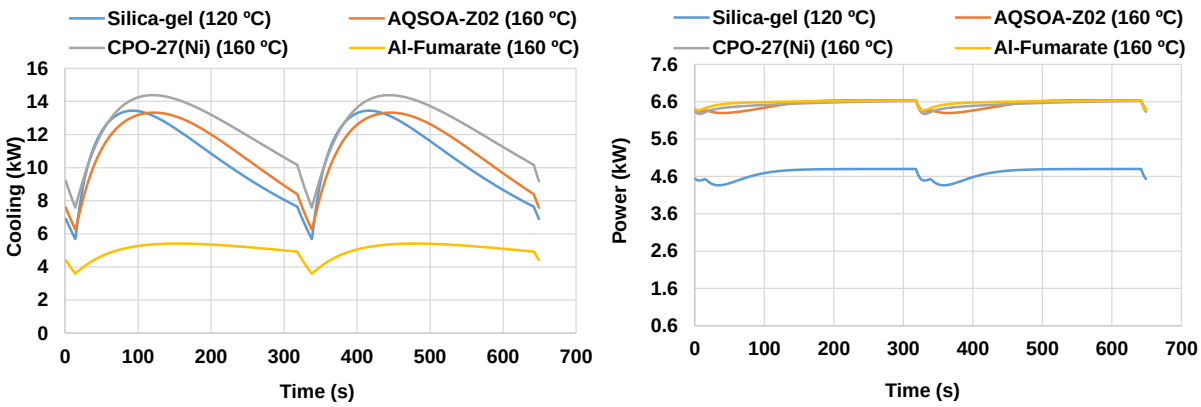

Figure 5-13: Cooling and power generated by IAOSCE using scenario 2 and R141b as ORC fluid

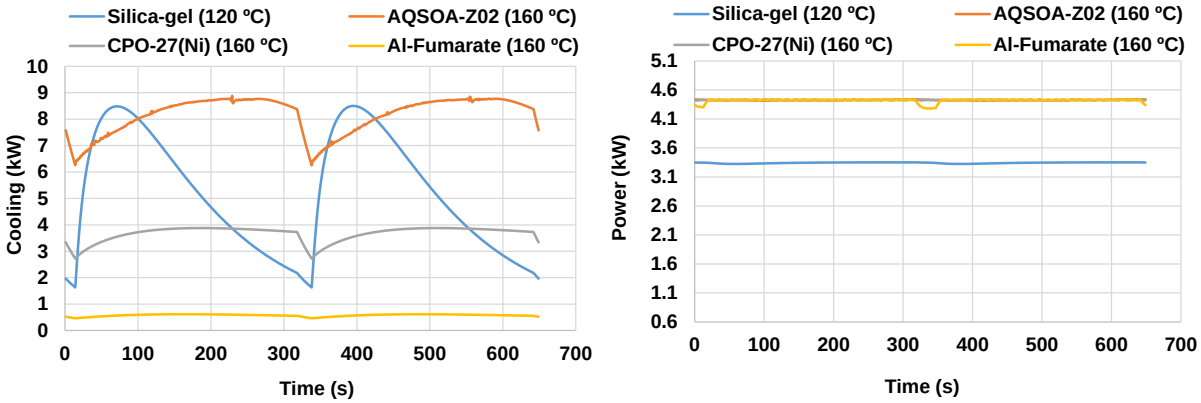

Figure 5-14: Cooling and power generated by IAOSCE using scenario 3 and R141b as ORC fluid

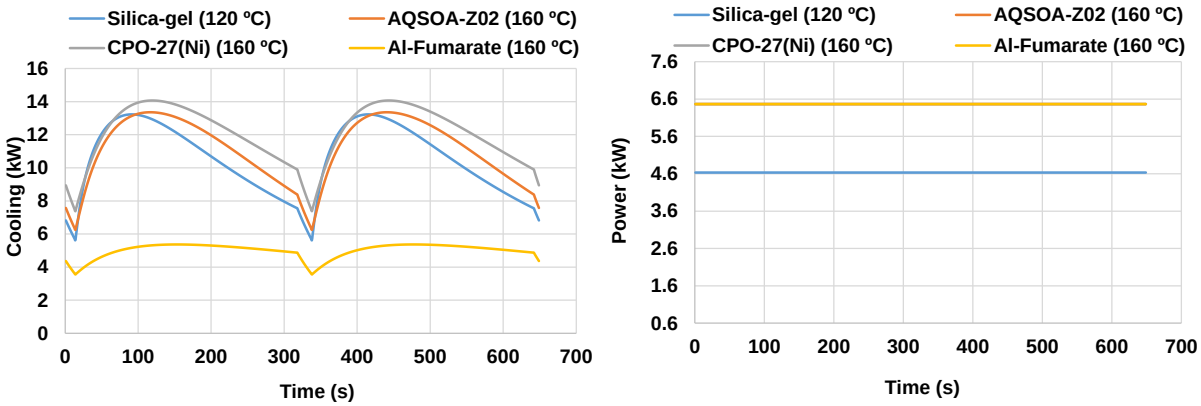

Figure 5-15: Cooling and power generated by IAOSCE using scenario 4 and R141b as ORC fluid

Figure 5-16 shows the effect of using four scenarios, three adsorbent materials, three ORC fluids and heat source temperature on the COP of the IAOSCE. Results show that scenarios 2 and 4 have the highest COP of about 0.75 (utilizing Silica-gel with heating fluid temperature of 80°C) [22]. This is because Silica-gel has high uptake at low bed cooling water temperature such that used in scenarios 2 and 4. Figure 5-17 shows the effect of using different scenarios, different adsorbent materials, different ORC fluids and heat source temperature on the COPe of the IAOSCE. Results show that scenario 1 shows the highest COPe values compared to those of other scenarios, and this is because of no additional heat from the main heat source is needed to power the ORC cycle. A maximum COPe of 1.14 is achieved utilising Silica-gel and R141b and heat source temperature of 80 ºC.

Figure 5-18 shows the effect of using different adsorbent materials, ORC fluids and heat source temperature on SCP of the IAOSCE respectively. Results show that scenarios 1 and 3 produce the lowest values of SCP and this is due to using relatively high cooling temperature in these two scenarios which affects the water uptake and then affects the cooling capacity of the system. A maximum SCP of 892 W/kg_{ads} is achieved in scenario 2 utilising CPO-27(Ni) and heat source temperature of 160 ºC and this value is the same for all ORC fluids except for scenario 4, because the value of the cooling is not affected by the ORC fluid used in the first three scenarios. Also, scenarios 1 and 3 with AQSOA-Z02 produce higher SCP than Silica-gel and CPO-27(Ni) at all temperatures. With scenarios 2 and 4, Silica-gel produces higher SCP than Silica-gel and CPO-27(Ni) at heat source temperature of 80 °C, while CPO-27(Ni) produces higher values than Silica-gel and AQSOA-Z02 at heat source temperature of over 100 °C.

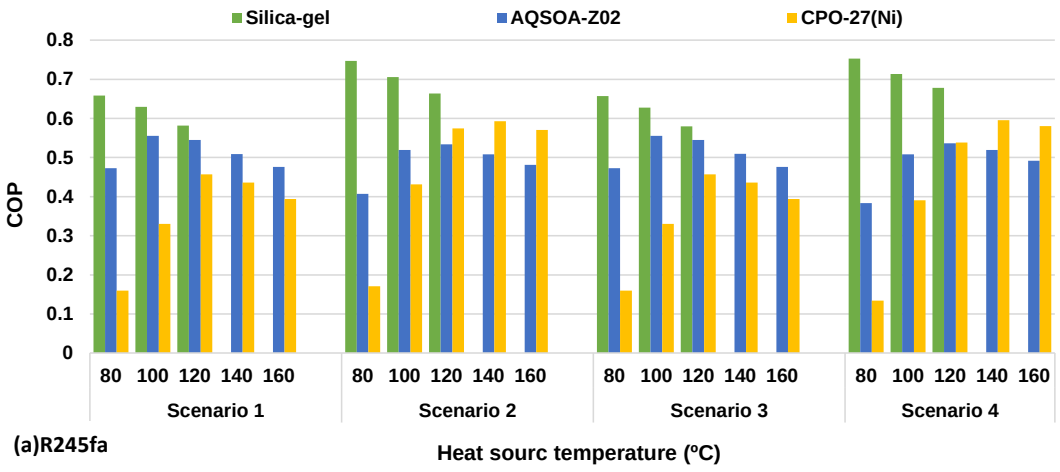

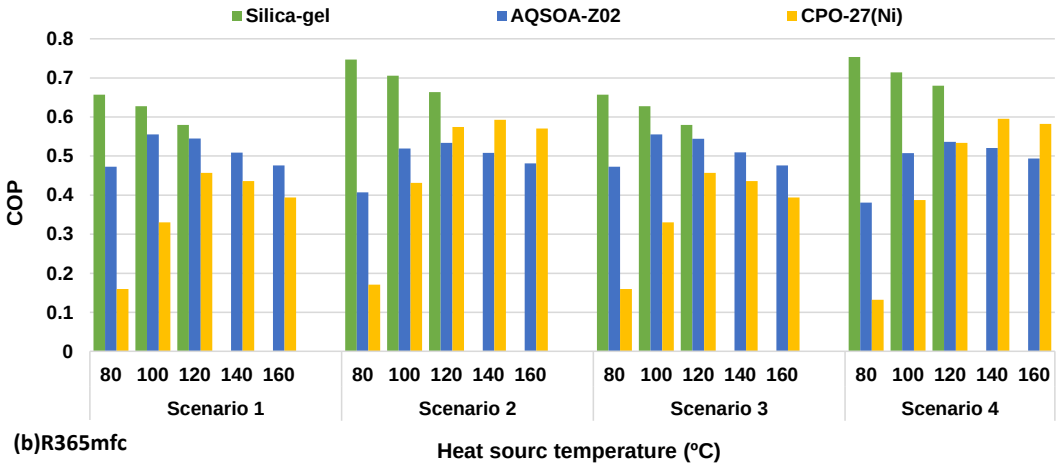

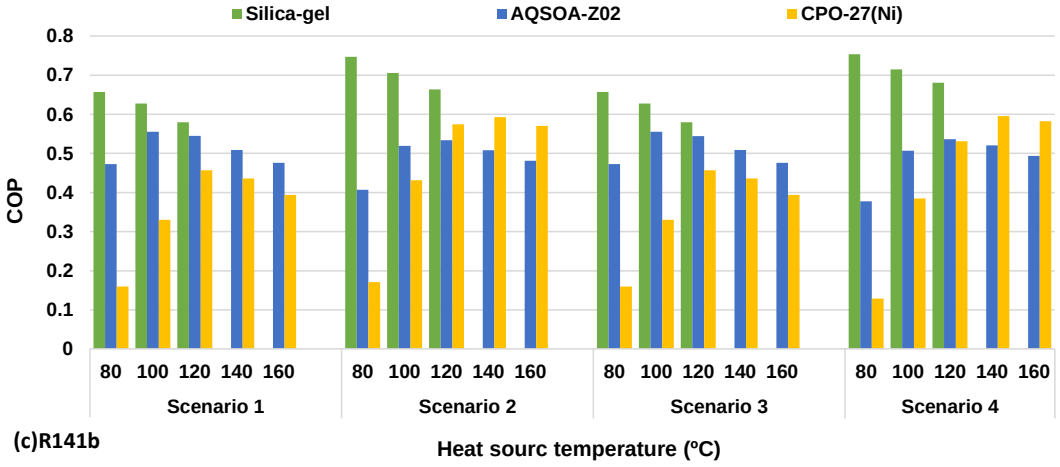

Figure 5-16: Effect of using different scenarios, adsorbent materials, ORC fluids and heat source temperatures on the COP of the IAOSCE

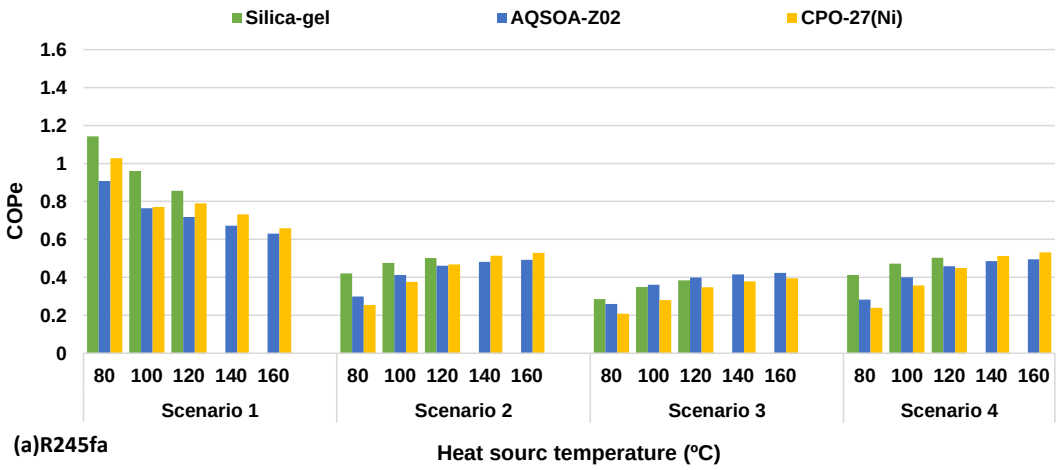

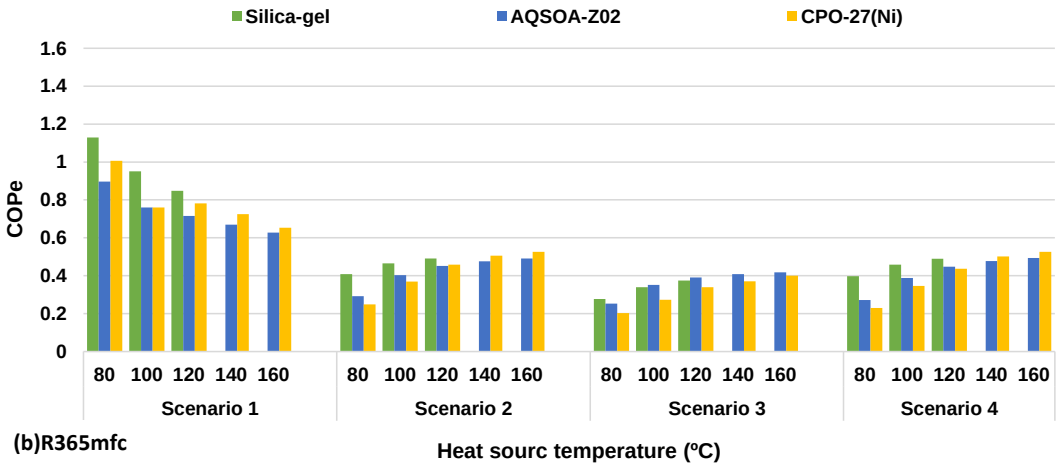

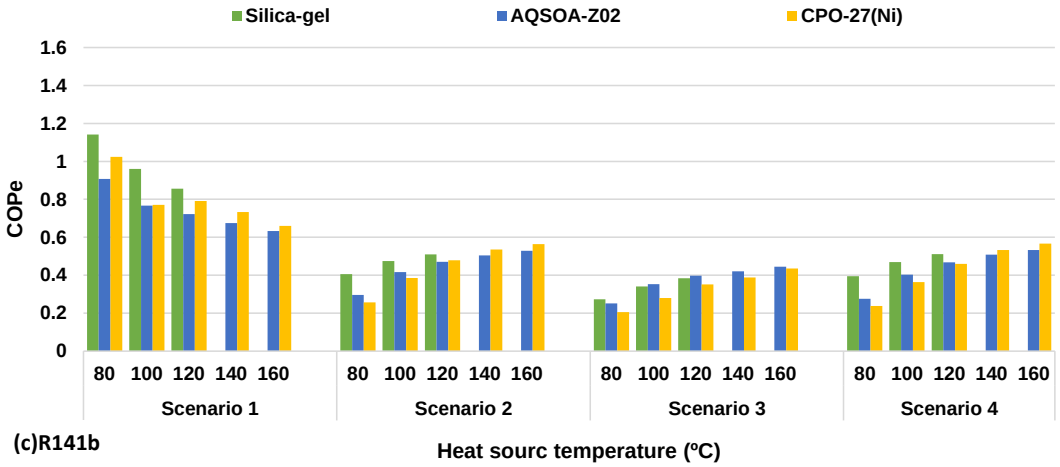

Figure 5-17: Effect of using different scenarios, adsorbent materials, ORC fluids and heat source temperatures on the COPe of the IAOSCE

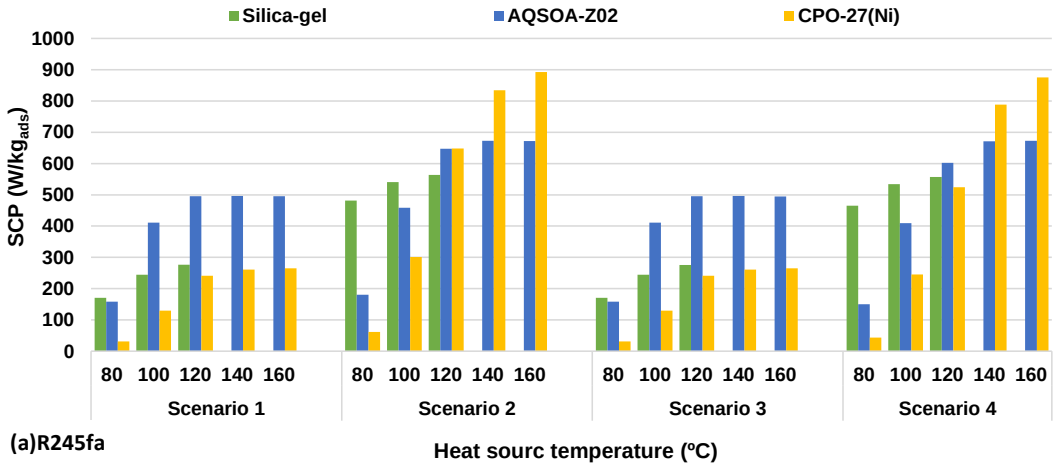

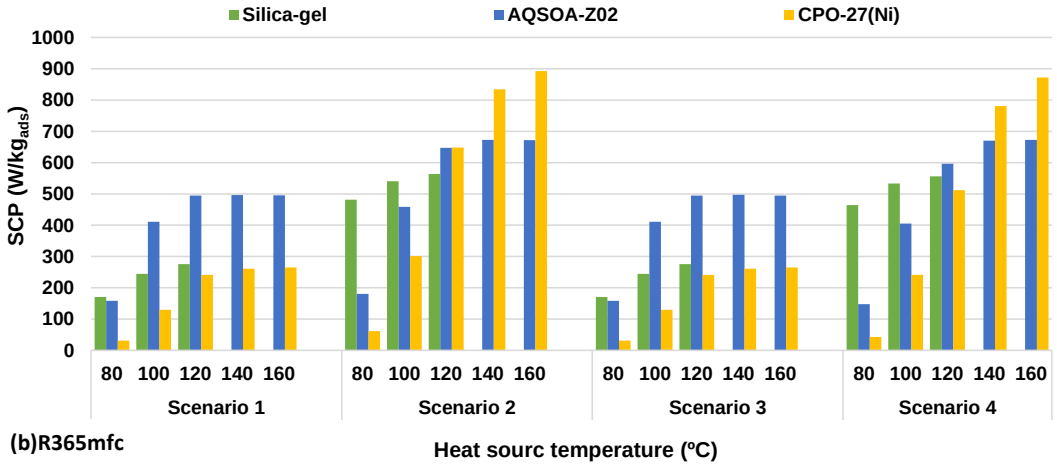

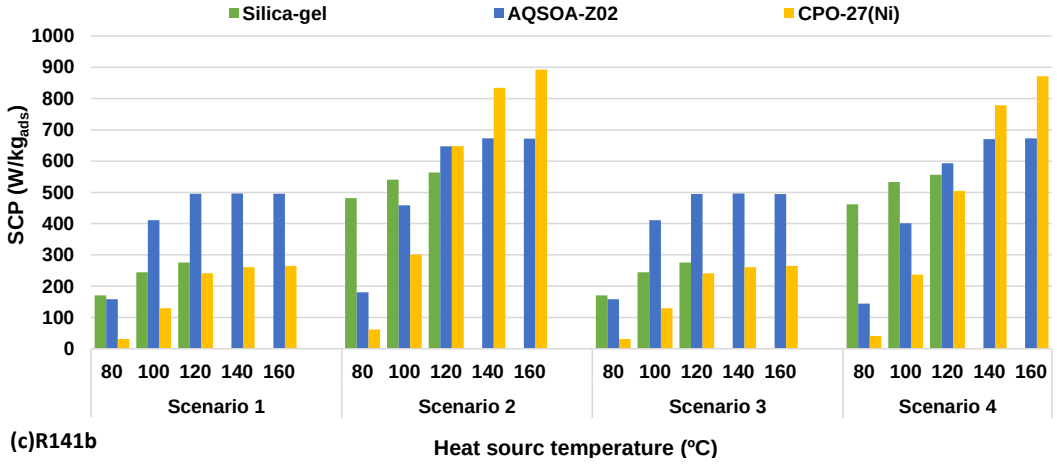

Figure 5-18: Effect of using different scenarios, adsorbent materials, ORC fluids and heat source temperatures on SCP of the IAOSCE

Figure 5-19 shows the effect of using different adsorbent materials, ORC fluids and heat source temperature on SCPe of the IAOSCE. Scenarios 2 and 4 show the highest SCPe because of using relatively high cooling temperature in scenarios 1 and 3 and more power is generated in these two scenarios. Maximum values of SCPe of 2311 W/kg_{ads} and 2276 W/kg_{ads} were achieved in scenario 2 and scenario 4 respectively utilising CPO-27(Ni) and heat source temperature of 160 ºC and this is for the same reasons discussed before. Figure 5-20 and Figure 5-21 show the effect of using different adsorbent materials, ORC fluids and heat source temperature on SP and ORC efficiency respectively. Scenarios 2 shows the highest values of the SP of 473 W/kg_{ads} and the ORC efficiency of 18.6% respectively utilising CPO-27(Ni) and R141b at heat source temperature of 160 ºC. Scenarios 1 and 3 show the lowest values of the SP and the ORC efficiency and this is because of using relatively high cooling water temperature used in the adsorber beds which affects the water uptake of the adsorption cycle and also, because of low-pressure ratio in the ORC cycle due to using low heat source temperature for powering the ORC evaporator.

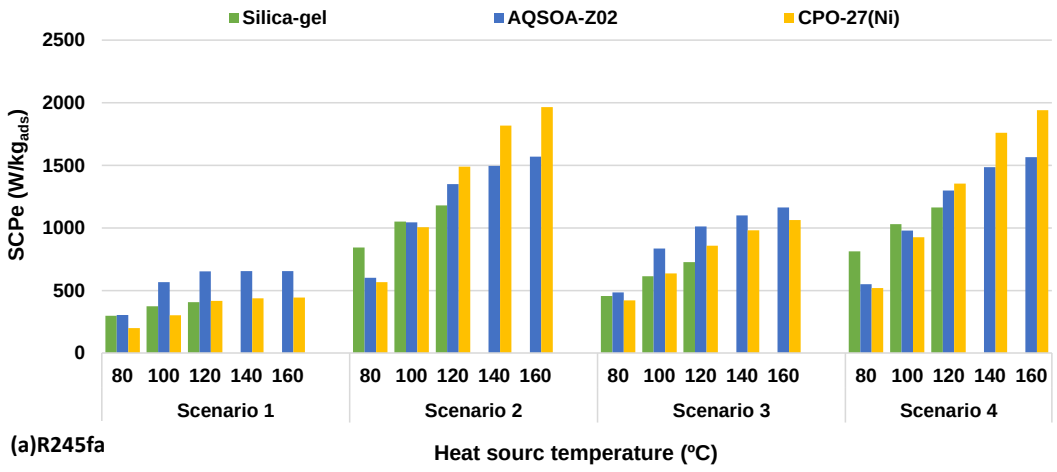

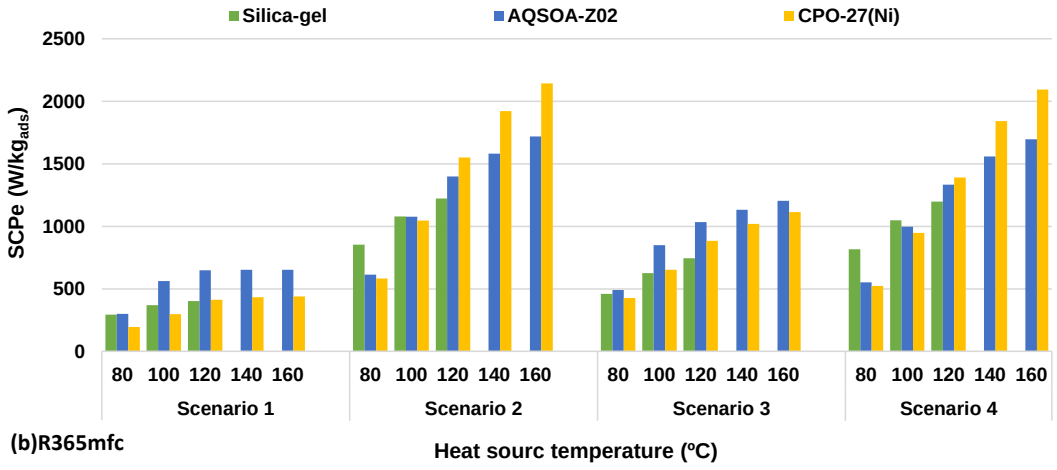

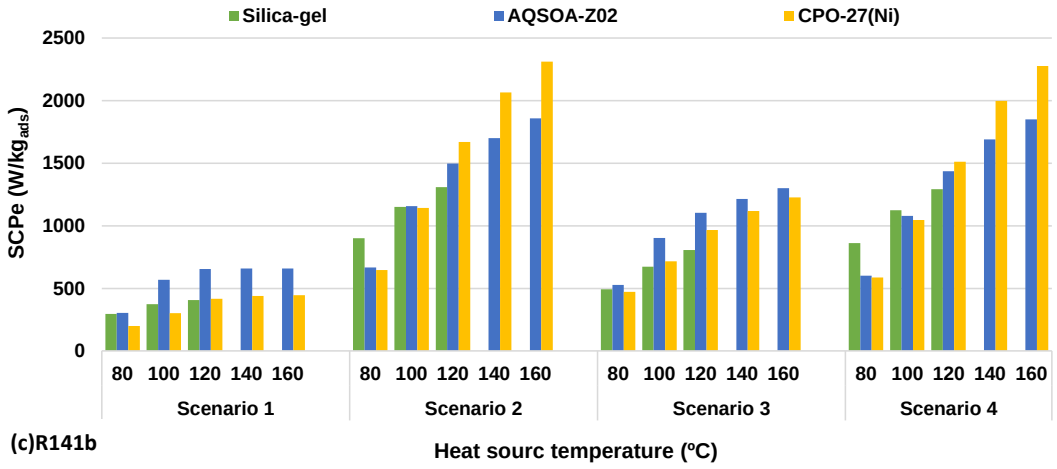

Figure 5-19: Effect of using different scenarios, adsorbent materials, ORC fluids and heat source temperatures on SCPe of the IAOSCE

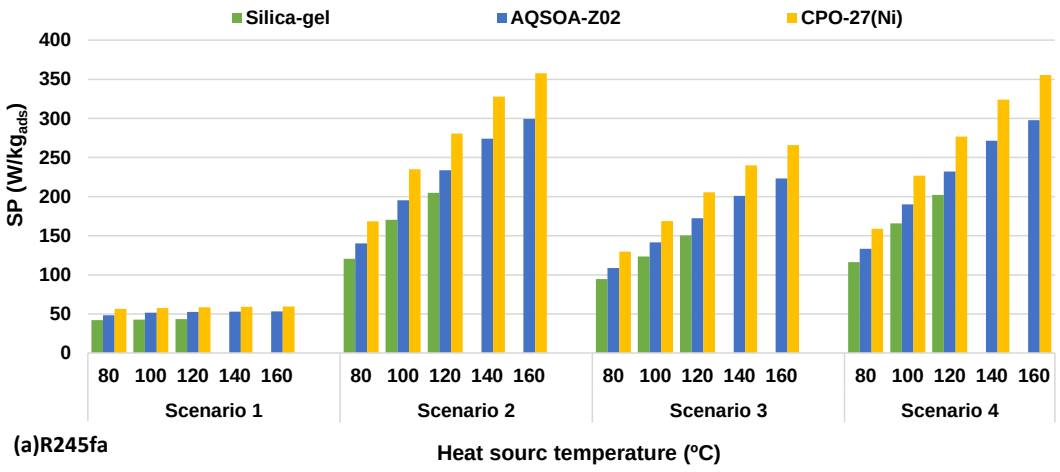

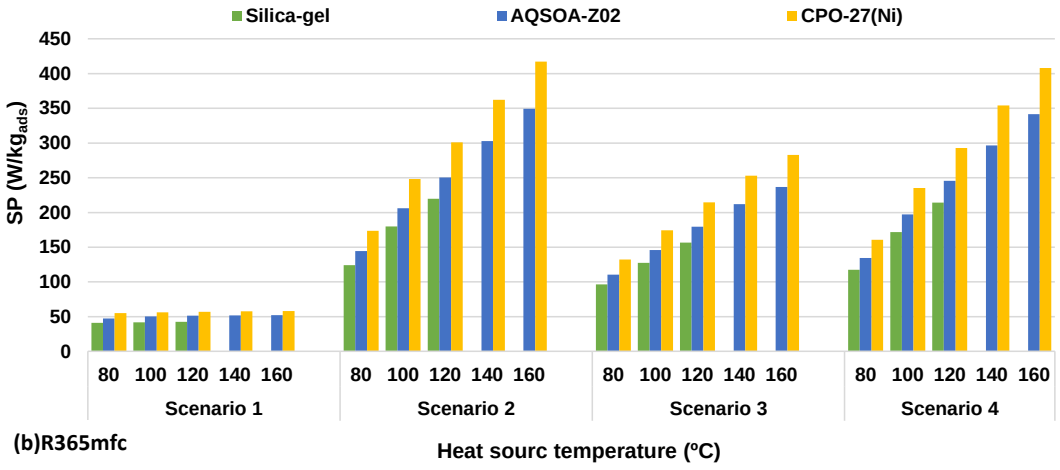

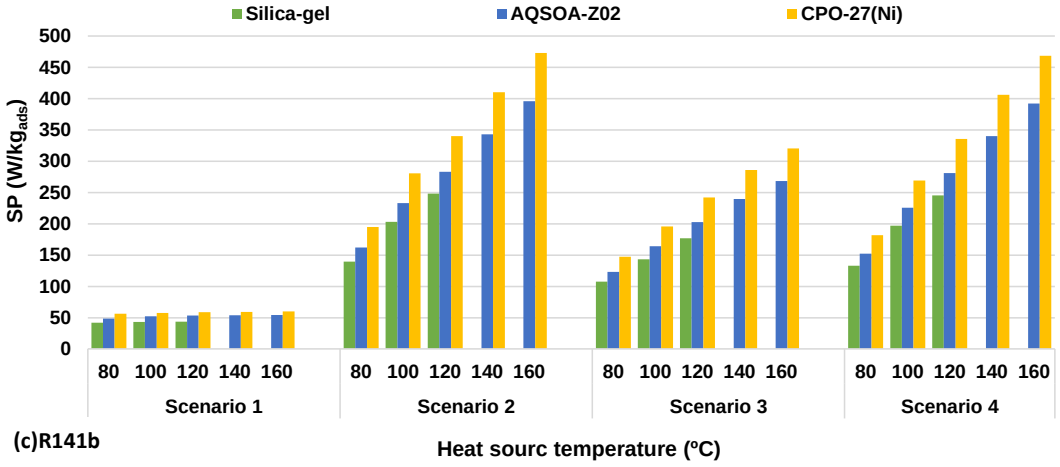

Figure 5-20: Effect of using different scenarios, adsorbent materials, ORC fluids and heat source temperatures on SP of the IAOSCE

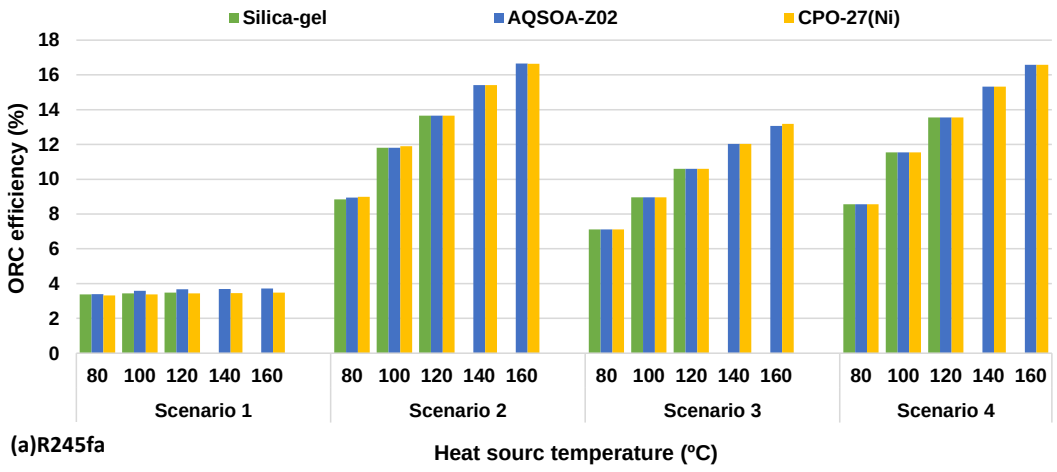

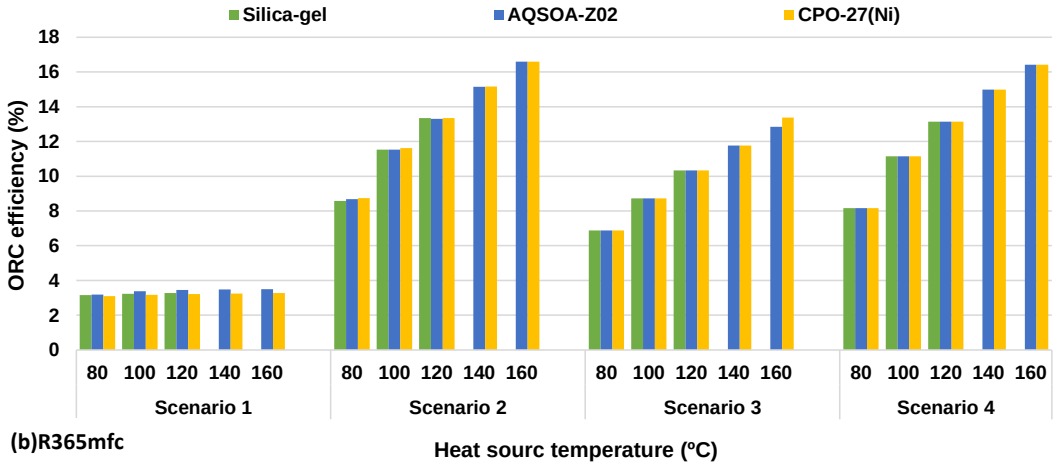

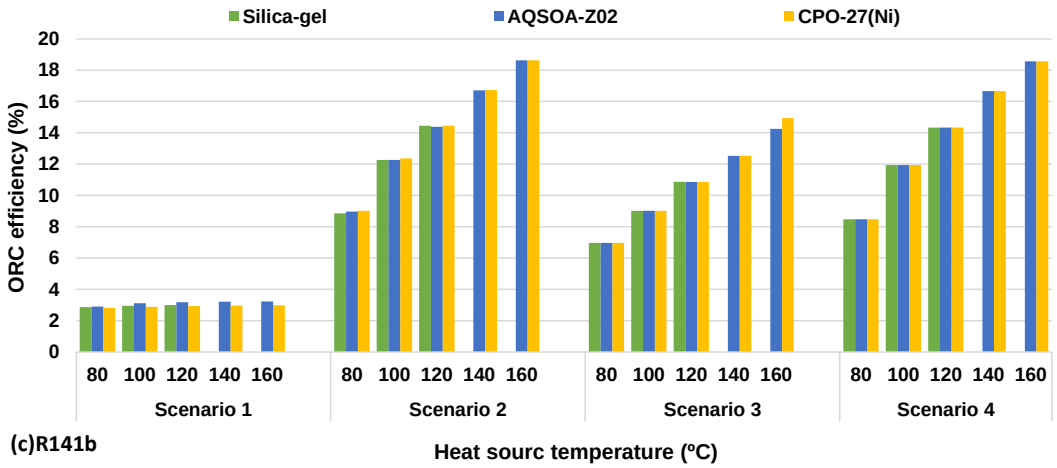

Figure 5-21: Effect of using different scenarios, adsorbent materials, ORC fluids and heat source temperatures on the ORC efficiency of the IAOSCE

The four scenarios examined in this work offer different options for energy designers and consumers to choose a suitable design for different applications. For instant, in hot climate countries, refrigeration and air conditioning consume large amount of energy while in many developing countries, the national electricity grid fails to supply the required demand of electricity, especially in summer. This problem can be solved by means of using such integrated systems as localized units not only to generate cooling and electricity simultaneously but also to enhance the overall system performance. For example, when infinite or semi-infinite low-grade heat sources are available like solar energy as in many hot countries, scenarios 2 and 4 can be preferable because they generate more cooling and power which means smaller size systems. Conversely, if there is a limited amount of low-grade heat sources, scenario 1 may be preferable because it has higher COPe thus more energy can be saved.

5.6 Performance of IAOSCE with two expanders [64]

Figure 5-22 shows the COP of four scenarios of the IAOSCE with two expanders utilising CPO-27(Ni), AQSOA-Z02, and Silica-gel and three different ORC fluids using heat source temperature ranging from 80 to 160 ºC [64]. ORC fluids do not affect the COP of the IAOSCE, so for the first three cases, the corresponding COP is the same except for scenario 4, where the adsorption system is the bottoming system. Silica-gel shows the highest COP of about 0.7 utilising scenarios 2 and 4. Figure 5-23 shows the COPe of the IAOSCE with two expanders using Silica-gel, AQSOA-Z02, and CPO-27(Ni) and three different ORC with heat source temperature of 80-160 ºC. Results show that the maximum COPe of about 1.27 can be achieved using Silica-gel and R141b using scenario 1 with heating fluid temperature of 80 ºC [64]. This is due to high Silica-gel performance and low consumption of heat at low heat source temperature, also the ORC is powered using the return cooling line of the adsorption

system so that no additional heat is added from the main heat source. In scenario 2, the maximum COPe of 0.61 is achieved using CPO-27(Ni) and R141b at 160 °C.

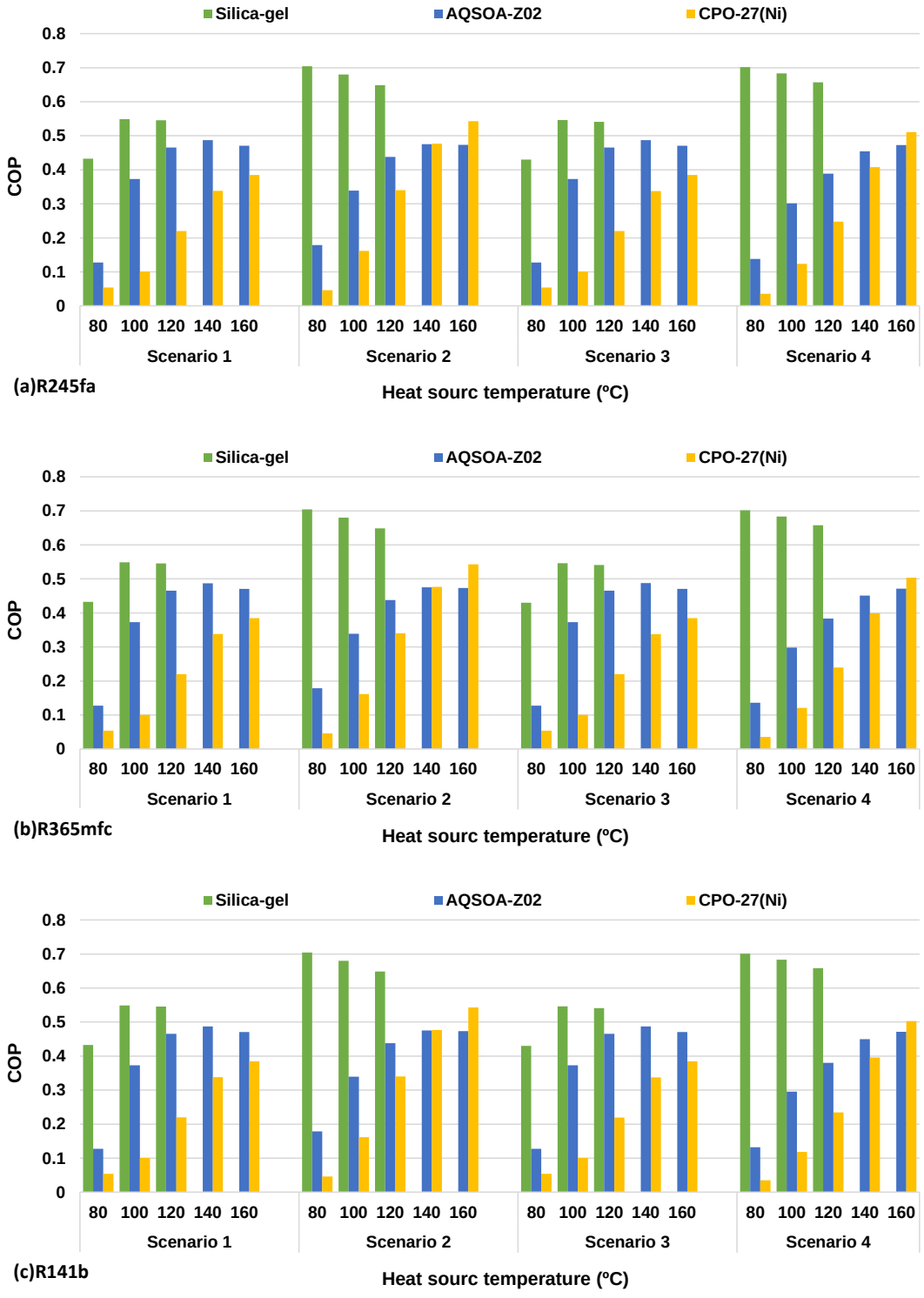

Figure 5-22: Effect of using different scenarios, adsorbent materials, ORC fluids and heat source temperatures on the COP of the IAOSCE with two expanders

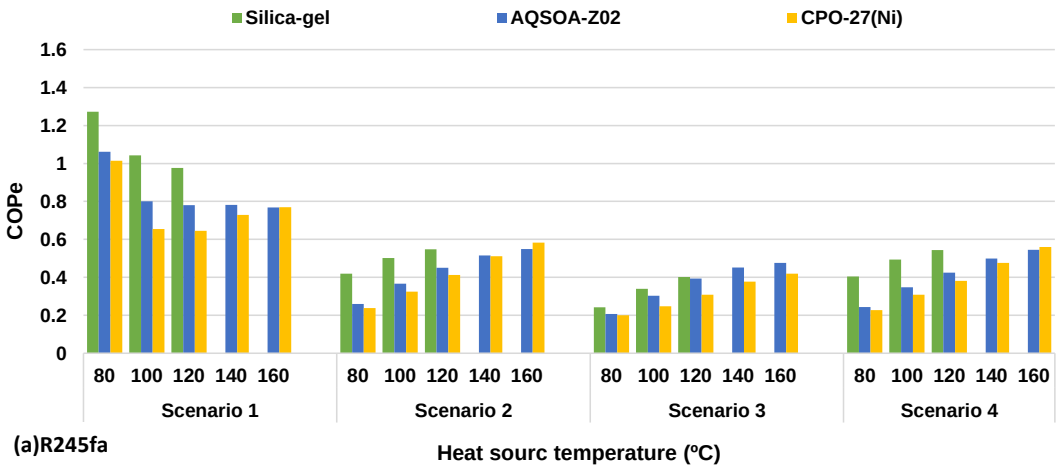

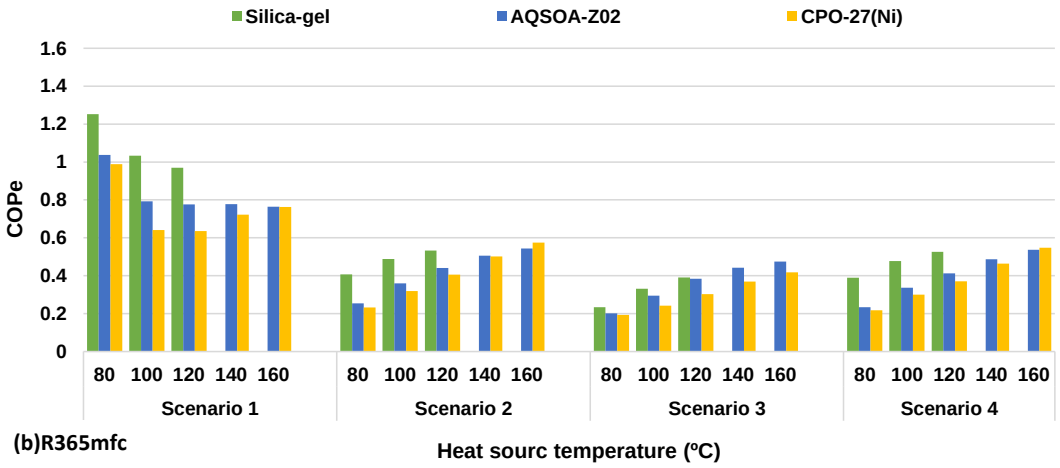

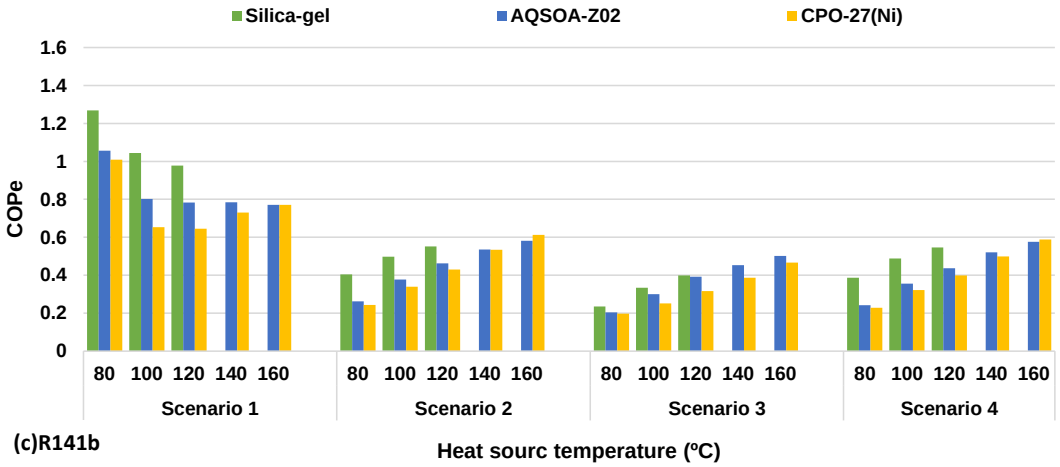

Figure 5-23: Effect of using different scenarios, adsorbent materials, ORC fluids and heat source temperatures on the COPe of the IAOSCE with two expanders

Figure 5-24 and Figure 5-25 show the values of SCP and SCPe of the IAOSCE with two expanders utilising three different adsorbent materials and three different ORC fluids with heat source temperature of 80-160 ºC, cooling water temperature of 28 °C and inlet chilled water temperature of 18 °C [64]. Results show that, maximum SCP of 800 W/kg_{ads} can be achieved in scenario 2 utilising CPO-27(Ni) at heating fluid temperature of 160 ºC and this is because CPO-27(Ni) shows high adsorption uptake at high regeneration temperature which leads to producing lower desorption pressure ratio and then higher water uptake and refrigerant mass flow rate as described in Chapter 3. SCP is not affected by the ORC fluid in the first three scenarios, because cooling is generated in the topping system (adsorption cooling system which set up as a topping system), except for scenario 4, where the adsorption system is set up as a bottoming system.

Maximum SCPe of 2460 W/kg_{ads} is achieved in scenario 2 using CPO-27(Ni) as an adsorbent material and R141b as an ORC fluid with heat source temperature of 160 ºC. This is due to the high cooling and power generated in this scenario compared to the other scenarios as high uptake can be achieved in the adsorption system and high-pressure ratio can be achieved in the ORC. Also, this is because two expanders are used in this time so that more power is generated and as power has higher grade than cooling, the equivalent cooling generated i.e. SCPe is relatively high in this case [64].

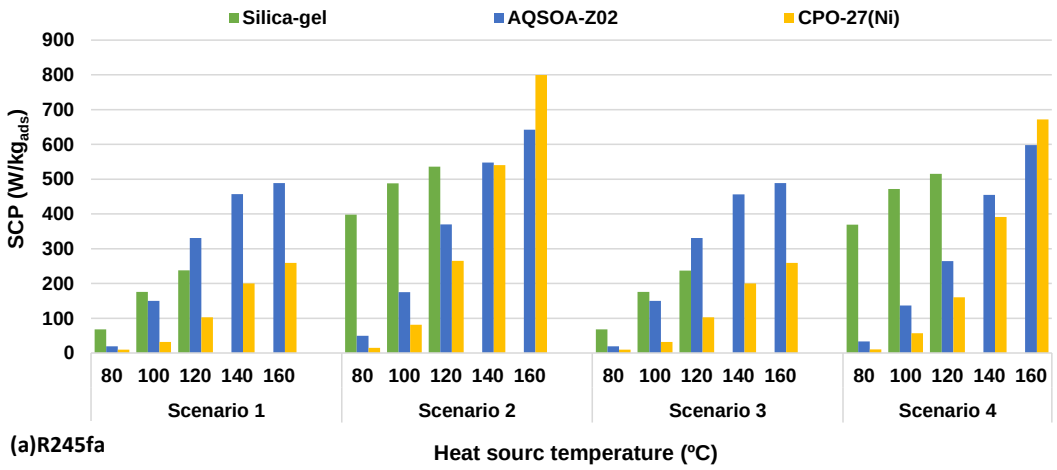

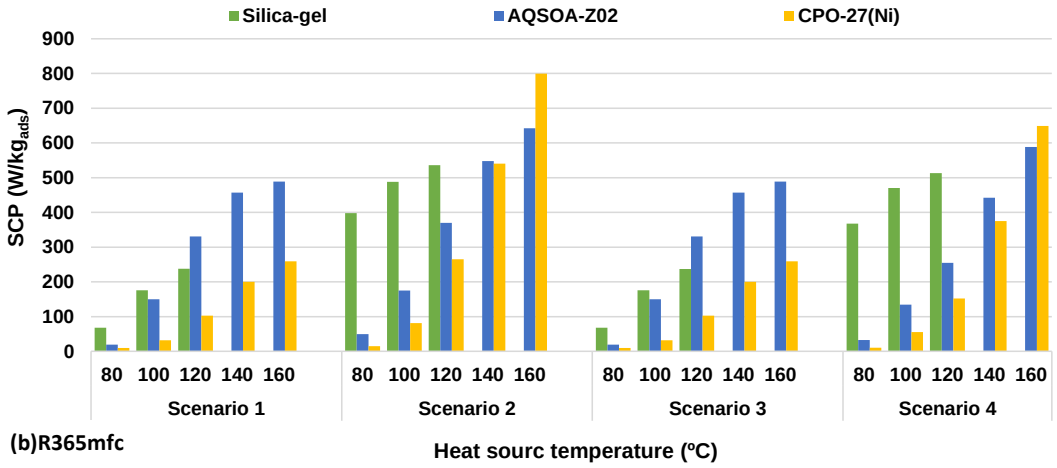

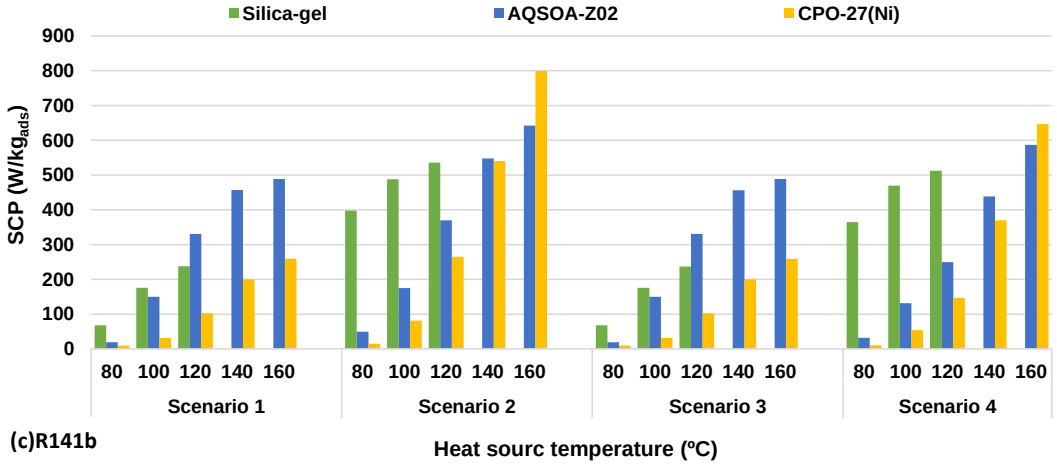

Figure 5-24: Effect of using different scenarios, adsorbent materials, ORC fluids and heat source temperatures on SCP of the IAOSCE with two expanders

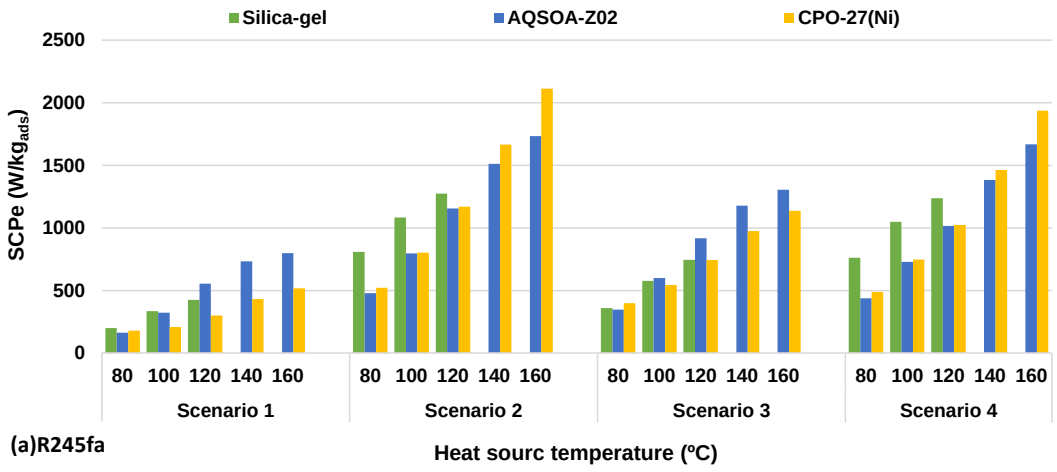

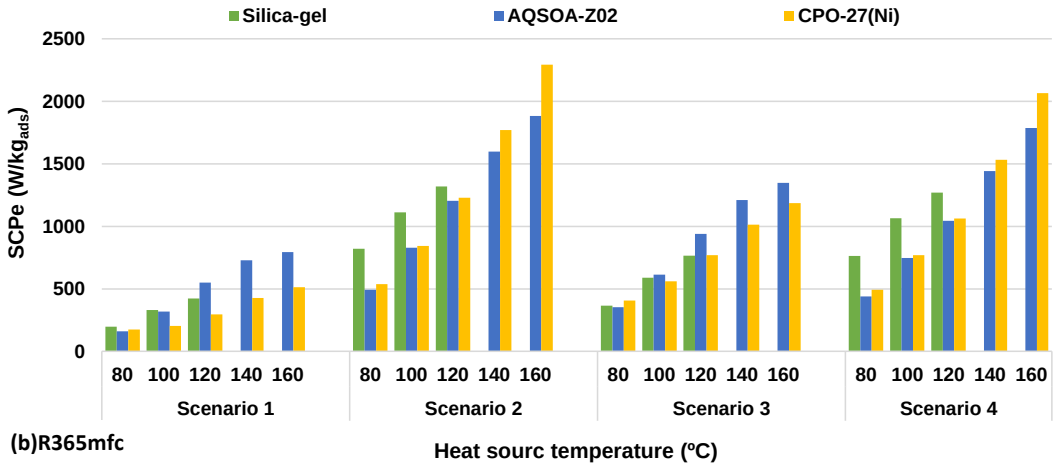

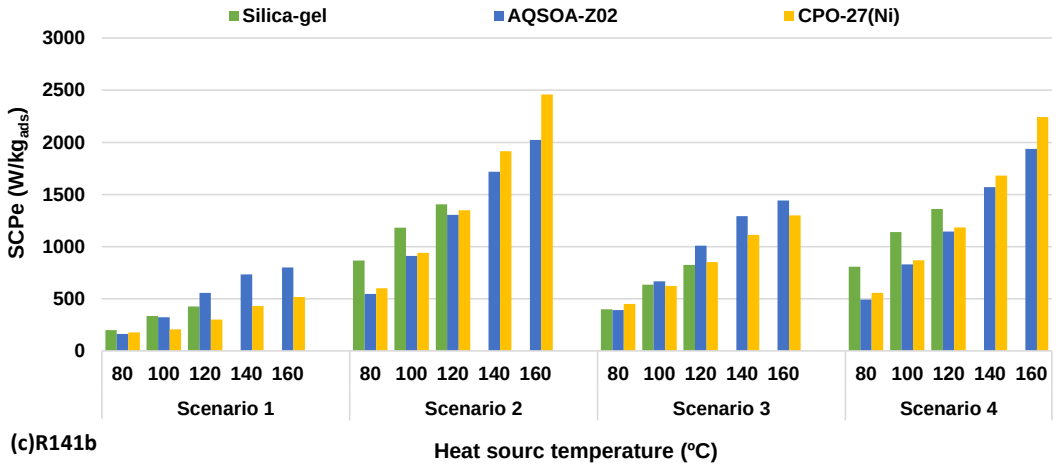

Figure 5-25: Effect of using different scenarios, adsorbent materials, ORC fluids and heat source temperatures on SCPe of the IAOSCE with two expanders

Figure 5-26 and Figure 5-27 show the SP and the adsorption power efficiency of the IAOSCE with two expanders using different scenarios, adsorbent materials, ORC fluids and heat source temperature respectively. As SP includes the power generated by both expanders, different ORC fluids generate different values of power from the ORC cycle. As a result, the overall SP is affected by the different ORC fluid utilised and R141b with CPO-27(Ni) produce the highest SP of 553 W/kg_{ads} in scenario 2 with heating fluid temperature of 160 ºC. Adsorption power efficiency is not affected by the ORC fluids for the first three scenarios, as adsorption system is set up as a topping one, while for scenario 4, it is affected slightly as the ORC is set up as a topping system. Also, maximum adsorption power efficiency of 5.44% was achieved using CPO-27(Ni) in scenario 2 with heating fluid temperature of 160 ºC.

Figure 5-28 shows the ORC efficiency of the different scenarios, adsorbent materials and ORC fluids used in this study with heat source temperature ranging from 80 to 160 ºC. Results show that maximum ORC efficiency of 18.64% and 18.54% were achieved in scenarios 2 and 4 respectively using R141b at heating fluid temperature of 160 ºC. The effect of different adsorbent materials on the ORC efficiency is very limited in the first three scenarios, while there is no effect in scenario 4 because the ORC is the topping cycle [64]. It is worthy to note that, the expanders used in this study are assumed to be ideal with isentropic efficiency of 100% so that the different configurations and scenarios can be compared, while in the next chapter, full detailed CFD analysis of both the adsorption and the ORC expander will be carried out to highlight the range of efficiency and power generated by each turbine.

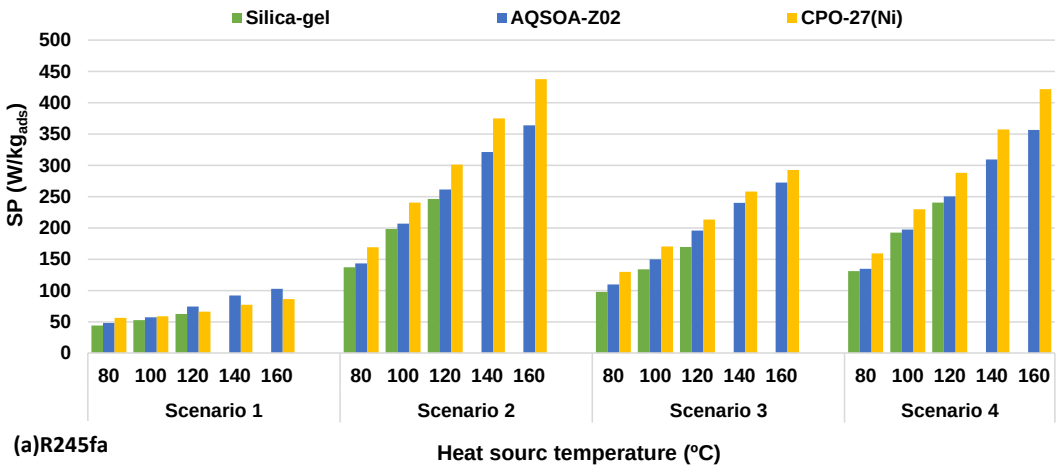

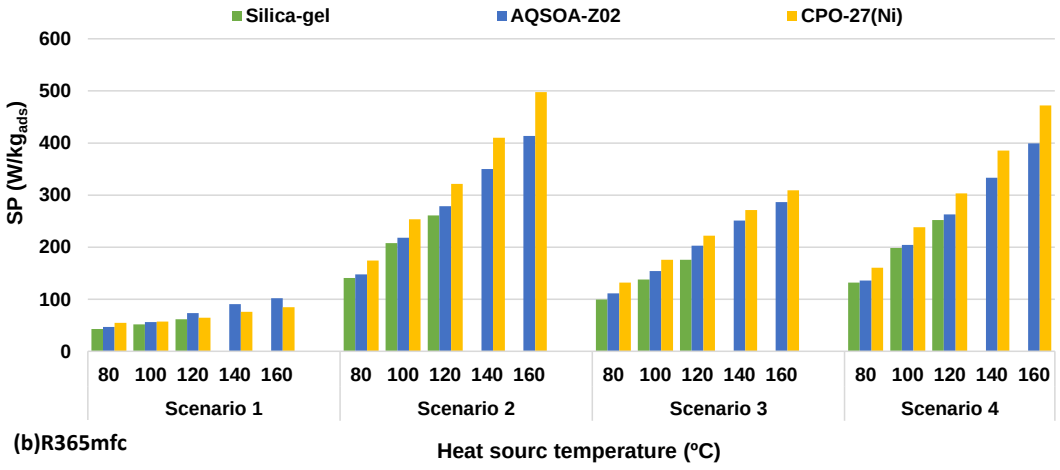

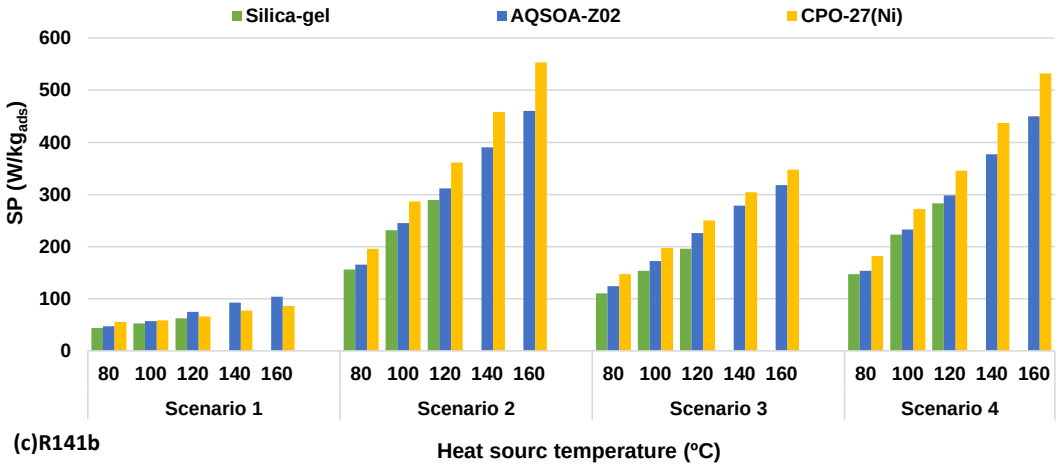

Figure 5-26: Effect of using different scenarios, adsorbent materials, ORC fluids and heat source temperatures on SP of the IAOSCE with two expanders

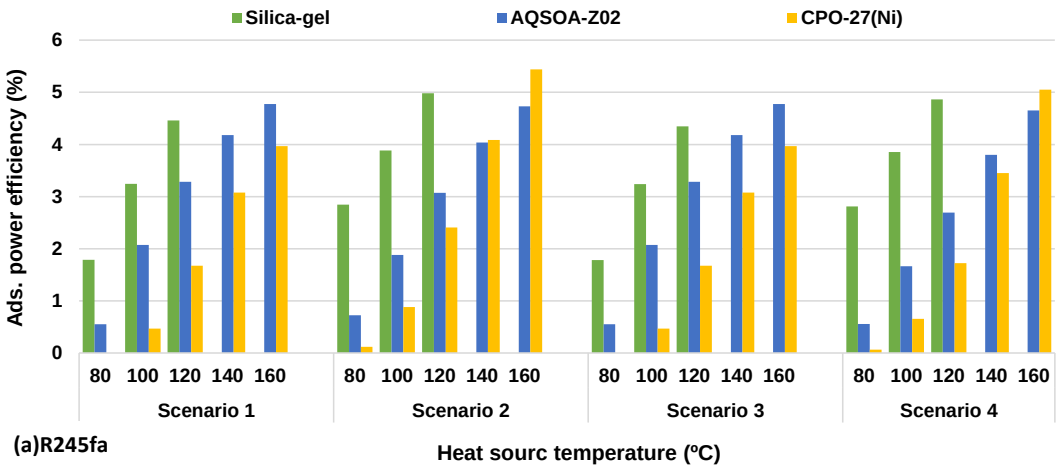

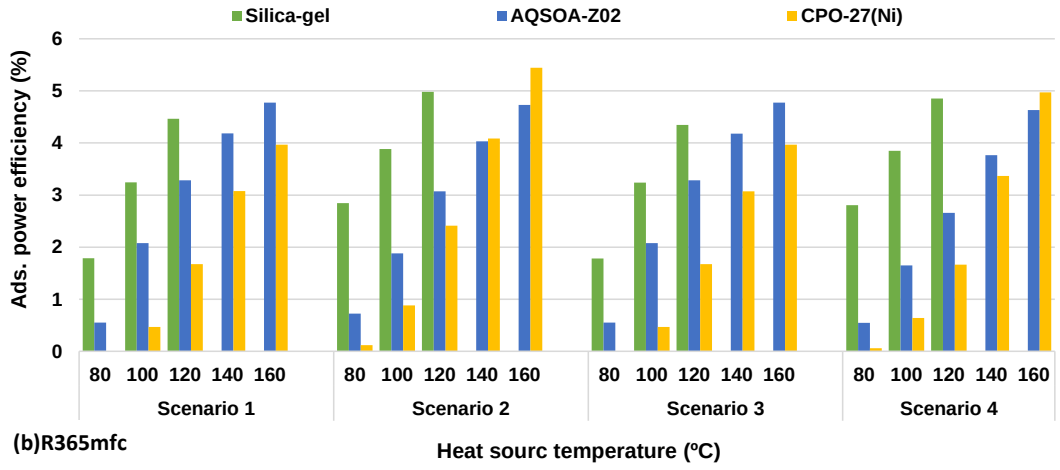

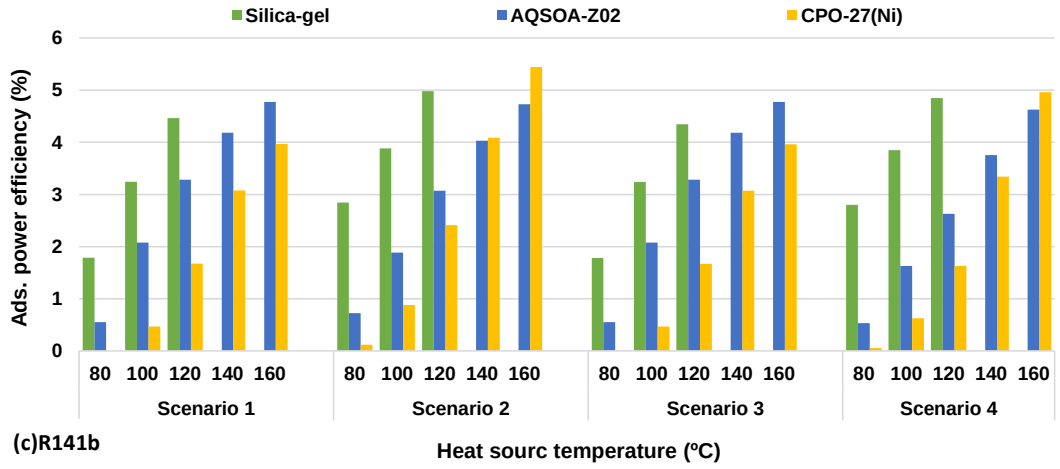

Figure 5-27: Effect of using different scenarios, adsorbent materials, ORC fluids and heat source temperatures on the adsorption power efficiency of the IAOSCE with two expanders

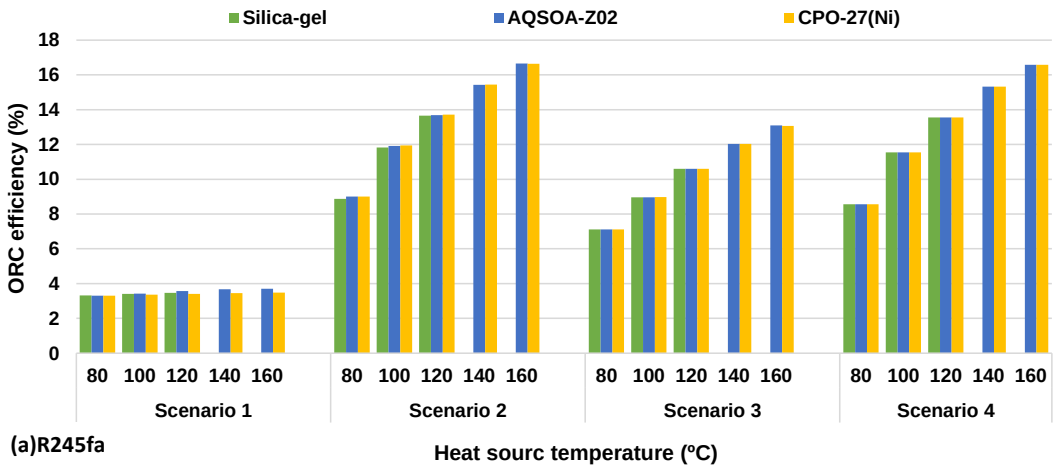

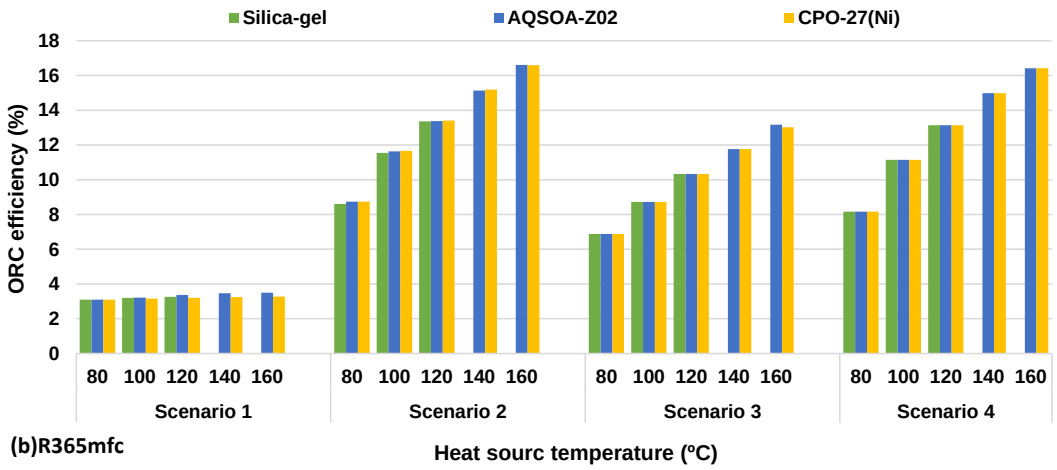

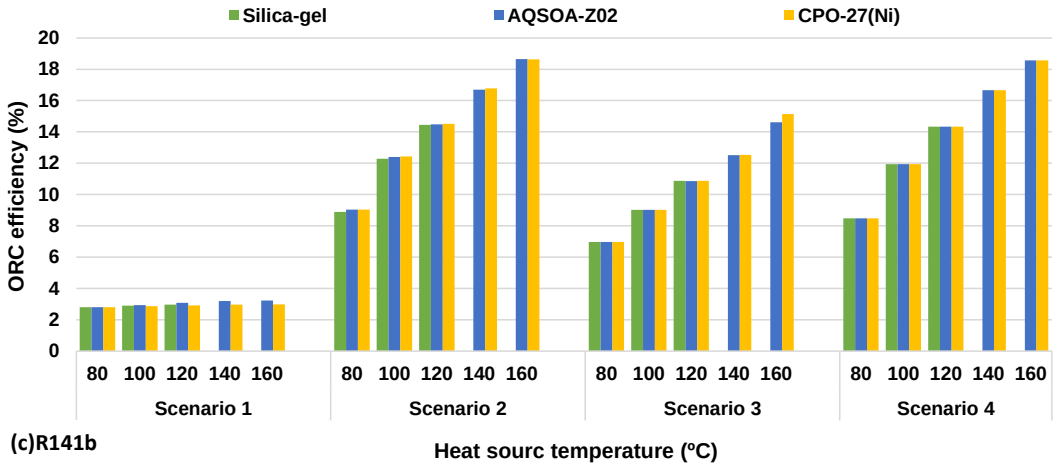

Figure 5-28: Effect of using different scenarios, adsorbent materials, ORC fluids and heat source temperatures on the ORC efficiency of the IAOSCE with two expanders

The four proposed scenarios of the IAOSCE with two expanders again can offer more options for energy designers and consumers to choose the suitable scenario or configuration for different applications. The main advantage of IAOSCE with two expanders is that more power can be generated because of using two expanders. Scenario 1 is preferable when limited amount of heat is available as this scenario can generate cooling and power simultaneously with a high coefficient of performance (COPe). However, the amount of cooling and power generated are relatively low when using this scenario. Scenarios 2 and 4 can generate cooling and power at the same time with relatively high SP and SCP with COPe approaching 0.6 [64]. These two scenarios can be considered as good scenarios when compromising between the amount of cooling and power generation and the coefficient of performance is needed. Therefore, if the low-grade heat source available is infinite or semi-infinite like solar energy (as in many hot countries around the world) scenarios 2 and 4 can be preferable [64].

Figure 5-29 shows COP/COPe of a number of configurations and scenarios of adsorption systems for cooling and electricity used in Chapter 4 and Chapter 5 for heat source temperature ranging from 100 to 160 ºC, cooling water temperature of 28 °C and inlet chilled water temperature of 18 °C. The comparison started with heat source temperature of 100 °C because HASCE was started from this value as very low cooling with almost no power were achieved below 100 °C. HASCE has the highest COPe of about 0.97 and 0.9 utilising AQSOA-Z02/Silica-gel and CPO-27(Ni)/Silica-gel respectively at heat source temperature of 100 °C which is clearly higher than BACS and the other scenarios and configurations used to generate cooling and electricity. This is due to HASCE has an additional evaporator that associated with the bottoming adsorbent beds which are powered by the cooling water leaving the topping adsorbent beds after recovering the heat of adsorption process [28].

Also Figure 5-29 shows that scenario 1 of the IAOSCE-2EXP (with two expanders) shows COPe of 0.8 utilising AQSOA-Z02 and R141b at heat source temperature of 100 °C, while scenario 1 of the IAOSCE-1EXP (with one expander) shows COPe of 0.79 utilising CPO-27(Ni) and R141b at heat source temperature of 120 °C. Scenario 2 of the IAOSCE-2EXP shows COPe of 0.61 utilising CPO-27(Ni) and R141b at heat source temperature of 160 °C, while scenario 2 of the IAOSCE-2EXP shows COPe of 0.58 utilising AQSOA-Z02 and R141b.

However, Figure 5-30 shows SCP/SCPe of a number of configurations and scenarios of adsorption systems for cooling and electricity used in Chapter 4 and Chapter 5 for heat source temperature ranging from 100 to 160 ºC. HASCE has the lowest SCPe compared to that of BACS and other cooling and electricity scenarios and configurations. Again scenario 1 IAOSCE-1EXP and IAOSCE-2EXP show low SCPe. Meanwhile, scenario 2 of the IAOSCE-2EXP shows the highest SCPe of about 2460 W/kgads utilising CPO-27(Ni) and R141b at heat source temperature of 160 °C and 2022 W/kgads utilising AQSOA-Z02 and R141b at heat source temperature of 160 °C.

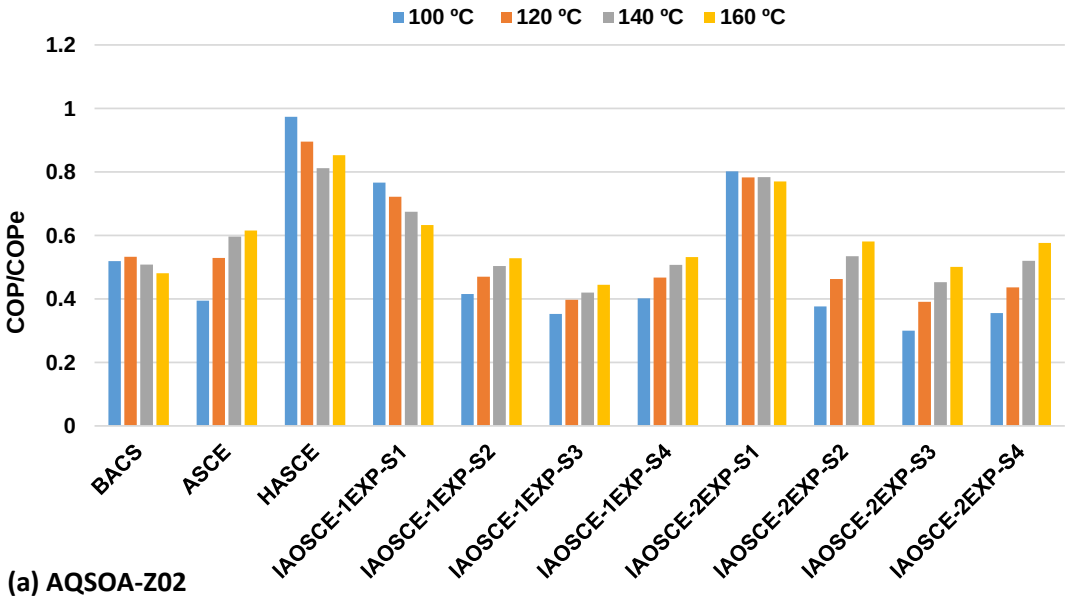

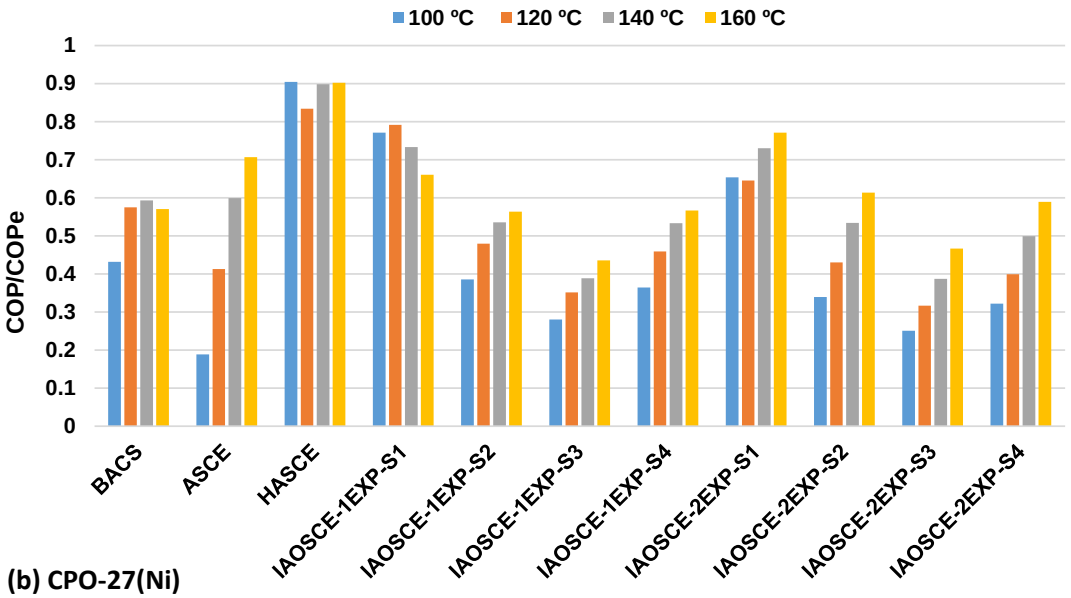

Figure 5-29: COP/COPe of different adsorption configuration, and scenarios used to generate cooling and electricity compared to that of BACS with a range of heat source temperature and R141b for (a) AQSOA-Z02 (b) CPO-27(Ni)

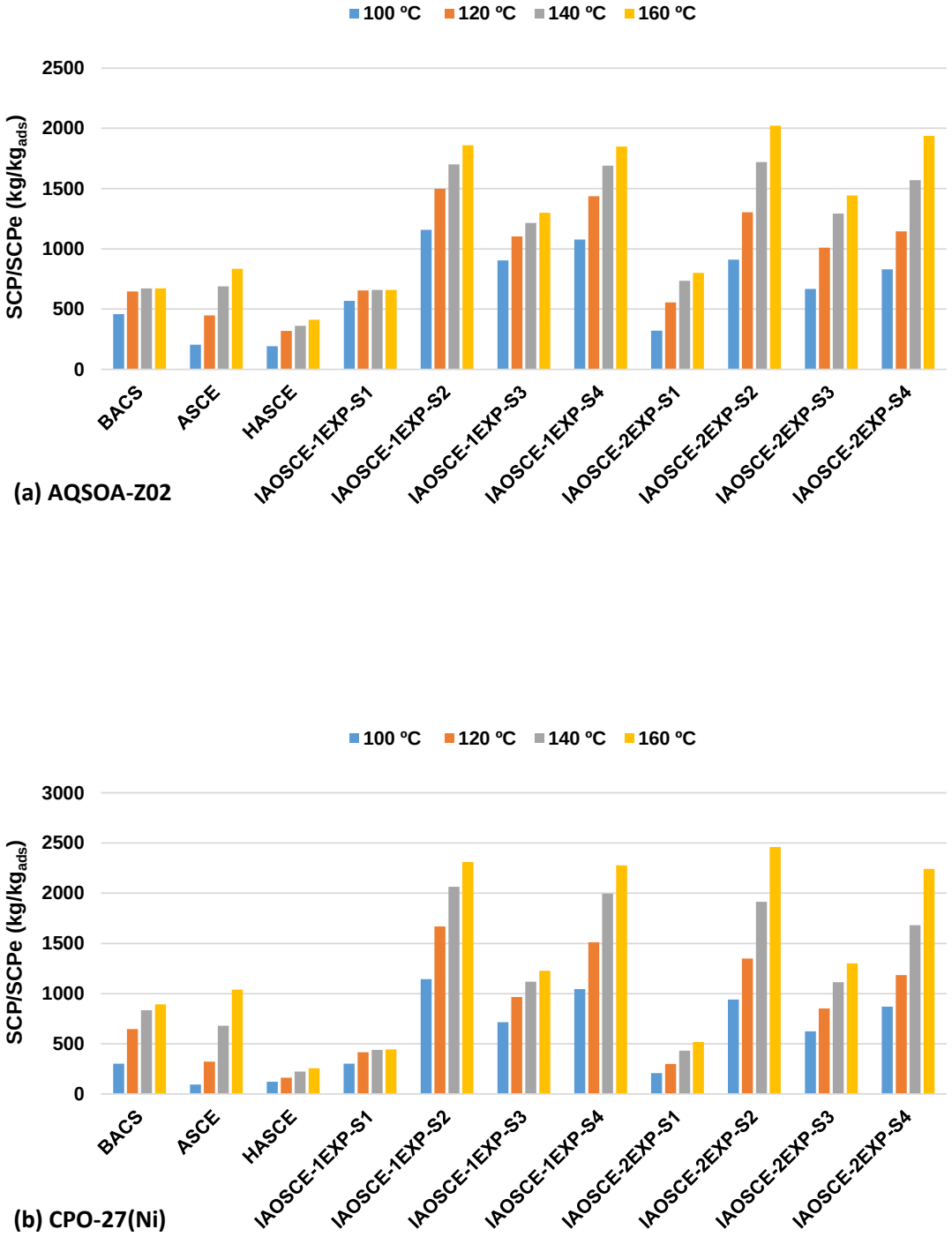

Figure 5-30: SCP/SCPe of different adsorption configuration, and scenarios used to generate cooling and electricity compared to that BACS with a range of heat source temperature and R141b for (a) AQSOA-Z02 (b) CPO-27(Ni)

Figure 5-31 shows the exergy efficiency for a number of scenarios and configurations used in Chapter 4 and Chapter 5. Scenarios 2, and 4 of the IAOSCE-2EXP show the highest exergy efficiency of about 57.6 %, and 57.52 % respectively utilising CPO-27(Ni) and R141b at heat source temperature of 120 ºC compared to the maximum value of exergy efficiency accomplished by BACS and ASCE of about 19.46% and 21.9% respectively for range of heat source temperatures of 120-160 ºC. Generally, IAOSCE (configuration 2) investigated in this chapter shows better performance than ASCE investigated in Chapter 4 (configuration 1).

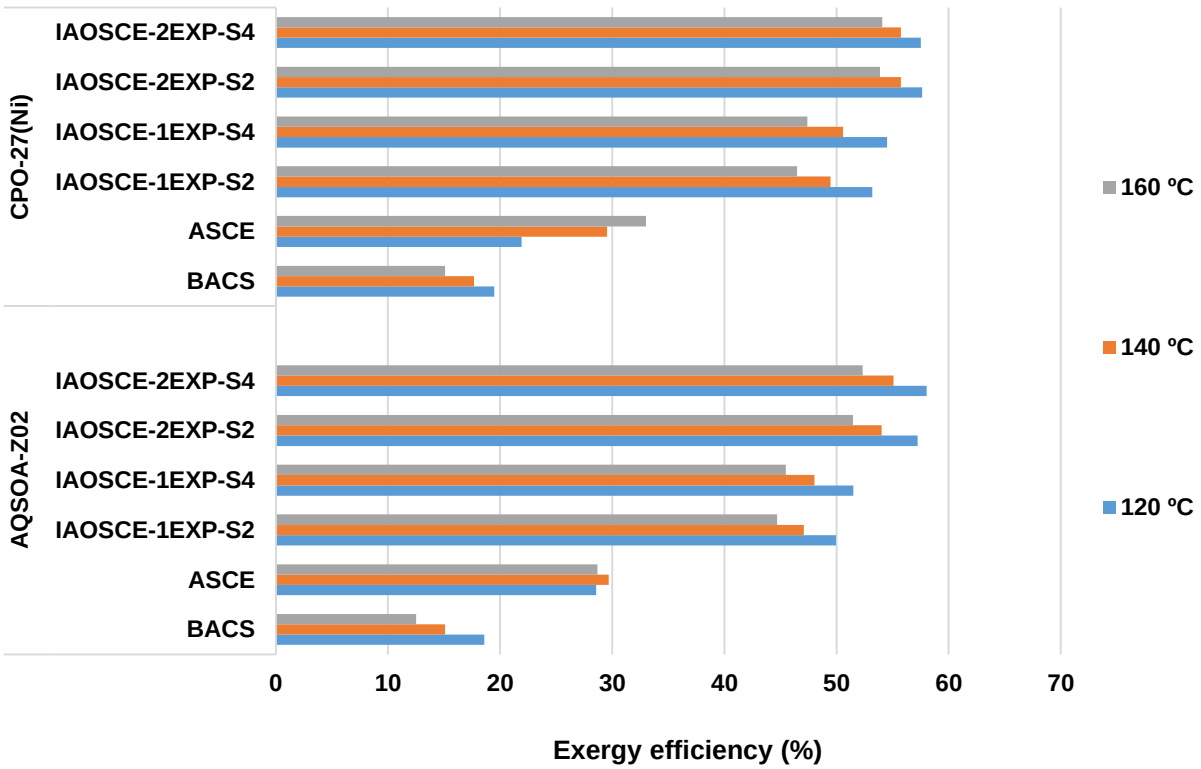

Figure 5-31: Exergy efficiency of a number of adsorption scenarios and configurations used to generate cooling and electricity with a range of heat source temperature utilising AQSOA-Z02, CPO-27(Ni) and R141b

5.7 Summary

In this chapter, novel scenarios of integrating adsorption cooling system with ORC to simultaneously generate cooling and electricity utilising low-grade heat source are established. The integrated adsorption-ORC system for cooling and electricity (IAOSCE) [22] is carried out in the first part of this chapter, while IAOSCE with two expanders [64] is carried out in the second part of this chapter by incorporating a steam expander in the adsorption cycle, so that the system has two expanders which increase the amount of generated power. Four different scenarios are adopted with IAOSCE-1EXP (with one expander) and IAOSCE-2EXP (with two expanders), where in scenario 1 the adsorption system (topping cycle) is powered by an external heat source, while ORC (bottoming cycle) is driven by the return cooling line of the adsorber bed without using the main heat source. Scenario 2 is similar to scenario 1 but the ORC is powered using the same heating fluid leaving the adsorber bed. In scenario 3, an adiabatic mixer is used to power ORC with the mixture of the heating and cooling fluids leaving the adsorption system, while in scenario 4; the adsorption system (bottoming cycle) is powered using the heating fluid leaving ORC (topping cycle). Advanced adsorbent materials (AQSOA-ZO2, Al-Fumarate and CPO-27(Ni)) are investigated and compared to Silica-gel, while R245fa, R365mfc, and R141b are used as ORC working fluids. Results show that using scenario 1 of the IAOSCE-1EXP and the IAOSCE-2EXP can achieve maximum values of the system COPe of 1.14 and 1.27 respectively utilising Silica-gel and R141b and heat source temperature of 80 ºC, while scenario 2 of the IAOSCE-1EXP and the IAOSCE-2EXP can achieve maximum equivalent SCP of about 2311 W/kg_{ads} and 2460 W/kg_{ads} respectively utilising CPO-27(Ni) and R141b with heat source temperature of 160 ºC. The last part of this chapter compares the different scenarios and configuration investigated in chapters 4 and 5 to generate cooling and electricity.

CHAPTER SIX

RADIAL INFLOW TURBINES DEVELOPMENT

6.1 Introduction

Turbine is the most important part of any power generation cycle and its performance can affect significantly the overall efficiency of such system. In this chapter a full detailed CFD analysis (using ANSYS$^{@2018}$ CFX and VISTA RTD) is established to design three small-scale radial inflow turbines that can work efficiently with the main configurations adopted in this work. For the first configuration (adsorption system for cooling and electricity ASCE), a small-scale steam radial inflow turbine has been developed to meet the requirements of the adsorption system using CPO-27(Ni) and AQSOA-Z02 as adsorbent materials, because they generated the maximum cooling and power as discussed in Chapter 4 [20]. For the second configuration (integrated adsorption-ORC system for cooling and electricity IAOSCE), two small-scale radial inflow turbines are developed to work efficiently with the main scenarios of this configuration with R141b as an ORC working fluid, where this fluid showed the maximum power generated as mentioned in Chapter 5 [64].

6.2 Expanders and turbines

Expanders are expansion devices where a high-pressure flow of a working fluid expands producing useful work. Generally, they can be classified into the volumetric type like screw, scroll, rotary vane, and reciprocating piston expanders, and the velocity type such as radial, and axial turbines. Selecting turbines depends on system size, working fluid properties, and cycle operating conditions used [145]. Radial inflow turbines are attractive for small-scale

applications, as radial inflow turbine has less sensitivity to blade profile and it requires fewer blades which can offer a key cost advantage [147]

6.2.1 Axial turbine

Axial turbine consists mainly of a row of fixed stator blades (nozzles) followed by a row of running rotor blades. The working fluid passing through the stator is accelerated in the axial direction, as a result the working fluid leaves the stator with a high velocity which converts the flow of the fluid into useful mechanical energy. Subsequently, the fluid is accelerated again in the rotor blades, meanwhile the pressure is reduced and work is done on the rotor blades [216]. Figure 6-1 shows the flow through an axial turbine stage defined using velocity triangles [217]. Subscripts (θ) and (m) refer to the tangential and meridional directions.

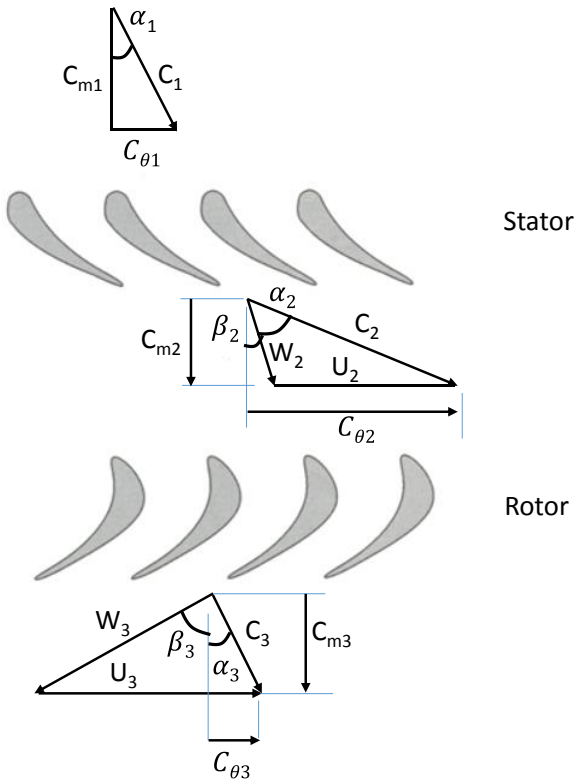

Figure 6-1: Velocity triangles of an axial turbine stage [217]

6.2.2 Radial inflow turbine

The high pressure working fluid passing through the radial inflow turbine (RIT) transfers its energy to the rotor shaft and compared to the axial turbine, RIT has the advantage of additional centrifugal energy (because the fluid passes from a large radius to a smaller one) which can be added to the total energy transferred through the turbine rotor. RIT can work with a relatively high-pressure ratio (around 4 per every single stage) with lower mass flow rate [146]. Figure 6-2 shows the geometry of a typical RIT stage which consists mainly of four different components namely; volute, stator (nozzle), rotor and diffuser. The fluid arrives at the stage through an inlet volute, and then it flows through a vaneless annular passage to the stator blades row. After that, the fluid flows through another vaneless annular passage before passing through the rotor. A diffuser is usually used after the rotor to convert some of the rotor exit velocity to static pressure [147].

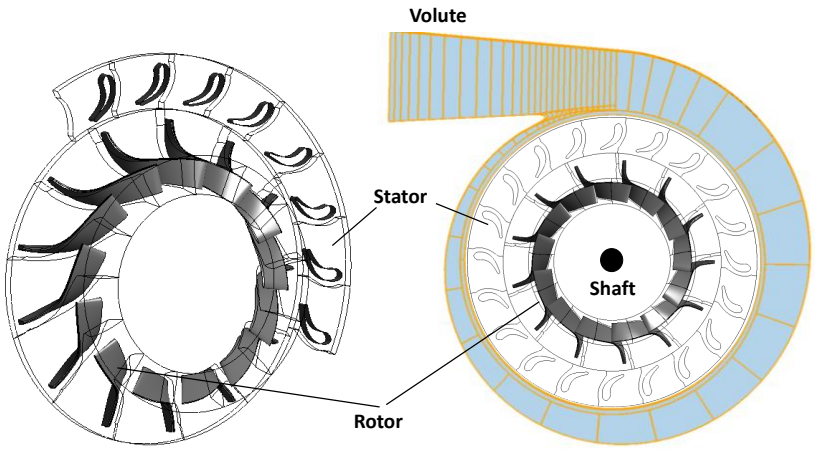

Figure 6-2: Main components of RIT [218]

6.3 Methodology of developing RIT

The design process of the RIT includes a number of steps starting from the preliminary design to the detailed CFD analysis. Figure 6-3 shows the main steps carried out to accomplish the final turbine design. From the cycle analysis of adsorption system for cooling and electricity or the integrated adsorption-ORC system for cooling and electricity generation, all the required operating conditions are available. The mean-line design using VISTA RTD software is the first step of this process and this step is an important step because of its ability to predict the performance maps for a range of various operating parameters.

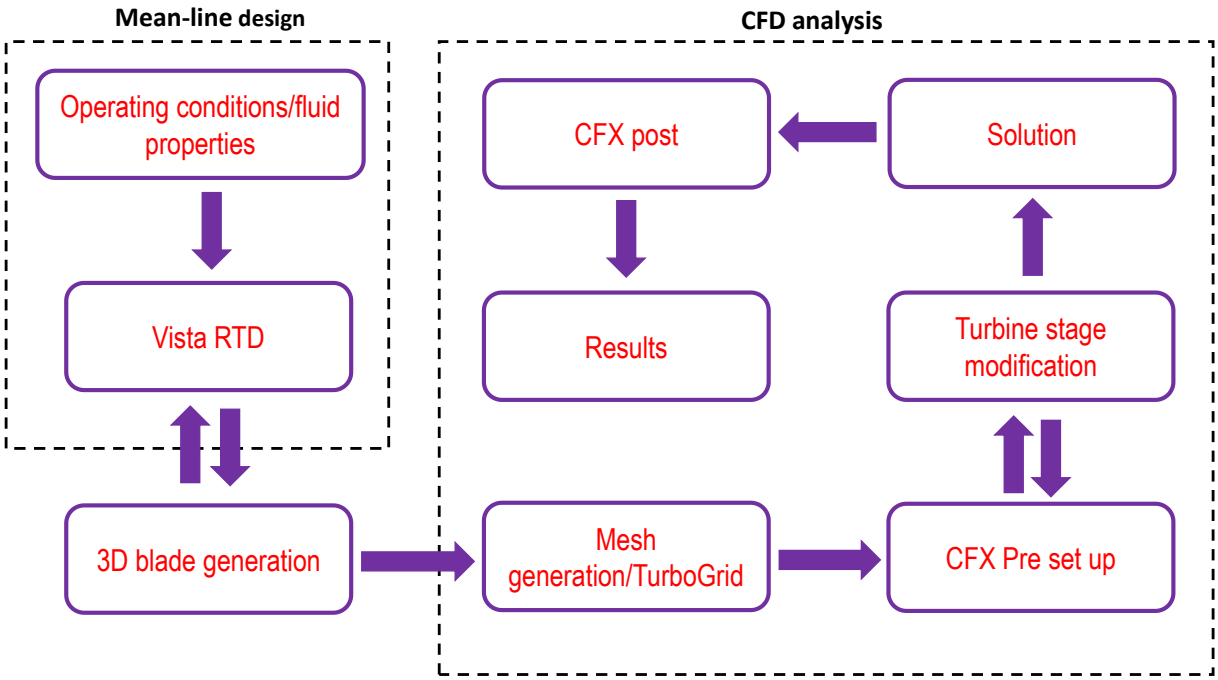

Figure 6-3: Methodology of developing the RIT

6.3.1 Mean-line design approach

In the mean-line (one-dimensional) procedure, the fluid properties are assumed to be constant and the variation in the fluid properties can be only in one direction that follows the mean

streamline of the blade geometry [218]. Also, this procedure can determine the dynamic properties of the fluid in addition to the blade geometric parameters like rotor and stator inlet and exit triangles, blades radii and heights [218].

Figure 6-4 shows the velocity angles and the basic geometry of the RIT, where C is the absolute velocity (m/s), U_4 and U_5 are the rotor blade velocities at the inlet and the outlet respectively (m/s), W is the relative flow velocity (m/s), α is the absolute flow angle with respect to radial (degree), β is the relative flow angle with respect to radial (degree) [218, 219]. Figure 6-5 shows RIT stage cross-section including volute, stator, rotor and diffuser (left) and the corresponding expansion process on the h-s diagram of the radial turbine stage (right), where l_{rotor} is the rotor length (m), b_4, and b_5 are the rotor blade inlet and outlet widths, r_4, $r_{5,hub}$, and $r_{5,tip}$ are the rotor inlet, exit rotor hub, and exit rotor tip radii (m).

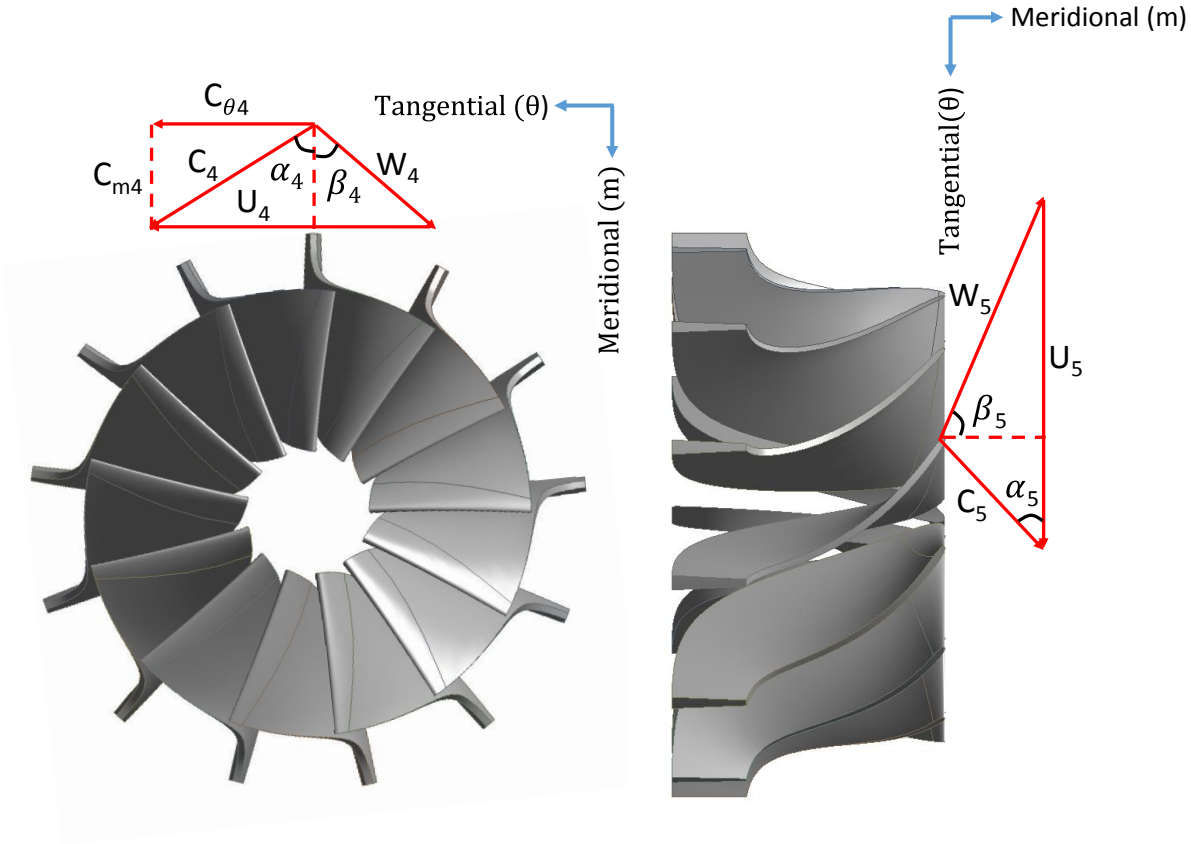

Figure 6-4: Velocity triangles and rotor blade profile of RIT [218, 219]

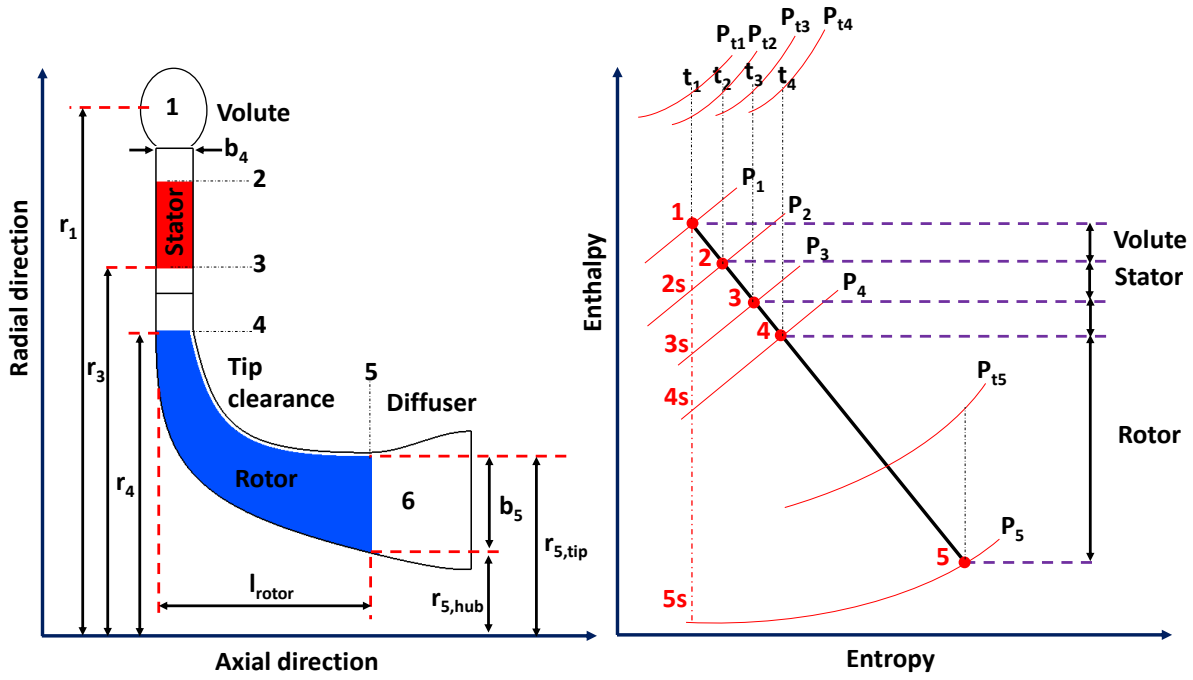

Figure 6-5: RIT stage cross-section (left), enthalpy-entropy diagram of turbine expansion (right) [218]

The mean-line procedure depends mainly on Euler turbomachinery equation and fluid dynamics (conservation of mass, momentum and energy) and aerodynamic losses [218]. Generally, the operating conditions of the turbine such as mass flow rate, inlet temperature, inlet pressure, pressure ratio, loading coefficient, velocity ratio and specific speed are the main inputs to the mean-line design software. The main characteristics of the remaining components like stator blades, volute and diffuser can be estimated depending on the results of the velocity triangles. For the radial turbine, the loading coefficient and the flow coefficient can be written as [156, 217]:

$$\psi = \frac{\Delta h_{actual}}{U_4^2} \qquad 6\text{-}1$$

$$\varphi = \frac{C_{m5}}{U_4} \qquad 6\text{-}2$$

Spouting velocity or isentropic velocity is a reference velocity with related kinetics energy equal to the difference of the isentropic expansion [220]. Spouting velocity (C_s), rotor inlet velocity (U_4) can be written [147] as:

$$C_s = \sqrt{2\Delta h_{ideal}} \quad 6\text{-}3$$

$$U_4 = C_s \nu_{ts} \quad 6\text{-}4$$

$$r_4 = \frac{U_4}{\omega} \quad 6\text{-}5$$

Where, ν_{ts} is the total to static velocity ratio and ω is the rotational speed (RPM). Tip diameter, rotor blades number and rotor axial length can be calculated as [147, 167]:

$$r_{5,tip} = \sqrt{\frac{A_5}{\pi} + r_{5,hub}^2} \quad 6\text{-}6$$

$$Z_{rotor} = \frac{\pi}{30}(110 - \alpha_2)\tan(\alpha_2) \quad 6\text{-}7$$

$$l_{rotor} = 1.5(r_{5,tip} - r_{5,hub}) \quad 6\text{-}8$$

The volute radius and the maximum turbine diameter can be calculated as:

$$r_{volute} = \sqrt{\frac{A_1}{(0.75\pi+1)}} \quad 6\text{-}9$$

$$d_{max} = 2(r_1 + r_{volute}) \quad 6\text{-}10$$

Euler turbomachinery equations [218, 221], can be used to define the velocity triangles at the inlet and the outlet of the rotor blade and work transfer per unit mass can be determined as:

$$W/\dot{m} = U_4 C_{\theta 4} - U_5 C_{\theta 5} = \frac{1}{2}\left[(U_4^2 - U_5^2)\right] - (W_4^2 - W_5^2) + (C_4^2 - C_5^2) \quad 6\text{-}11$$

Subscripts 4 and 5 refer to the rotor inlet and outlet respectively, while subscript θ refers to the tangential direction. Also $\dot{m}$ is mass flow rate (kg/s). Euler equation shows the advantage of using RIT compared to an axial turbine, where for the axial turbine, the value of rotor blade velocity is constant, and thus the first term in the above equation becomes zero. For the RIT, as a result of the significant radius change, the term $(U_4^2 - U_5^2)$ has an important contribution to the overall specific power (specific enthalpy). For the second term, to be positive, W_5 must be greater than W_4. The third term is the opposite of the second one, where the difference between the absolute velocities at the inlet and the outlet is needed to be maximized.

In the mean-line method, the losses models are used to predict the performance of the RIT. These losses are the total enthalpy drop which consists of incidence, passage, secondary, exit, tip clearance, nozzle and volute losses.

The incident and friction losses can be calculated [218, 222] as:

$$\Delta h_{\text{incidence}} = \frac{W_{\theta 4}^2}{2} \quad 6\text{-}12$$

$$\Delta h_{\text{disk friction}} = \frac{K_f \rho U_4^3 r_4^2}{4\dot{m}} \quad 6\text{-}13$$

The symbol ρ refers to the density (kg/m^3), and K_f is a friction coefficient.

$$\Delta h_{\text{friction}} = f_{\text{curve}} \left[\frac{W_4 + \left(\frac{W_{5,\text{tip}} + W_{5,\text{hub}}}{2}\right)}{2}\right] \frac{l_{\text{hyd}}}{d_{\text{hyd}}} \quad 6\text{-}14$$

Symbol f_{curve} is the friction factor that accounts the curvature effect, while symbols l_{hyd} and d_{hyd} are the hydraulic length and diameter respectively (m) [156].

The secondary losses can be calculated [218] as:

$$\Delta h_{secondary} = \frac{C_4^2 d_4}{Z_{rotor} r_c} \quad 6\text{-}15$$

Z_{rotor} is the number of the rotor blades, while r_c is the rotor mean radius of curvature (m) [156].

The exit energy losses can be calculated [222] by:

$$\Delta h_{exit} = 0.5 C_5^2 \quad 6\text{-}16$$

The enthalpy drop caused by the tip clearance in both axial and radial directions can be calculated [217, 223] using the following correlations:

$$\Delta h_{tip,clearance} = \frac{U_3^4 Z_{rotor}}{8\pi}\left(0.4\varepsilon_x + 0.75\varepsilon_r C_r - 0.3\sqrt{\varepsilon_x \varepsilon_r C_x C_r}\right) \quad 6\text{-}17$$

$$C_x = \frac{1-\left(\frac{r_{5,tip}}{r_4}\right)}{C_{m4} b_4} \quad 6\text{-}18$$

$$C_r = \left(\frac{r_{5,tip}}{r_4}\right)\frac{l_{rotor}-b_4}{C_{m5} r_5 b_5} \quad 6\text{-}19$$

$$\varepsilon_x = \varepsilon_r = 0.04\left(r_{5,tip} - r_{5,hub}\right) \quad 6\text{-}20$$

Where ε_x and ε_r are the clearances of the axial and radial tips (m). The losses from the friction generated in the stator (nozzle) can be calculated [218] as:

$$\Delta h_{friction,nozzle} = 4 f_{nozzle} \bar{C}^2 \frac{l_{hyd,nozzle}}{d_{hyd,nozzle}} \quad 6\text{-}21$$

f_{nozzle}, is the stator (nozzle) friction factor. $\bar{C}$ is the average absolute velocities of the stator [218]. Volute losses can be calculated [218] using:

$$\Delta h_{volute,loss} = \frac{K_{volute} C_2^2}{2} \quad 6\text{-}22$$

The total losses in enthalpy through the RIT stage can be calculated as:

$$\Delta h_{total,losses} = \Delta h_{incidence} + \Delta h_{disk\,friction} + \Delta h_{friction} + \Delta h_{secondary} + \Delta h_{exit} + \Delta h_{tip,clearance} + \Delta h_{friction,nozzle} + \Delta h_{volute,loss} \quad 6\text{-}23$$

After calculating the total losses through the RIT stage, the total to static efficiency can be calculated as [160, 224]:

$$\eta_{t,s} = \frac{\Delta h_{actual}}{\Delta h_{actual} + \Delta h_{total,losses}} \quad 6\text{-}24$$

More details about the dimensions calculations of the RIT can be found in Whitfield and Baines [218] and Glassman [225].

6.3.2 VISTA RTD method

Vista software included in ANSYS$^{@2018}$ Workbench offers mean-line design and off-design with performance prediction for a range of turbomachinery applications including radial turbines, axial compressors, axial fans, centrifugal compressors, and centrifugal pumps [226]. It can be used to produce a mean-line design for the RIT and the generated geometry can be exported to BladeGen, BladeEditor and other three-dimensional CFD analysis tools provided

by ANSYS CFX. Figure 6-6 summarises the main steps of the RIT mean-line design from the aerodynamic properties and operating conditions to the velocity triangles and the performance result. Results from VISTA RTD can then be exported to the BladeGen to generate the required geometry for the RIT rotor. More details about the VSTA RTD design are provided in Appendix A.

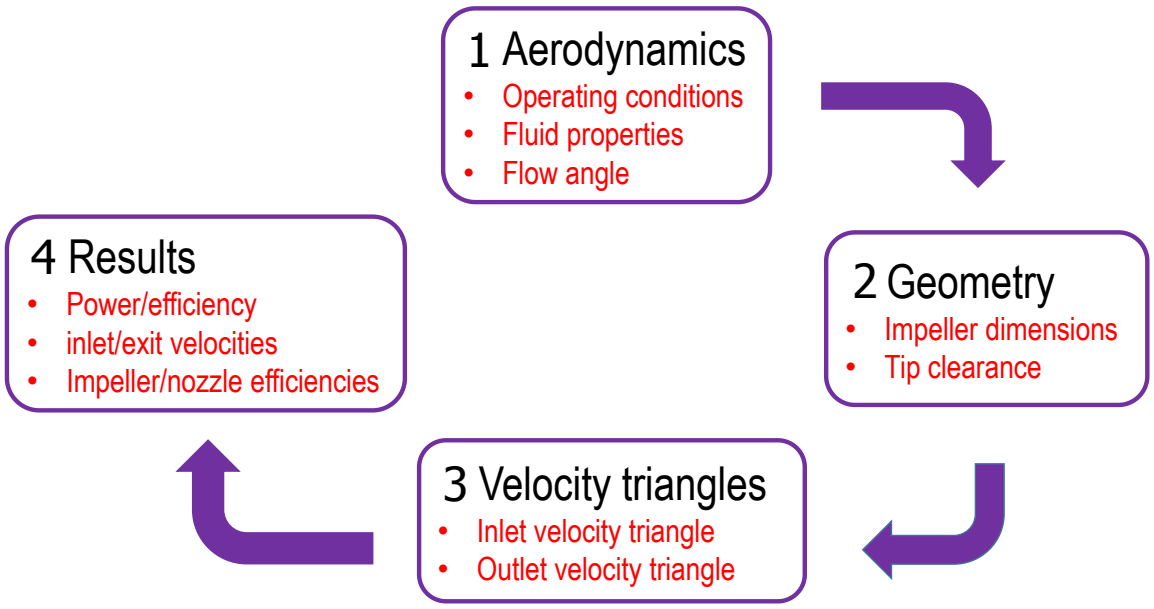

Figure 6-6: VISTA RTD mean-line design steps

6.3.3 CFD Analysis

CFD (Computational Fluid Dynamics) is defined as a numerical approach to solve the flow field problem (Navier–Stokes equations) using computer simulation tools that including finite elements and finite difference methods [227]. By using VISTA RTD, the initial geometry parameters like stagger angle, tip and hub radii, leading and trailing edge radii, blade angles, and chord are already defined. Then the blade geometry can be generated by the CFX BladeGen tool which can be imported to the CFX TurboGrid tool (ANSYS$^{@2018}$ Workbench

tool) to produce the meshing for the fluid domain. The Optimized Automatic Topology (ATM) can be used to create the required mesh. Generally, this technique of meshing is easier than the traditional topology methods with better mesh quality [228] and after defining the topology, the mesh can be generated.

CFX-Pre is the pre-processor tool for the ANSYS CFX simulation set up, where the turbomachine type can be defined (such as radial or axial). Furthermore, the main components (like rotor blade R1 and the stator blade S1) can be added, and all the interfaces and boundaries can be defined. Also, this tool supports the Inflow/Outflow boundary conditions and the fluid selection. Shear Stress Transport (SST) turbulent model can be chosen because of its ability of near-wall treatment and it was developed to overcome deficiencies in the K-ε and BSL K-ε models and using the SST model over the other models is recommended by ANSYS [229]. After all the operating conditions and the setup parameters are defined in the CFX-Pre tool, all files are sent to the CFX-Solver which can start or stop the solution process, and monitor its progress and for this study, the solution stops normally when the residuals reach convergence of 10^{-5}. Once the solution reaches this convergence limit, all the results data are sent to the CFX-Post which is a presenting tool for the simulation CFD results.

6.4 Radial inflow turbines development

Using the three-dimensional CFD modelling can enhance the aerodynamic performance of the baseline design (baseline design is a three-dimensional design based on the mean line design obtained by VISTA RTD) of the RIT [151, 159, 215, 230]. In this work three different radial inflow turbines namely Steam, ORC1, and ORC2 are designed and developed using VISTA RTD ANSYS$^{@2018}$ and the three-dimensional modelling with ANSYS$^{@2018}$ CFX to meet the operating parameters of the two main system configurations adopted in this work. Steam

turbine is designed to meet the operating conditions of the adsorption system for cooling and electricity (ASCE). Turbines 'ORC1' and 'ORC2' are designed to work efficiently with the integrated adsorption-ORC system for cooling and electricity (IAOSCE) described in Chapter 5, where ORC1 is designed for the scenarios 1 and 3 which have a relatively low-pressure ratio, while ORC2 can be used with scenarios 2 and 4 which have a relatively high-pressure ratio. Table 6-1 illustrates the main operating conditions and parameters used in this chapter for development of the three different turbines.

Table 6-1: Main parameters used in the baseline design

Steam turbine	
Refrigerant	steam
Mass flow rate kg/s	0.016
Speed RPM	60,000-70,000
Pressure ratio	3.2-3.5
Number of blade (stator)	18
Number of blade (rotor)	15
ORC1turbine	
Refrigerant	R141b
Mass flow rate kg/s	0.16
Speed RPM	24,000-30,000
Pressure ratio	1.6-1.8
Number of blade (stator)	16
Number of blade (rotor)	13
ORC2turbine	
Refrigerant	R141b
Mass flow rate kg/s	0.16
Speed RPM	26,000-40,000
Pressure ratio	2.8-3
Number of blade (stator)	16
Number of blade (rotor)	13

Figure 6-7 shows the mesh sensitivity depending on total-to-static efficiency for the three different turbine designs. It is clear that the effect of the number of nodes on the total-to-static efficiency for the three turbines is negligible with nodes number of one million (500,000 for the stator and 500,000 for the rotor).

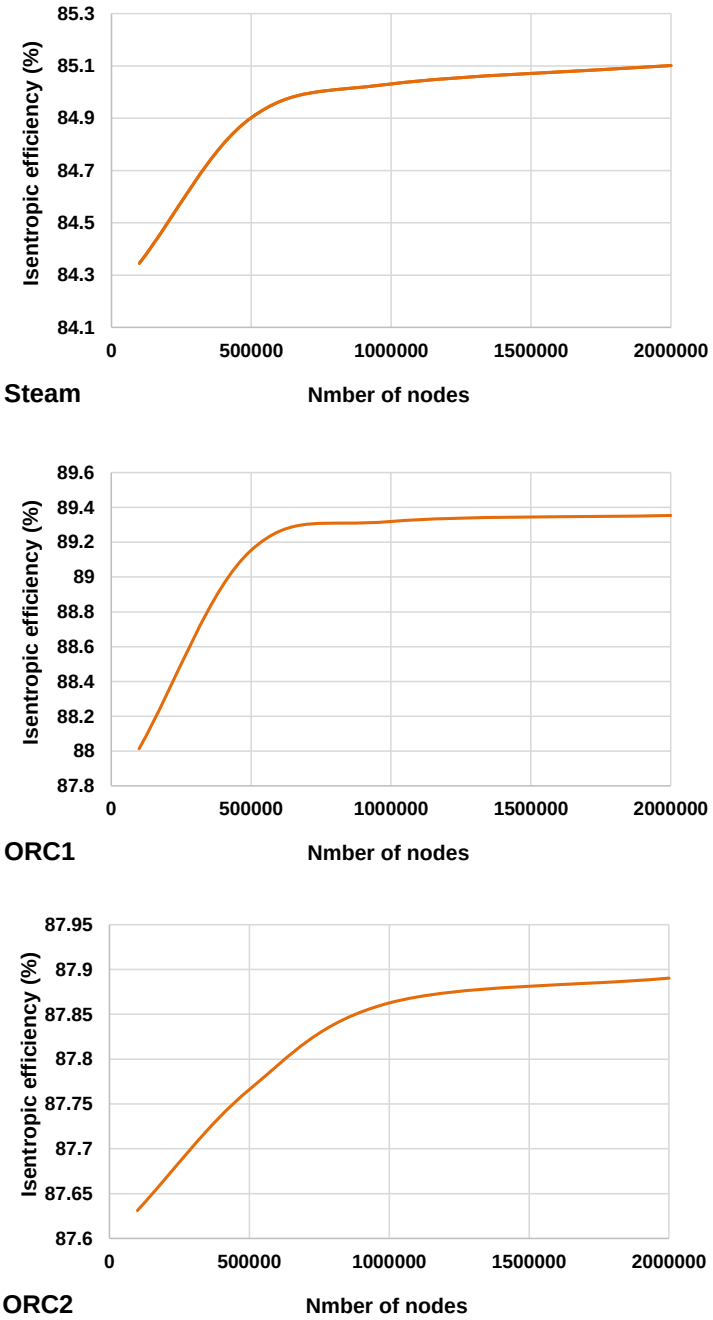

Figure 6-7: Mesh sensitivity depending on total-to-static efficiency for Steam, ORC1 and ORC2 turbines

In this study, the modelling of the three-dimensional turbulent viscous flow in RIT is accomplished using the k-ε SST turbulence model. This model has the ability to take into account the effect of the first node nearby the walls and capture the turbulence closure to the wall [231].

6.4.1 Steam turbine

A small-scale RIT is developed to work with the adsorption system for cooling and electricity cycle defined in Chapter 4. Figure 6-8 shows the two dimensional and three-dimensional views of the steam turbine geometry including stator and rotor blades stages.

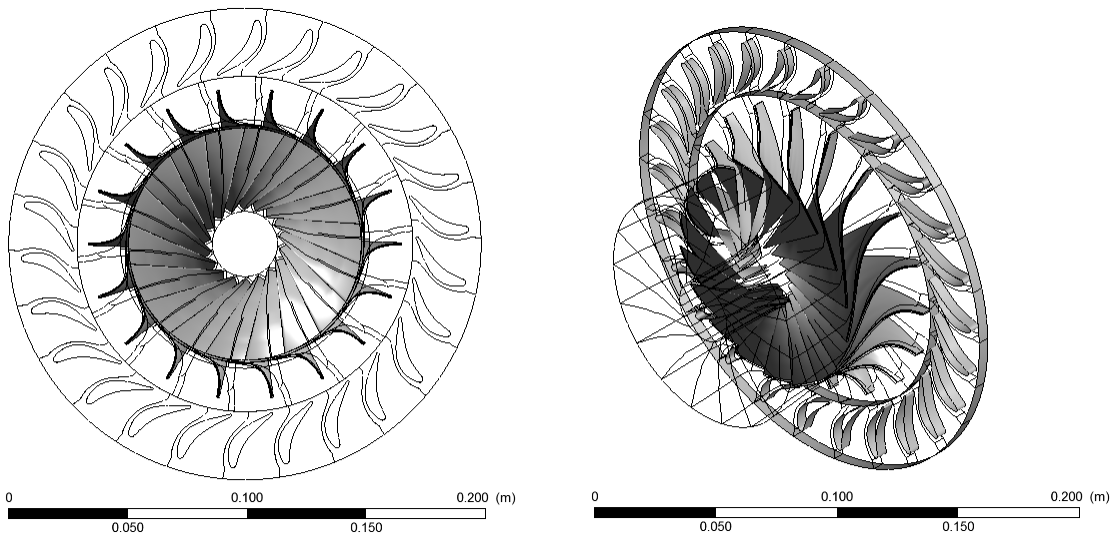

Figure 6-8: 2D and 3D views of the Steam RIT geometry

Figure 6-9 shows the three-dimensional blade-to-blade passage mesh generation of the Steam turbine. The grid consists of one million cells; 500,000 for the stator and 500,000 for the rotor with the refined mesh near the edges in order to compromise between the solution accuracy and the computational time.

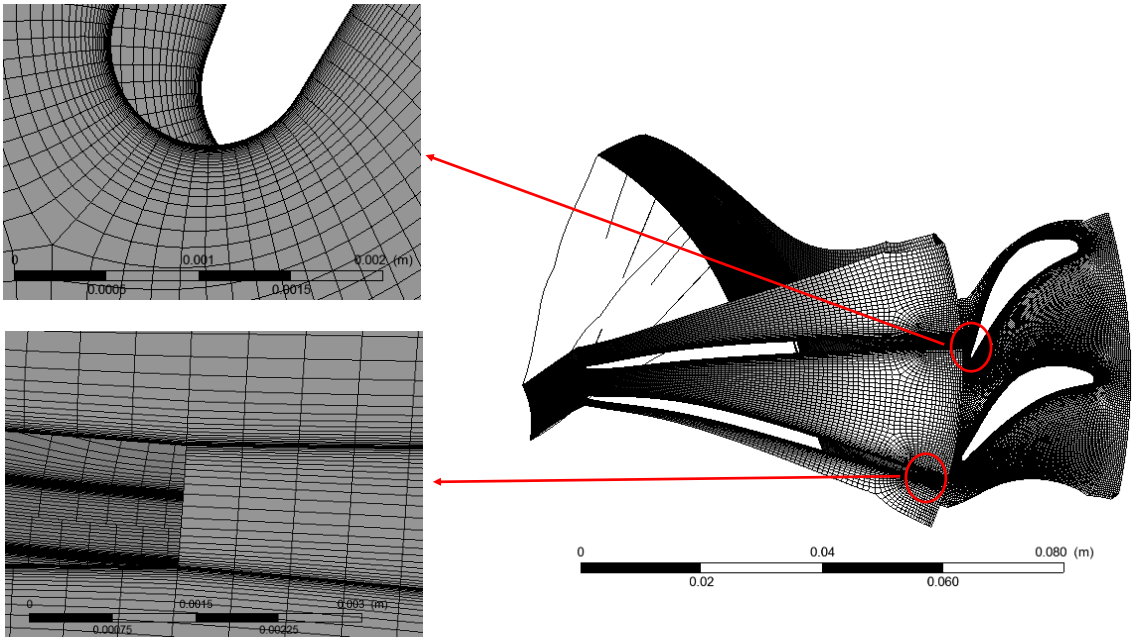

Figure 6-9: 3D mesh generation blade-to-blade passage for the Steam turbine

Figure 6-10 compares the baseline design (the initial design obtained from the VISTA RTD and the BladeGen) and the improved design (improved by the 3D CFD) in terms of power and efficiency. The improved design is developed by changing the number of blades for both rotor and stator, and improving the shape of the stator and the rotor blades to enhance the flow and reduce the losses. The power is increased from about 2000 W to about 2590 W, while the efficiency is increased from 75% to about 85%.

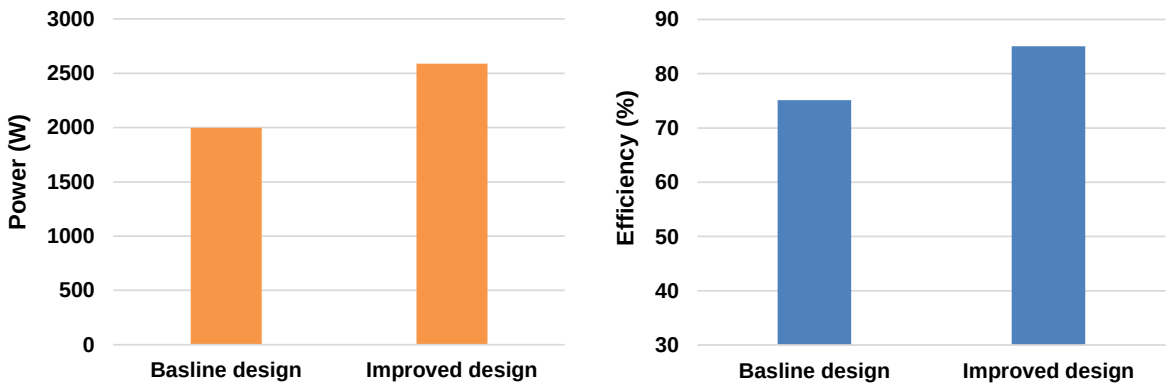

Figure 6-10: Power and efficiency of the baseline and the improved design of the Steam turbine

Figure 6-11 shows that the Steam turbine can work efficiently through a range of mass flow rate between 0.01 to 0.02 kg/s and as it increases, power and efficiency increases, so the mass flow rate has an important influence on the power generated.

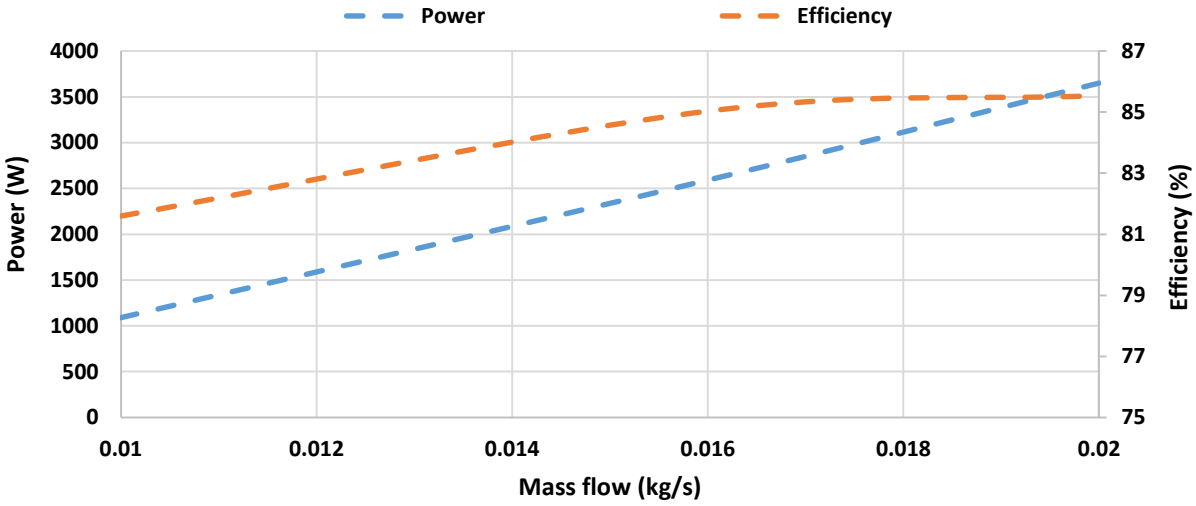

Figure 6-11: Effect of mass flow rate on power and efficiency of the Steam turbine

Figure 6-12 shows that Steam turbine can work within a range of rotational speed ranging from 61000 to 69000 RPM. It is clear that as the rotational speed increases, the speed and the power generated increase and the power generated is more sensitive to the rotational speed because it is directly proportional to the speed.

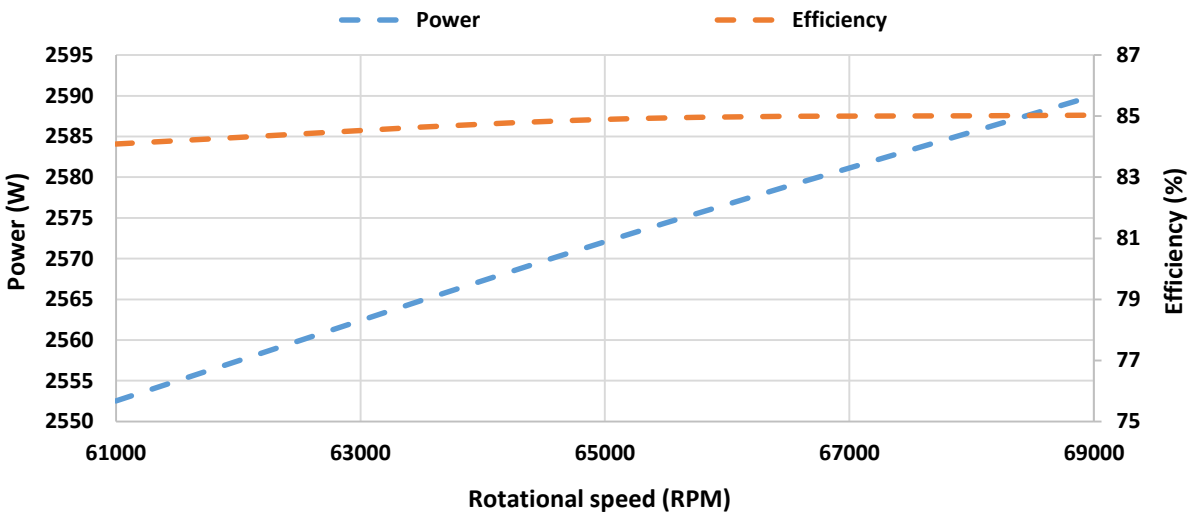

Figure 6-12: Effect of rotational speed on power and efficiency of the Steam turbine

Figure 6-13 shows the velocity distribution at 50% span for the baseline, and the improved designs of the Steam turbine. It can be noticed that the baseline design contour has a flow reversal (which increases the secondary losses) compared to the improved design contour which shows a smooth flow.

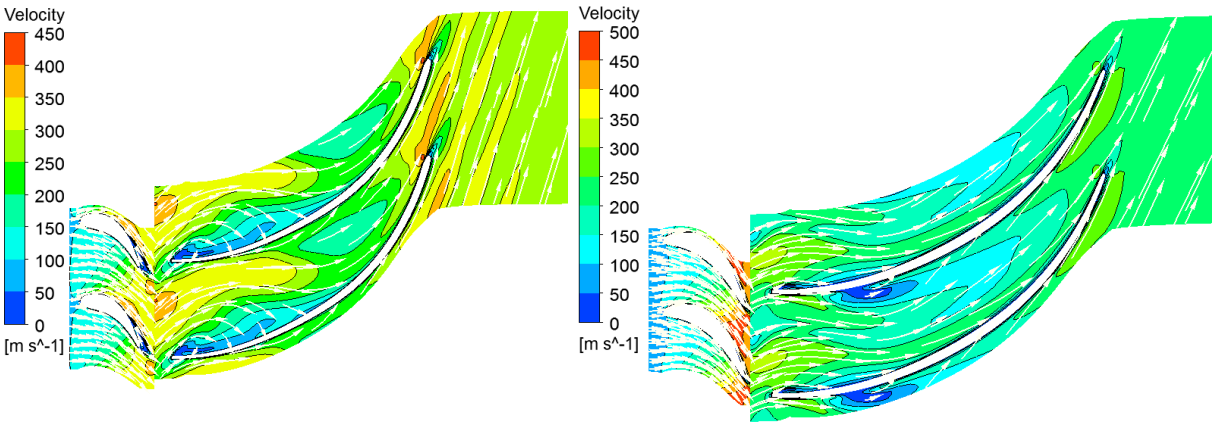

Figure 6-13: Velocity at mid-span for the baseline design (left), and the improved design (right) of Steam RIT

Figure 6-14 shows the pressure distribution at mid-span for the baseline and the improved designs of the Steam turbine. The improved design has less pressure on the pressure side which reduces the mechanical load on the rotor blades.

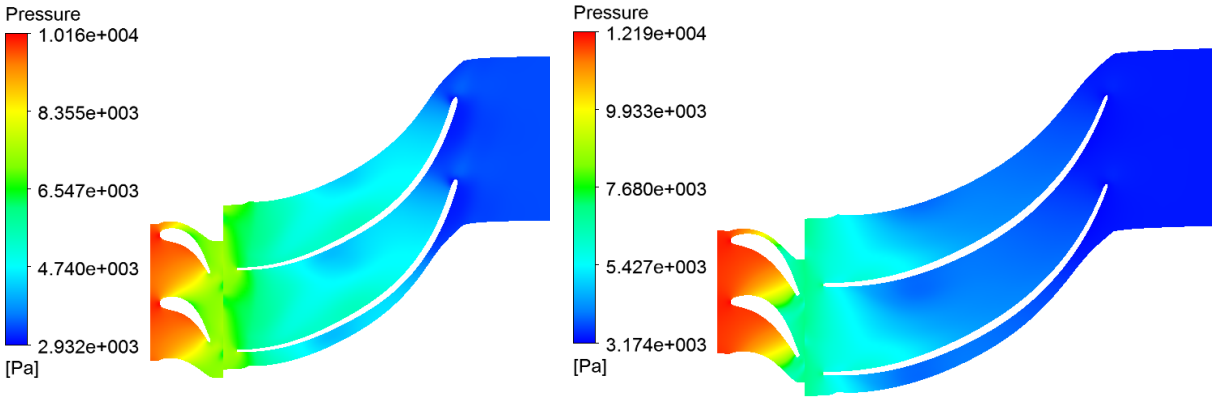

Figure 6-14: Pressure distribution at mid-span for the baseline design (left), and the improved design (right) of Steam RIT

Figure 6-15 shows the static entropy at mid-span for the baseline and the improved designs of the steam turbine. It is clear that the improved design has significantly less entropy generation compared to that of the baseline design. Entropy is one of the losses indicators, where the secondary flows and flow separation lead to considerable entropy generation which reduces the turbine efficiency [219].

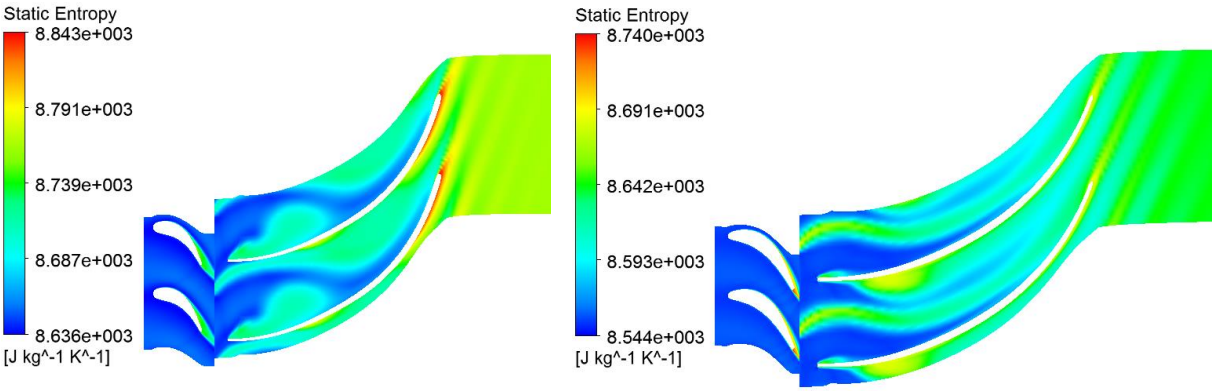

Figure 6-15: Static entropy at mid-span for the baseline design (left), and the improved design (right) of the Steam RIT

Figure 6-16 shows the meridional Mach number for the baseline and the improved designs of the Steam turbine. Mach number is still less than unity (subsonic) for both the baseline and the improved designs, but the baseline design contour shows relatively high Mach number at the diffuser (exit) which means more exit losses. For the improved design, the highest Mach number of about 0.93 occurred at the interspace between stator (nozzle) and rotor and this is due to the relatively high-pressure ratio of about 3.4. Figure 6-17 shows the blade loading (pressure distribution) of the baseline, and the improved designs for the Steam turbine at rotor mid-span and it shows the pressure profile at the suction and pressure sides. The blade loading is important because the enclosed area of such pressure curves is an indicator of the net torque and then it is an indicator of the shaft work. The improved design has lower blade loading with a better profile, however, the area enclosed by the curves are close, but the improved design has a larger net torque because it has a larger number of blades.

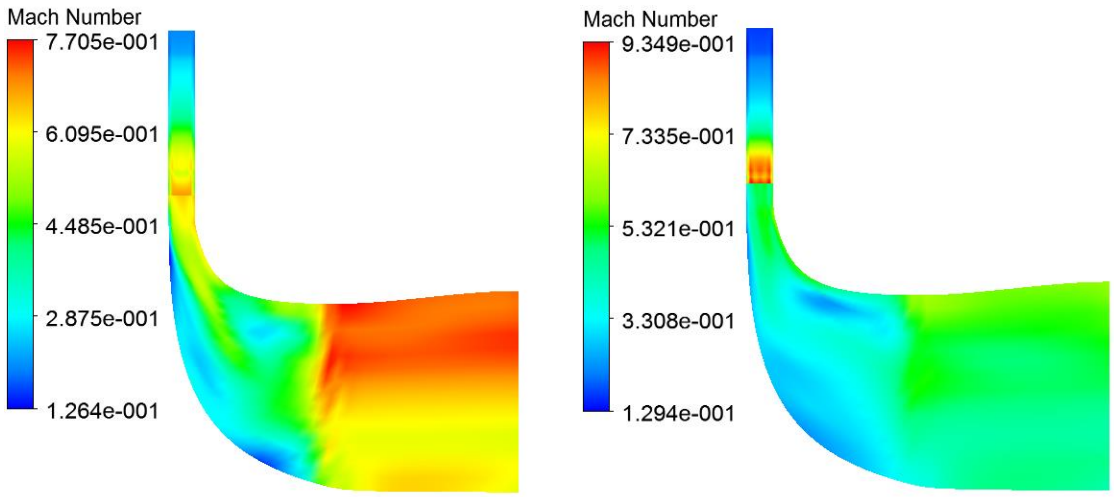

Figure 6-16: Meridional Mach number for the baseline design (left), and the improved design (right) of the Steam RIT

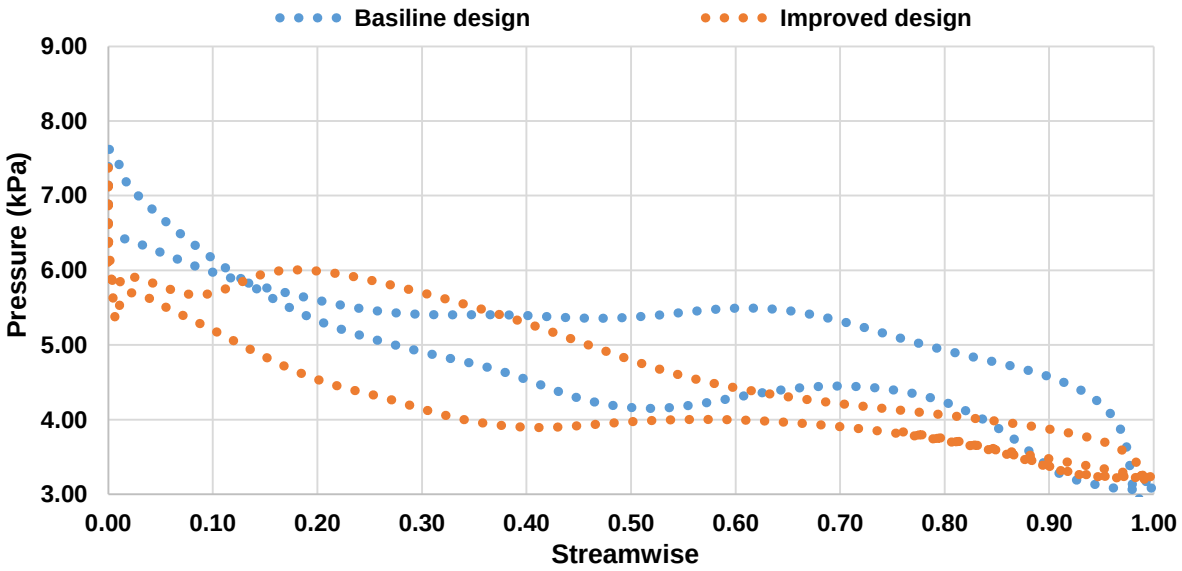

Figure 6-17: Blade loading at rotor mid-span for the baseline, and the improved designs of the Steam RIT

6.4.2 ORC1 turbine

ORC1 turbine is a small-scale RIT developed to work efficiently with scenario 1 and scenario 3 (with low-pressure ratio) of the integrated adsorption-ORC system for cooling and electricity as discussed in Chapter 5. Figure 6-18 shows the two-dimensional and three-dimensional views of the ORC1 turbine geometry. Figure 6-19 shows the three-dimensional mesh generation of the ORC1 turbine including the stator and rotor blade stages. Again for this turbine, one million nodes are used; 500,000 for the stator and 500,000 for the rotor with refined mesh near the edges to compromise between the solution accuracy and the computational cost.

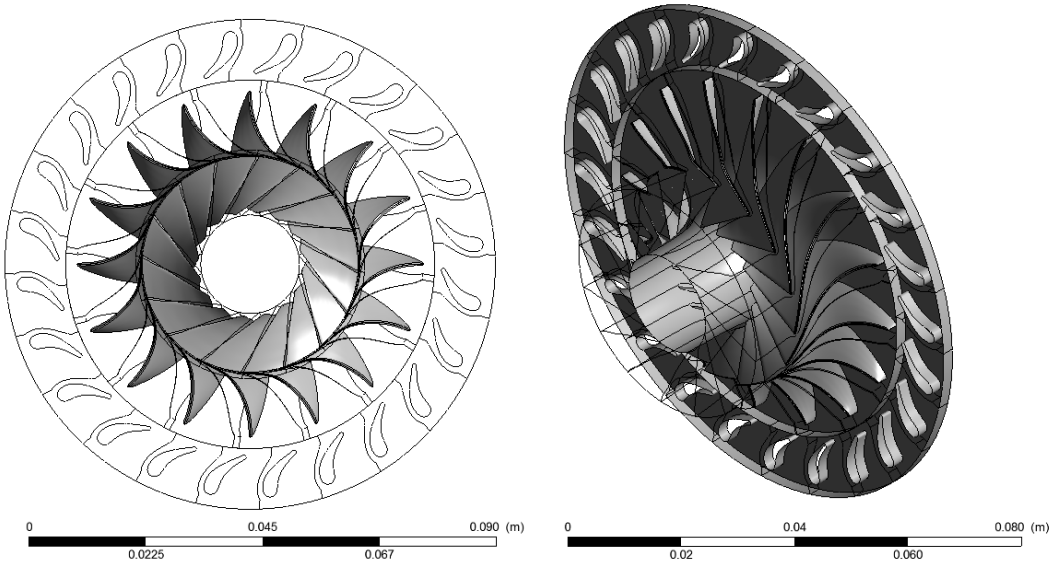

Figure 6-18:2 D and 3D views of the ORC1 RIT geometry

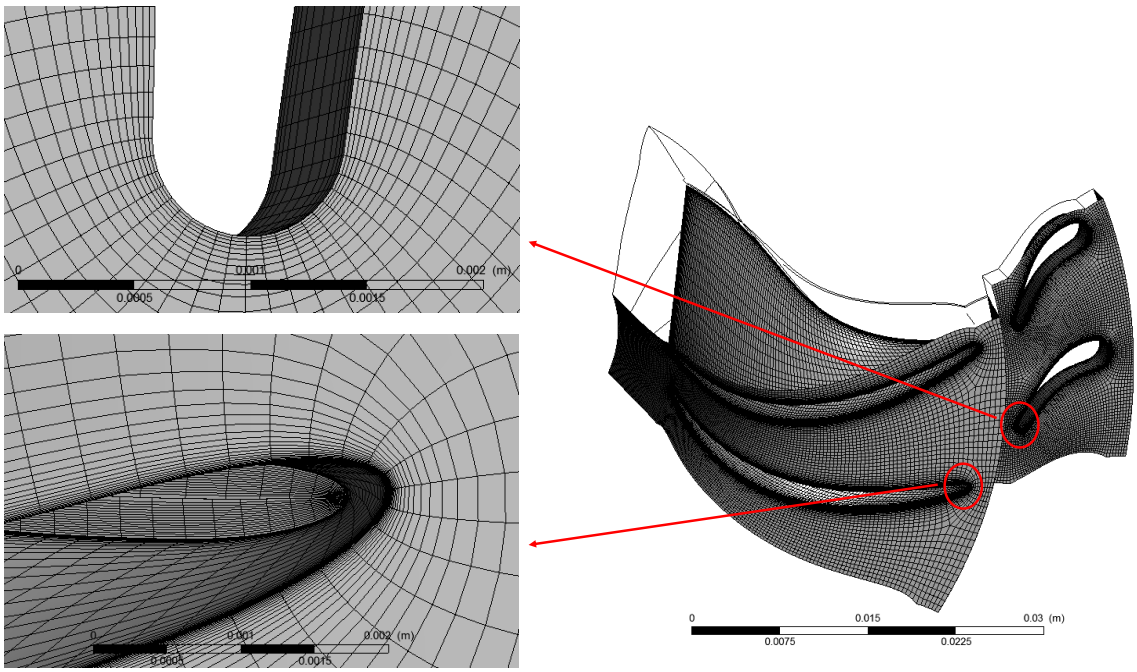

Figure 6-19: 3D mesh generation blade-to-blade passage for the ORC1 turbine

Figure 6-20 compares between the baseline and the improved designs of the ORC1 turbine in terms of the power and efficiency. The baseline design is improved by changing the number

of blades for the stator and the rotor, while the blade shape of the stator and the rotor were improved to reduce the losses and enhance the flow. The power of the ORC1 turbine is improved from 1303 to 1634 W, while the efficiency is increased from about 76% to about 89%. Figure 6-21 illustrates the effect of fluid mass flow rate on power and efficiency of the ORC1 turbine. The results showed that the turbine can work at high efficiency for mass flow rate ranging from 0.1 to 0.2 kg/s. Also, results show that the power is very sensitive to the mass flow rate, where it increases from 568 W at 0.1 kg/s to 2455 W at 0.2 kg/s.

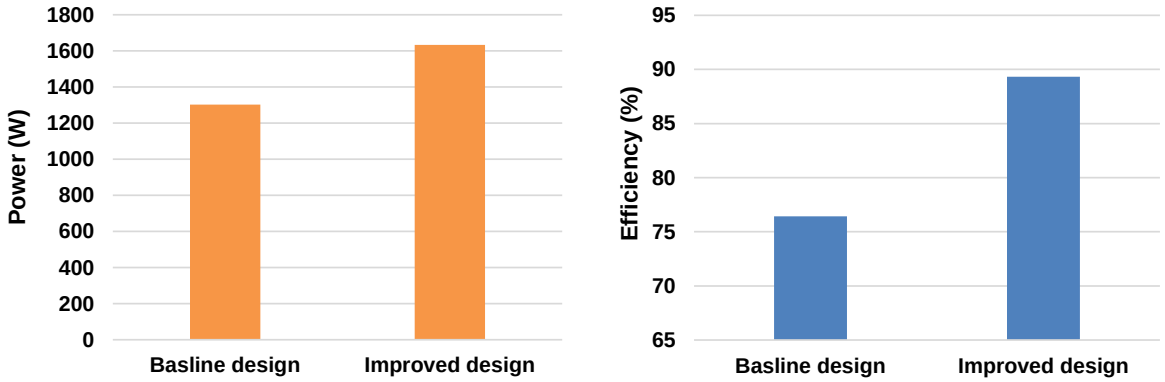

Figure 6-20: Power and efficiency of the baseline and the improved design of the ORC1 turbine

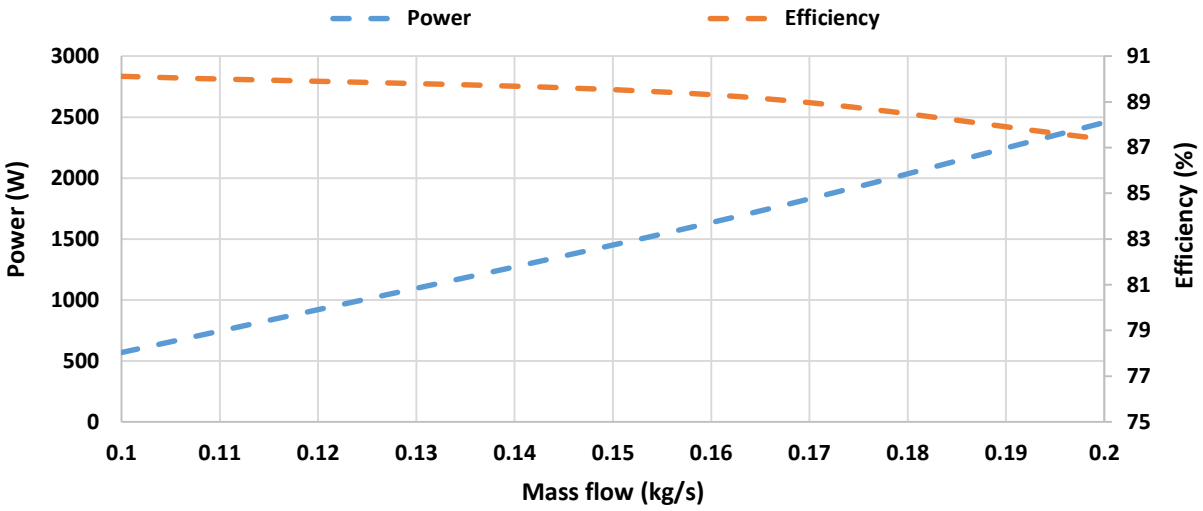

Figure 6-21: Effect of mass flow rate on power and efficiency of the ORC1 turbine

Figure 6-22 illustrates the effect of the rotational speed on power and efficiency of the ORC1 turbine. Generally, this turbine can work at high efficiency for a wide range of rotational speed (between 20000 and 30000 RPM) and as the speed increases, both power and efficiency increase. Figure 6-23 shows the effect of turbine inlet temperature on power generated and efficiency of the ORC1. It is clear that the turbine can work efficiently with a range of turbine inlet temperature between 328 and 348K. The power is affected noticeably by the inlet temperature, as it affects the turbine inlet enthalpy.

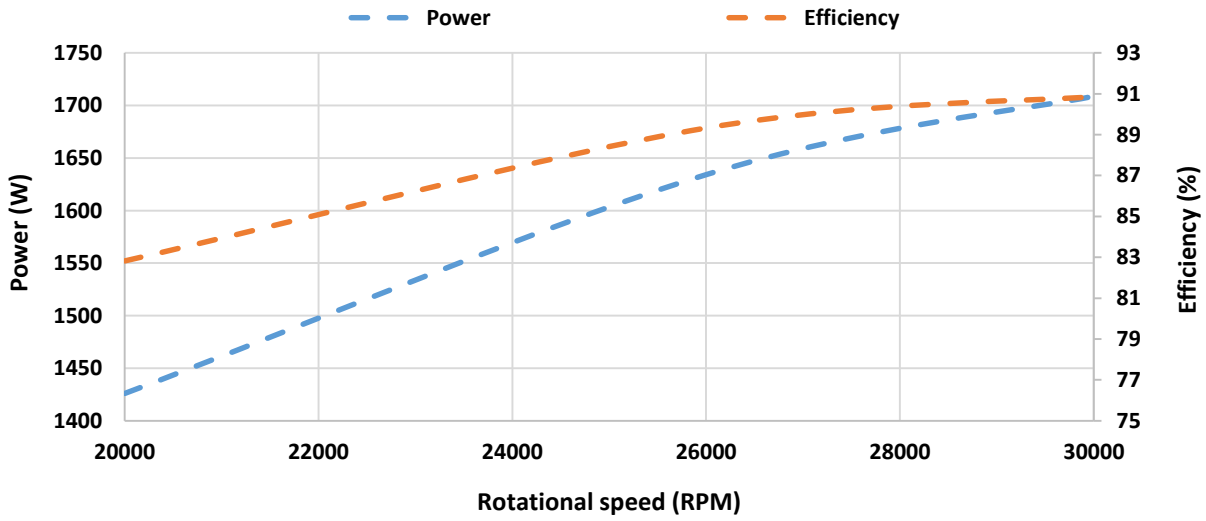

Figure 6-22: Effect of rotational speed on power and efficiency of the ORC1 turbine

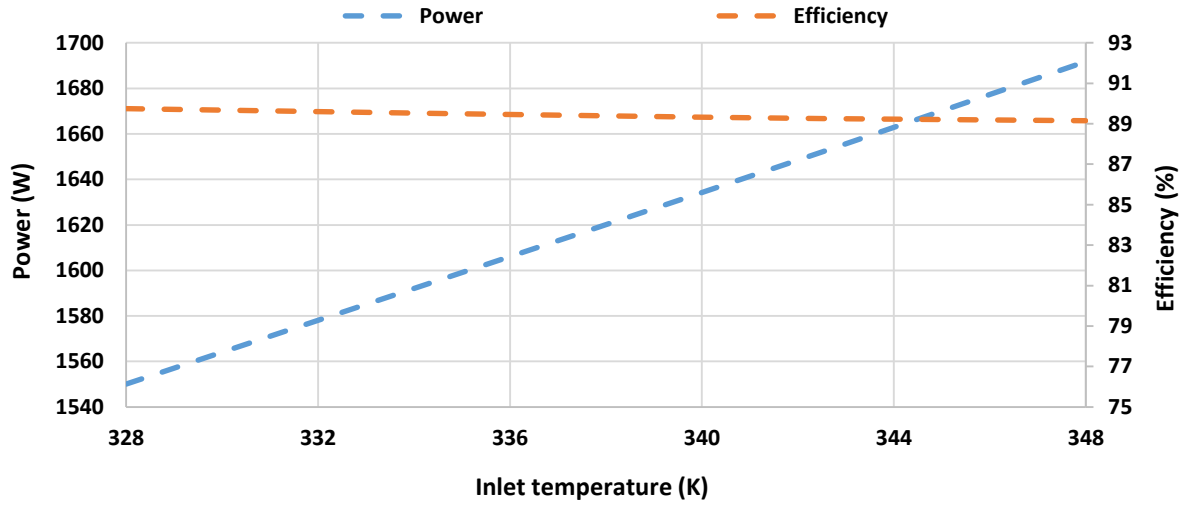

Figure 6-23: Effect of inlet temperature on power and efficiency of the ORC1 turbine

Figure 6-24 shows the velocity vectors (blade to blade view) at mid-span for the baseline, and the improved designs of the ORC1 turbine. The improved design has a smooth flow and less flow reversal in comparison to the baseline design, also the velocity at the trailing edge of the improved design is lower than that of the baseline design which means lower exit losses and higher efficiency. Figure 6-25 shows the pressure distribution (blade to blade view) at mid-span for the baseline and the improved designs of this turbine. The improved design contour shows less pressure dissipated to the rotor blades, which means low mechanical load is exerted on them.

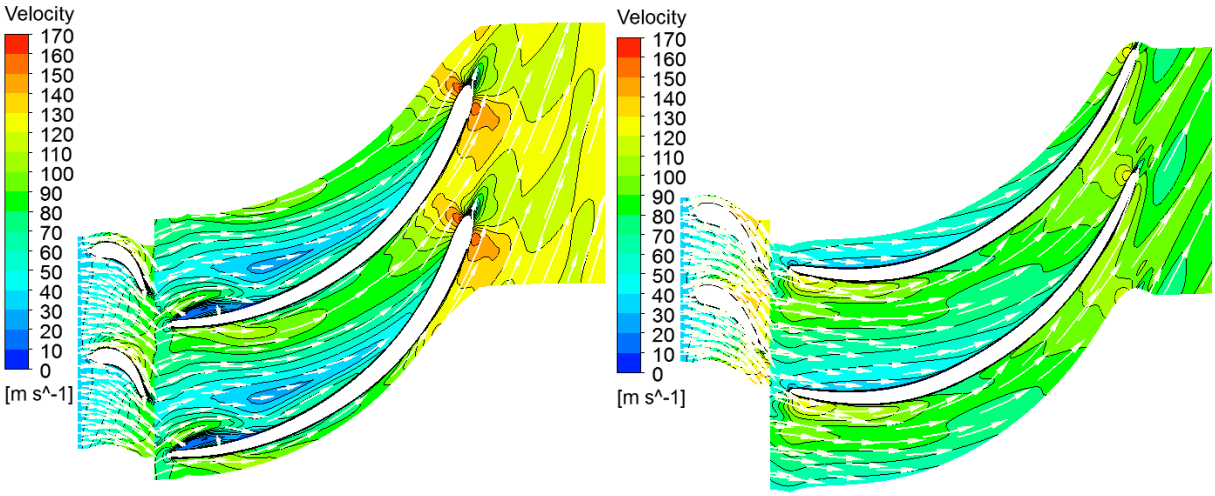

Figure 6-24: Velocity at mid-span for the baseline design (left), and the improved design (right) of ORC1 RIT

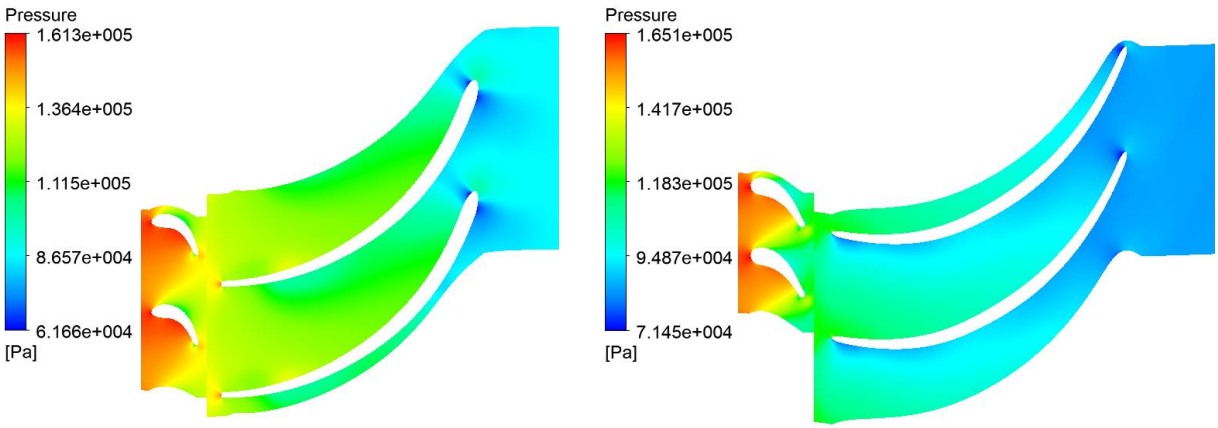

Figure 6-25: Pressure distribution at mid-span for the baseline design (left), and the improved design (right) of ORC1 RIT

Figure 6-26 shows the static entropy distribution at mid-span for the baseline and the improved designs of the ORC1 turbine. The improved design has a noticeably less entropy generation compared to that of the baseline design which leads to higher isentropic efficiency. Figure 6-27 shows the meridional Mach number for the baseline and the improved designs of the ORC1 turbine. Mach number is transonic for the baseline design, while it is subsonic for the improved design with a maximum value of 0.8 which occurred at the interspace between stator and rotor.

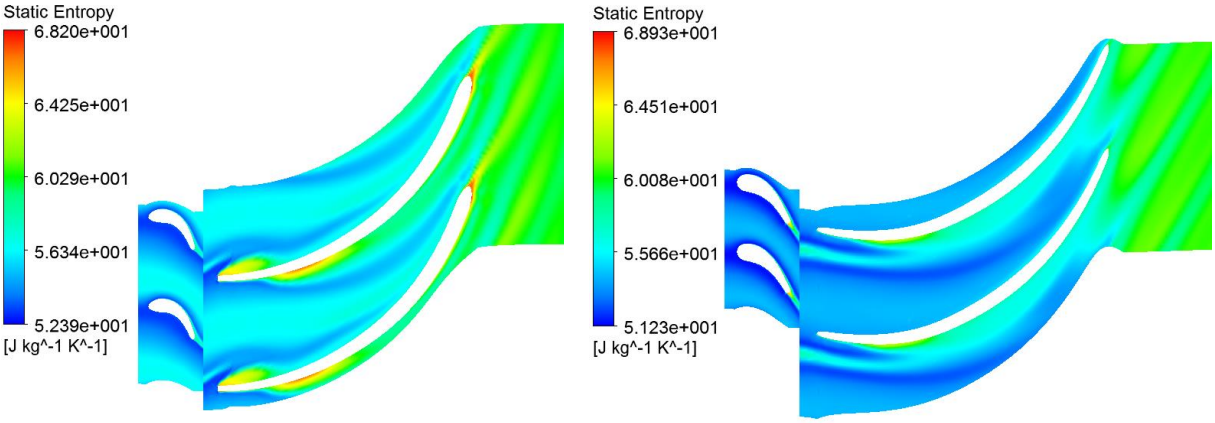

Figure 6-26: Static entropy at mid-span for the baseline design (left), and the improved design (right) of ORC1 RIT

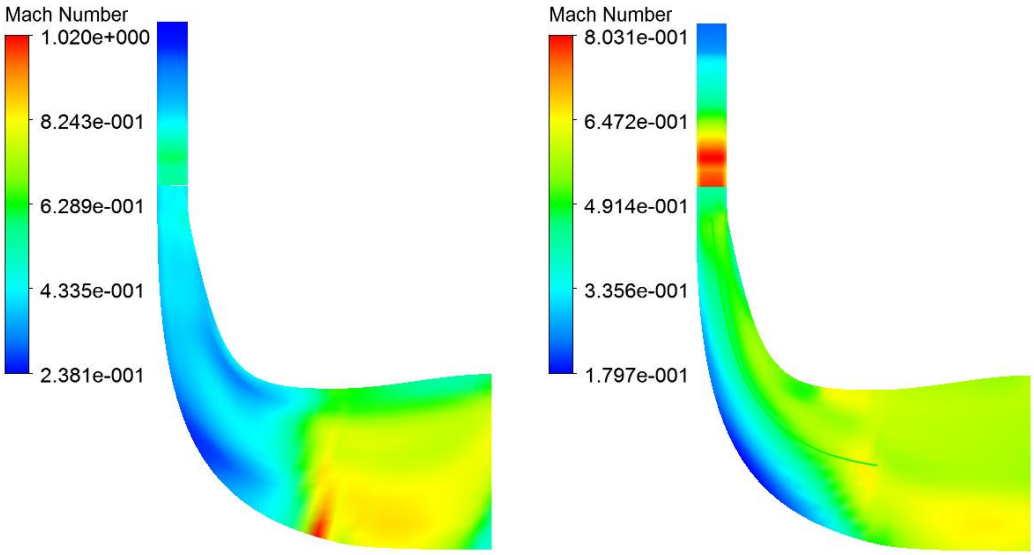

Figure 6-27: Meridional Mach number for the baseline design (left), and the improved design (right) of ORC1 RIT

Figure 6-28 shows the blade loading of the baseline and the improved designs of this turbine and results showed that the improved design has lower blade loading compared to the baseline design which is good to reduce the mechanical load applied to the rotor. Moreover, the improved design has better pressure profile with considerably larger area and the total net torque is larger because the improved design has a larger number of blades.

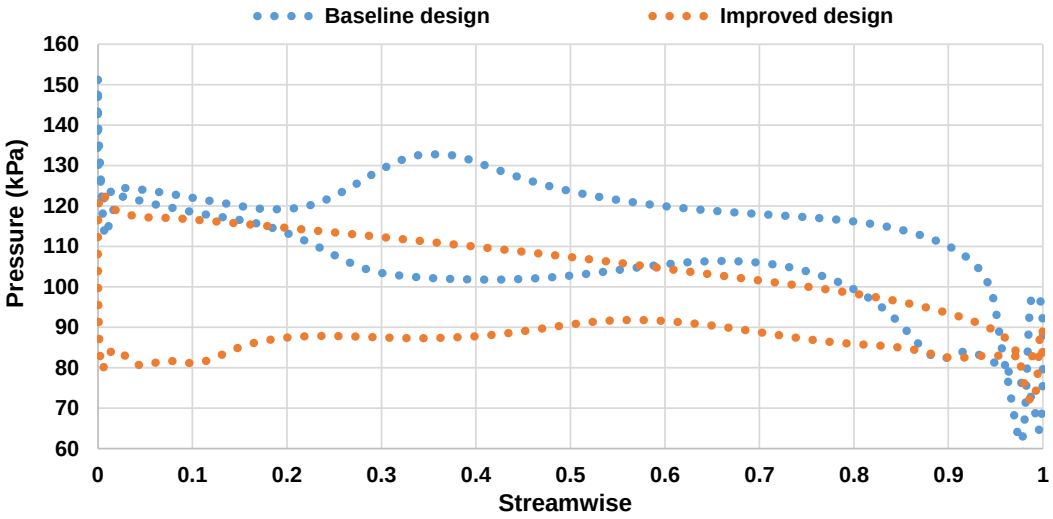

Figure 6-28: Blade loading at rotor mid-span for the baseline, and the improved designs of ORC1 RIT

6.4.3 ORC2 turbine

This small-scale RIT is developed to work efficiently with scenarios 2 and 4 of the integrated adsorption-ORC system for cooling and power discussed in Chapter 5 which has a relatively high-pressure ratio. Figure 6-29 shows two-dimensional and three-dimensional views of this turbine, while Figure 6-30 shows the three-dimensional mesh generation for the rotor and stator passages of the ORC2 turbine. One million nodes are used in this design; 500,000 for each of the stator and the rotor passages, while the mesh near the edges is refined to keep reasonable solution accuracy and computational cost.

Geometrically, ORC2 turbine differs from the ORC1 turbine in terms of many parameters like reference radius, shroud/hub exit and inlet radii, stator/rotor blade angles and number of blades. For example, ORC1 turbine has a reference radius of 33.3 cm with number of blades for stator and rotor of 24 and 16 respectively (see Figure 6-18), while ORC2 turbine has a reference radius of 34.3 cm with number of blades for stator and rotor of 26 and 30 respectively as shown in Figure 6-29.

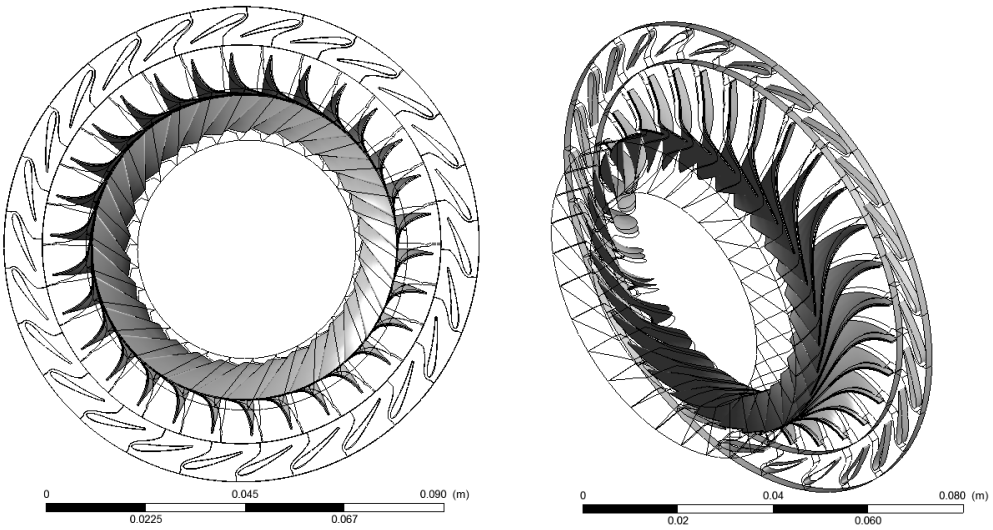

Figure 6-29: 2D and 3D views of the ORC2 RIT geometry

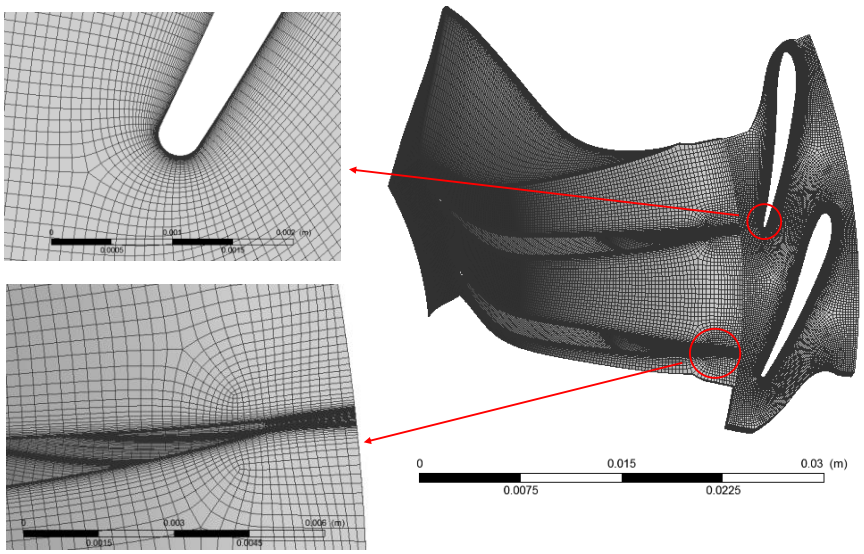

Figure 6-30: 3D mesh generation blade-to-blade passage for the ORC2 turbine

The baseline design is improved by changing the blades number for the rotor and the stator, also the shape of the blade (for both the stator and the rotor) is improved in order to enhance the flow through the turbine. Figure 6-31 shows that the improved design of the ORC2 turbine can outperform the baseline design with power and efficiency of 3556 W and 88% respectively compare to those of 2802 W and 68% respectively achieved by the baseline design. Figure 6-32 shows that ORC2 turbine can work efficiently through a mass flow rate ranging from 0.1 to 0.2 kg/s, however the power is very sensitive to the mass flow rate, where with 0.1 kg/s the turbine can generate 1331 W only, while with 0.2 kg/s the same turbine can generate 5289 W.

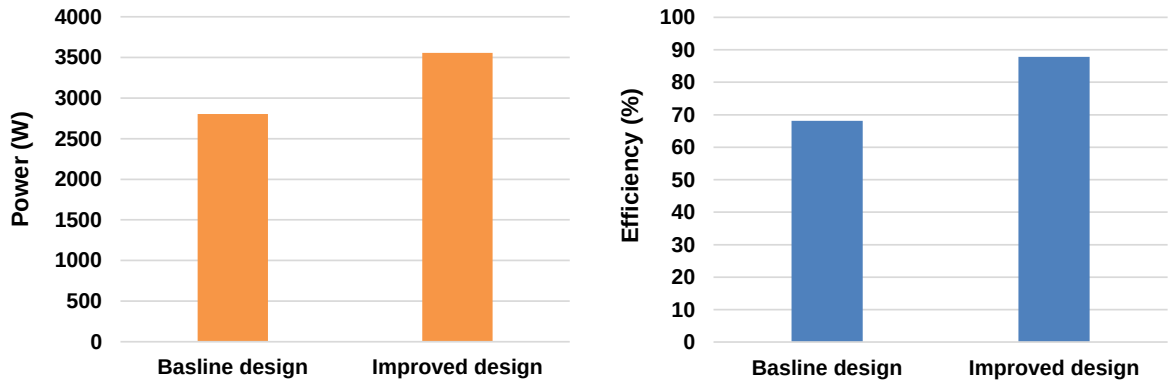

Figure 6-31: Power and efficiency of the baseline (initial design) and the improved design of the ORC2 turbine

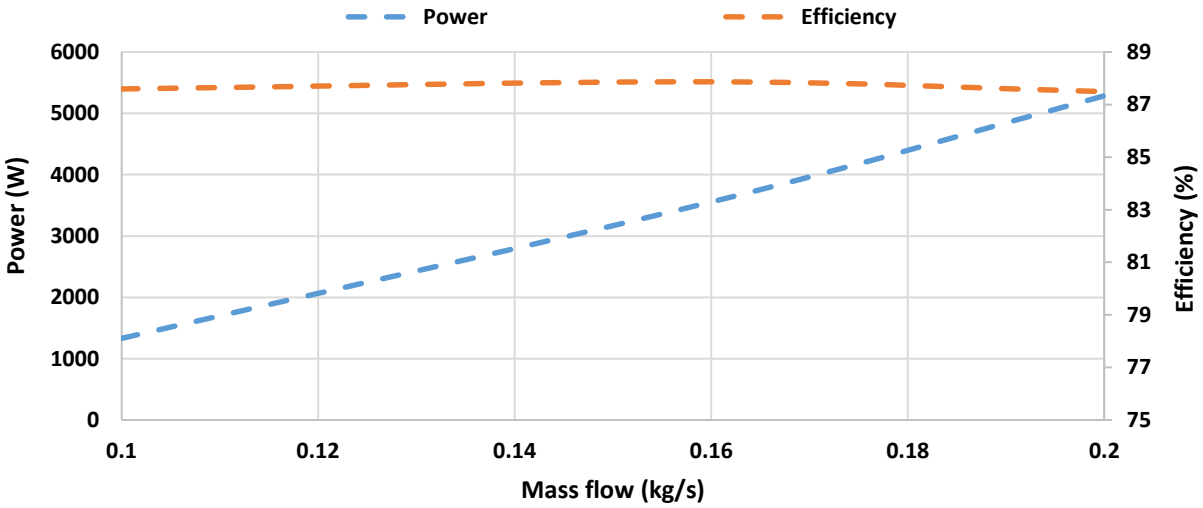

Figure 6-32: Effect of mass flow rate on power and efficiency of the ORC2 turbine

Figure 6-33 also shows that the turbine can work efficiently through a rotational speed ranging from 29000 to 39000 RPM. The power output ranges from 3448 W at 29000 RPM to 3584 W at 36000 RPM, while the efficiency ranges from 80.5% at 29000 RPM to about 88% at 39000 RPM.

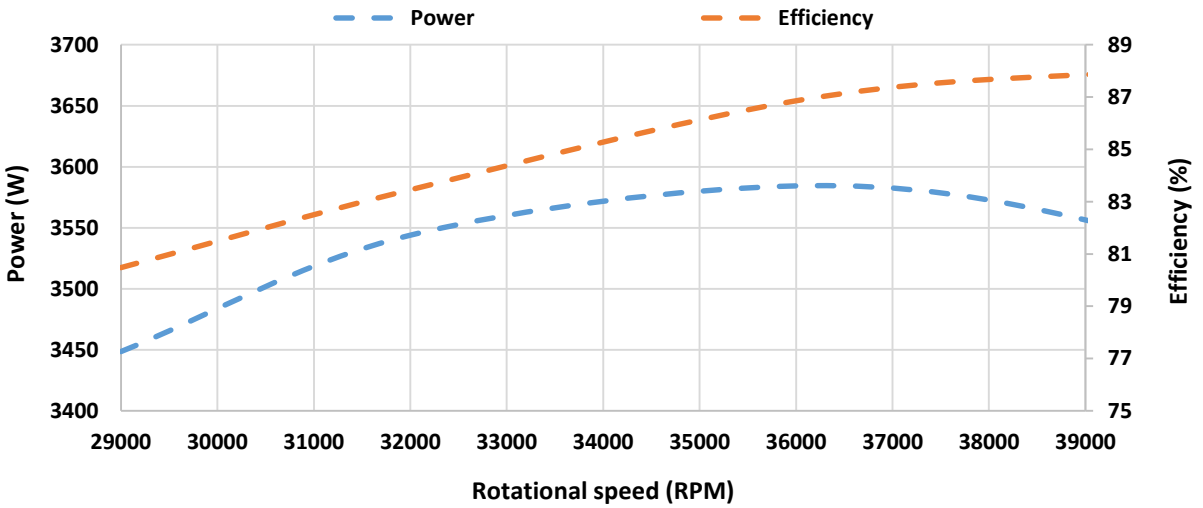

Figure 6-33: Effect of rotational speed on power and efficiency of the ORC2 turbine

Figure 6-34 shows that the velocity vectors (blade to blade view) at mid-span for the baseline, and the improved designs of the ORC2 turbine. The improved design contour shows better flow (homogeneous flow) and less flow reversal compared to the baseline design contour which shows a vortex generation.

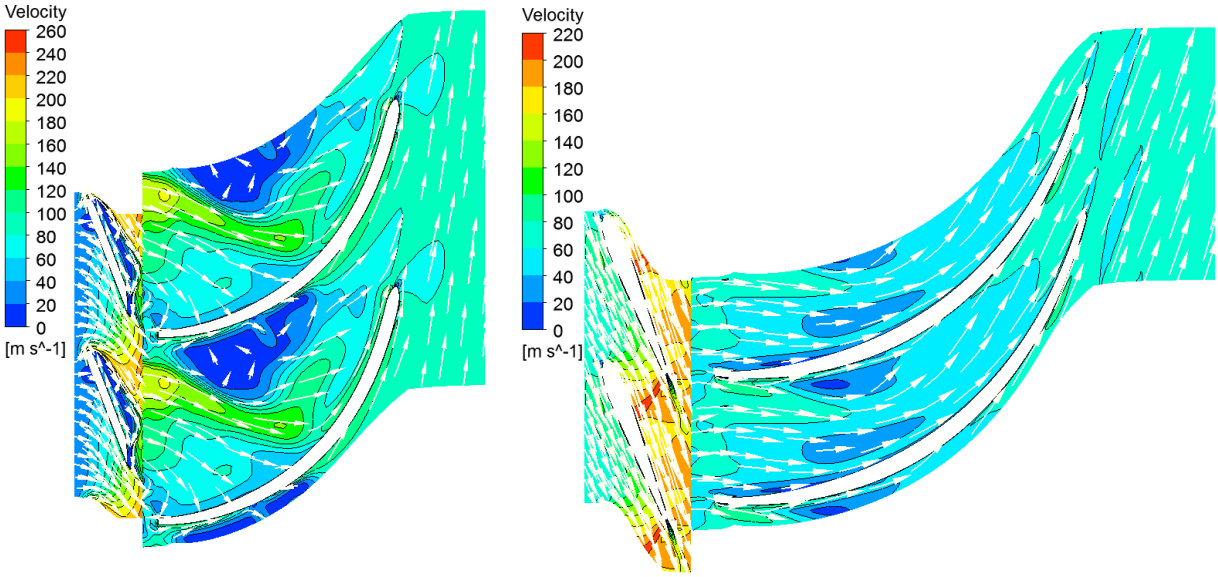

Figure 6-34: Velocity at mid-span for the baseline design (left), and the improved design (right) of ORC2 RIT

Figure 6-35 shows the pressure distribution (blade to blade view) at mid-span for the baseline and the improved designs of the ORC2 turbine. The improved design shows better pressure distribution than that of the baseline design where less pressure applied to the rotor blades, which means low mechanical load is exerted on them. Figure 6-36 shows the static entropy distribution at mid-span for the baseline and the improved designs of the ORC2 turbine. The improved design has less entropy generation compared to that of the baseline one which means fewer losses and higher isentropic efficiency. The baseline contour shows higher entropy generation because of the viscous shear force that is dominant through the baseline passage.

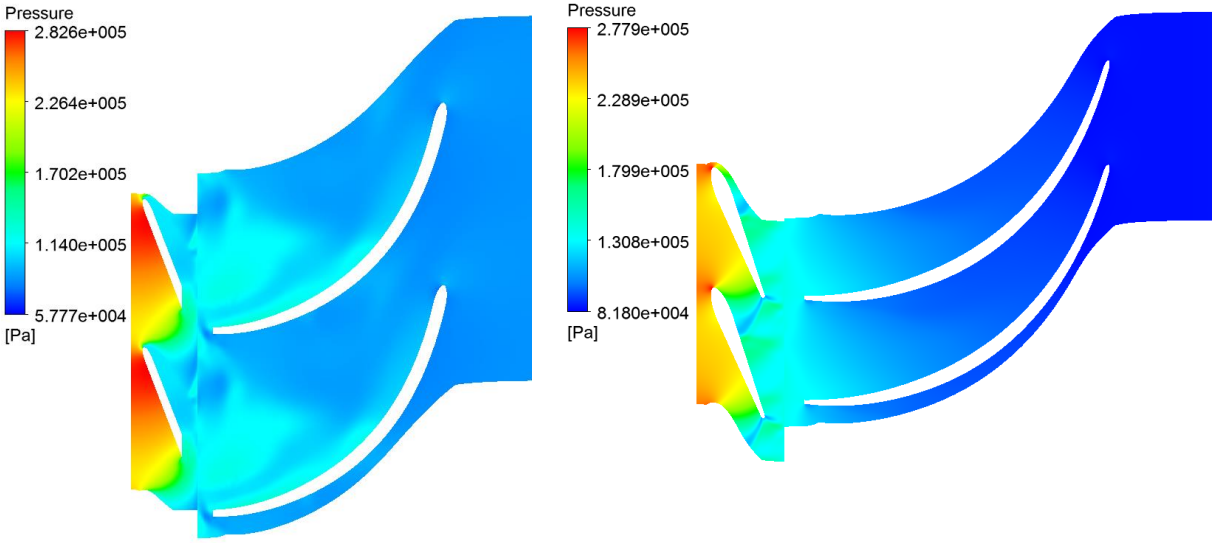

Figure 6-35: Pressure distribution at mid-span for the baseline design (left), and the improved design (right) of ORC2 RIT

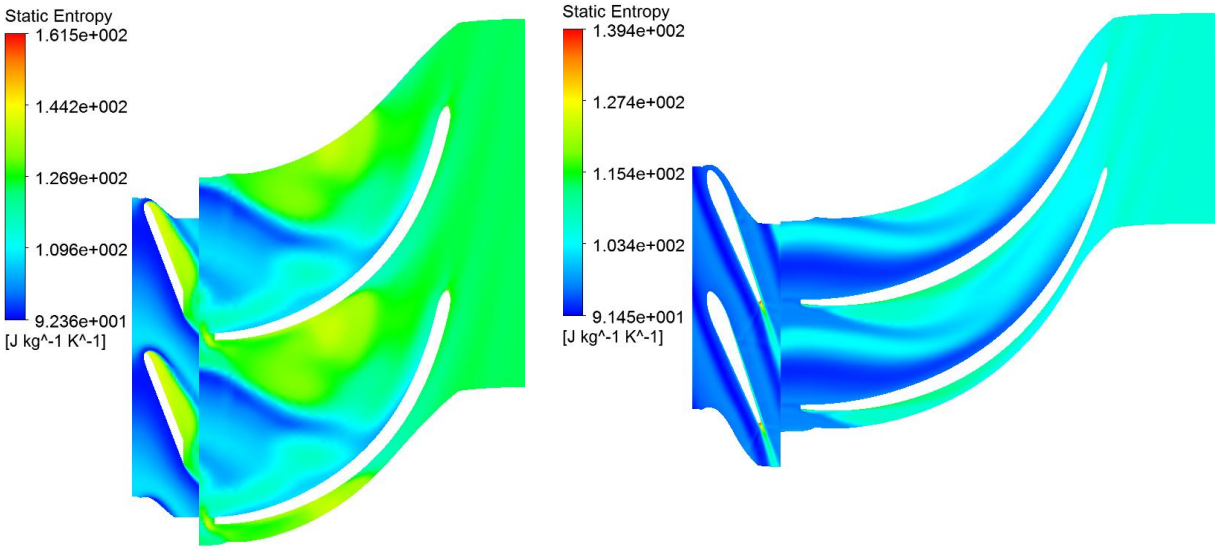

Figure 6-36: Static entropy at mid-span for the baseline design (left), and the improved design (right) of ORC2 RIT

Figure 6-37 shows the meridional Mach number for the baseline and the improved designs of the ORC2 turbine. The two contours show that Mach numbers have values higher than one with supersonic expansion at stator exit and rotor inlet and this is because of the high-pressure ratio of the design point. The Mach number of the improved design is slightly higher than one however, it has no important influence on the turbine performance as it still has high power and efficiency of 3556 W and 87.86%. Organic fluids easily turn into supersonic with the choked flow at stator throat, and this is because of the low sound speed associated with high density and molecular mass organic fluids.

Figure 6-38 shows the blade loading at rotor mid-span for the baseline and the improved designs of the ORC2 turbine. The improved design shows better pressure profile with lower blade loading compared to the baseline design. Even though the improved design has smaller enclosed area compared to the baseline one, the latter has larger total torque as it has a larger number of blades of 30 blades compared to 13 for the baseline design.

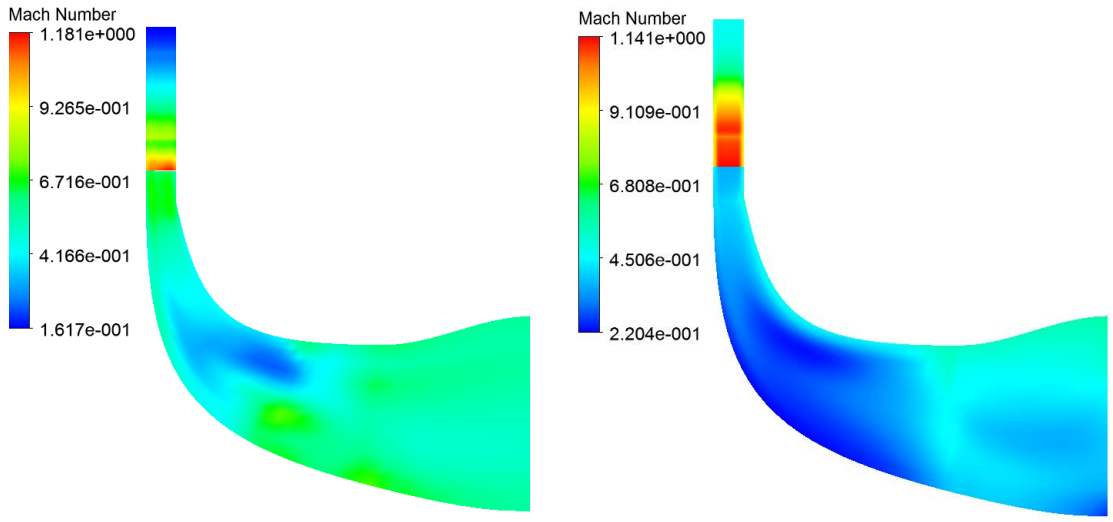

Figure 6-37: Meridional Mach number for the baseline design (left), and the improved design (right) of ORC2 RIT

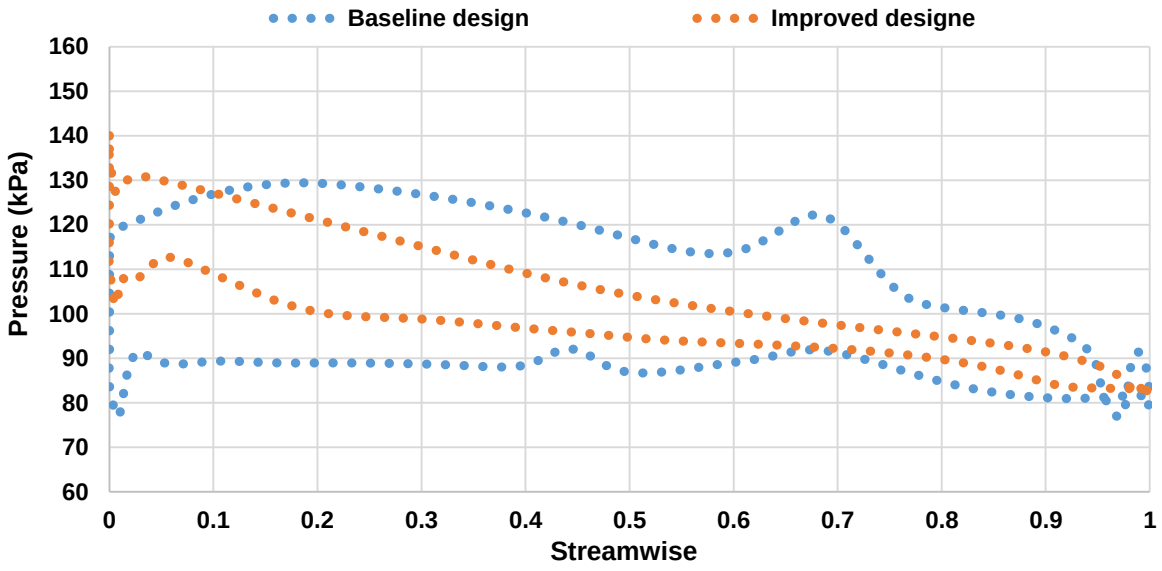

Figure 6-38: Blade loading at rotor mid-span for the baseline, and the improved designs of ORC2 RIT

Table 6-2 summarises the performance results for Steam, ORC1, and ORC2 turbines including input and output parameters.

Table 6-2: Summary of the performance results for Steam, ORC1, and ORC2 turbines

Steam turbine		
Mass flow rate	0.0160	kg/s
Total pressure ratio	3.4156	-
Isentropic efficiency %	85.0311	-
Polytropic efficiency %	83.0821	-
Rotation speed	69000	RPM
Shaft power	2590.0000	W
Reference radius	0.0648	m
Nozzle efficiency %	83.4061	-
Number of blade (stator)	26	-
Number of blade (rotor)	18	-
ORC1 turbine		
Mass flow rate	0.1600	kg/s
Total pressure ratio	1.7753	-
Isentropic efficiency %	89.3192	-
Polytropic efficiency %	89.1759	-
Rotation speed	26000	RPM
Shaft power	1634.2300	W
Reference radius	0.0333	m
Nozzle efficiency %	91.3061	-
Number of blade (stator)	24	-
Number of blade (rotor)	16	-
ORC2 turbine		
Mass flow rate	0.1600	kg/s
Total pressure ratio	2.9647	-
Isentropic efficiency %	87.8626	-
Polytropic efficiency %	87.3270	-
Rotation speed	39000	RPM
Shaft power	3556.4500	W
Reference radius	0.0433	m
Nozzle efficiency %	82.2004	-
Number of blade (stator)	26	-
Number of blade (rotor)	30	-

6.5 Summary

In this chapter detailed designs for three small-scale radial inflow turbines namely Steam, ORC1 and ORC2 have been developed to work efficiently with the adsorption system for cooling and electricity (ASCE) and the integrated adsorption-ORC system for cooling and electricity (IAOSCE). The baseline design (for each turbine) is developed using VISTA RTD ANSYS@^{2018}, then this design is improved by using detailed 3D CFD simulation using ANSYS@^{2018} Workbench BladeGen tool where different number of blades and different blade profile for the stator and the rotor are used to improve the turbine performance (power and efficiency).

CFD results show that the three designed turbines have high performance in terms of power and efficiency using a range of rotational speed and fluid mass flow rate. Modelling results show that a steam radial inflow turbine can be designed to meet the requirements of the ASCE with maximum power and efficiency of 2590W and 85% respectively. Also, additional two ORC radial inflow turbines can be designed to meet the requirement of the different scenarios of the IAOSCE. For the ORC1 turbine, results show that the CFD design has maximum power and efficiency of 1634 W and 89% respectively so that this turbine can work efficiently with scenarios 1and 3 (with low-pressure ratio). For the ORC2 turbine, results show that the CFD design has maximum power and efficiency of 3556 W and 88% respectively and this turbine work efficiently with scenarios 2 and 4 (with high-pressure ratio).

CHAPTER SEVEN

EXPERIMENTAL FACILITY AND VALIDATION

7.1 Introduction

Adsorption cooling and Organic Rankine Cycle (ORC) systems are promising technologies that can utilise the abundant low-grade heat sources such as solar thermal energy and geothermal energy [98, 232]. This chapter experimentally investigates the feasibility of integrating adsorption cooling system with an ORC to generate power and cooling at the same time. Two different scenarios (scenario 1 and scenario 2) are investigated experimentally at various heat source temperatures. In scenario 1, ORC can be powered using the waste heat of the adsorption system (by using the return cooling line) and no additional heat is used, while in scenario 2, ORC can be powered using the hot line leaving the adsorption system. The two scenarios are compared to each other in terms of COP, SCP, SP. COPe, and SCPe.

7.2 Description of the test facility

The test facility consists of two systems namely; two-bed adsorption cooling system and Organic Rankine Cycle (ORC) system. The adsorption system contains two adsorber beds, condenser, and evaporator, while the ORC system contains condenser, evaporator, pump and turbine. Figure 7-1 shows a pictorial diagram, while Figure 7-2 shows a schematic diagram of the test facility including the connection between the adsorption system (topping system)

and the ORC system (bottoming system). The hot fluid circulation system used in this test facility consists of hot water tank with an electrical heater with a capacity of 18 kW, hot water pump, valves and pipes, while, the cooling system consists of cold water tank fitted with a heater capacity of 3 kW and connected directly to the mains and drain. The cooling system is fitted with a controller to keep the water at a constant temperature ranging between 15 and 50 °C. Adsorption and ORC condensers are connected to another cold water tank as shown in Figure 7-2. To keep the temperature of chilled water provided to the adsorption system evaporator constant, the evaporator is connected to chiller/heater unit.

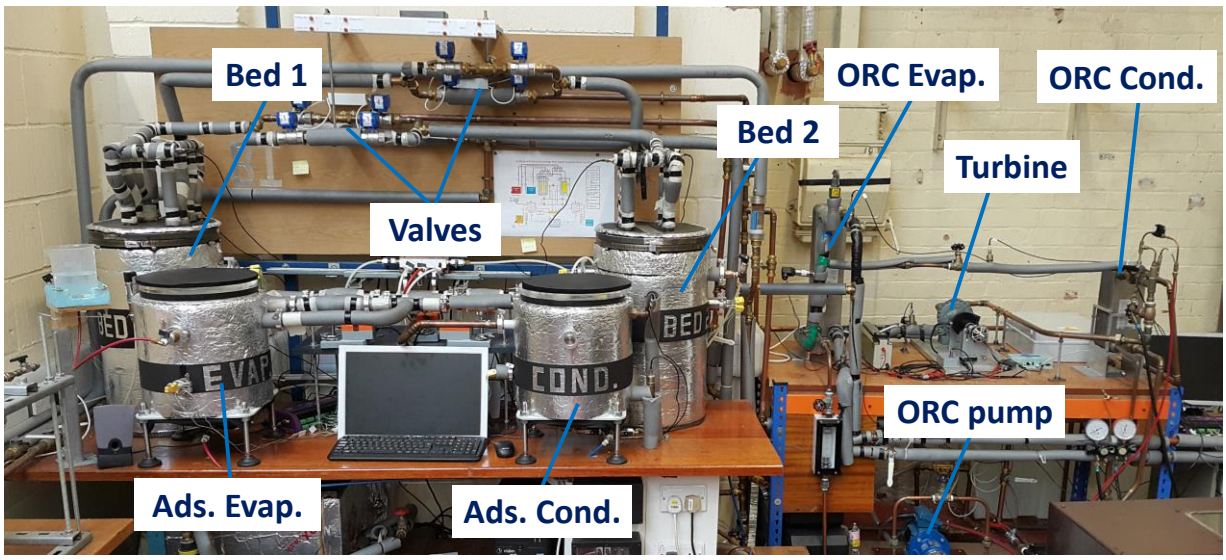

Figure 7-1: Experimental facility of the integrated adsorption-ORC system for cooling and power generation

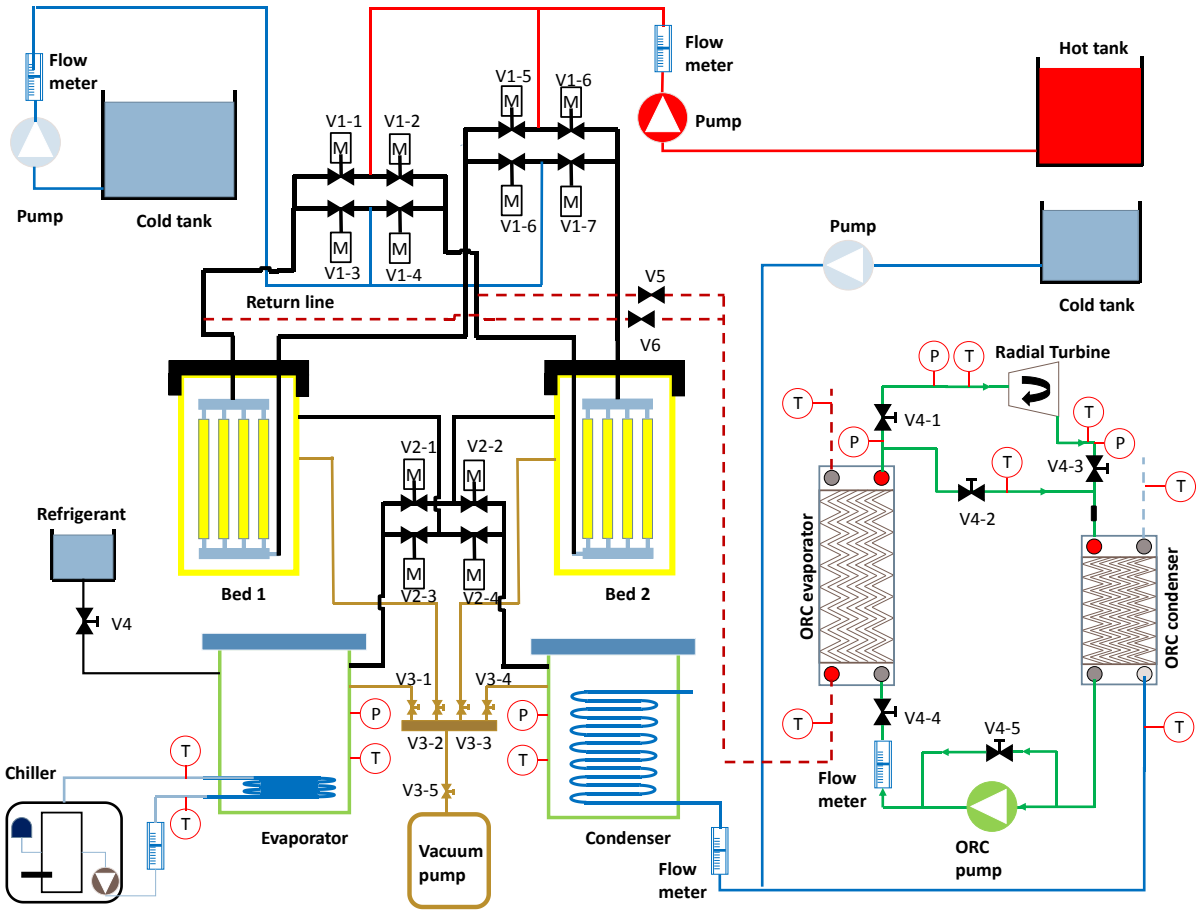

Figure 7-2: Schematic diagram of the experimental facility of the integrated adsorption-ORC system

7.2.1 Experimental procedure

Experimental work was carried out with the aim of validating the numerical model against the experimental results utilising two different scenarios. Also, to study the effect of various heat source temperatures on the system performance of the two scenarios adopted with the integrated adsorption-ORC test facility. Three different heat source temperatures were applied namely 75, 85 and 95 °C, while an average cooling water temperature of about 24 °C is applied for the adsorber bed cooling. The cooling water temperature of 16 °C is applied at the condenser, while the chilled water is kept at 8 °C. The experimental facility works automatically using an electronic controller and LabVIEW software. The flow rate of the bed heating water, bed cooling water, condenser cooling water and evaporator chilled water are

controlled to be constant. Heating water is fed to the adsorber bed from the main hot tank as shown in Figure 7-2. To start the test facility the following steps were carried out:

1. Checking the levels of water in the hot and cold tanks to ensure that the pumps can work properly.
2. Setting the thermostats of the cold and hot water tanks.
3. Running the LabVIEW software and setting the adsorption time, switching time and the number of required cycles as shown in Figure 7-3.
4. Setting the flow rates of the cold and hot water to the desired values.
5. Starting the heater/chiller circulating unit and open its valves.
6. Starting the experiment and then recording the data.

7.3 Adsorption cooling system

Adsorption system is the topping cycle in this experimental facility and it consists of the following main components:

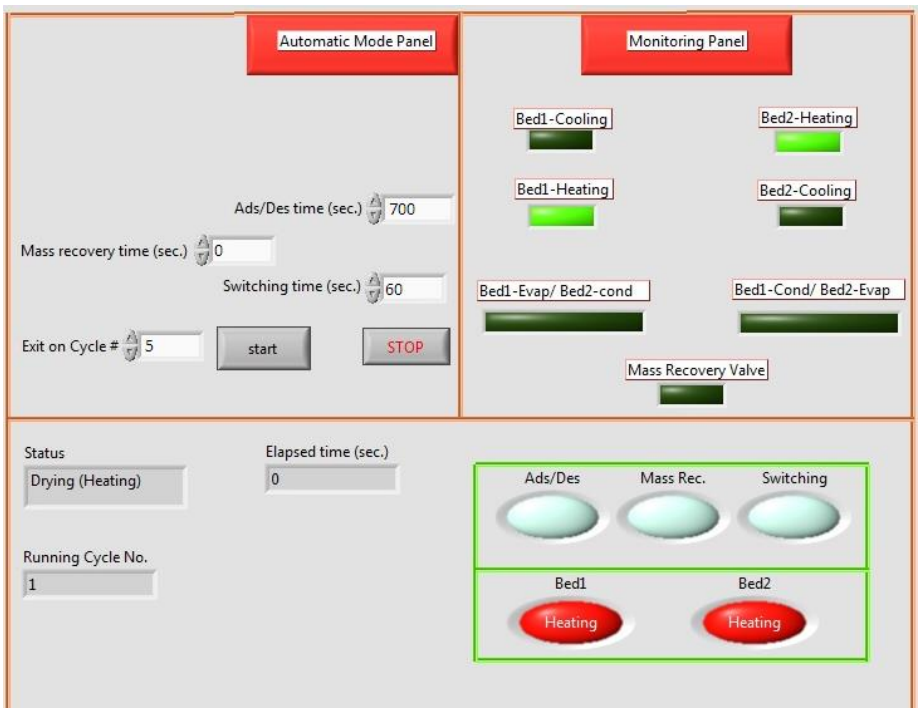

Figure 7-3: Operating interface in the LabVIEW software

7.3.1 Adsorber bed

Adsorber bed is one of the key components of this experimental facility and it consists mainly of three parts: heat exchangers, shell, and cover or lid. Two finned tube type heat exchangers with a rectangular shape (manufactured by Weatherite Air conditioning Ltd) are packed with granules of CPO-27(Ni) MOFs adsorbent material and they are fitted inside the bed cylinder as shown in Figure 7-4 [70]. Each adsorbent bed consists of four modules and each module has the dimensions of 0.45m × 0.172m with 6 copper tubes of 15.87mm diameter and it was weighted before and after the packing process. A piece of metal mesh was cut with appropriate size and stuck to one side of the module. After that, the adsorbent granules are packed into the module and spread gently by patting them till filling the gap between the fins of the heat exchanger. During packing process, shaking the module heat exchanger is used to ensure that the adsorbent granules are filling all the gaps. After that, the other side of the module heat exchanger can be covered with another metal mesh sheet as shown in Figure 7-5 to prevent the adsorbent material from falling out of the heat exchanger. In the end, each adsorber bed contains an average value of 1.05 kg of CPO-27(Ni).

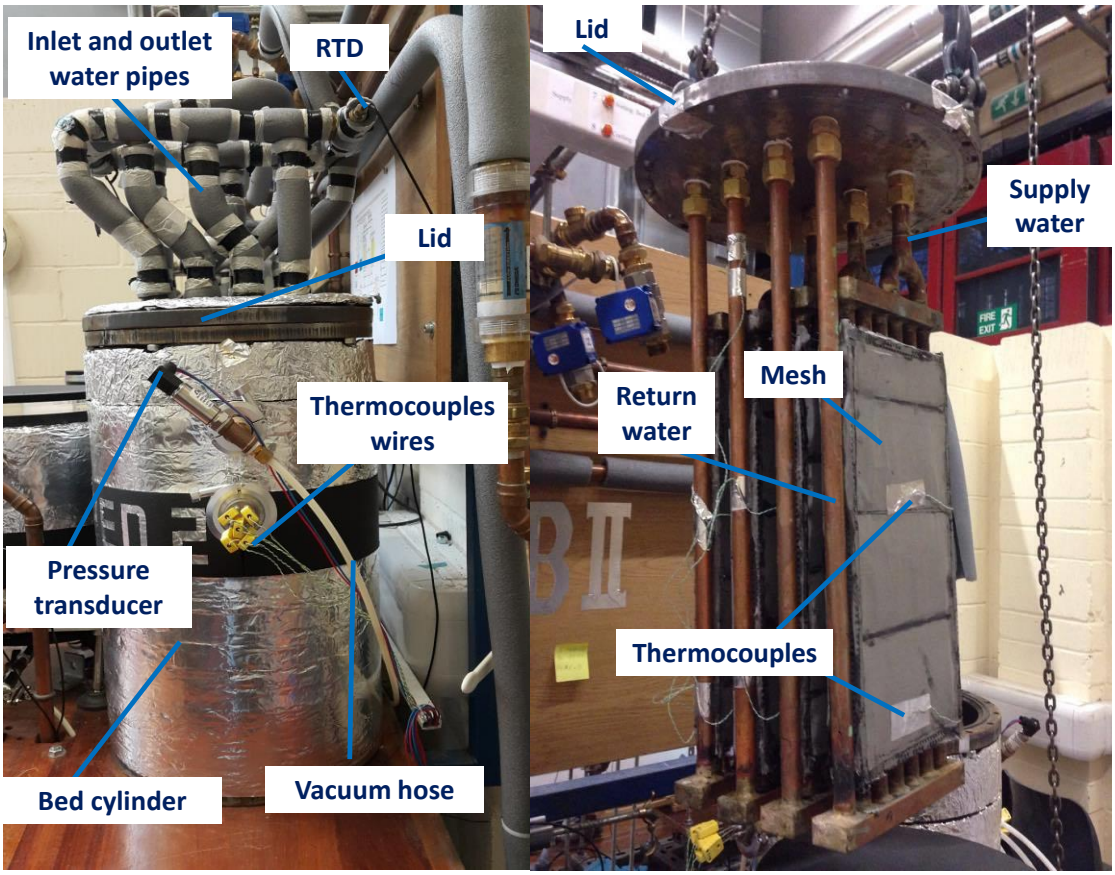

Figure 7-4: components of the adsorber bed

To obtain the required vacuum seal, an O-ring of 3 mm diameter made from rubber is placed in the groove on the frontal plate of the bed cylinder. The lid of the adsorption cylinder contains 8 holes for the fitting of the module heat exchangers.

In this study each bed cylinder has four vacuum KF fittings, to be used for connecting thermocouples, pressure transducers, vacuum pump, and refrigerant flow line. A thermal insulation material with 20mm thickness is used to insulate the bed, the condenser and the evaporator.

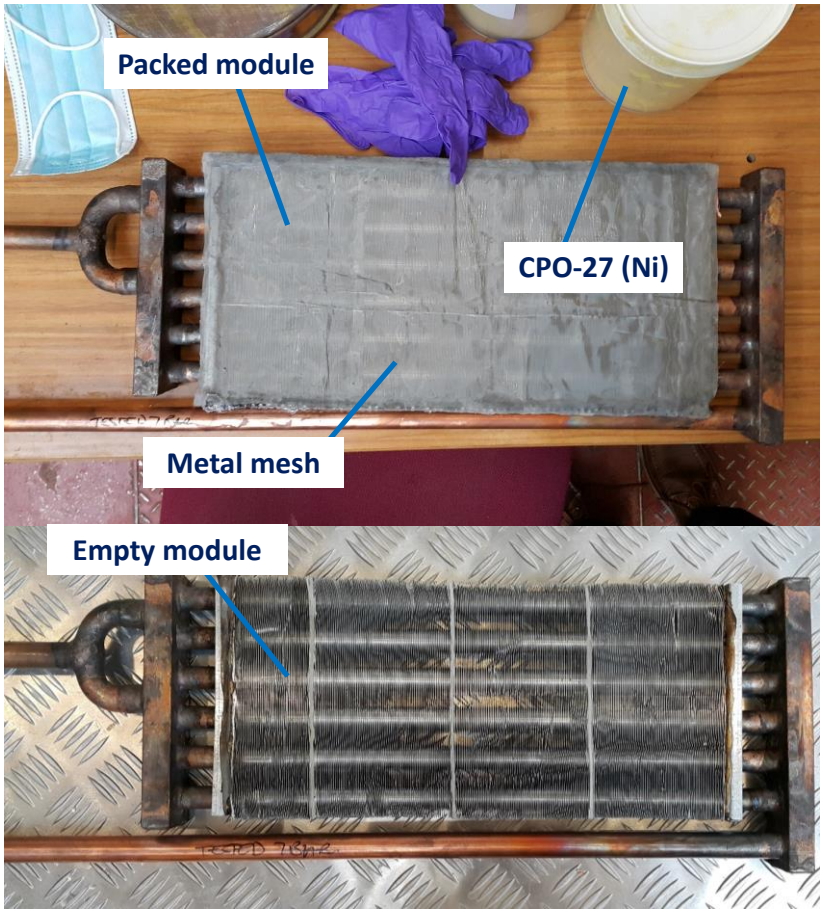

Figure 7-5: Adsorption system packing

Each module heat exchanger is provided with supply and return water pipes to cool/heat the adsorber bed through adsorption/desorption processes. Figure 7-6 shows how the thermocouples are connected to each adsorber bed using vacuum KF clamp fitting for thermocouples connection to prevent any leakage.

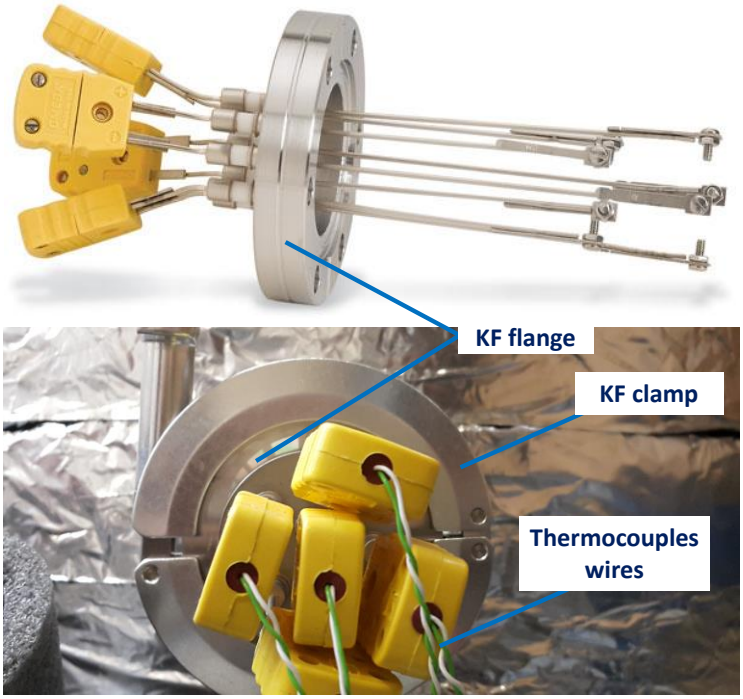

Figure 7-6: KF clamp fitting vacuum thermocouples used with adsorber bed, condenser and evaporator

7.3.2 Adsorption condenser

Adsorption condenser is one of the key parts of the adsorption system which consists of a stainless steel cylinder with diameter and height of 320mm and 340mm respectively, a transparent lid, sealing gasket, copper coil and inlet and outlet water tubes as shown in Figure 7-7. The condenser is connected to the adsorber beds via a motorised valve and it is connected to the evaporator using a throttling valve. The motorised valve is used to connect the condenser to the adsorber bed operating in desorption mode, while the throttling valve controls the flow from the condenser to the evaporator to generate continuous cooling. The condenser copper coil is connected to the heater/chiller unit which supplies chilled water at constant temperature. The condenser is also, linked to the drain line using a discharge hose to enable cleaning the condenser or discharging any excess water.

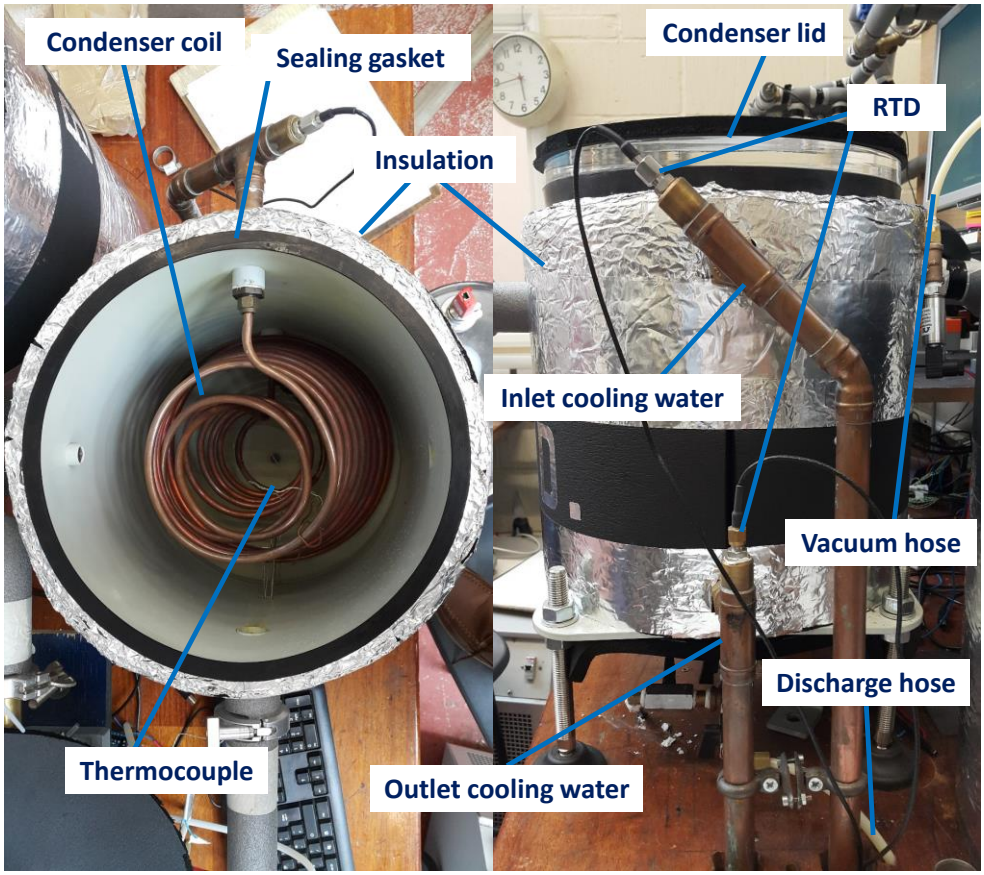

Figure 7-7: Adsorption condenser

7.3.3 Adsorption Evaporator

Similar to the condenser, adsorption evaporator is an important part where the cooling is generated. It consists mainly of a stainless steel cylinder with diameter and height of 320mm and 340mm respectively, a transparent lid, sealing gasket, and copper tube coil as shown in Figure 7-8. The evaporator is connected to the adsorber beds using a motorised valve and to the condenser via a throttling valve. The motorised valve controls the flow of water vapour from the evaporator to the bed operating in adsorption process. The evaporator copper coil is connected to the heater/chiller unit which supplies chilled water at controlled constant temperature.

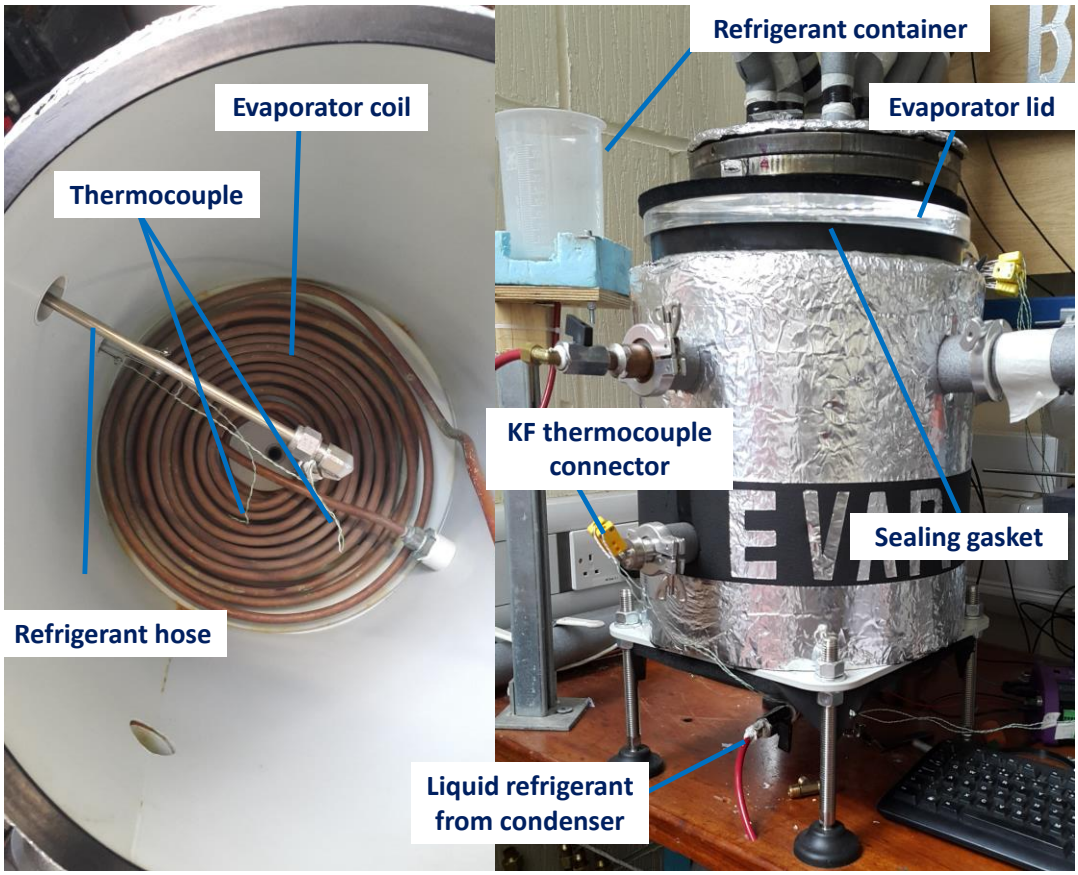

Figure 7-8: Adsorption evaporator

7.3.4 Chiller/heater unit

To keep the chilled water temperature entering the evaporator constant, chiller/heater unit is used (see Figure 7-9). This unit is developed by Betta-Tech Company (model number of CU 700 LT) for laboratory-based applications, where the cooling/heating liquid can be cooled or heated to temperatures ranging from -35°C to +70°C. In this study, the chiller/heater unit is set at 8 °C, while the mass flow rate is set at 5 liter/min.

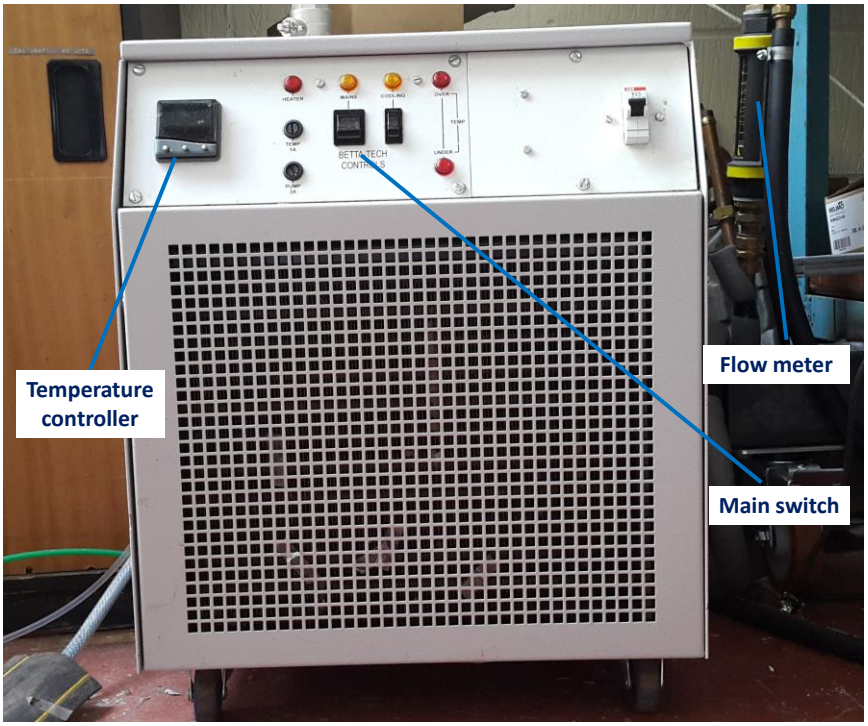

Figure 7-9: Chiller/heater unit

7.3.5 Vacuum pump unit

A vacuum pump unit as shown in Figure 7-10 is used in this experimental facility to maintain the pressure inside the adsorption system at the required level. The oil lubricated pump unit is manufactured by DVP vacuum technology (Type LC106) and has an electrical motor with a capacity of 2.2 kW installed within the unit and connected via a flexible drive coupling. The oil system is easy to check and refill with a sealing device to prevent the oil from depletion. The unit is suitable for continuous operation pressure ranging from 400 to 0.1 mbar. The vacuum pump is connected to all components of the adsorption system including adsorber beds, condenser, and evaporator via a vacuum manifold using separate valves which enables vacuuming each component independently.

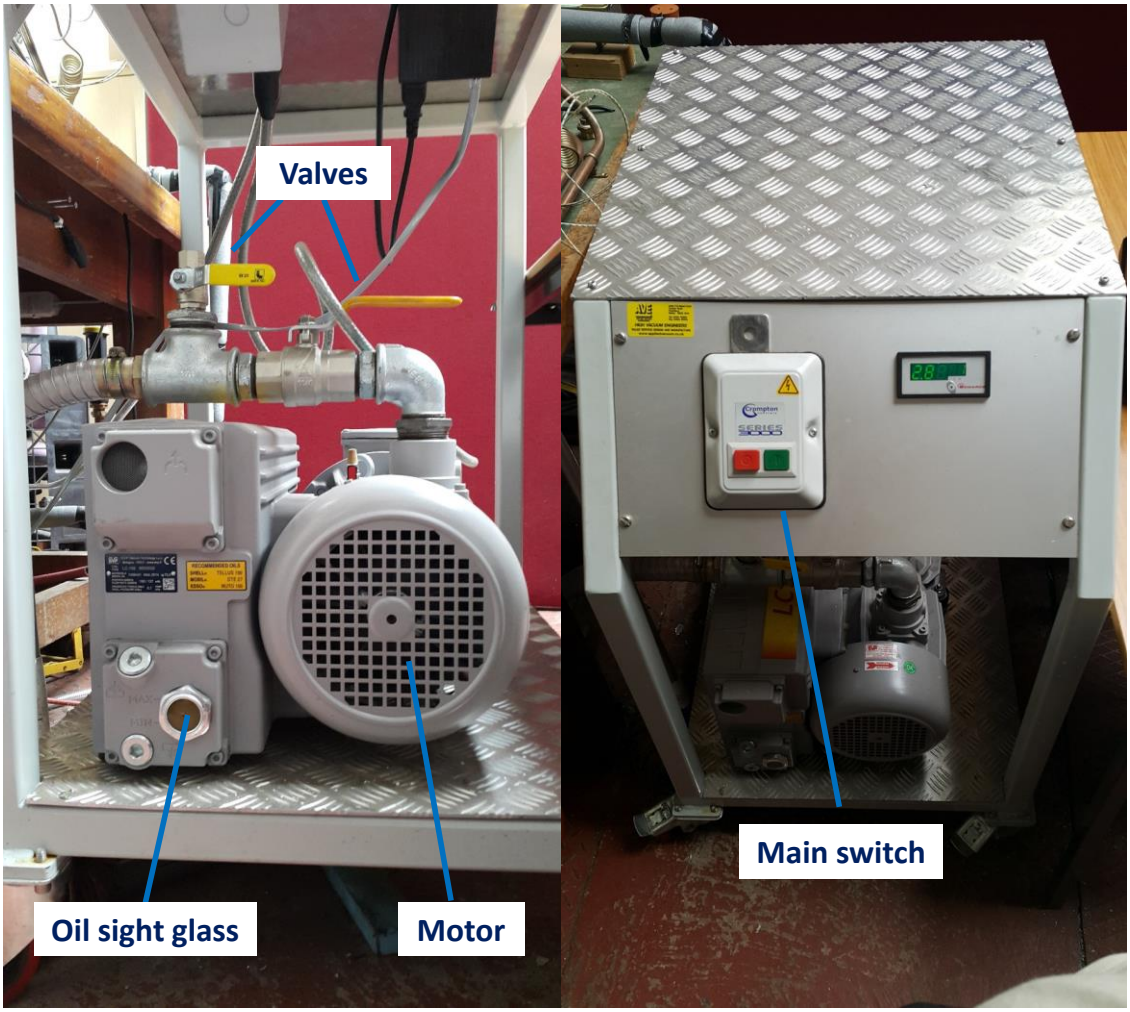

Figure 7-10: Vacuum pump unit

7.3.6 Vacuum manifold

A vacuum manifold is used to connect each component of the adsorption system to the vacuum pump and to the atmosphere or to the drain. The manifold has 8 different valves and connects the adsorption system to the vacuum unit using 1/6″ plastic hoses. Figure 7-11 shows the manifold used in this test facility, where valve V3-5 connects the system to the vacuum pump. Valves V3-1, V3-2, V3-3 and V3-4 are connected to the evaporator, bed 1, bed 2 and the condenser respectively, while V3-6 and V3-7 are connected to the drain and the atmosphere pressure respectively. This manifold unit is used to vacuum the system

components to the required vacuum pressure (in the range of 5-10 kPa) and dry the system from any previous refrigerant before starting any experiment.

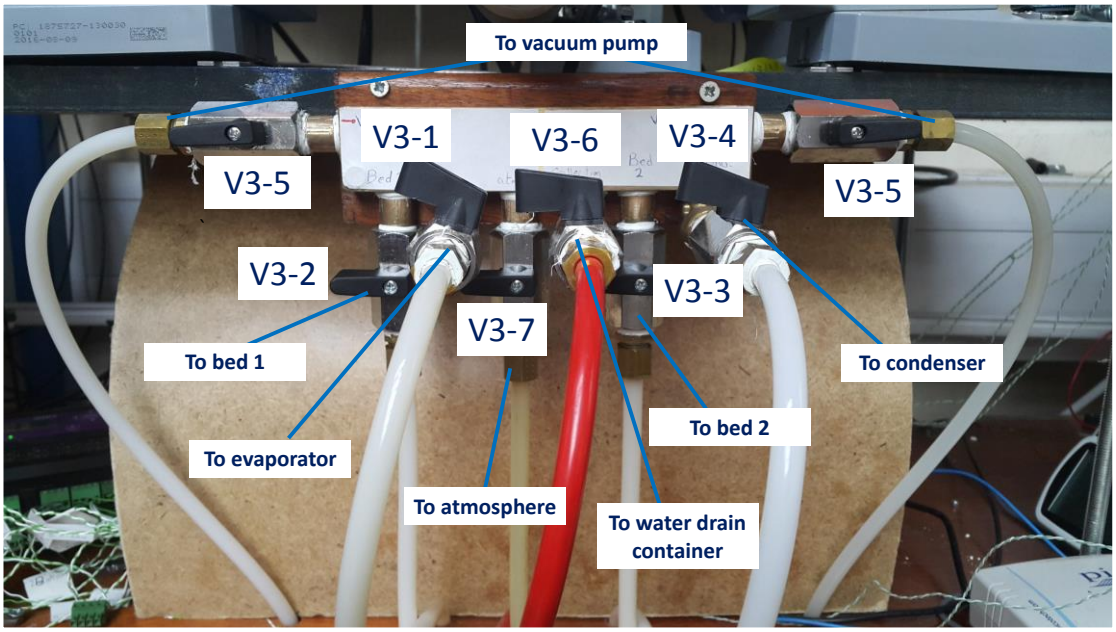

Figure 7-11: Vacuum manifold of the adsorption system

7.4 ORC system

Figure 7-12 shows a pictorial diagram of the ORC system developed to produce power output with the adsorption system as a bottoming cycle. The ORC system consists of an evaporator, condenser, radial inflow turbine, and circulating pump. It utilises refrigerant R245fa as a working fluid and is fitted with power, pressure, temperature, and flow measuring devices to enable evaluating its performance. A detailed description of all its components are given in the following section

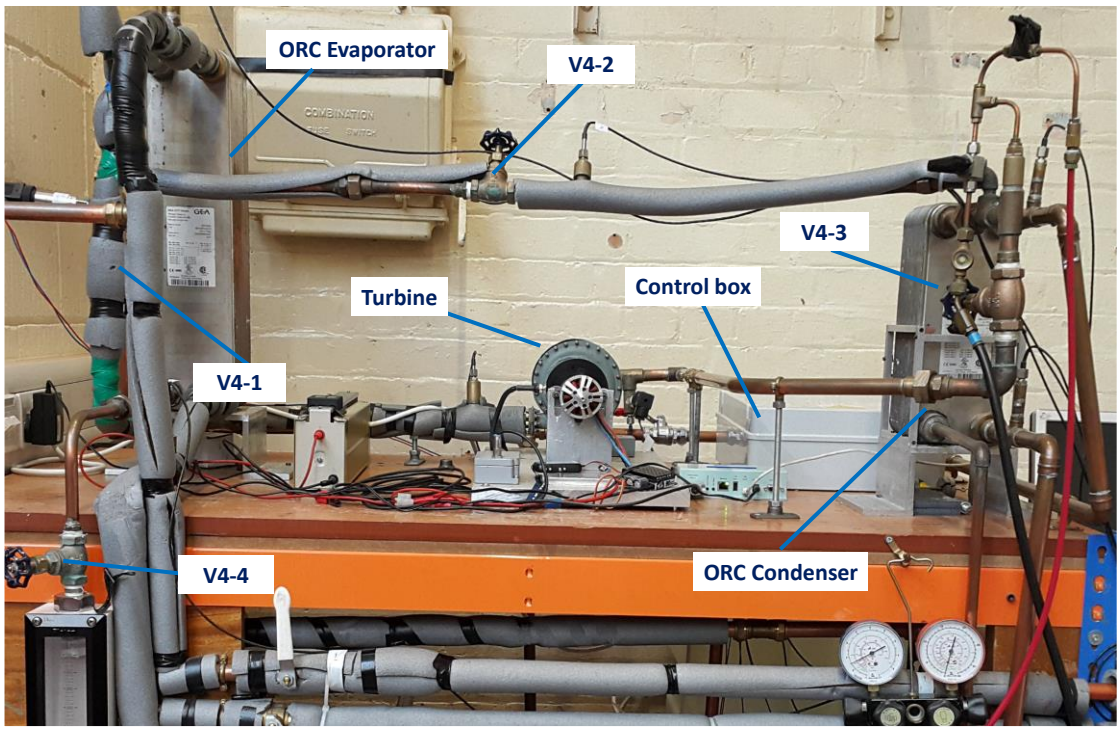

Figure 7-12: ORC radial turbine location and valves

7.4.1 Radial inflow turbine

A radial inflow ORC turbine with output of 900 W was manufactured using 3D printing technology. Figure 7-13 shows the main components of the turbine, where the rotor was made of steel while the nozzles were made of aluminum. More details about the turbine drawings can be found in Appendix B. The turbine is coupled with a torque meter mechanism and to prevent leakage a shaft seal ring is used after the bearing. In this experimental facility, the radial turbine is incorporated between the ORC evaporator and the ORC condenser, while RTD sensors and pressure traducers are installed at the inlet and outlet of the turbine to monitor and record the refrigerant properties (R245fa). Valves V4-1 and V4-3 (see Figure 7-12) can be used to isolate the turbine during starting up of the system. In the begging of the operation process both valves V4-1 and V4-3 are closed, while the flow passes through

valve V4-2 to ensure that the refrigerant leaving the ORC evaporator has the necessary pressure and temperature with the required degree of superheat.

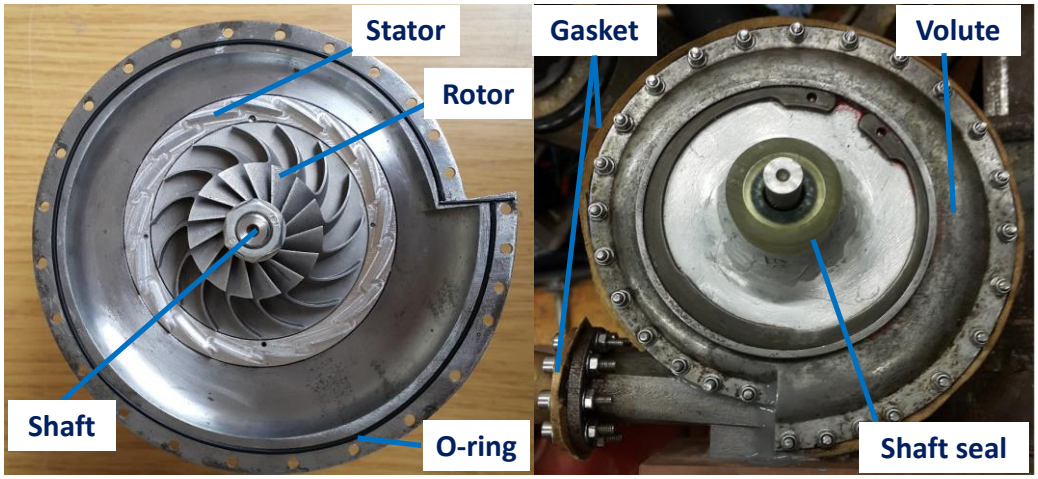

Figure 7-13: ORC radial inflow turbine used in the experimental facility

7.4.2 ORC evaporator

The evaporator is the ORC system component where the heat of adsorption or low-grade heat return from adsorption system can be used to produce high-pressure superheated refrigerant that can expand in the turbine producing power. In this experimental facility, a brazed plate heat exchanger from Kelvion Company is used with a maximum pressure of 31 bar and maximum temperature of 200°C respectively. This type of heat exchanger is compact and has 50 plates with cross-section area of 52×12cm. Figure 7-14 shows the brazed plate heat exchanger used in this experimental facility as an ORC evaporator. The evaporator is connected to the turbine using valve V4-1 and to the refrigerant pump via a flow meter and valve V4-4.

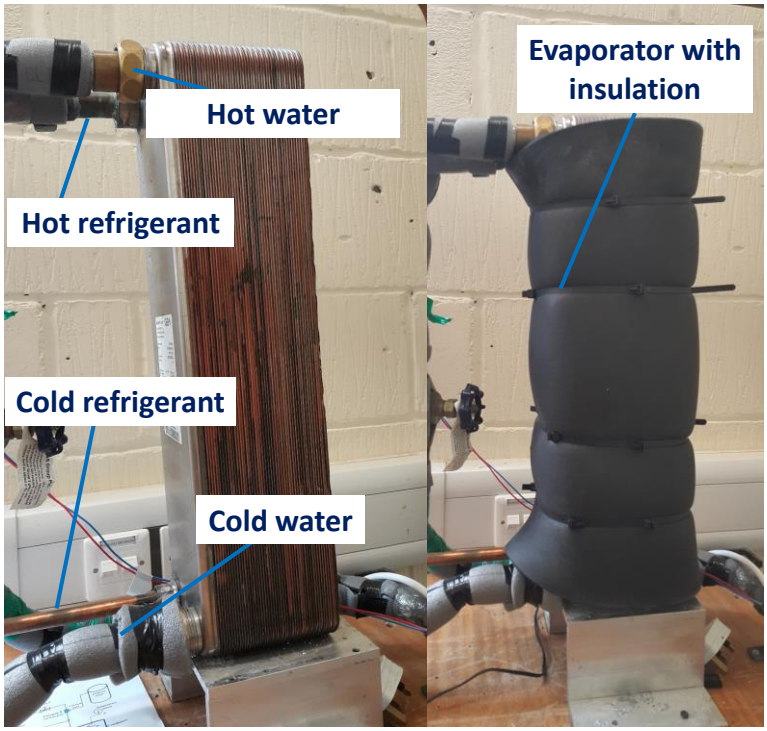

Figure 7-14: ORC evaporator (plate heat exchanger type)

The evaporator is heated using either the return cooling water from the bed after absorbing heat through the adsorption process or the return heating water from the adsorber bed after losing heat during the desorption process.

7.4.3 ORC condenser

The condenser used in the ORC system is similar to the ORC evaporator, but with smaller size. A brazed plate heat exchanger from Kelvion Company is used as an ORC condenser with 50 plates and cross-section area of 33×12cm. Figure 7-15 shows the ORC condenser used in this experimental facility. The condenser is provided with two gate valves at the inlet and the outlet to isolate the condenser for maintenance purpose. The condenser is cooled using water which is circulated from a cold water tank using a water pump.

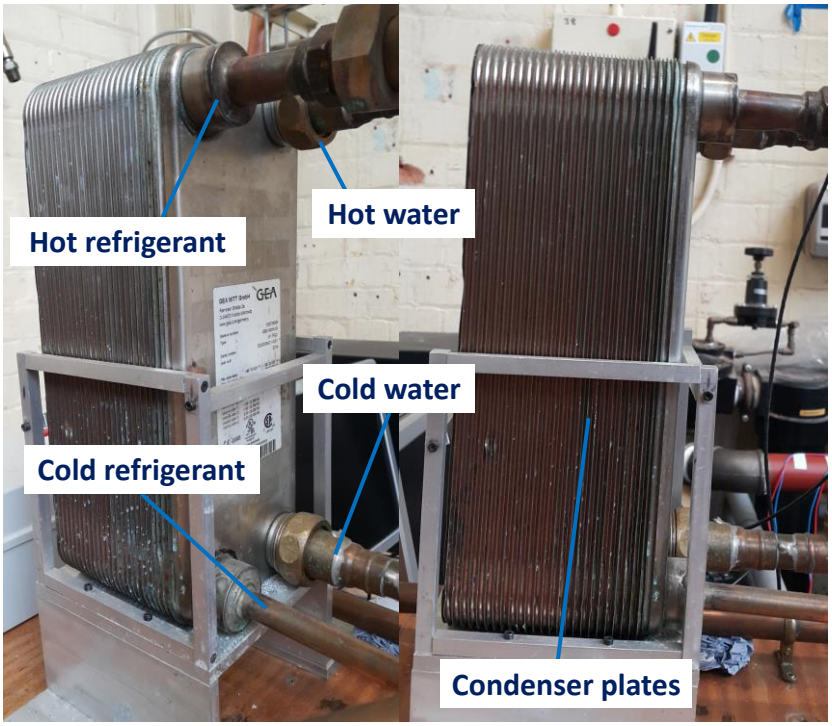

Figure 7-15: ORC condenser (plate heat exchanger type)

7.4.4 ORC pump

A three-phase 380V pump with power consumption of 0.37 kW from the WEG Company as shown in Figure 7-16 is used in this experimental facility. The pump is connected between the condenser outlet and the evaporator inlet. As the capacity of the pump is relatively high, a bypass pipe with a gate valve is connected between the inlet and the outlet to adjust the flow of R245fa as required. In addition, a sight glass is incorporated to the refrigerant line entering the ORC pump to ensure that the refrigerant passing through the pump is in a liquid phase to prevent damaging the pump.

Figure 7-16: Three phase ORC pump used in the experimental facility

7.4.5 ORC system charging

Charging the system with the appropriate amount of refrigerant (R245fa) is essential to make sure effective operation of the system as in the case of under charging, it reduces the mass flow rate passing through the turbine thus reducing the power generated. On the other hand, overcharging can cause flooding of the evaporator leading to potential liquid flow to the turbine. The following steps were carried out to charge the system with R245fa as shown in Figure 7-17 and Figure 7-18. Although process of commission was used to ensure the ORC system has no leakage as follows:

1. During the installation of the ORC system, care was taken to ensure all fittings are appropriately tightened or welded to ensure that the system can achieve the required operating conditions and enable achieving vacuum condition before charging with the refrigerant.
2. Open all valves V4-1, V4-2, V4-3, V4-4, and V4-5 and connect the charging valve V4-6 to the charging manifold.
3. Switch the vacuum pump on with the valve V4-8 closed, and then open the valve V4-7 to connect the vacuum pump to the ORC system.

4. The system will be vacuumed for about one hour time, till it reaches a minimum vacuum pressure of about 5kPa which can be monitored either directly from the manifold pressure gage or from the computer screen.
5. The vacuum pump is then turned off and the ORC is left under vacuum for about 5 hours and if any change noticed in the system pressure, the system should be checked again for leakage by charging the system with air and using the soap and water method or any other method to find the leakage.

After ensuring the ORC system is well installed with no leakage the refrigerant is charged throughout the following steps:

6. After the ORC system is vacuumed, manifold valve V4-8 should be opened to the nitrogen cylinder to charge the system with nitrogen to dry the system from any moisture content.
7. Adjusting the nitrogen cylinder valves carefully, and setting the maximum pressure at 30 bars, and the low-pressure valve to 6 bar to charge the system with nitrogen by opening the valve V4-8.
8. The system should be left charged with nitrogen for few hours to ensure absorbing all the moisture inside the system.
9. Repeating the vacuum process (step 4 and 5) to evacuate the system from the nitrogen.
10. Reading the initial weight of refrigerant cylinder using an appropriate balance.
11. Vent the hoses and the manifold with the refrigerant (R245fa) to avoid the introduction of air into the ORC system.
12. Charging the ORC system with the appropriate amount of refrigerant of about 1.5 kg of R245fa.

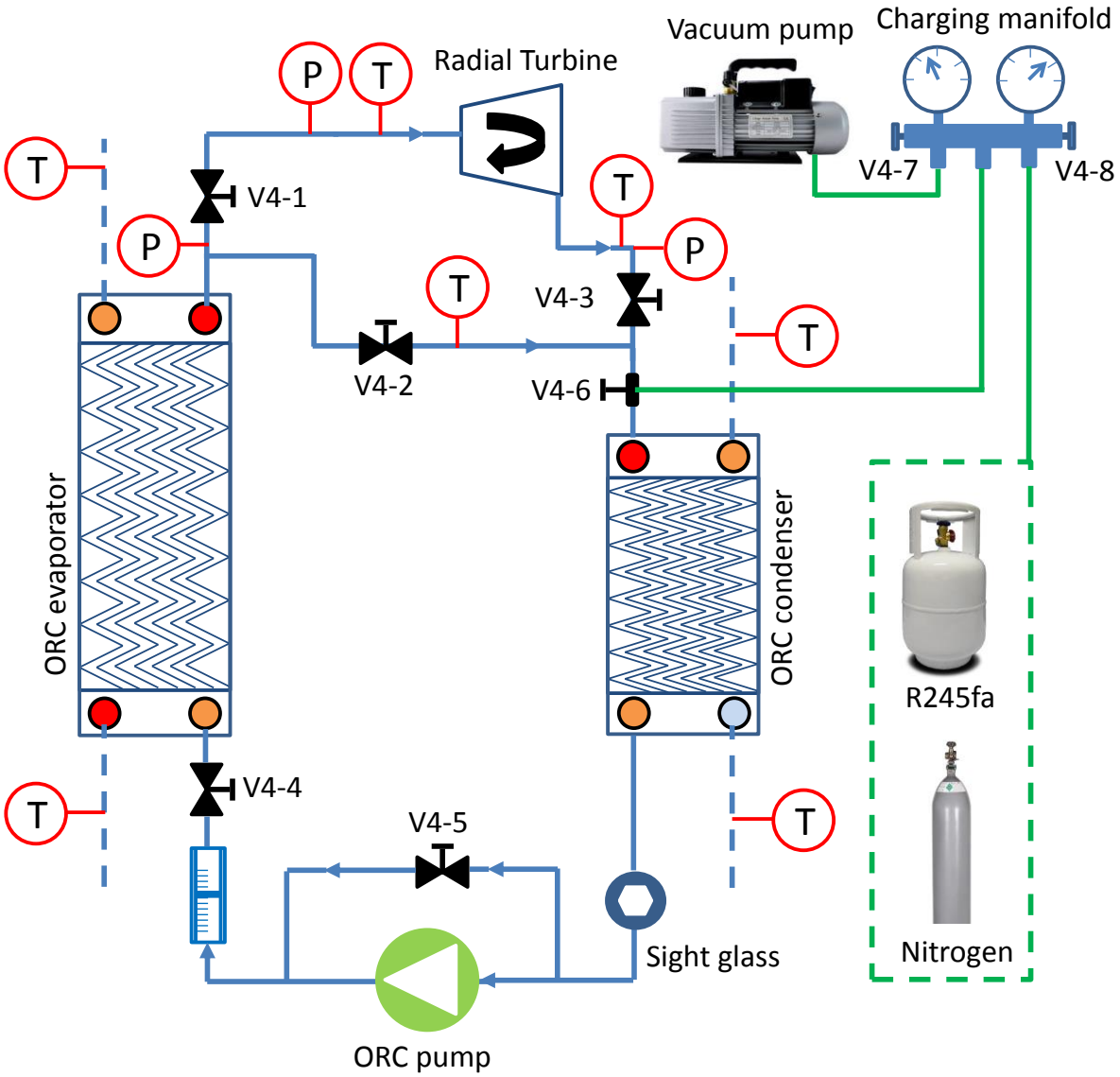

Figure 7-17: Schematic diagram of an ORC system charging equipment

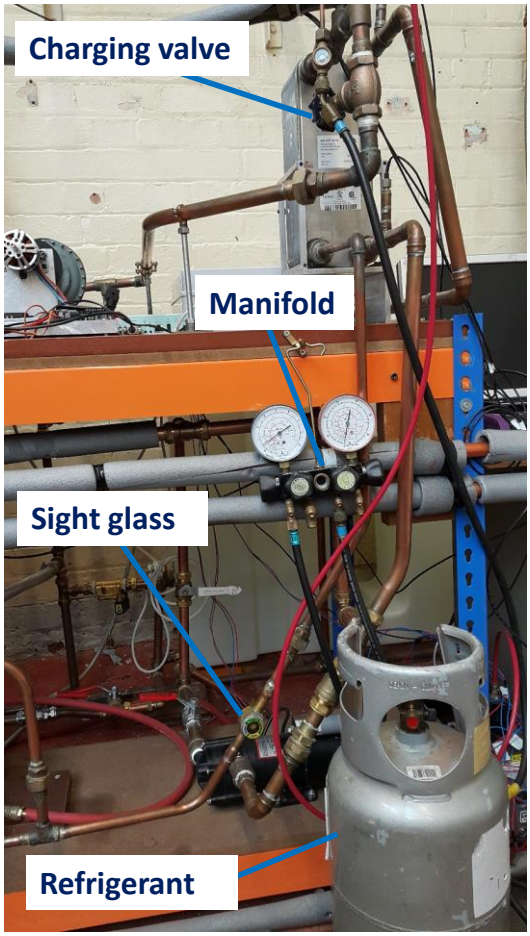

Figure 7-18: Charging the ORC system of the experimental facility with the refrigerant

7.5 Integration of adsorption and ORC systems

In this experimental study, the adsorption and ORC systems are integrated to produce both cooling and power output (IAOSCE). The adsorption system is set up as the topping system (powered using an external heat source), while the ORC served as the bottoming system (powered by the adsorption system). Two different scenarios are used to connect the two systems. The first scenario (scenario 1) is carried out by connecting the return cooling water of the adsorption system to power the ORC system, while in the second scenario (scenario 2), the ORC is powered by the return heating water of the adsorption system. Figure 7-19 shows a schematic diagram of the integrated adsorption and ORC systems illustrating the

piping/valves used to operate the two scenarios where in the first scenario V6 is open and V5 is closed while in the second scenario V6 is closed and V5 is open.

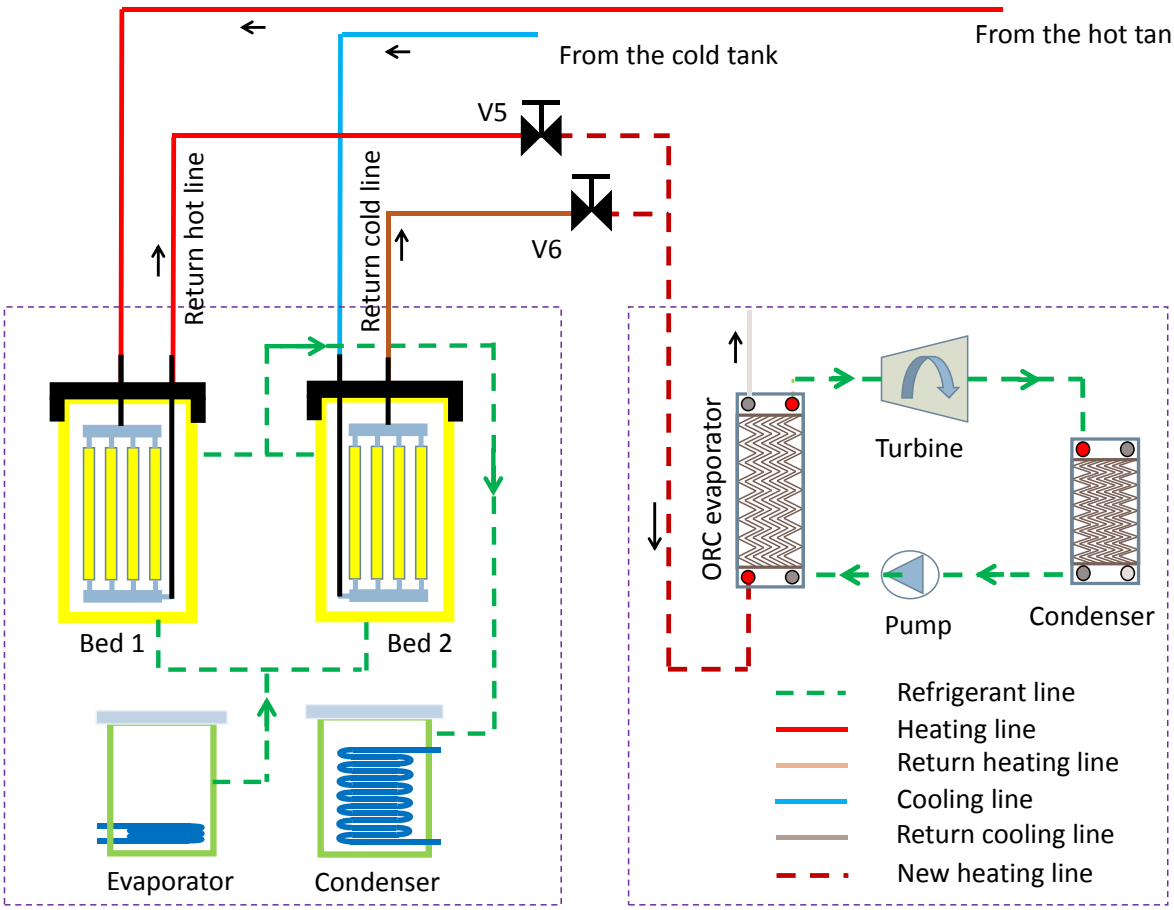

Figure 7-19: Connections between adsorption and ORC systems

7.6 Measuring instruments

Many measuring devices were used in this experimental facility including thermocouples, pressure transducers, flow meters, and torque meter. These devices were used to evaluate the cooling produced by the adsorption evaporator, the power generated by the turbine and the heat consumed in both adsorption and ORC systems in order to calculate COP, SCP, SP and ORC power efficiency in addition to the COPe and SCPe.

7.6.1 Thermocouples

Two type K thermocouples from Omega Engineering Ltd similar to that shown in Figure 7-20 (left) were installed in each module heat exchanger of adsorber bed 1 and adsorber bed 2, the first one was in the middle, while the other one was in the bottom and they were stuck to the metal mesh to keep contact with the adsorbent material for monitoring the adsorber bed temperature. In addition, two thermocouples (type K) were installed in the adsorption system evaporator to monitor the temperatures of the liquid/vapour refrigerant (water), also two thermocouples were installed in the condenser to monitor the liquid and vapour temperatures of the refrigerant. Eight RTD sensors similar to that shown in Figure 7-20 (right) were fitted at the inlet and outlet of heating/cooling water pipes of each adsorber bed, cooling water to the condenser, and chilled water to the evaporator to monitor the inlet and outlet temperatures.

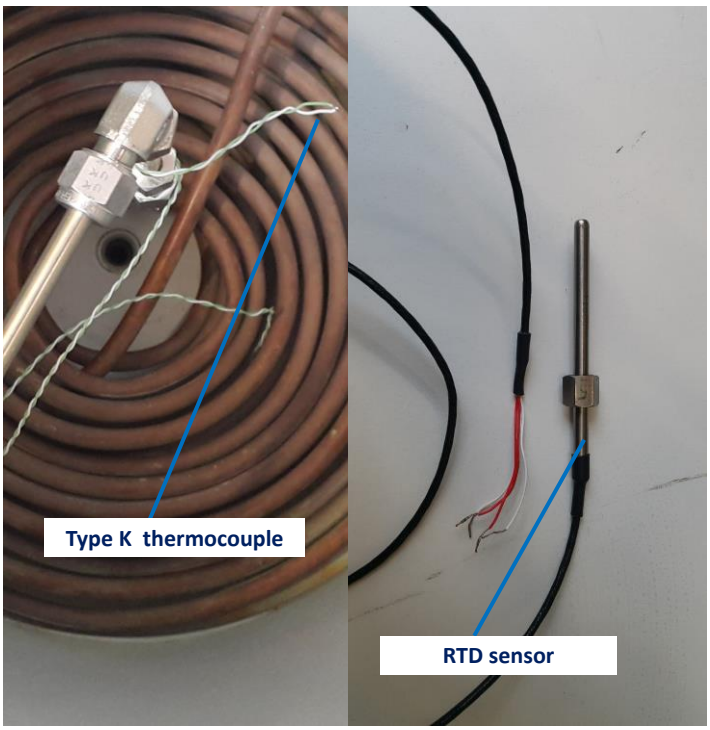

Figure 7-20: Thermocouples type K and RTD sensors used in the test facility

On the ORC system, RTD sensors were fitted at inlet and outlet of evaporator, condenser and turbine to measure the temperature of the refrigerant. Also, four RTD sensors were installed at the heating and cooling water pipes entering and leaving the evaporator and the condenser.

7.6.2 Pressure transducers

Four vacuum pressure transducers (0-350 mbar) were fitted at the two adsorber beds, adsorption condenser, and adsorption evaporator. This group of pressure transducers have an accuracy of ±0.087 % according to the manufacturing company giving an output current of 4-20 mA. Also, three pressure transducers type UNIK 5000 series with a range of 1 - 10 bars (absolute pressure) were installed, at the radial turbine inlet and outlet of and in the ORC bypass pipe. These pressure transducers have an accuracy of ±0.04% according to the manufacturing company giving an output current of 4-20 mA. To convert the current signal into a voltage signal, 100 Ω resistances were connected to the data logger. The pressure transducers were powered with a voltage of 24V and 0.005A using a DC power supply (ISO-TECH IPS4303 laboratory DC) and the electronic circuit of connecting the power supply and the data logger to the pressure transducers is shown in Figure 7-21.

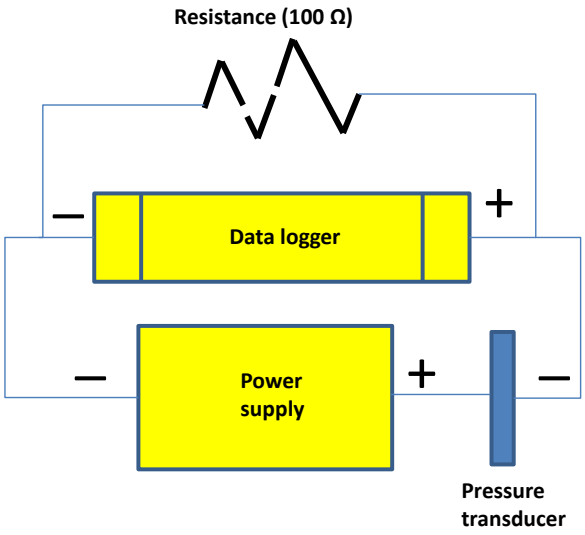

Figure 7-21: Pressure transducer connection

7.6.3 Power supply

The test facility included a number of power supply units from ISO-TECH Company. Each power supply unit as shown in Figure 7-22 has the range of DC tracking series voltage output between 0 and 60V, while it is set at 24V to power the pressure transducers. Each power supply can power only two pressure transducers, so a number of power supply units were needed to power all the pressure transducers used in the adsorption and the ORC systems.

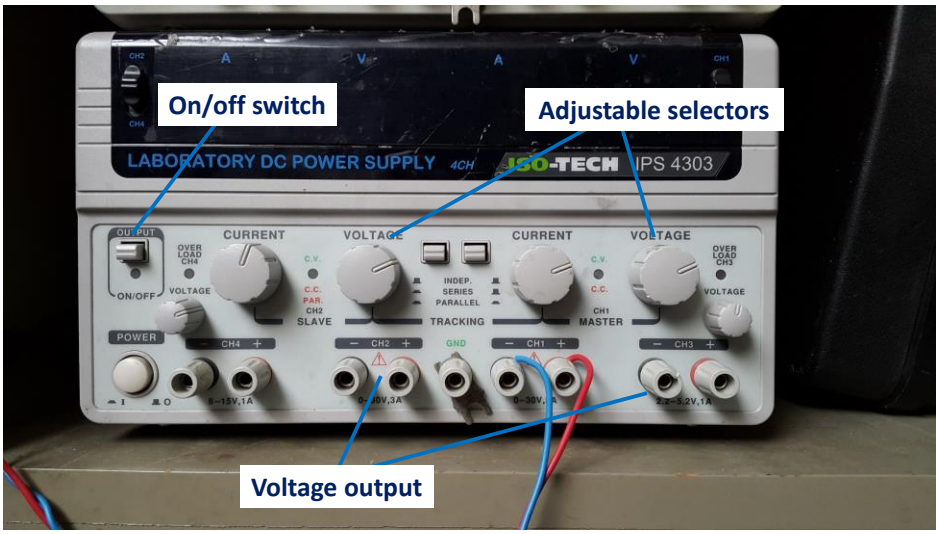

Figure 7-22: DC power supply

7.6.4 Torque meter

A torque meter from Datum Electronics Company was used to measure the rotational speed, torque, and power produced from the ORC turbine as shown in Figure 7-23. One side of the torque meter was connected to the turbine shaft through coupling while its other side was connected the DC generator. The torque meter can read the rotational speed, and torque of up to 20,000 rpm, and 10Nm respectively with an accuracy of 0.1%. The data from torque meter was transferred to PC for monitoring and recording.

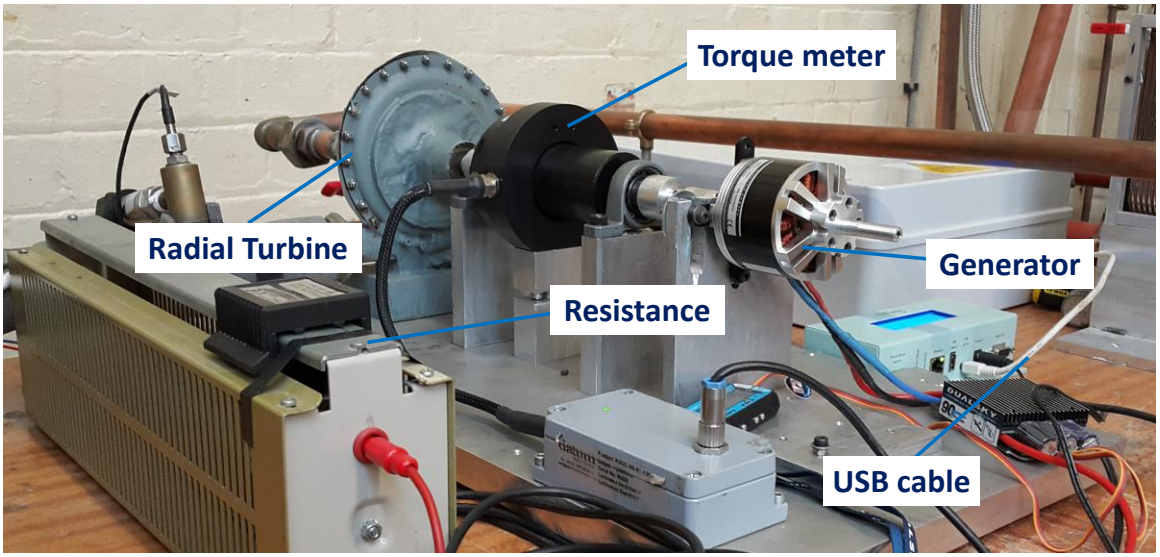

Figure 7-23: Torque meter unit

7.6.5 Flow meters

A number of flow meters were fitted in the test facility as shown in Figure 7-24. For R245fa refrigerant, PLATON GMTB flow meter from the RM&C Company with a range of 50 - 500 L/HR liquid R245fa at 20 °C was used. To prevent the continuous fluctuating of the float during the system operation the range of the flow meter is chosen to be slightly higher than the required range and the flow meter was provided with a plastic tube instead of glass.

Figure 7-24: Flow meters used (left) water flow meter (right) R24fa flow meter

Two water flow meters from Omega UK were used to measure the water flow rate from the heating and cooling water of the adsorber beds with a range of 0-55 LPM. For the adsorption condenser, a flow meter with a flow capacity of 0 to 25 LPM was used while for the chiller/heater a water flow meter with a flow capacity of 0 to 25 LPM was used.

7.6.6 Data acquisition System

Most of the measuring instruments used in this experimental facility were connected to a data logger as shown in Figure 7-25 to read and monitor the data. For adsorption system, all the thermocouples were connected to the data logger model DT85 from dataTaker with 16 channels, while the pressure transducers (bed 1, bed 2, condenser, and evaporator) were connected to a data logger model Pico Logger 1012 from Pico technology with voltage rate of 0-2.5 V. For the ORC system, all pressure transducers and RTD sensors were connected to another data taker model DT85-3 with 16 channels.

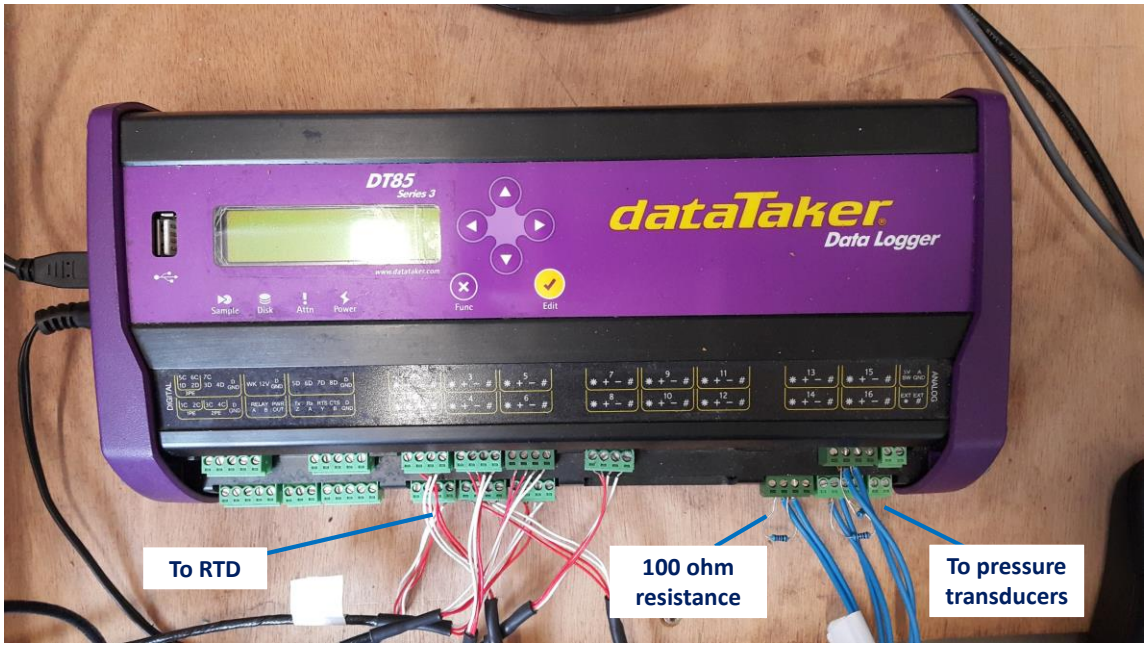

Figure 7-25: Data taker

7.7 System performance analysis

The overall performance of the integrated adsorption-ORC system for cooling and electricity used in this experimental work is evaluated using the terms coefficient of performance COP, specific cooling power SCP, equivalent coefficient of performance COPe, equivalent specific cooling power SCPe, specific power SP, and ORC efficiency η_{ORC} using equations 5-5 to 5-10.

7.8 Measurement calibration and uncertainty propagation

For accurate results, the measuring instruments for pressure and temperature were calibrated against standard instruments. In order to calibrate pressure transducers used in this work, each instrument was connected to a calibration kit to compare the pressure measured by the pressure transducer to that measured by a standard gage pressure instrument. The pressure of the calibration kit (see Figure 7-26) was increased gradually to the required pressure. Type K thermocouples and RTD sensors were used in the test facility and were calibrated. All thermocouples were immersed in a water bath, while the reading was compared to the

standard RTD sensor. During the calibration process, heat was added gradually and different readings at various temperatures ranging from 15 °C to 100 °C were recorded. All the calibrated thermocouples or RTD sensors were connected to the data logger and their readings displayed on the PC as shown in Figure 7-26.

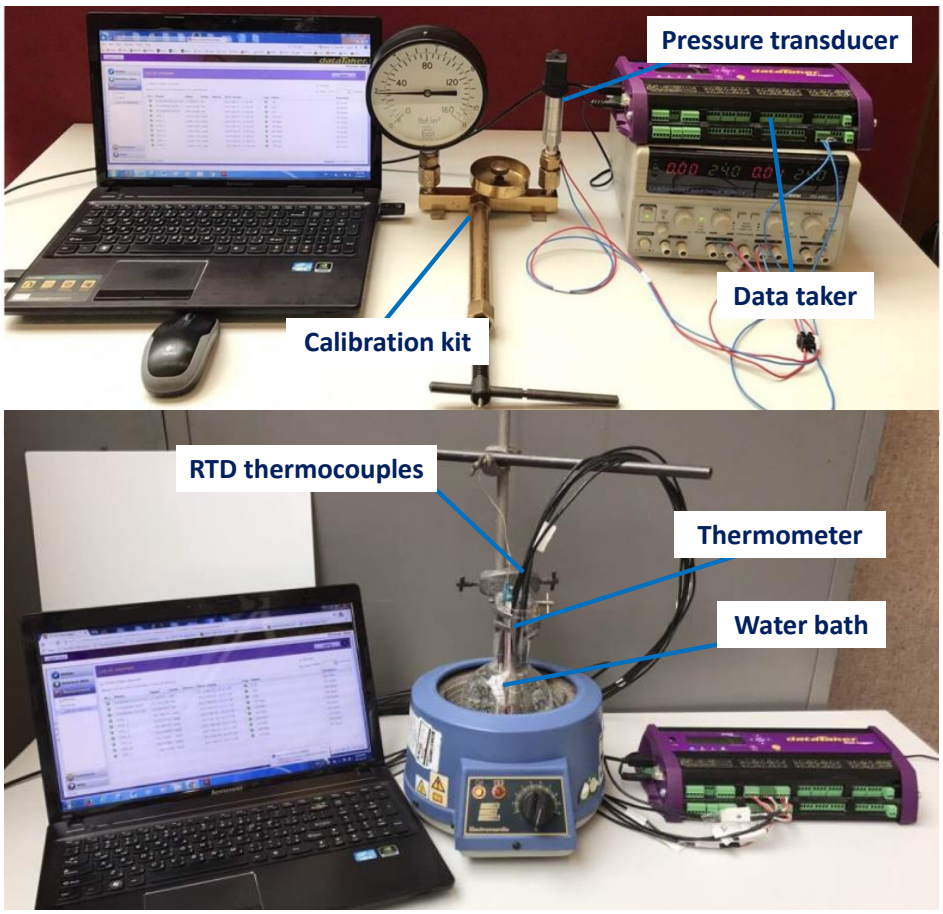

Figure 7-26: Calibration of the thermocouples and the pressure transducers

More details about the calibration results and uncertainty propagation are given in Appendix C. Table 7-1 and Table 7-2 list the uncertainties of thermocouples and RTD sensors and, pressure transducers used in the test facility respectively. Table 7-3 lists the propagated uncertainties of measuring devices into the cooling and power generation.

Table 7-1: Uncertainties of thermocouples and RTD sensors used in the experimental facility

Item	Location	Curve fitting	Uncertainty
T1	Bed1/middle	0.9992x + 0.0755	±0.26˚C
T2	Bed1/bottom	0.9984x +0.3155	±0.49˚C
3	Bed2/middle	0.9955x + 0.3134	±0.36˚C
T4	Bed2/bottom	1.0002x + 0.1028	±0.33˚C
RTD1	Bed1/inlet water	1.0004x - 0.1798	±0.33˚C
RTD2	Bed1/outlet water	0.9986x + 0.0484	±0.18˚C
RTD3	Bed2/inlet water	0.9966x + 0.1038	±0.29˚C
RTD4	Bed2/outlet water	1.0005x + 0.0127	±0.18˚C
RTD5	Evaporator/inlet water	0.9988x + 0.0537	±0.10˚C
RTD6	Evaporator/outlet water	1.0008x - 0.0665	±0.11˚C
RTD7	Condenser/inlet water	0.9995x + 0.0437	±0.12˚C
RTD8	Condenser/outlet water	0.9979x + 0.0589	±0.23˚C
RTD9	ORC evap. outlet water	1.0028x - 0.0385	± 0.26 ˚C
RTD10	ORC evap. inlet water	0.999x + 0.1931	± 0.25 ˚C
RTD11	ORC turbine inlet	1.0008x + 0.0408	± 0.18 ˚C
RTD12	ORC turbine outlet	1.0012x + 0.0372	±0.19 ˚C
RTD13	Bypass line	1.0017x + 0.0114	±0.21 ˚C
RTD14	ORC cond. inlet water	0.999x + 0.1593	±0.18 ˚C
RTD15	ORC cond. outlet water	0.9997x + 0.0554	±0.10 ˚C

Table 7-2: Uncertainties of the pressure transducers used in the experimental facility

Item	Location	Curve fitting	Uncertainty
P1	Turbine inlet	1.0039x + 0.0148	±0.0462 bar
P2	Turbine outlet	1.001x + 0.0367	±0.0668 bar
P3	By-pass line	0.9995x + 0.0487	±0.0737 bar
P4	Bed1	0.9902x+ 1.714	±1.95 mbar
P5	Bed2	0.999x+ 1.027	±1.18 mbar
P6	Condenser	0.9997x+ 0.144	±0.5 mbar
P7	Evaporator	1.0036x+ 0.5134	±1.5 mbar

Table 7-3: Uncertainty propagation of cooling and power

Parameter	Net output	Uncertainty
Cooling	78-529 W	±8.47%
Power	96-341W	±2.11%

7.9 Experimental results, modelling validation and discussions

In this research, an integrated two-bed adsorption-ORC system utilising CPO-27(Ni) /water as an adsorption pair and R245fa as an ORC fluid to generate cooling and electricity simultaneously was experimentally tested and the results were discussed. Two different scenarios of integrating the adsorption system with the ORC were described in section 7.5 and Figure 7-19. In scenario 1, the heat of adsorption can be recovered from the adsorption process as the cold water passes through the adsorber beds (with cooling water temperature of 46-48 °C) was used to power the ORC system. In scenario 2, the same heat source used in the adsorption systems for desorption process was used to power the ORC system.

Figure 7-27 compares the experimentally measured temperatures of adsorber beds, condenser and evaporator to those predicted by the modelling of the two-bed CPO-27(Ni)/water adsorption system. The predicted temperature profiles show good agreements with the experimental results with a maximum deviation of less than 10% highlighting the validity of the developed adsorption system model. Figure 7-28 shows the experimental temperature

values of each adsorber beds during cycles 2 to 4 showing steady state operation of the adsorption system. Also, the two beds show similar operating temperature values where in the desorption mode, the average bed temperature is 81 °C and in the adsorption mode, the average bed temperature is 32 °C.

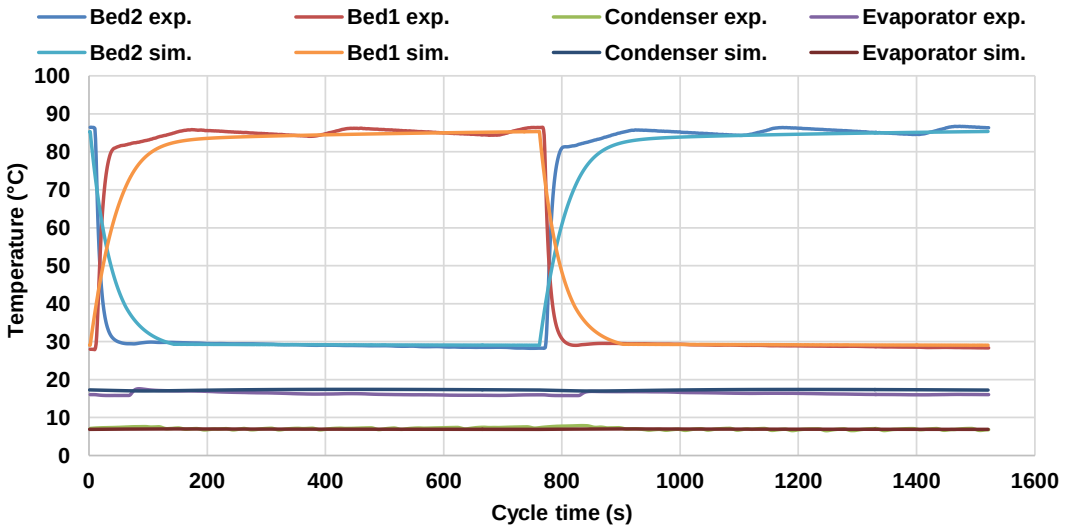

Figure 7-27: Simulated and experimental temperatures of adsorber beds condenser and evaporator for the two-bed CPO-27(Ni) /water adsorption system utilizing heat source temperature of 85 °C

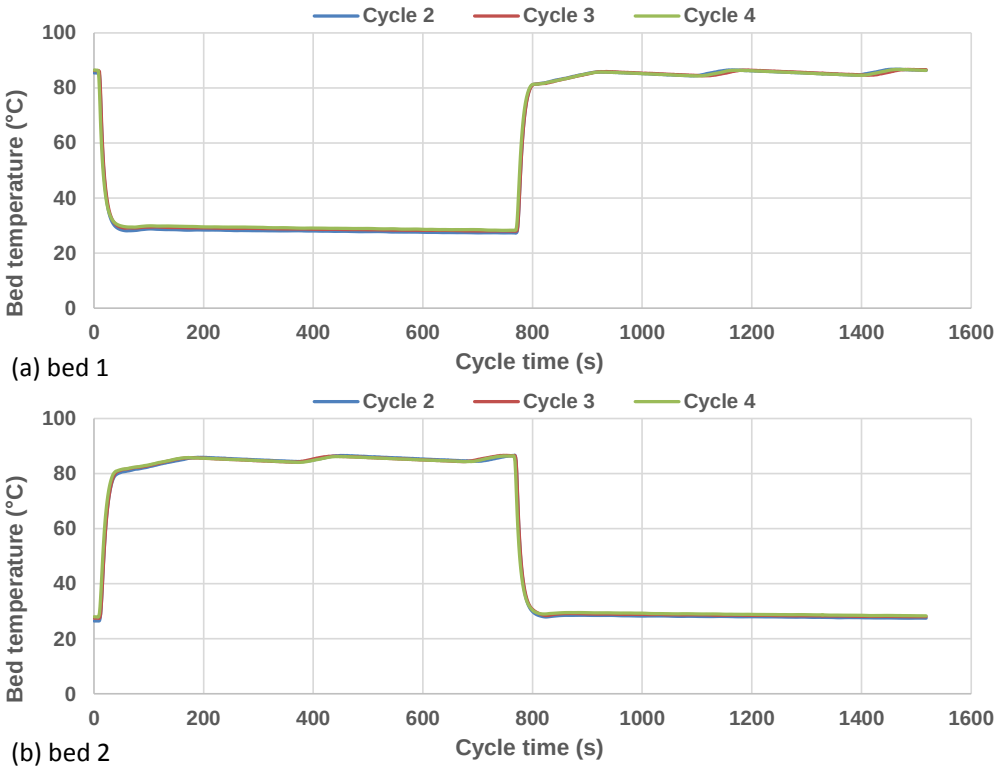

Figure 7-28: adsorber bed temperature through cycle 2-4 utilizing CPO-27(Ni) /water at heat source temperature of 85 °C, (a) bed1, and (b) bed2

Figure 7-29 shows the effect of heat source temperature on the cooling and power generated simultaneously from the integrated adsorption-ORC system. Results showed that, as the heating fluid temperature increases the cooling and the power generated increase [22]. For scenario 1, the power generated did not increase significantly by increasing the main heat source temperature, because the ORC system is powered by the cooling water returned from the adsorption system in this scenario.

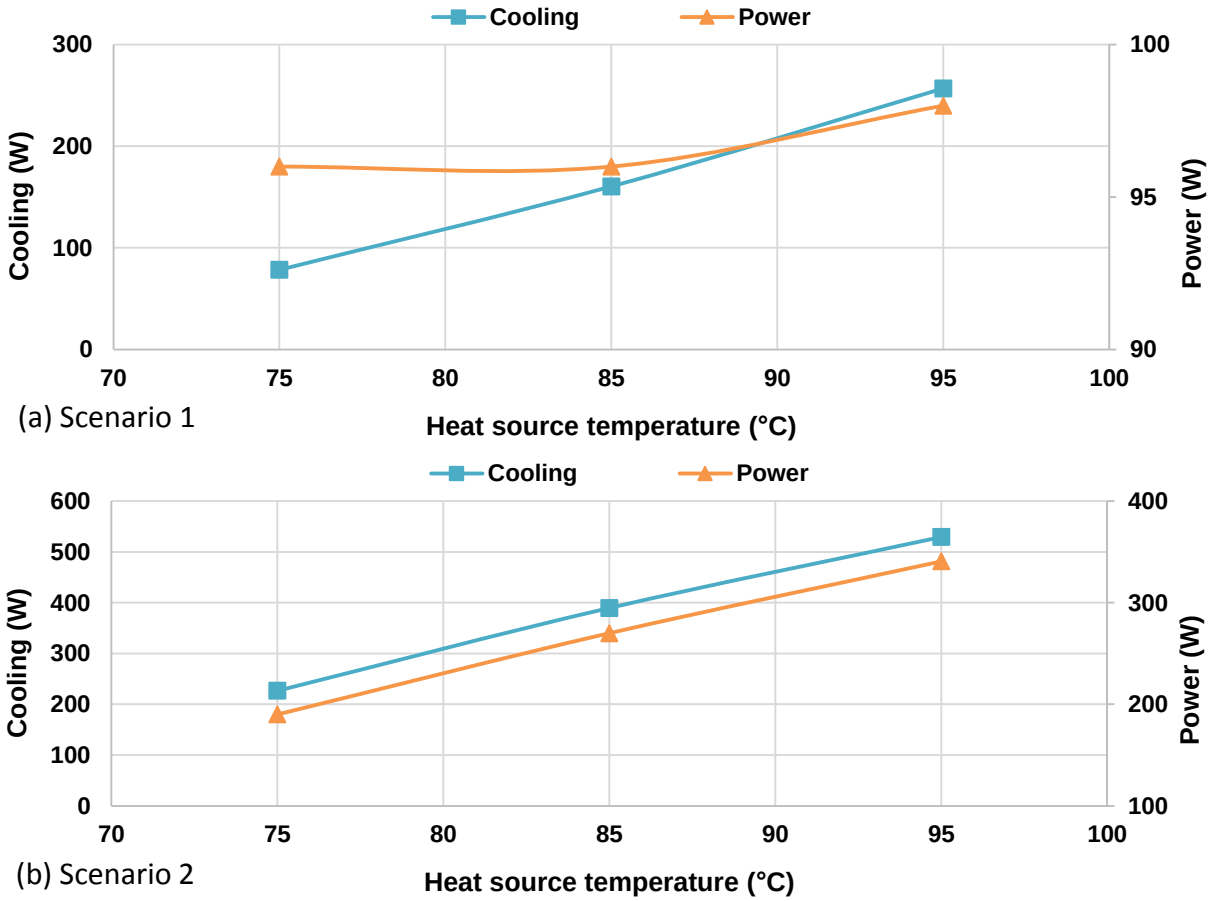

Figure 7-29: Cooling and power generated from the integrated two-bed CPO-27(Ni) /water adsorption-ORC system (a) scenario 1 (b) scenario 2

Figure 7-30 and Figure 7-31 compare the experimental power and efficiency of the ORC system using R245fa as a refrigerant. The predicted power and efficiency show good agreements with the experimental results with maximum deviations of 16% and 17% respectively showing the validity of the developed ORC system model.

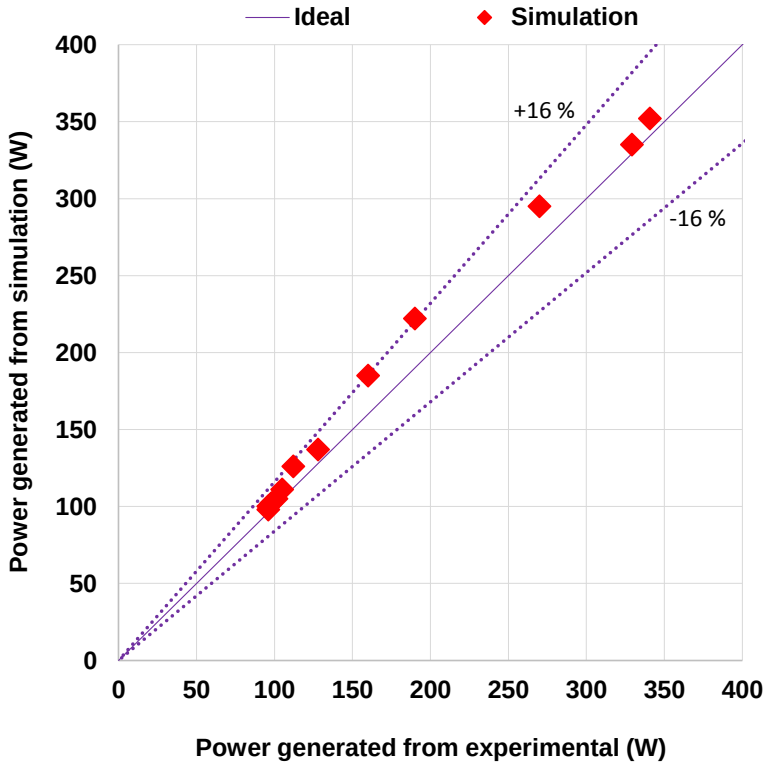

Figure 7-30: Simulated and experimental values of power generated of the ORC system utilizing R245fa as a working fluid

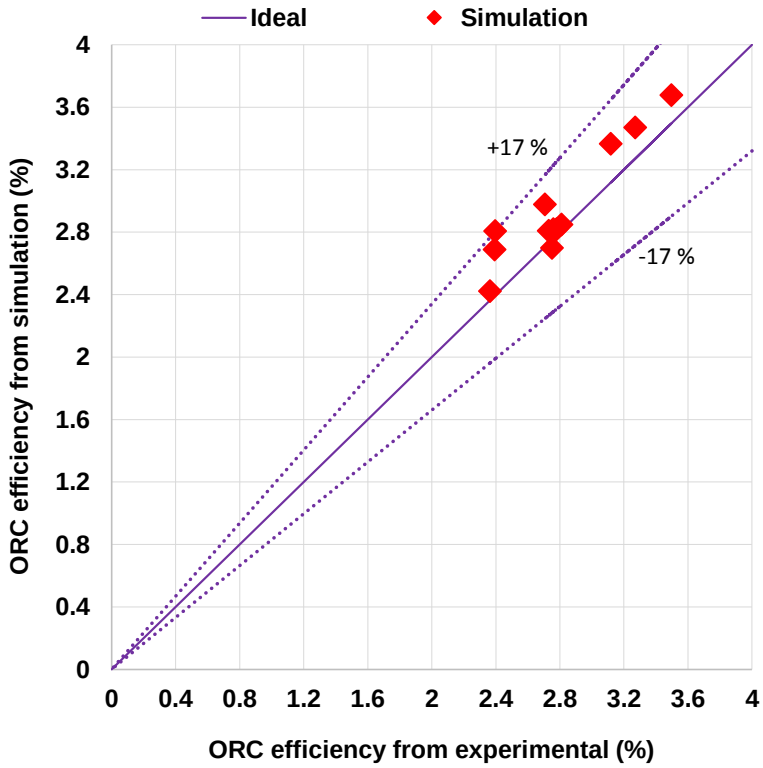

Figure 7-31: Simulated and experimental values of efficiency of the ORC system utilizing R245fa as a working fluid

Figure 7-32 and Figure 7-33 compare the CFD simulation with the experimental results for the power and efficiency of the ORC turbine using R245fa as a refrigerant. For both power and efficiency, the CFD simulation data show good agreements with the experimental results with maximum deviations of 15% and 16% respectively. The maximum power generated from the turbine was about 415 W and about 18% of this power is used for the pump. The radial inflow turbine achieved an isentropic efficiency ranging between 35% and 50% which are relatively low and this is due to using off-design conditions such as the low mass flow rate of about 0.06 -0.1 kg/s compared to the design mass flow rate of 0.19 kg/s.

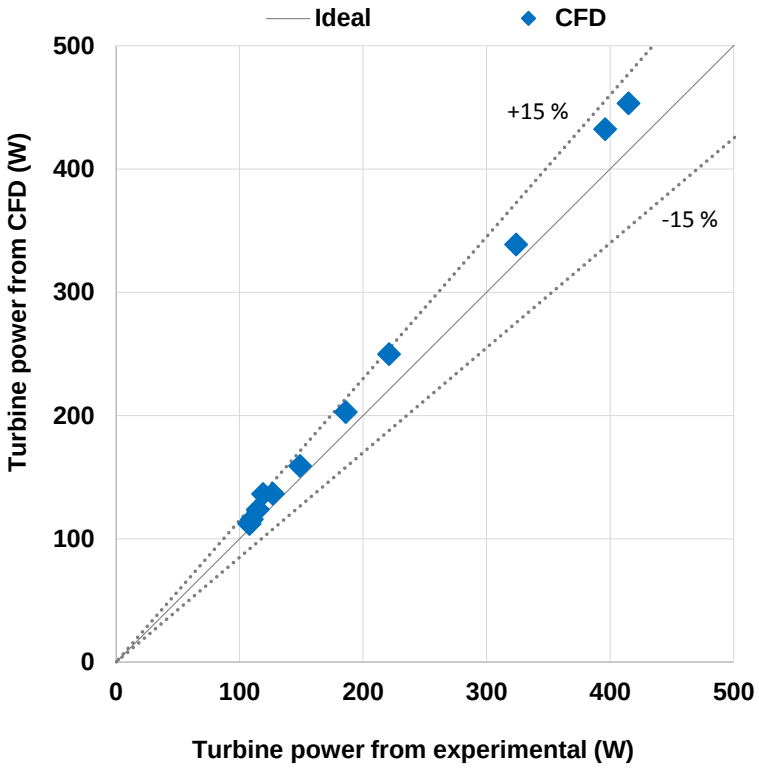

Figure 7-32: Comparison of power generated from CFD simulations with experimental data of the ORC turbine utilizing R245fa as a working fluid

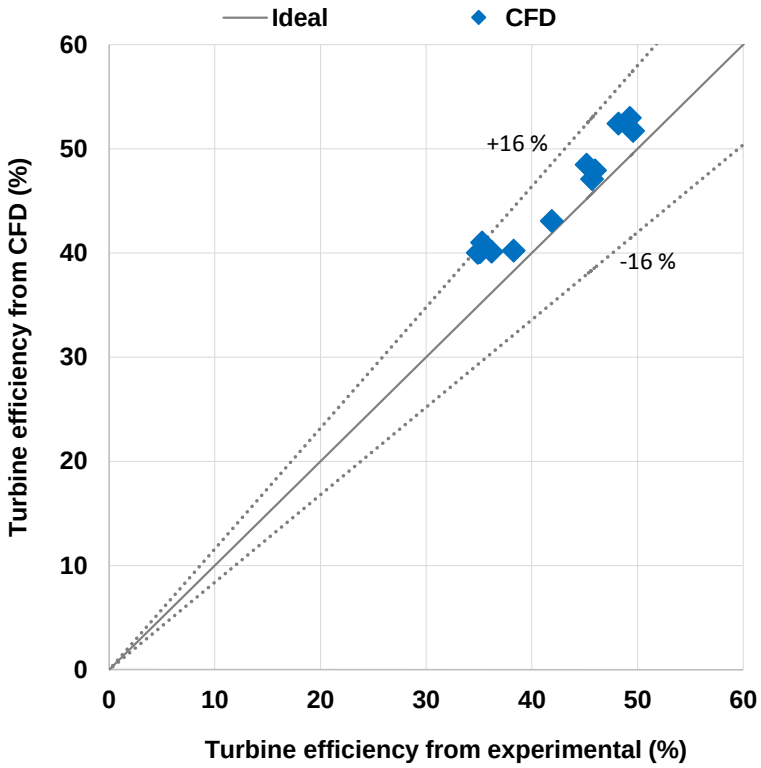

Figure 7-33: Comparison of efficiency from CFD simulations with experimental data of the ORC turbine utilizing R245fa as a working fluid

Figure 7-34 shows the experimental and numerical values of COP of the integrated two-bed adsorption-ORC system (IAOSCE) using CPO-27(Ni) and R245fa for scenario 1 and scenario 2. Results show that scenario 2 has higher values of COP with a maximum value of 0.35 compared to 0.23 that achieved by scenario 1 and this is because of the relatively high cooling water temperature (46-48 °C) used in scenario 1, which affected the cooling capacity obtained from the adsorption system. Results also show that, for both scenarios, as the heating fluid temperature increases, COP increases and the predicted values show good agreements with the experimental results with a maximum deviation of about 10.5%. Figure 7-35 and Figure 7-36 show the values of the specific cooling power SCP and specific power SP generated from the integrated adsorption-ORC system for scenarios 1 and 2.

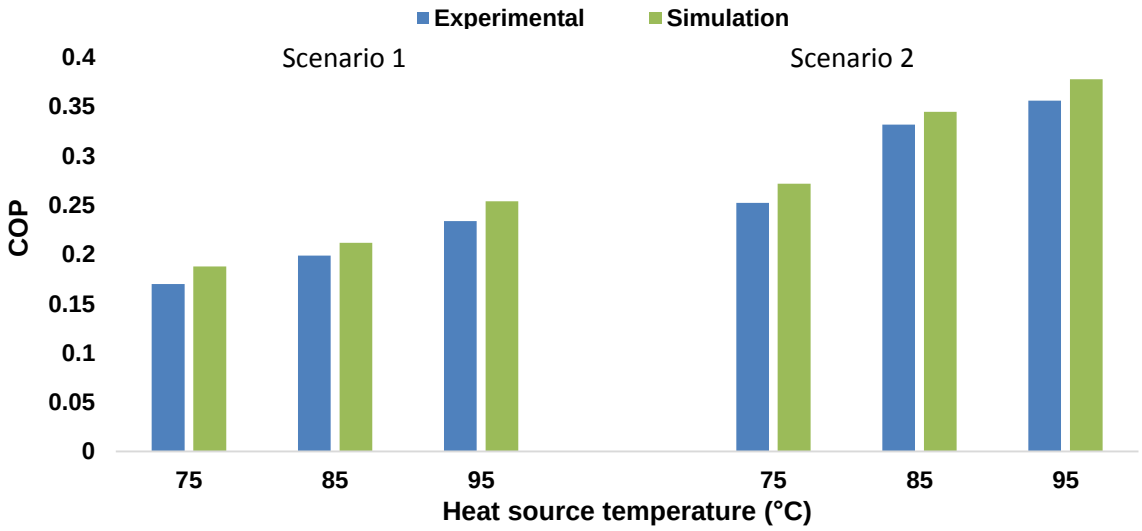

Figure 7-34: Experimental and numerical values of COP for the IAOSCE utilizing CPO-27(Ni) /water and R245fa with half cycle time, condenser temperature and adsorption evaporator temperature of 700 s, 16 °C and 8 °C respectively

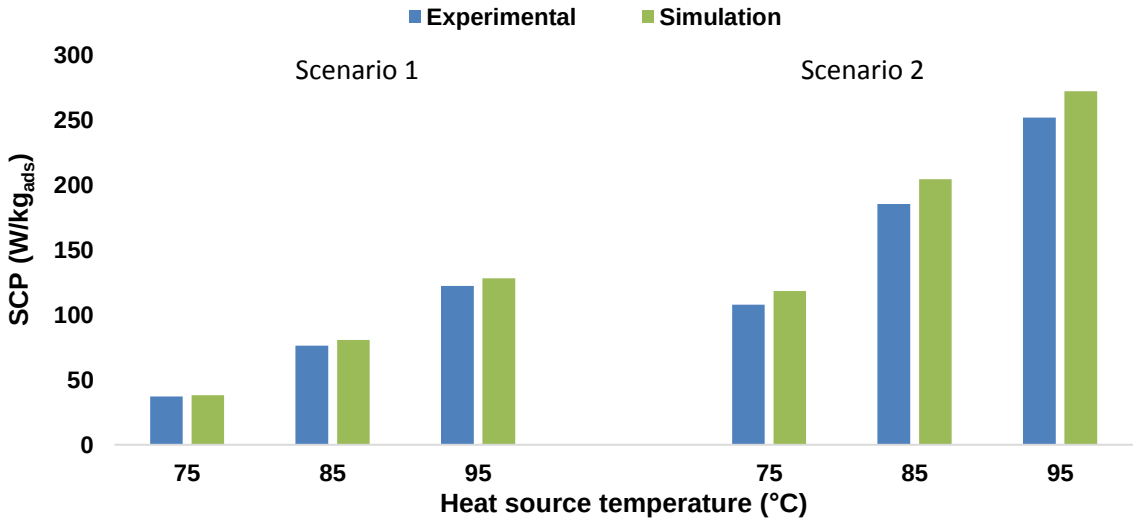

Figure 7-35: Experimental and numerical values of SCP for the IAOSCE utilizing CPO-27(Ni) /water and R245fa with half cycle time, condenser temperature and adsorption evaporator temperature of 700 s, 16 °C and 8 °C respectively

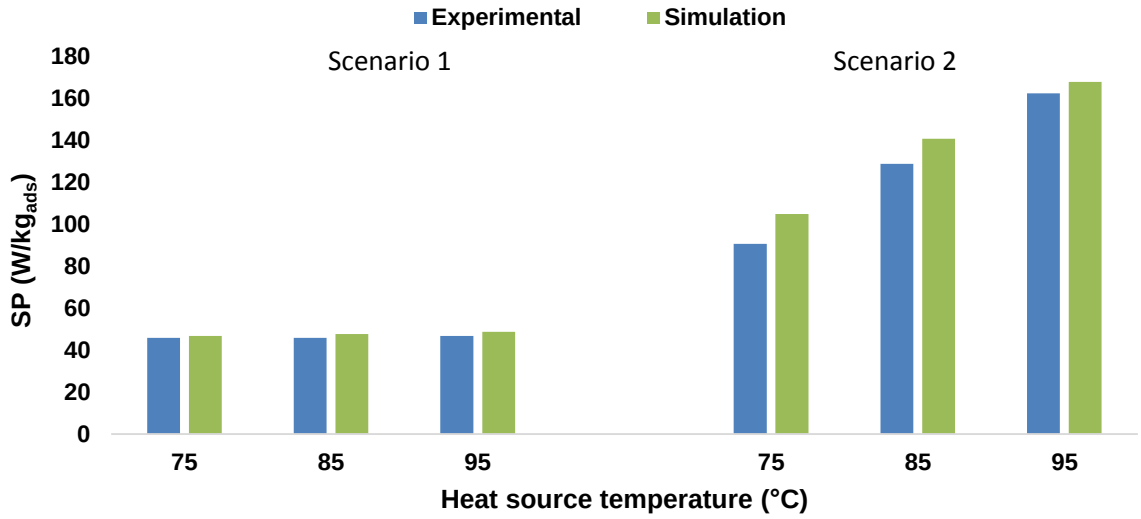

Figure 7-36: Experimental and numerical values of SP for the IAOSCE utilizing CPO-27(Ni) /water and R245fa with half cycle time, condenser temperature and adsorption evaporator temperature of 700 s, 16 °C and 8 °C respectively

Scenario 2 shows higher SCP and SP than those of scenario 1 with maximum values of 252 W/kg$_{ads}$ and 162 W/kg$_{ads}$ respectively and this is because of using lower cooling water temperature than that used in scenario 2. Results show that for scenario 1 and scenario 2 as the heating fluid temperature increases SCP increases, and for scenario 2 as the heating fluid temperature increases SP increases, while SP of scenario 1 is not affected by the main heat source temperature. Experimental and simulation values show a good agreement with a maximum deviation of about 10.3% for SCP and 15.8% for SP.

Figure 7-37 shows the experimental and numerical values of ORC efficiency for the integrated two-bed adsorption-ORC system. A maximum ORC efficiency of 3.3% is achieved using scenario 2 with heating temperature of 85 °C and this is due to less heat is absorbed in the ORC evaporator than that at 95 °C. Results again show good agreements between the experimental and the simulation results with a maximum deviation of about 14.1%.

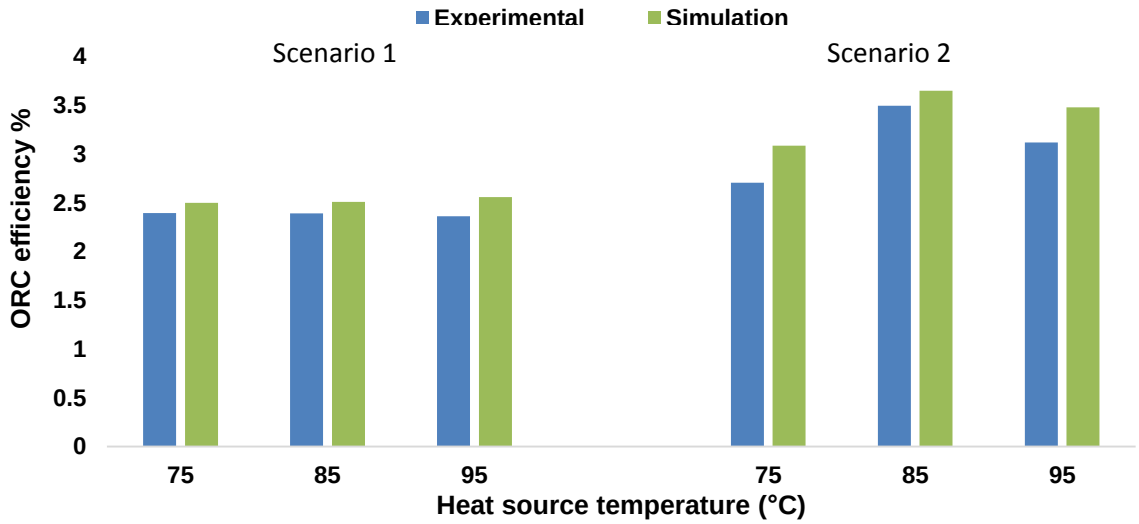

Figure 7-37: Experimental and numerical values of ORC efficiency for the IAOSCE utilizing CPO-27(Ni) /water and R245fa with half cycle time, condenser temperature and adsorption evaporator temperature of 700 s, 16 °C and 8 °C respectively

Figure 7-38 shows the experimental and numerical values of COPe (equivalent COP) for the integrated two-bed adsorption-ORC system. Scenario 1 shows higher COPe values than those of scenario 2 with maximum value of 0.79 achieved at heat source temperature of 75 ° C and this is due to the ORC being powered by the heat of adsorption without consuming additional external heat and as the power has a higher grade than that of cooling, higher COPe is achieved. Scenario 2 shows relatively low COPe due to the additional heat consumed by the ORC evaporator during this scenario. Figure 7-39 shows the experimental values of SCPe of the integrated adsorption-ORC system for a range of heat source temperature. Scenario 2 shows higher SCPe values (with a maximum value of 739 W/kg_{ads}) compared to those of scenario 1, and this is due to more cooling and power are generated during this scenario as discussed above. Results show acceptable agreements between the experimental and the simulation data for the COPe and SCPe with maximum deviations of about 13.6% and 14.1% respectively.

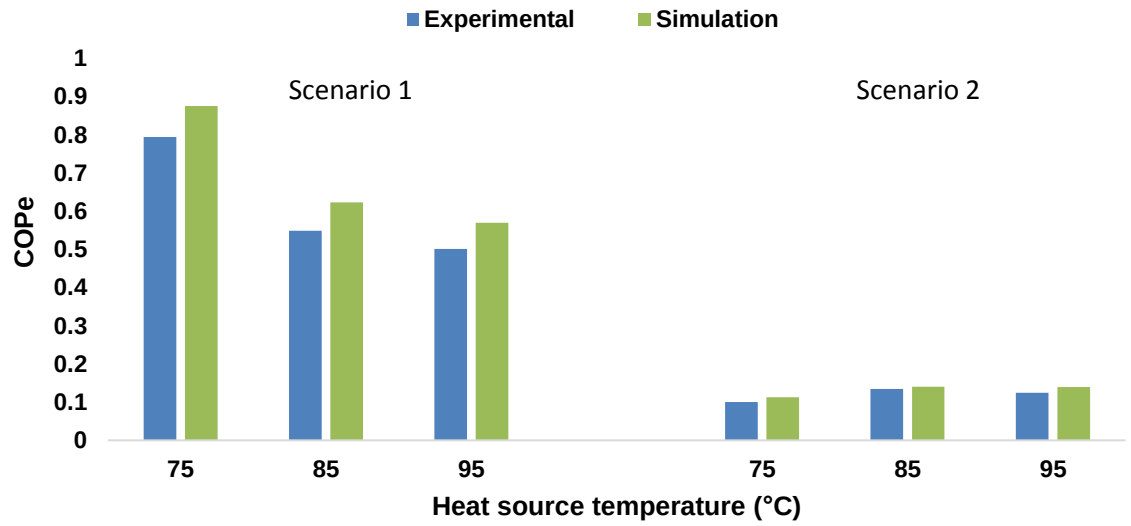

Figure 7-38: Experimental and numerical values of COPe for the IAOSCE utilizing CPO-27(Ni) /water and R245fa with half cycle time, condenser temperature and adsorption evaporator temperature of 700 s, 16 °C and 8 °C respectively

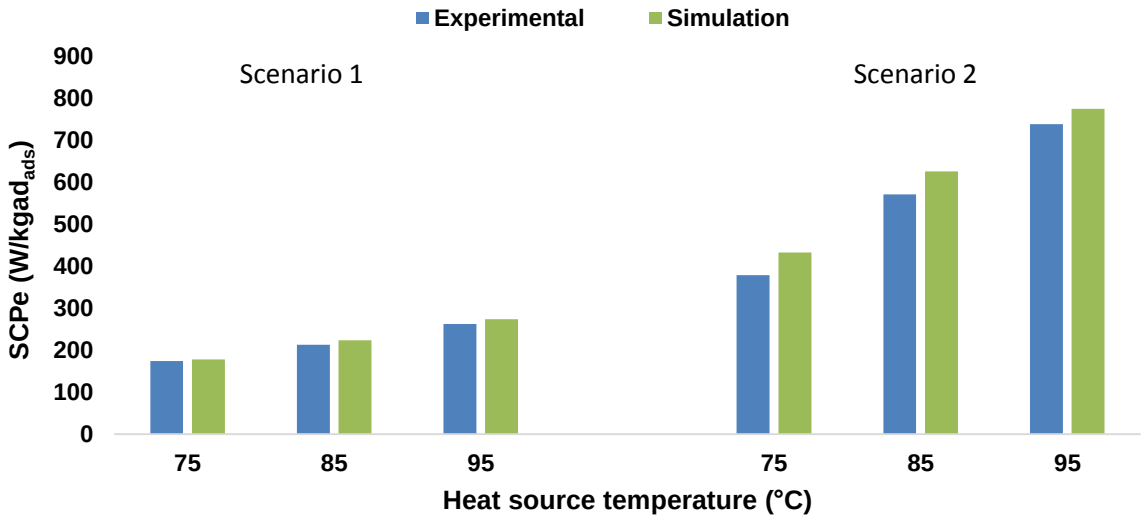

Figure 7-39: Experimental and numerical values of SCPe for the IAOSCE utilizing CPO-27(Ni) /water and R245fa with half cycle time, condenser temperature and adsorption evaporator temperature of 700 s, 16 °C and 8 °C respectively

Currently, the ORC turbine used in this experimental study has low efficiency ranging from 35% to 50%, however using efficient turbine in the ORC system is essential as its performance can affect directly the overall performance of the IAOSCE. Two efficient radial inflow turbines namely ORC1 and ORC2 have been designed in Chapter 6 using 3D CFD

modelling to work efficiently with scenarios 1 and 2 of the IAOSCE with maximum efficiency of 89% and 88% respectively. As a result, using these turbines with the design conditions can be reflected significantly on the amount of power generated by the ORC system which enhances the overall performance of the IAOSCE in terms of COPe, SCPe and SP.

Figure 7-40 shows the effect of inlet chilled water temperature on the COP and SCP for the CPO-27(Ni)/water adsorption cooling system only. Results show that as the chilled water temperature increases COP increases, while SCP decreases.

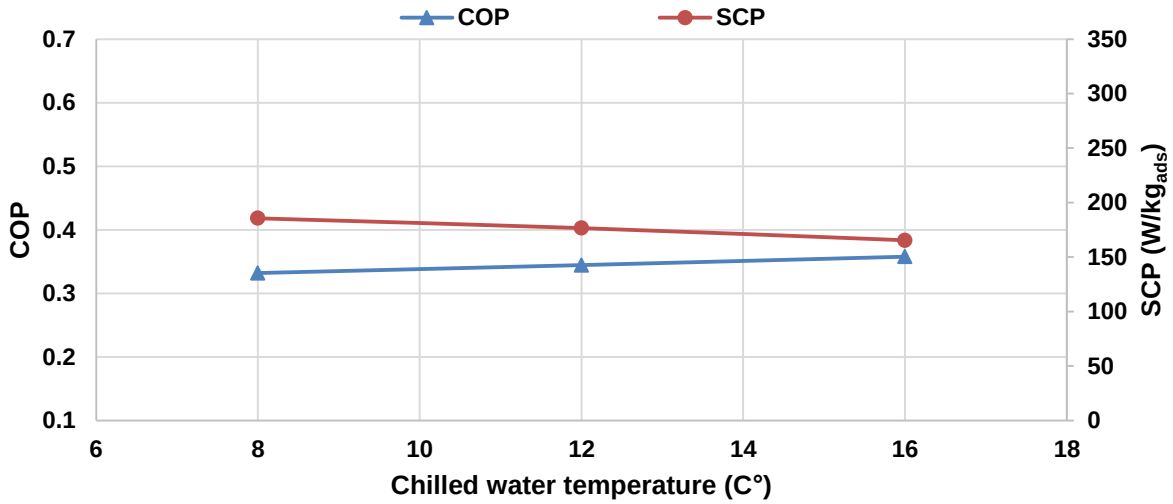

Figure 7-40: Experimental values of COP and SCP for the two-bed water adsorption system using CPO-27(Ni) with a range of chilled water temperatures at half cycle time, heat source temperature, and condenser temperature of 700 s, 85 °C and 16 °C respectively

Figure 7-41 illustrates the effect of the condenser cooling water temperature on the COP and SCP for the CPO-27(Ni)/water adsorption cooling system only. It was found that as the condenser inlet water temperature increases, the COP and SCP decrease. Figure 7-42 illustrates the effect of half cycle time on the COP and SCP for the adsorption cooling system

only utilising CPO-27(Ni)/water. Also, as the half cycle time increases, COP increases, while SCP decreases.

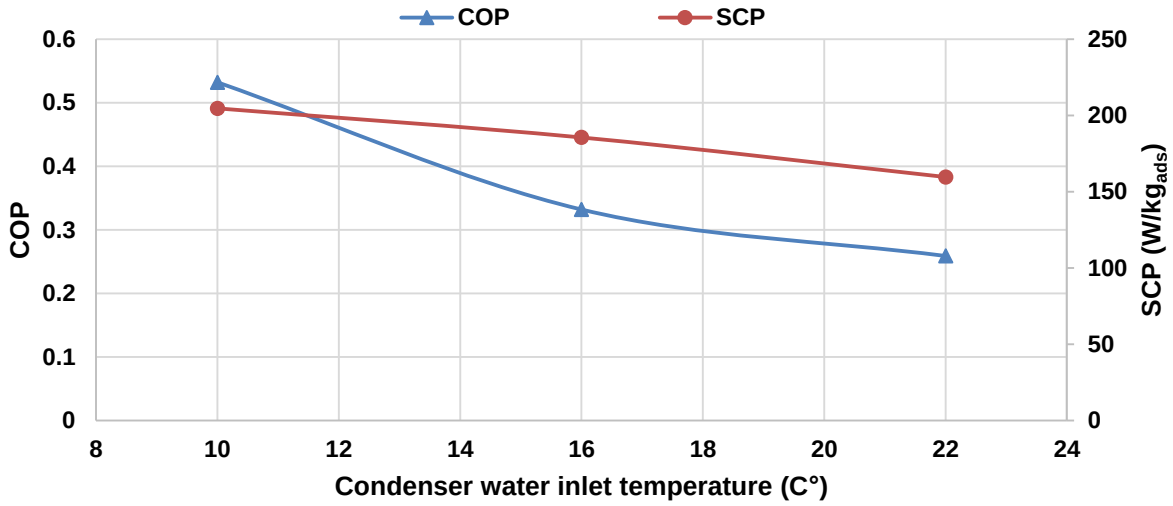

Figure 7-41: Experimental values of COP and SCP for the two-bed water adsorption system using CPO-27(Ni) with a range of condenser cooling water temperatures at half cycle time, heat source temperature, and evaporator temperature of 700 s, 85 °C and 8 °C respectively

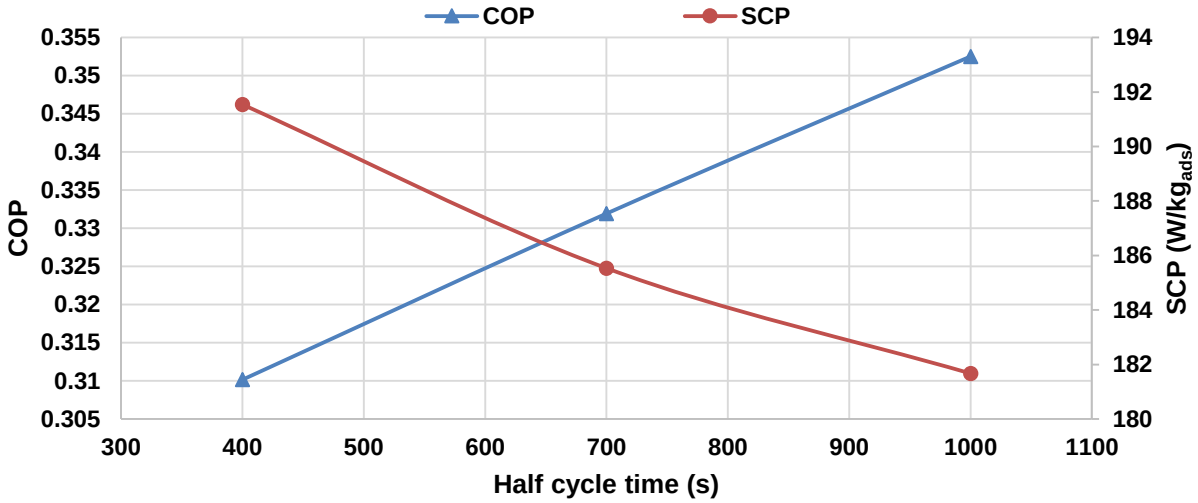

Figure 7-42: Experimental values of COP and SCP for the two-bed water adsorption system using CPO-27(Ni) with a range of half-cycle time, at heat source temperature, condenser temperature and evaporator temperature of 85 °C 16 °C and 8 °C respectively

This work highlights the feasibility of generating cooling and electricity simultaneously from an integrated adsorption-ORC system utilising CPO-27(Ni)/water and R245fa. None of the

previous work studied the integrated adsorption-ORC system for cooling and electricity using the proposed two scenarios, where the adsorption system is set as a topping system, while ORC cycle as a bottoming system. Compared to [117], [118], and [119], this study has the advantage of recovering the heat of adsorption and generating higher COPe. In addition, the two integrating scenarios investigated in this study can offer good options for energy designers and consumers to use the appropriate scenario of integration for different applications. Even though scenario 2 can generate relatively higher SCP, SP and SCPe than scenario 1, the COPe of this scenario is relatively low compared to that of scenario 1. However, if the heat source used is infinite or semi-infinite like solar energy this scenario can be more advantageous.

7.10 Summary

In this chapter, each component of the experimental facility namely the integrated adsorption-ORC system for cooling and power generation has been described. The test facility consists mainly of two adsorber beds, adsorption condenser, and adsorption evaporator in the adsorption system, while in the ORC system, it has ORC evaporator, ORC condenser, ORC pump and radial inflow turbine. Two scenarios of integrating adsorption system with ORC cycle utilising CPO-27(Ni) as an adsorbent material and R245fa as an ORC working fluid have been investigated experimentally. The experimental study validated the numerical models of the two-bed adsorption system and the ORC cycle individually, also, it validated the integrated adsorption-ORC system as one system where good agreements were obtained with a maximum deviation of less than 17%. Experimental results also showed that maximum COPe of 0.79 can be achieved using scenario 1 at heat source temperature of 75 °C, while maximum SCPe of 739 W/kg_{ads} can be achieved using scenario 2 with heat source temperature of 95 °C.

CHAPTER EIGHT
CONCLUSIONS AND RECOMMENDATIONS

8.1 Introduction

For decades, fossil fuels are still one of the most important energy sources, however, this leads to rapid depletion of such important resources and production of global warming gases like CO_2. Worldwide, one of the main energy consumption sectors is air conditioning of buildings, especially in hot countries. Low-grade heat driven cooling and electricity systems like adsorption and Organic Rankine Cycle (ORC) offer environmentally friendly technology that can reduce dependence on traditional systems [20, 28, 64].

This thesis investigated numerically and experimentally, the feasibility of producing electricity and cooling at the same time using adsorption and ORC systems driven by low-grade heat sources. Two novel configurations of adsorption system are developed to improve the overall system performance and upgrade the adsorption cooling system to produce cooling and electricity simultaneously using one unit. Also, several novel scenarios of integrating adsorption cooling system with Organic Rankine Cycle have been investigated. This helps to build localised cogeneration units that can meet the cooling and electricity requirements of houses and offices and improve the overall heat utilization performance. Such systems can

help to find affordable, reliable and clean power systems especially in developing countries and remote areas, where millions of people lack access to secure electrical grids.

Advanced physical adsorbent materials with superior water adsorption characteristics like CPO-27(Ni), MIL101(Cr), and Al-Fumarate MOFs and AQSOA-Z02 zeolite have been used in this investigation for the first time to produce cooling and power at the same time [20, 28, 64]. The water adsorption characteristics of MIL101(Cr) and AQSOA-ZO2 are experimentally tested using a DVS analyser to be used in the numerical investigation. Numerical models of different operating scenarios for the two configurations are developed using MATLAB Simulink software. Also, in this thesis 3D CFD modelling designs of small-scale radial inflow turbines are developed to work efficiently with the different configurations and scenarios. Finally, based on the numerical investigation, an experimental facility is built to study the performance of the integrated adsorption system for cooling and electricity and validate the numerical results.

8.2 Conclusions

8.2.1 Conclusions of the first configuration (ASCE)

In this configuration, the basic two-bed adsorption cooling system (BACS) is improved by including an expander (turbine) between the hot adsorber bed and the condenser to produce cooling and electricity (ASCE) simultaneously [20]. This configuration can also utilise multiple bed arrangements namely; two-bed, three-bed, four-bed, five-bed and six-bed and employ different adsorption/desorption time allocations corresponding to each case. The following points summarize the main conclusions of this configuration:

1. The adsorption system for cooling and electricity ASCE is feasible and can generate cooling and power of up to 800 W/kg_{ads} and 80 W/kg_{ads} respectively utilising CPO-27(Ni) MOFs. Moreover, incorporating the expander with the basic adsorption cooling system

(BACS) has improved the overall system coefficient of performance (COP) from 0.7 to 0.8 for heat source temperature ranging from 100 and 160 °C. Also, the equivalent specific cooling power is increased from 892 W/kg_{ads} using BACS to 1040 W/kg_{ads} using ASCE. Results also showed that, as the heat source temperature increases, the cooling and the electricity generated increase for all adsorbent pairs used in this work.

2. For different adsorbent pairs and heat source temperatures used with ASCE, the exergy efficiency of ASCE is greater than that of BACS (except for CPO-27(Ni)/water at 100 °C).
3. For the multi-bed utilisation in ASCE, results show that, the two-bed system with R=1 (R is ratio of the total adsorption time to the total desorption time) has the highest coefficient of performance (COP) values for all adsorbent materials and heat source temperatures used with maximum value of 0.7. For the specific cooling power (SCP) and specific power (SP), three-bed arrangement with R=½ shows the highest values using Silica-gel and Al-Fumarate. For AQSOA-Z02 the three-bed arrangement with R=½ shows the maximum SCP of 678 W/kg_{ads} and SP of 67 W/kg_{ads} at heat source temperature of 160 °C, while for CPO-27(Ni) the two-bed arrangement with R=1 shows the maximum SCP of 800 W/kg_{ads} and SP of 80 W/kg_{ads} at heat source temperature of 160 °C. Also results show that, as the number of bed increases, more stability in cooling and power can be obtained.
4. Hybrid adsorption system for cooling and electricity (HASCE) is another form of the first configuration (ASCE) with four beds and two evaporators. HASCE shows higher equivalent coefficient of performance (COPe) with maximum value of 0.97 compared to maximum COPe of 0.8 achieved by ASCE, but with relatively lower cooling and electricity outputs.

8.2.2 Conclusions of the second configuration (IAOSCE)

In this configuration, the basic adsorption cooling system (BACS) is combined with a basic ORC cycle to form an integrated adsorption-ORC system for cooling and electricity (IAOSCE). Four innovative scenarios based on the way of integration and the method of powering the adsorption and the ORC systems were investigated. For the first three scenarios, the adsorption system is set up as a topping system, and ORC is set up as a bottoming system, while for the last scenario, ORC is considered to be as a topping cycle, and the adsorption system as bottoming cycle. In scenario 1, the adsorption system is powered by an external heat source, while the ORC is powered by cooling line leaving the adsorption side after recovering the heat of adsorption. Scenario 2 is similar to scenario 1, but ORC is powered by the heating source after leaving the adsorption system. In scenario 3, the cooling and heating lines of the adsorption system are mixed to power the ORC, while in scenario 4 ORC is powered by an external source and the adsorption system is powered by the heating source after leaving the ORC. The second configuration is also investigated with two expanders one in the adsorption system and the other in the ORC to increase the power generated with similar four integration scenarios.

1. Results show that the integrated adsorption-ORC systems for cooling and electricity with one expander (IAOSCE-1EXP) and two expanders (IAOSCE-2EXP) are feasible and can generate cooling and power simultaneously.
2. In terms of using different integration scenarios, scenario 1 of the IAOSCE-1EXP and the IAOSCE-2EXP produce the maximum equivalent coefficient of performance of 1.14 and 1.27 respectively using Silica-gel and R141b at heating temperature of 80 ºC. On the other hand, scenario 2 achieves the maximum equivalent specific cooling power of about 2311 W/kg_{ad}s with IAOSCE-1EXP and 2460 W/kg_{ads} IAOSCE-2EXP using CPO-27(Ni) and R141b at heat source temperature of 160 ºC. Also, scenario 4 shows relatively high SP

and SCP with COPe approaching 0.6, so it can be considered as a good scenario when compromising between the amount of cooling, power and the equivalent coefficient of performance (COPe).

3. The proposed scenarios can offer more options for designers and consumers to choose the suitable system for the different applications. For instance, if the available heat source is infinite as solar energy, scenarios 2 and 4 are more practical, because they generate more amounts of cooling and power and this leads to cheap and compact systems as they have a smaller size. In contrast, if the heat source is limited, scenario 1 may be preferable because of its high equivalent coefficient of performance (COPe).
4. The IAOSCE shows maximum exergy efficiency of 54.5 and 57.6 % for the cases of one expander and two expanders respectively utilising CPO-27(Ni) and R141b at heat source temperature of 120 ºC.

8.2.3 General conclusions

1. This study showed that adsorption technology can generate cooling and electricity simultaneously by integrating the adsorption cooling system with an expander or by using an adsorption-ORC combination [20, 28, 64] .
2. Compared to previous work, the advanced physical adsorbent materials utilised in this work like CPO-27(Ni) and ZQSOA-Z02 show higher coefficient of performance (COP), specific cooling power (SCP) and specific power (SP) than these of the cogeneration chemisorption systems reported in the literature.
3. Generating cooling and electricity simultaneously is more effective at heat source temperature higher than 120 °C and generally as the heat source temperature increases, the specific cooling power (SCP) and specific power (SP) increase [20].

4. In terms of equivalent coefficient of performance (COPe), scenario 1 of configuration 2 (IAOSCE-2EXP) shows a maximum value of 1.27 utilising Silica-gel and R141b at heat source temperature of 80 ºC, however, this case shows low SCPe compared to the other cases.
5. In terms of equivalent specific cooling power (SCPe) and specific power (SP), scenario 2 of configuration 2 (IAOSCE-2EXP) shows a maximum value of 2460 W/kg_{ads} and 553W/kg_{ads} respectively utilising CPO-27(Ni) and R141b with heat source temperature of 160 ºC.
6. In terms of compromising between the coefficient of performance (COPe) and the specific cooling power (SCPe), scenario 4 shows relatively high SCPe of 2242 W/kg_{ads} with a COPe value approaching 0.6, so this scenario can also be considered a good option.
7. In terms of exergy efficiency, scenario 2 of the IAOSCE-2EXP has the maximum exergy efficiency of about 57.6% utilising CPO-27(Ni) and R141b at 120 ºC for a heat source temperature ranging between 120 and 160 ºC.
8. CFD results show that a steam radial inflow turbine can be designed to meet the requirements of the ASCE with maximum efficiency of 85%, also additional two ORC radial inflow turbines can be designed to meet the requirement of the IAOSCE with maximum efficiency of 89% and 88% respectively.
9. Experimental results show that combing an adsorption cooling system with an ORC system (IAOSCE) is feasible and the integrated system can generate cooling and power simultaneously with maximum COPe of 0.79 using scenario 1 at heating temperature of 75 °C, while maximum SCPe of 739 W/kg_{ads} can be achieved using scenario 2 with heat source temperature of 95 °C. Also satisfactory agreements between the experimental and numerical results was obtained with a maximum deviation of less than 17%.

8.3 Recommendations and future work

In order to further enhance the performance of the adsorption systems for cooling and electricity investigated in this thesis, a number of recommendations for future work are listed below:

1. This project covers the integration of the basic adsorption cooling system with the basic ORC system. It is suggested that advanced adsorption cooling systems such as multi-bed, multi-stage and heat recovery systems to be investigated. Also, advanced ORC cycles like supercritical ORC and pumpless ORC are suggested to improve the integrated system performance.
2. This thesis presents the construction of an experimental facility for the integrated adsorption-ORC system for cooling and electricity with one expander. It is suggested to use additional steam expander in the adsorption side to improve the overall performance of the integration system.
3. As the adsorbent materials are the main drive of the adsorption system for cooling and electricity, more investigations of new adsorption pairs with better adsorption characteristics are suggested. Also for the ORC side, further ORC fluids are suggested to be investigated to increase efficiency and power generation from the ORC system.
4. More experimental and numerical studies including the CFD modelling for the adsorbent bed heat exchanger are recommended to improve its performance as it is a key component of any adsorption system.
5. It is recommended to develop a two-stage small-scale turbine for the adsorption system for cooling and electricity including the steam and ORC turbines in order to exploit the high-pressure ratio that usually available and prevent the supersonic flow.

6. For large scale adsorption systems generating cooling and electricity, axial turbines can be a more effective option for the steam or the ORC turbines. It is recommended to carry out a detailed CFD design of this turbine type to be integrated within such adsorption systems for cooling and electricity generation.

APPENDIX A
VISTA RTD DESIGN

Vista RTD is a software for the mean-line design of radial inflow turbine and it can be run directly from the ANSYS Workbench as shown in Figure A-1. The 1D design geometry generated by VISTA RTD can be passed to the BladeGen tool.

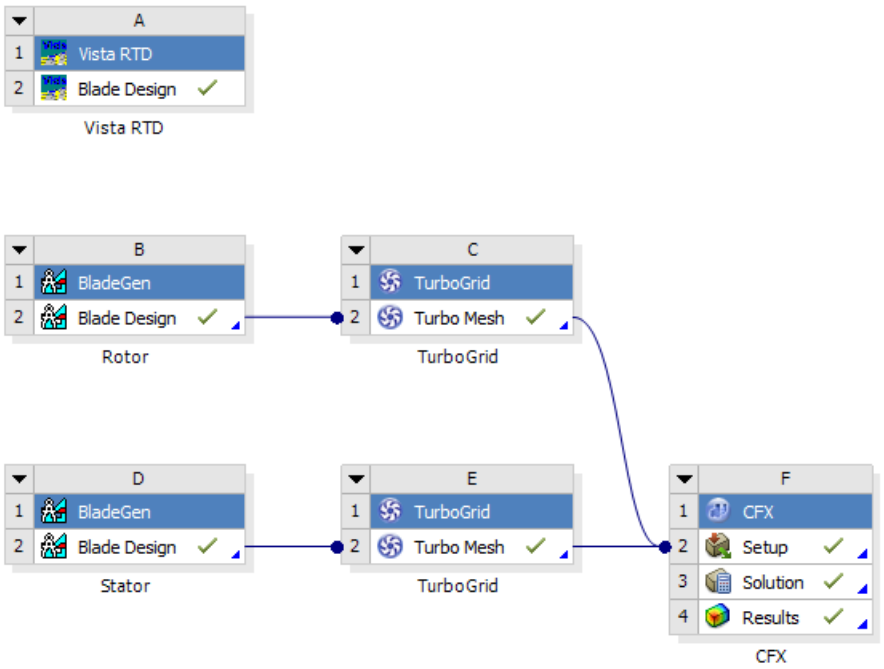

Figure A-1: Project schematic of an ANSYS Workbench

Figure A-2 Figure A-3 Figure A-4 and Figure A-5 show the main four windows of the Vista RTD software. The operating conditions and the fluid properties can be defined using the Aerodynamics window as shown in Figure A-2. The impeller diameters, the number of blades, and the tip clearance can be defined using the Geometry window as shown in Figure A-3. The design results and the velocity triangles are presented in the Results and velocity windows as shown in Figure A-4 and Figure A-5.

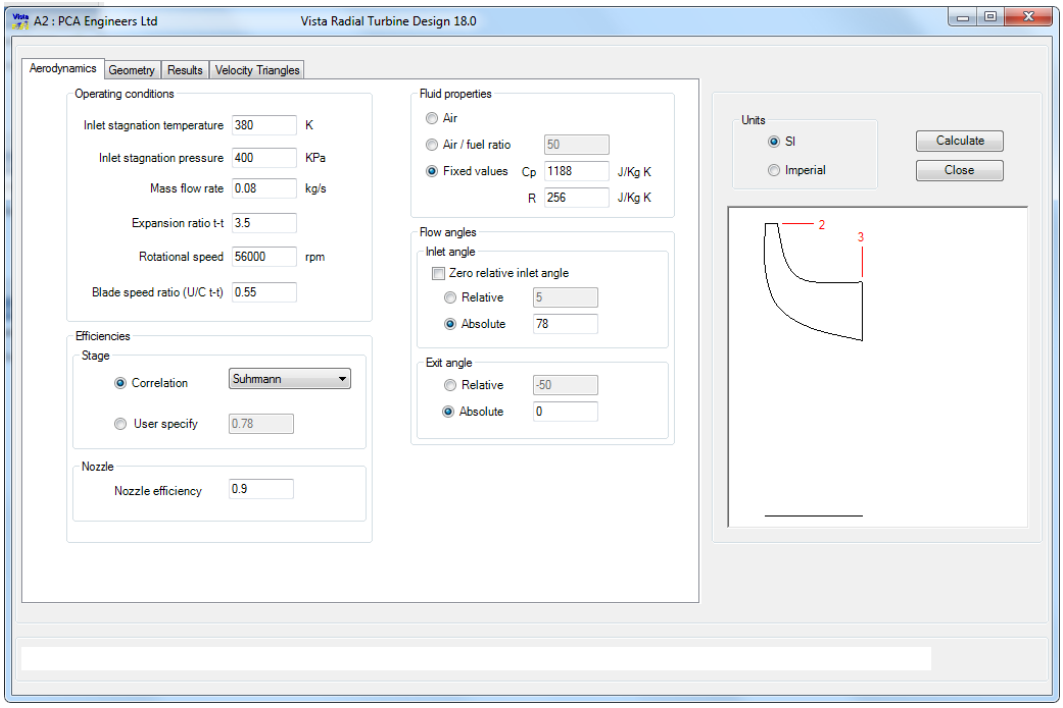

Figure A-2: Aerodynamic window in Vista RTD which defines the operating conditions, the fluid properties, and the flow angles

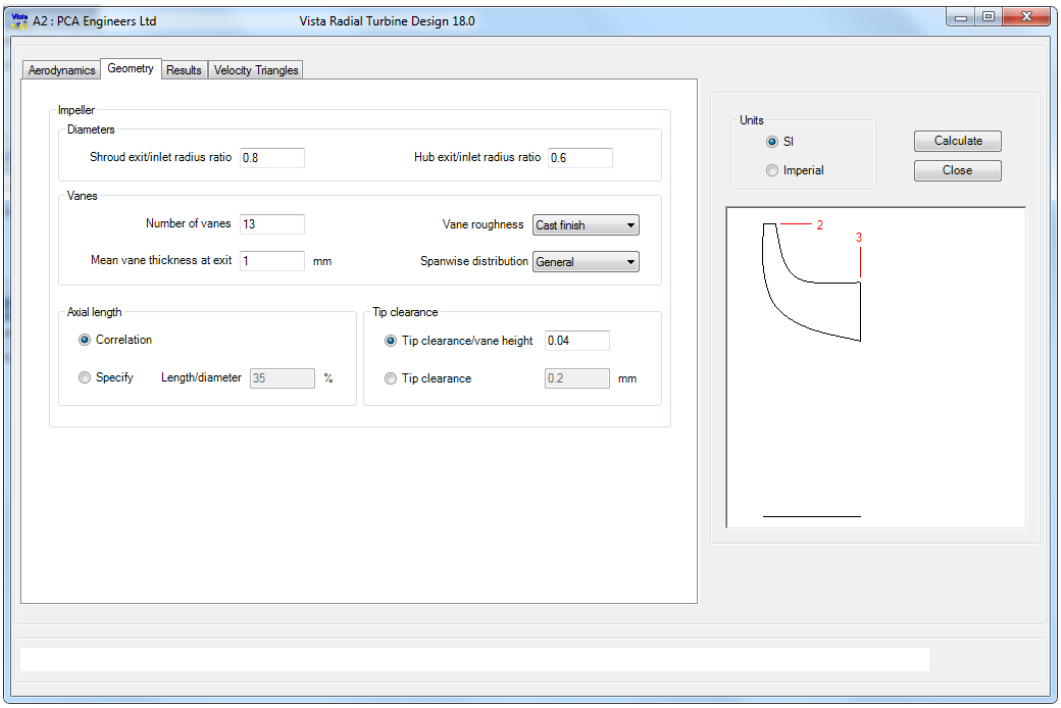

Figure A-3: Geometry window in Vista RTD which defines the impeller diameters, the number of blades, and the tip clearance

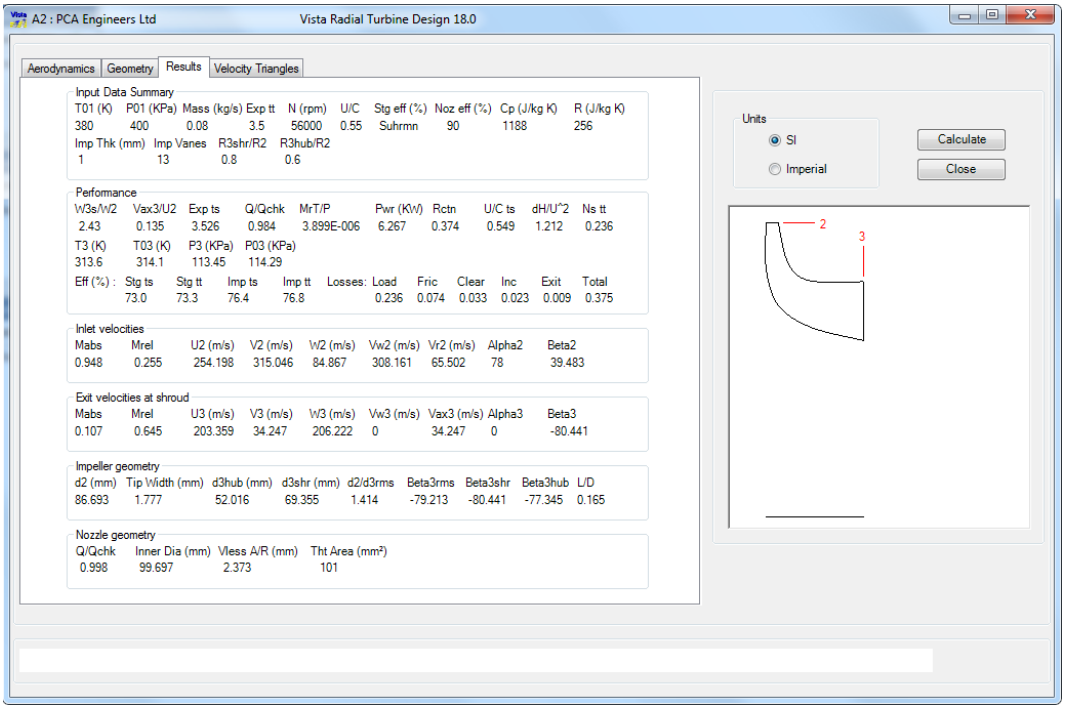

Figure A-4: Results window in Vista RTD which provides information about the turbine performance, and the rotor/stator geometries

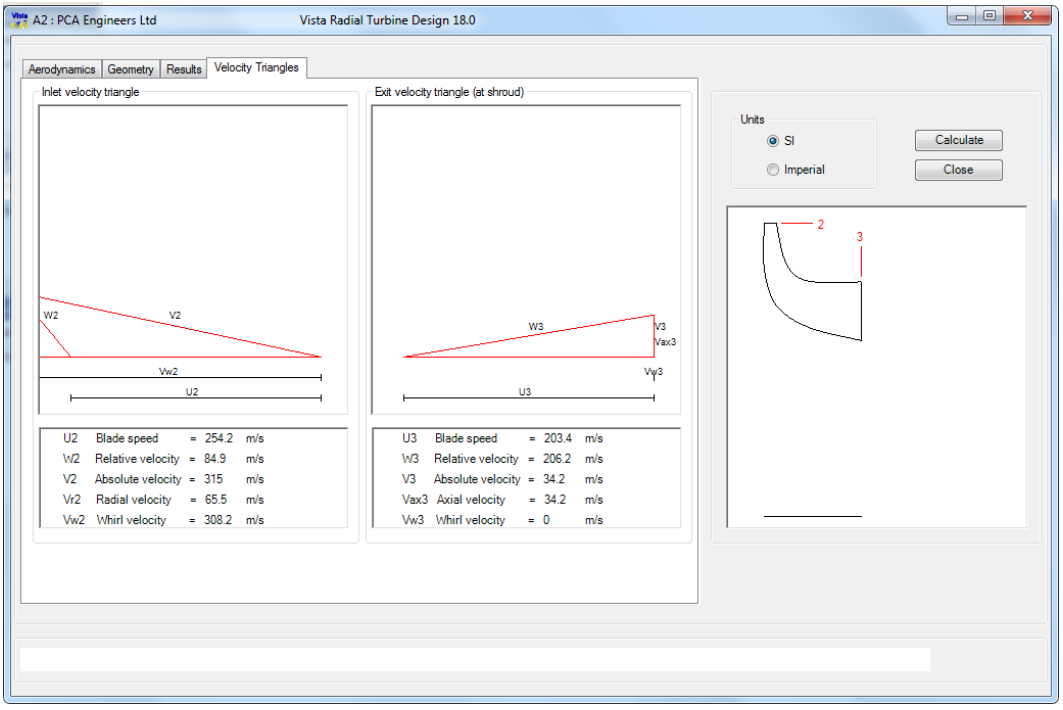

Figure A-5: Velocity triangles window in Vista RTD

APPENDIX B

TURBINE CAD DRAWINGS

Figure B-1 shows the 3D assembly of the radial inflow turbine used in the experimental facility. Figure B-2 and Figure B-3 show the three and two dimensional of the rotor and the stator respectively.

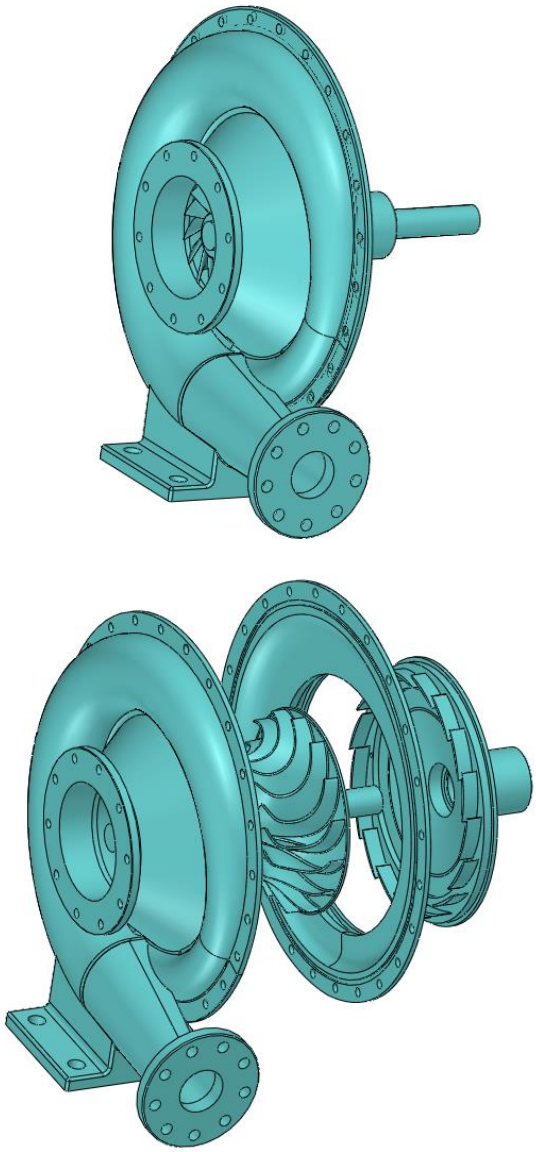

Figure B-1: Three-dimensional assembly of radial inflow turbine

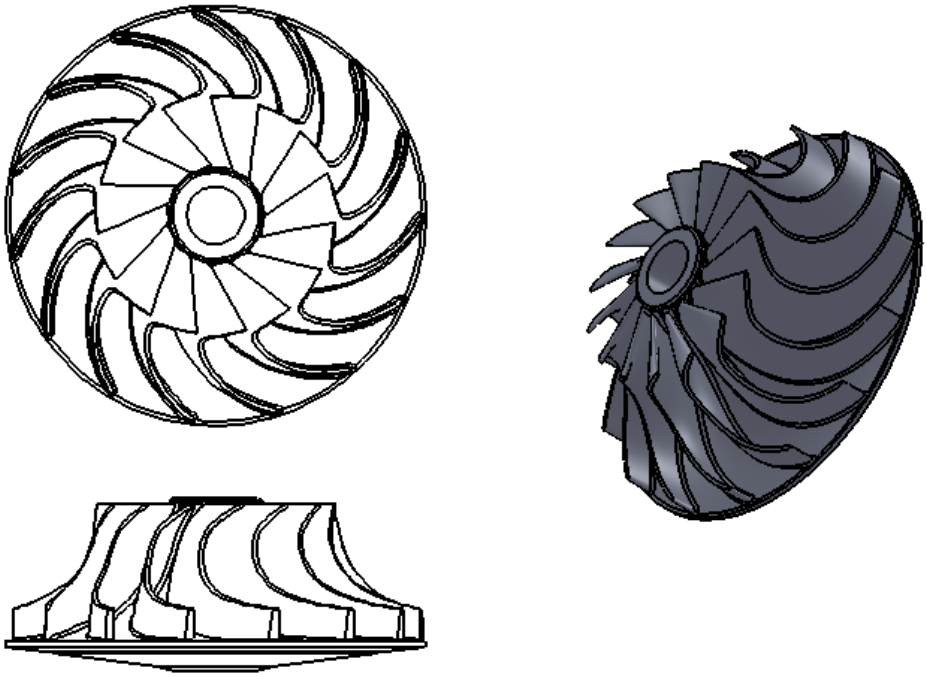

Figure B-2: Two and three-dimensional rotor drawing

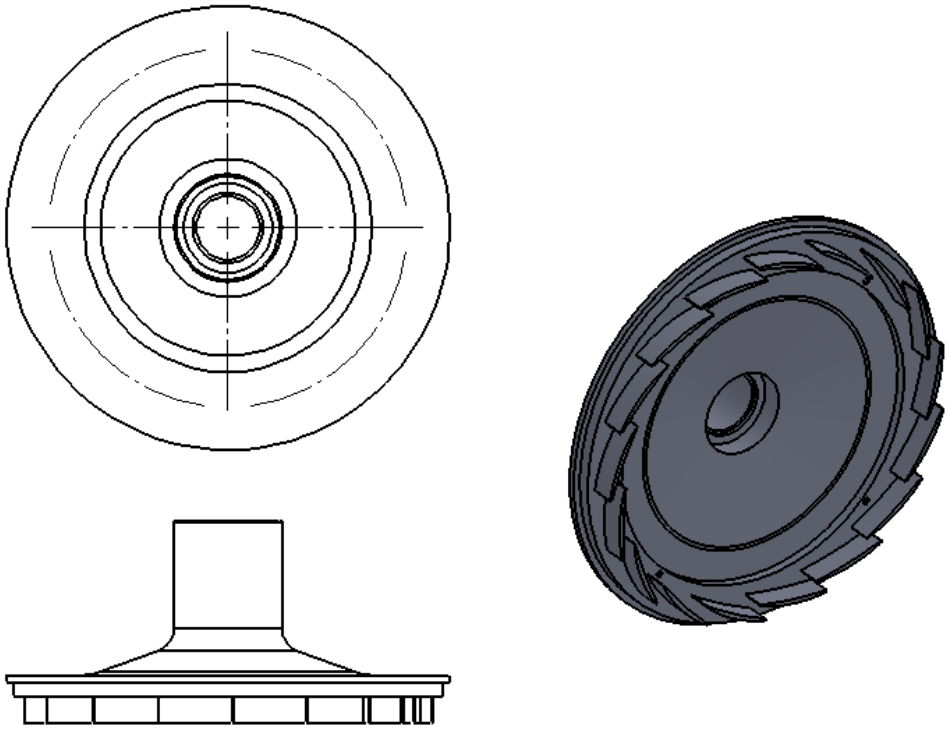

Figure B-3: Two and three-dimensional stator drawing

APPENDIX C
INSTRUMENTS CALIBRATION AND UNCERTAINTIES

C.1 Instruments calibration and curve fitting

The type K thermocouples, the RTD temperature sensors and the pressure transducers used in the experimental facility are calibrated and their uncertainties are calculated using the root square summation method and they are listed in Chapter 7 section 7.9.

C.2.1 Thermocouples curve fitting

The curve fittings of the thermocouples type K are listed in Figure C-1, while the curve fittings of the RTD sensors are listed in Figure C-2, Figure C-3, Figure C-4, and Figure C-5.

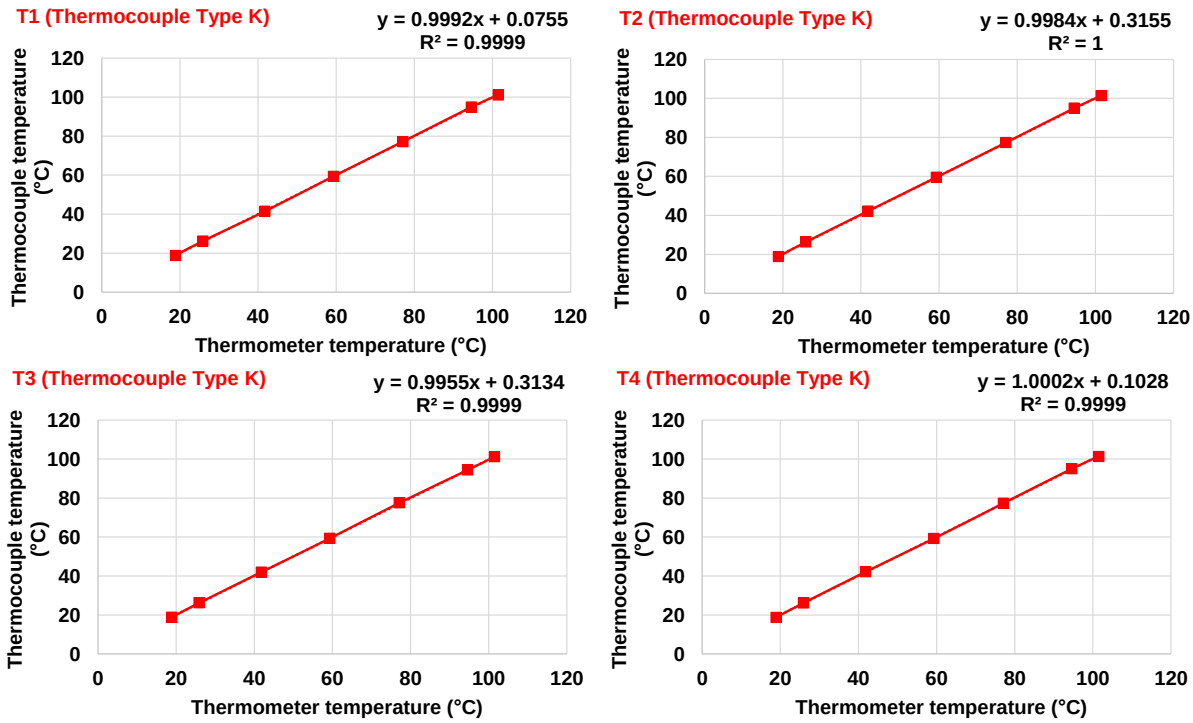

Figure C-1: Curve fitting of the thermocouples type K (T1, T2, T3, and T4)

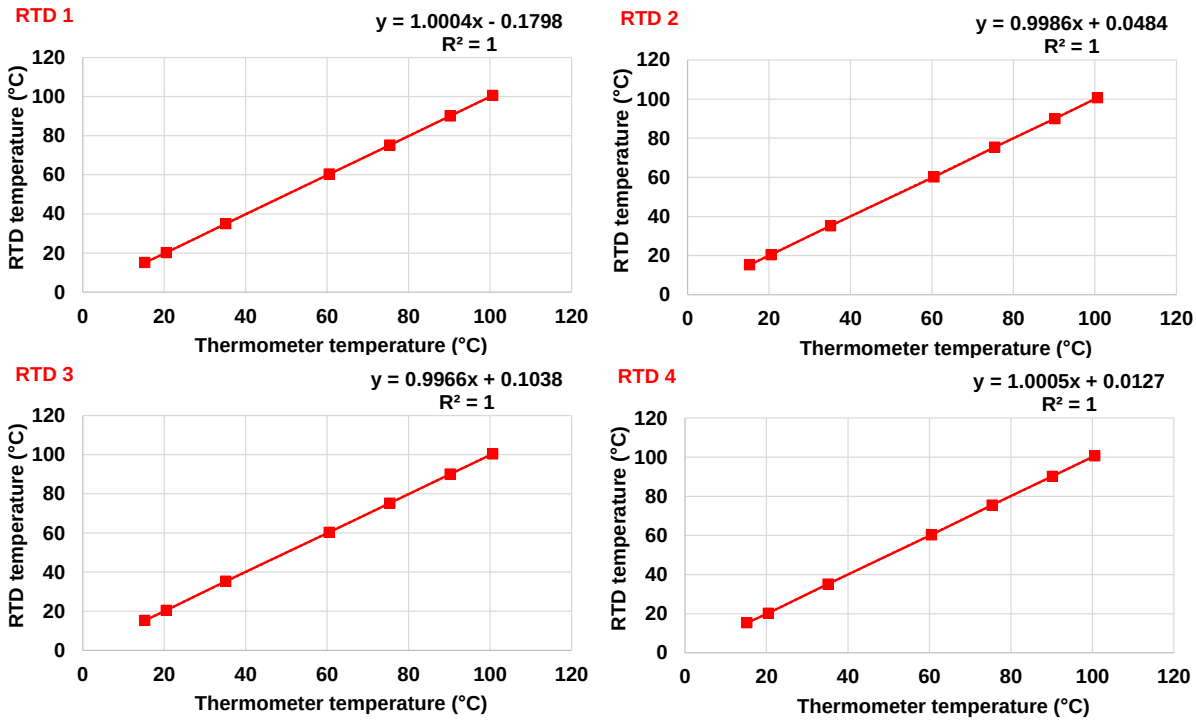

Figure C-2: Curve fitting of the RTD sensors (RTD 1, RTD 2, RTD 3, and RTD 4)

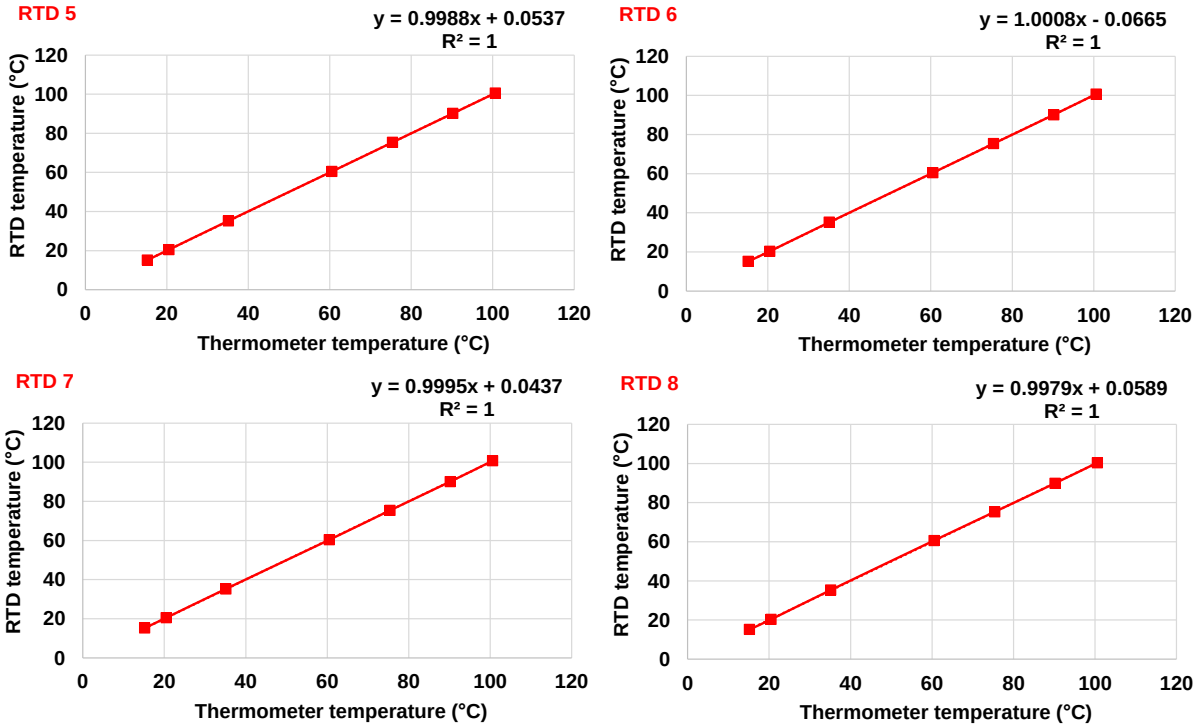

Figure C-3: Curve fitting of the RTD sensors (RTD 5, RTD 6, RTD 7, and RTD 8)

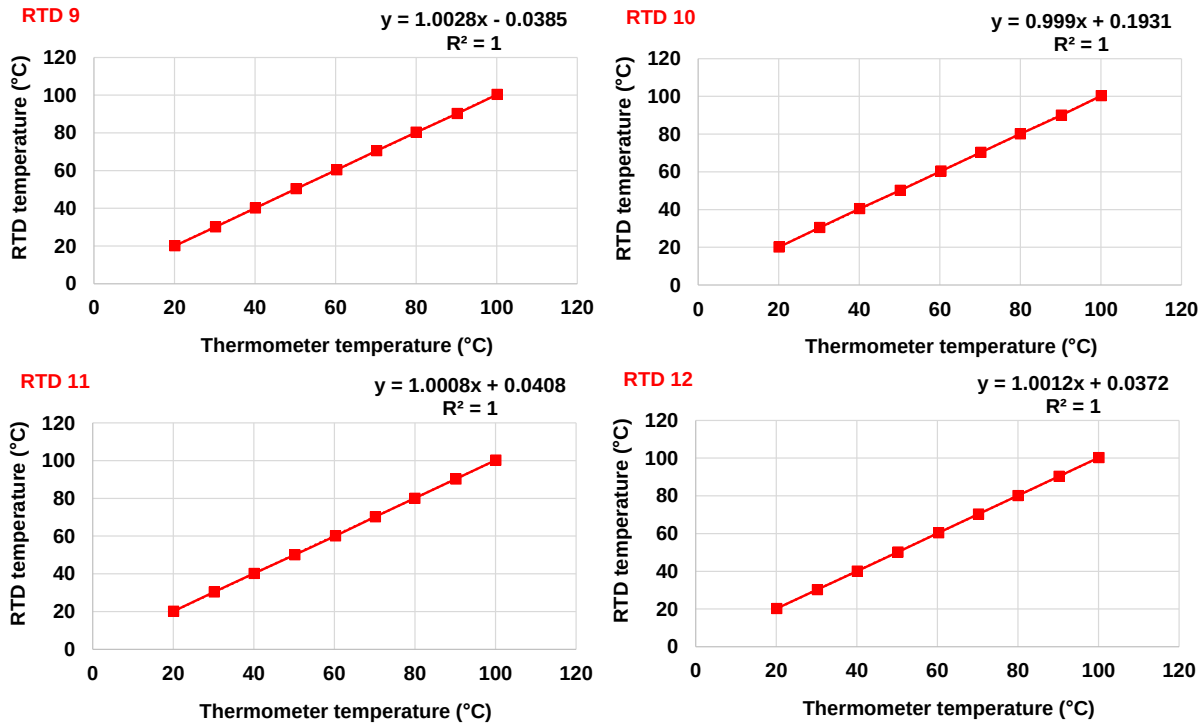

Figure C-4: Curve fitting of the RTD sensors (RTD 9, RTD 10, RTD 11, and RTD 12)

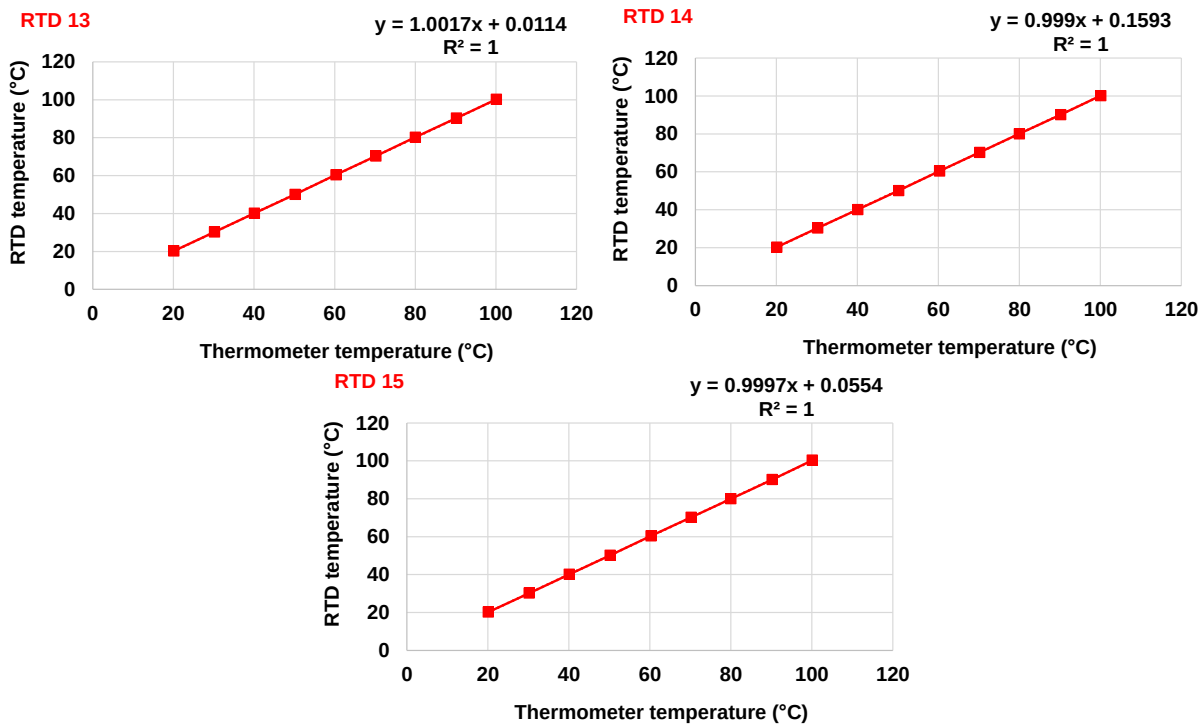

Figure C-5: Curve fitting of the RTD sensors (RTD 13, RTD 14, and RTD 15)

C.2.2 Pressure transducers curve fitting

The curve fittings of the pressure transducers are listed in Figure C-6.

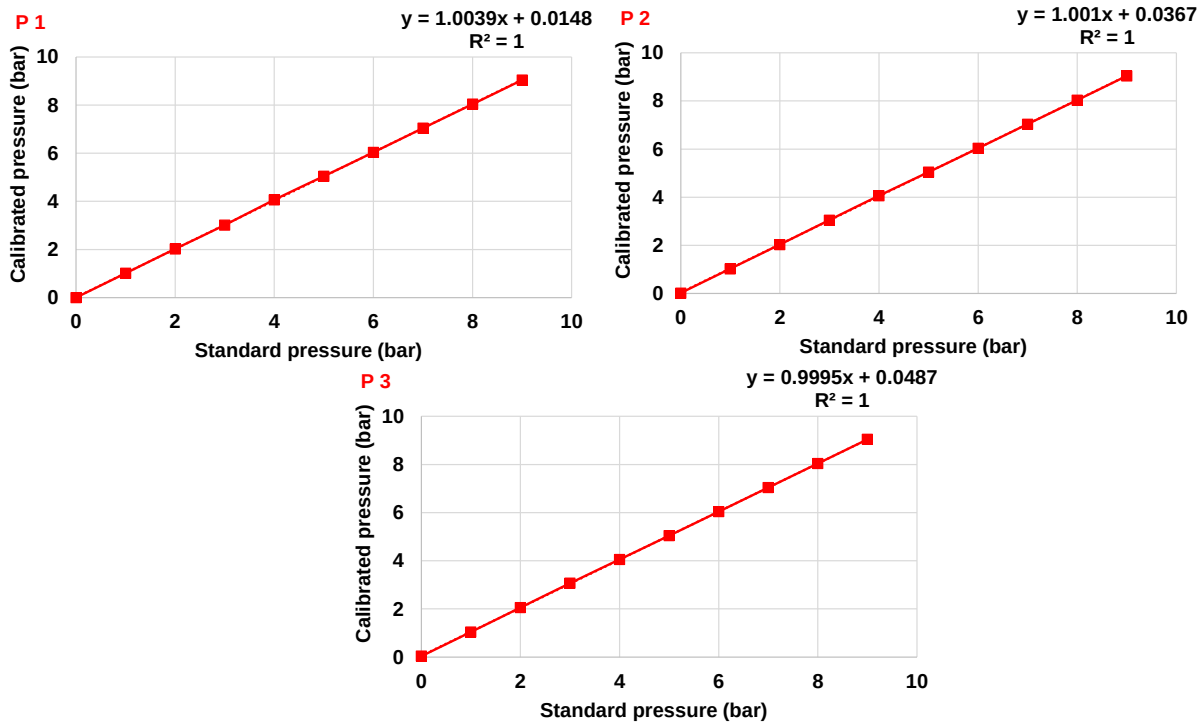

Figure C-6: Curve fitting of the pressure transducer (P1, P2, and P3)

C.3 Uncertainty propagation

Root Square Sum method is used to calculate the overall uncertainty for any parameter [233] as:

$$U_{Overall} = \pm\sqrt{U_{Sys}^2 + U_{curve-fitting}^2} \quad \text{C-1}$$

Where $U_{overall}$ is the overall uncertainty, U_{st} is the standard uncertainty, and $U_{curve\text{-}fitting}$ is curve fitting uncertainty.

Standard mean deviation method is used to calculate U_{random}, as below:

$$U_{curve-fitting} = t_{n-1,95\%} S_x \quad \text{C-2}$$

Where, $t_{n-1,95\%}$ is the student distribution coefficient with 95% confidence level, and S_x is the mean deviation which can be determined using:

$$S_x = \frac{\sigma}{\sqrt{n}} \quad \text{C-3}$$

σ is the standard deviation which can be determined [234] as:

$$\sigma = \left(\frac{\sum_{i=1}^{n}(x_i - \bar{x})^2}{n-1}\right)^{1/2} \quad \text{C-4}$$

Where x_i is the experimental instrument reading (such as thermocouple), $\bar{x}$ is the cure fitting value, $(x_i - \bar{x})^2$ is the deviation squared. A detailed calculation sample of an RTD sensor (RTD1) is listed in Table C-1.

Table C-1: Uncertainty detailed calculation sample of an RTD sensor (RTD1)

No	Standard reading	Measured reading	Fitting (y=1.0004x-0.1798)	Deviation $(x_i - \bar{x})^2$
1	15.2	15.1531	14.97886	0.048902
2	20.5	20.2041	20.03188	0.219135
3	35.1	34.9612	34.79488	0.093095
4	60.5	60.3147	60.15853	0.116605
5	75.4	75.1699	75.01967	0.144652
6	90.2	90.0652	89.92093	0.077882
7	100.6	100.5139	100.3738	0.051164

$\sum_{j=1}^{n}(x_i - \bar{x})^2$= 0.751435843
σ = 0.35389166
S_x = 0.133758475
t(n-1,95%) = 2.447
U_curve _fitting = 0.327306988
U_standard =0.03
U_overall = 0.328678969 °C

The main output parameters like cooling capacity and electricity are assumed to be a function of n measurements variables [233].

$$Y = f(x_1, x_2, x_3, \ldots., x_n) \quad \text{C-5}$$

The uncertainty in the output parameters can be calculated using the flowing equation as:

$$U_Y = \left[\left(\frac{\partial Y}{\partial x_1} U_{x_1}\right)^2 + \left(\frac{\partial Y}{\partial x_2} U_{x_2}\right)^2 + \left(\frac{\partial Y}{\partial x_3} U_{x_3}\right)^2 + \cdots + \left(\frac{\partial Y}{\partial x_n} U_{x_n}\right)^2\right]^{1/2} \quad \text{C-6}$$

The cooling capacity is calculated using the following equation:

$$q_{cooling} = \dot{m}\, C_p (T_{ch,in} - T_{ch,out}) \quad \text{C-7}$$

Therefore the uncertainty $U_{cooling}$ in determining the cooling capacity can be calculated as:

$$U_{cooling} = \sqrt{\left(\frac{\partial q_{cooling}}{\partial \dot{m}} U_{\dot{m}}\right)^2 + \left(\frac{\partial q_{cooling}}{\partial T_{ch,in}} U_{T_{ch,in}}\right)^2 + \left(\frac{\partial q_{cooling}}{\partial T_{ch,out}} U_{T_{ch,out}}\right)^2} \quad \text{C-8}$$

$U_{\dot{m}}$, $U_{T_{ch,in}}$, and $U_{T_{ch,out}}$ are the uncertainties of the adsorption evaporator flow meter, inlet and exit chilled water temperatures respectively.

The power (in Watt) is calculated depending on the following equation:

$$P = \frac{2\pi NT}{60} \quad \text{C-9}$$

N, and T are the revolution velocity (rpm) and the torque (Nm) respectively. The power uncertainty U_P can be calculated as:

$$U_P = \sqrt{(\frac{\partial P}{\partial N} U_N)^2 + (\frac{\partial P}{\partial T} U_T)^2} \quad \text{C-10}$$

U_N, and U_T are the uncertainties in the measured rotational speed and torque respectively. The propagated uncertainties of the cooling and electricity are listed Chapter 7 section 7.9.

REFERENCES

[1] Sarbu I, Sebarchievici C. General review of solar-powered closed sorption refrigeration systems. Energy Conversion and Management. 2015;105:403-22.

[2] Chan CW, Ling-Chin J, Roskilly AP. A review of chemical heat pumps, thermodynamic cycles and thermal energy storage technologies for low grade heat utilisation. Applied Thermal Engineering. 2013;50:1257-73.

[3] Kannan N, Vakeesan D. Solar energy for future world: - A review. Renewable and Sustainable Energy Reviews. 2016;62:1092-105.

[4] Wang E, Yu Z, Zhang H, Yang F. A regenerative supercritical-subcritical dual-loop organic Rankine cycle system for energy recovery from the waste heat of internal combustion engines. Applied Energy. 2017;190:574-90.

[5] Freeman J, Hellgardt K, Markides CN. An assessment of solar-powered organic Rankine cycle systems for combined heating and power in UK domestic applications. Applied Energy. 2015;138:605-20.

[6] Ma Z, Bao H, Roskilly AP. Principle investigation on advanced absorption power generation cycles. Energy Conversion and Management. 2017;150:800-13.

[7] Saeed IM, Ramli AT, Saleh MA. Assessment of sustainability in energy of Iraq, and achievable opportunities in the long run. Renewable and Sustainable Energy Reviews. 2016;58:1207-15.

[8] Liu M, Zhang N. Proposal and analysis of a novel ammonia–water cycle for power and refrigeration cogeneration. Energy. 2007;32:961-70.

[9] Zheng D, Chen B, Qi Y, Jin H. Thermodynamic analysis of a novel absorption power/cooling combined-cycle. Applied Energy. 2006;83:311-23.

[10] Zhang N, Lior N. Development of a Novel Combined Absorption Cycle for Power Generation and Refrigeration. Journal of Energy Resources Technology. 2007;129:254.

[11] Sah RP, Choudhury B, Das RK. A review on low grade heat powered adsorption cooling systems for ice production. Renewable and Sustainable Energy Reviews. 2016;62:109-20.

[12] H.T. Chua KCN, A. Malek, T. Kashiwagi, A. Akisawa, B.B. Saha Multi-bed regenerative adsorption chiller-improving the utilization of waste heat and reducing the chilled water outlet temperature fluctuation. International Journal of Refrigeration. 2001;24:124-36.

[13] Wang L, Ziegler F, Roskilly AP, Wang R, Wang Y. A resorption cycle for the cogeneration of electricity and refrigeration. Applied Energy. 2013;106:56-64.

[14] Jiang L, Wang LW, Roskilly AP, Wang RZ. Design and performance analysis of a resorption cogeneration system. International Journal of Low-Carbon Technologies. 2013;8:i85-i91.

[15] Bao H, Wang Y, Roskilly AP. Modelling of a chemisorption refrigeration and power cogeneration system. Applied Energy. 2014;119:351-62.

[16] Bao H, Wang Y, Charalambous C, Lu Z, Wang L, Wang R, et al. Chemisorption cooling and electric power cogeneration system driven by low grade heat. Energy. 2014;72:590-8.

[17] Jiang L, Wang LW, Zhang XF, Liu CZ, Wang RZ. Performance prediction on a resorption cogeneration cycle for power and refrigeration with energy storage. Renewable Energy. 2015;83:1250-9.

[18] Lu Y, Wang Y, Bao H, Yuan Y, Wang L, Roskilly AP. Analysis of an optimal resorption cogeneration using mass and heat recovery processes. Applied Energy. 2015;160:892-901.

[19] Jiang L, Wang LW, Liu CZ, Wang RZ. Experimental study on a resorption system for power and refrigeration cogeneration. Energy. 2016;97:182-90.

[20] Al-Mousawi FN, Al-Dadah R, Mahmoud S. Low grade heat driven adsorption system for cooling and power generation with small-scale radial inflow turbine. Applied Energy. 2016;183:1302-16.

[21] Al-Mousawi FN, Al-Dadah R, Mahmoud S. Low grade heat driven adsorption system for cooling and power generation using advanced adsorbent materials. Energy Conversion and Management. 2016;126:373-84.
[22] Al-Mousawi FN, Al-Dadah R, Mahmoud S. Integrated adsorption-ORC system: Comparative study of four scenarios to generate cooling and power simultaneously. Applied Thermal Engineering. 2017;114:1038-52.
[23] Petela K, Manfrida G, Szlek A. Advantages of variable driving temperature in solar absorption chiller. Renewable Energy. 2017;114:716-24.
[24] Zamora M, Bourouis M, Coronas A, Vallès M. Pre-industrial development and experimental characterization of new air-cooled and water-cooled ammonia/lithium nitrate absorption chillers. International Journal of Refrigeration. 2014;45:189-97.
[25] Hamdy M, Askalany AA, Harby K, Kora N. An overview on adsorption cooling systems powered by waste heat from internal combustion engine. Renewable and Sustainable Energy Reviews. 2015;51:1223-34.
[26] Sharafian A, Bahrami M. Assessment of adsorber bed designs in waste-heat driven adsorption cooling systems for vehicle air conditioning and refrigeration. Renewable and Sustainable Energy Reviews. 2014;30:440-51.
[27] Younes MM, El-Sharkawy II, Kabeel AE, Saha BB. A review on adsorbent-adsorbate pairs for cooling applications. Applied Thermal Engineering. 2017;114:394-414.
[28] Al-Mousawi FN, Raya Al-Dadah, and Saad Mahmoud. Novel adsorption system for cooling and power generation utilizing low grade heat sources. Students on Applied Engineering (ISCAE), International Conference for IEEE. 2016.
[29] Dutta P, Kumar P, Ng KC, Srinivasa Murthy S, Srinivasan K. Organic Brayton Cycles with solid sorption thermal compression for low grade heat utilization. Applied Thermal Engineering. 2014;62:171-5.
[30] Bao H, Ma Z, Roskilly AP. Integrated chemisorption cycles for ultra-low grade heat recovery and thermo-electric energy storage and exploitation. Applied Energy. 2016;164:228-36.
[31] Melikoglu M. Geothermal energy in Turkey and around the World: A review of the literature and an analysis based on Turkey's Vision 2023 energy targets. Renewable and Sustainable Energy Reviews. 2017;76:485-92.
[32] Franz Mauthner WW, Monika Spörk-Dür. Solar Heat Worldwide:Markets and Contribution to the Energy Supply 2014. In: edition, editor. Graz, Austria: AEE - Institute for Sustainable Technologies; May 2016.
[33] Garousi Farshi L, Seyed Mahmoudi SM, Rosen MA. Analysis of crystallization risk in double effect absorption refrigeration systems. Applied Thermal Engineering. 2011;31:1712-7.
[34] Wang LW, Wang RZ, Oliveira RG. A review on adsorption working pairs for refrigeration. Renewable and Sustainable Energy Reviews. 2009;13:518-34.
[35] Ibrahim NI, Al-Sulaiman FA, Ani FN. Performance characteristics of a solar driven lithium bromide-water absorption chiller integrated with absorption energy storage. Energy Conversion and Management. 2017;150:188-200.
[36] Aliane A, Abboudi S, Seladji C, Guendouz B. An illustrated review on solar absorption cooling experimental studies. Renewable and Sustainable Energy Reviews. 2016;65:443-58.
[37] Demir H, Mobedi M, Ülkü S. A review on adsorption heat pump: Problems and solutions. Renewable and Sustainable Energy Reviews. 2008;12:2381-403.
[38] Allouhi A, Kousksou T, Jamil A, Bruel P, Mourad Y, Zeraouli Y. Solar driven cooling systems: An updated review. Renewable and Sustainable Energy Reviews. 2015;44:159-81.
[39] Chen JF, Dai YJ, Wang RZ. Experimental and analytical study on an air-cooled single effect LiBr-H 2 O absorption chiller driven by evacuated glass tube solar collector for cooling application in residential buildings. Solar Energy. 2017;151:110-8.
[40] Yin YL, Song ZP, Li Y, Wang RZ, Zhai XQ. Experimental investigation of a mini-type solar absorption cooling system under different cooling modes. Energy and Buildings. 2012;47:131-8.

[41] Bellos E, Tzivanidis C, Antonopoulos KA. Exergetic and energetic comparison of LiCl-H2O and LiBr-H2O working pairs in a solar absorption cooling system. Energy Conversion and Management. 2016;123:453-61.
[42] Domínguez-Inzunza LA, Hernández-Magallanes JA, Soto P, Jiménez C, Gutiérrez-Urueta G, Rivera W. Experimental assessment of an absorption cooling system utilizing a falling film absorber and generator. Applied Thermal Engineering. 2016;103:1105-11.
[43] Sokhansefat T, Mohammadi D, Kasaeian A, Mahmoudi AR. Simulation and parametric study of a 5-ton solar absorption cooling system in Tehran. Energy Conversion and Management. 2017;148:339-51.
[44] Hernández-Magallanes JA, Domínguez-Inzunza LA, Gutiérrez-Urueta G, Soto P, Jiménez C, Rivera W. Experimental assessment of an absorption cooling system operating with the ammonia/lithium nitrate mixture. Energy. 2014;78:685-92.
[45] Arshi Banu PS, Sudharsan NM. Review of water based vapour absorption cooling systems using thermodynamic analysis. Renewable and Sustainable Energy Reviews. 2018;82:3750-61.
[46] Yilmaz C. Thermodynamic and economic investigation of geothermal powered absorption cooling system for buildings. Geothermics. 2017;70:239-48.
[47] Ibrahim NI, Khan MMA, Mahbubul IM, Saidur R, Al-Sulaiman FA. Experimental testing of the performance of a solar absorption cooling system assisted with ice-storage for an office space. Energy Conversion and Management. 2017;148:1399-408.
[48] Jawahar CP, Saravanan R. Experimental studies on air-cooled NH3–H2O based modified gax absorption cooling system. International Journal of Refrigeration. 2011;34:658-66.
[49] Weber C, Berger M, Mehling F, Heinrich A, Núñez T. Solar cooling with water–ammonia absorption chillers and concentrating solar collector – Operational experience. International Journal of Refrigeration. 2014;39:57-76.
[50] Kim DS, Infante Ferreira CA. Air-cooled LiBr–water absorption chillers for solar air conditioning in extremely hot weathers. Energy Conversion and Management. 2009;50:1018-25.
[51] Li M, Xu C, Hassanien RHE, Xu Y, Zhuang B. Experimental investigation on the performance of a solar powered lithium bromide–water absorption cooling system. International Journal of Refrigeration. 2016;71:46-59.
[52] Miyazaki T, Akisawa A, Saha BB, El-Sharkawy II, Chakraborty A. A new cycle time allocation for enhancing the performance of two-bed adsorption chillers. International Journal of Refrigeration. 2009;32:846-53.
[53] Tso CY, Chao CYH, Fu SC. Performance analysis of a waste heat driven activated carbon based composite adsorbent – Water adsorption chiller using simulation model. International Journal of Heat and Mass Transfer. 2012;55:7596-610.
[54] Sapienza A, Glaznev IS, Santamaria S, Freni A, Aristov YI. Adsorption chilling driven by low temperature heat: New adsorbent and cycle optimization. Applied Thermal Engineering. 2012;32:141-6.
[55] El-Sharkawy II, AbdelMeguid H, Saha BB. Towards an optimal performance of adsorption chillers: Reallocation of adsorption/desorption cycle times. International Journal of Heat and Mass Transfer. 2013;63:171-82.
[56] Glaznev IS, Aristov YI. The effect of cycle boundary conditions and adsorbent grain size on the water sorption dynamics in adsorption chillers. International Journal of Heat and Mass Transfer. 2010;53:1893-8.
[57] Xia Z, Wang D, Zhang J. Experimental study on improved two-bed silica gel–water adsorption chiller. Energy Conversion and Management. 2008;49:1469-79.
[58] He Z, Bai Y, Huang H, Li J, Huhetaoli, Kobayashi N, et al. Study on the performance of compact adsorption chiller with vapor valves. Applied Thermal Engineering. 2017;126:37-42.
[59] Saha BB, Koyama S, Choon Ng K, Hamamoto Y, Akisawa A, Kashiwagi T. Study on a dual-mode, multi-stage, multi-bed regenerative adsorption chiller. Renewable Energy. 2006;31:2076-90.

[60] Chorowski M, Pyrka P. Modelling and experimental investigation of an adsorption chiller using low-temperature heat from cogeneration. Energy. 2015;92:221-9.
[61] Khan MZI, Alam KCA, Saha BB, Akisawa A, Kashiwagi T. Performance evaluation of multi-stage, multi-bed adsorption chiller employing re-heat scheme. Renewable Energy. 2008;33:88-98.
[62] Farid SK, Billah MM, Khan MZI, Rahman MM, Sharif UM. A numerical analysis of cooling water temperature of two-stage adsorption chiller along with different mass ratios. International Communications in Heat and Mass Transfer. 2011;38:1086-92.
[63] Wang X, He Z, Chua HT. Performance simulation of multi-bed silica gel-water adsorption chillers. International Journal of Refrigeration. 2015;52:32-41.
[64] Al-Mousawi FN, Al-Dadah R, Mahmoud S. Novel system for cooling and electricity: Four different integrated adsorption-ORC configurations with two expanders. Energy Conversion and Management. 2017;152:72-87.
[65] Al-Mousawi FN, Al-Dadah R, Mahmoud S. Different bed configurations and time ratios: Performance analysis of low-grade heat driven adsorption system for cooling and electricity. Energy Conversion and Management. 2017;148:1028-40.
[66] Teo HWB, Chakraborty A, Han B. Water adsorption on CHA and AFI types zeolites: Modelling and investigation of adsorption chiller under static and dynamic conditions. Applied Thermal Engineering. 2017;127:35-45.
[67] Alahmer A, Wang X, Al-Rbaihat R, Amanul Alam KC, Saha BB. Performance evaluation of a solar adsorption chiller under different climatic conditions. Applied Energy. 2016;175:293-304.
[68] Habib K, Choudhury B, Chatterjee PK, Saha BB. Study on a solar heat driven dual-mode adsorption chiller. Energy. 2013;63:133-41.
[69] Sapienza A, Palomba V, Gullì G, Frazzica A, Vasta S. A new management strategy based on the reallocation of ads-/desorption times: Experimental operation of a full-scale 3 beds adsorption chiller. Applied Energy. 2017;205:1081-90.
[70] Shi B, Al-Dadah R, Mahmoud S, Elsayed A, Elsayed E. CPO-27(Ni) metal–organic framework based adsorption system for automotive air conditioning. Applied Thermal Engineering. 2016;106:325-33.
[71] Li A, Ismail AB, Thu K, Ng KC, Loh WS. Performance evaluation of a zeolite–water adsorption chiller with entropy analysis of thermodynamic insight. Applied Energy. 2014;130:702-11.
[72] Jribi S, Saha BB, Koyama S, Bentaher H. Modeling and simulation of an activated carbon–CO2 four bed based adsorption cooling system. Energy Conversion and Management. 2014;78:985-91.
[73] Sadeghlu A, Yari M, Mahmoudi SMS, Dizaji HB. Performance evaluation of Zeolite 13X/CaCl2 two-bed adsorption refrigeration system. International Journal of Thermal Sciences. 2014;80:76-82.
[74] Jribi S, Saha BB, Koyama S, Chakraborty A, Ng KC. Study on activated carbon/HFO-1234ze(E) based adsorption cooling cycle. Applied Thermal Engineering. 2013;50:1570-5.
[75] Tomasini-Montenegro C, Santoyo-Castelazo E, Gujba H, Romero RJ, Santoyo E. Life cycle assessment of geothermal power generation technologies: An updated review. Applied Thermal Engineering. 2017;114:1119-36.
[76] Ding LC, Akbarzadeh A, Tan L. A review of power generation with thermoelectric system and its alternative with solar ponds. Renewable and Sustainable Energy Reviews. 2018;81:799-812.
[77] Zare V, Mahmoudi SMS. A thermodynamic comparison between organic Rankine and Kalina cycles for waste heat recovery from the Gas Turbine-Modular Helium Reactor. Energy. 2015;79:398-406.
[78] Lecompte S, Huisseune H, van den Broek M, Vanslambrouck B, De Paepe M. Review of organic Rankine cycle (ORC) architectures for waste heat recovery. Renewable and Sustainable Energy Reviews. 2015;47:448-61.
[79] Rahbar K, Mahmoud S, Al-Dadah RK, Moazami N, Mirhadizadeh SA. Review of organic Rankine cycle for small-scale applications. Energy Conversion and Management. 2017;134:135-55.
[80] Usman M, Imran M, Yang Y, Lee DH, Park B-S. Thermo-economic comparison of air-cooled and cooling tower based Organic Rankine Cycle (ORC) with R245fa and R1233zde as candidate working fluids for different geographical climate conditions. Energy. 2017;123:353-66.

[81] Le VL, Feidt M, Kheiri A, Pelloux-Prayer S. Performance optimization of low-temperature power generation by supercritical ORCs (organic Rankine cycles) using low GWP (global warming potential) working fluids. Energy. 2014;67:513-26.
[82] Xu W, Zhang J, Zhao L, Deng S, Zhang Y. Novel experimental research on the compression process in organic Rankine cycle (ORC). Energy Conversion and Management. 2017;137:1-11.
[83] Ziviani D, Gusev S, Lecompte S, Groll EA, Braun JE, Horton WT, et al. Optimizing the performance of small-scale organic Rankine cycle that utilizes a single-screw expander. Applied Energy. 2017;189:416-32.
[84] AI K. Combined-cycle system with novel bottoming cycle. ASME Journal of Engineering for Gas Turbines and Power. 1984;106:737-42.
[85] Modi A, Haglind F. Performance analysis of a Kalina cycle for a central receiver solar thermal power plant with direct steam generation. Applied Thermal Engineering. 2014;65:201-8.
[86] Wang E, Yu Z. A numerical analysis of a composition-adjustable Kalina cycle power plant for power generation from low-temperature geothermal sources. Applied Energy. 2016;180:834-48.
[87] Cao L, Wang J, Dai Y. Thermodynamic analysis of a biomass-fired Kalina cycle with regenerative heater. Energy. 2014;77:760-70.
[88] Walraven D, Laenen B, D'haeseleer W. Comparison of thermodynamic cycles for power production from low-temperature geothermal heat sources. Energy Conversion and Management. 2013;66:220-33.
[89] Eller T, Heberle F, Brüggemann D. Second law analysis of novel working fluid pairs for waste heat recovery by the Kalina cycle. Energy. 2017;119:188-98.
[90] Bao H, Ma Z, Roskilly AP. Chemisorption power generation driven by low grade heat – Theoretical analysis and comparison with pumpless ORC. Applied Energy. 2017;186:282-90.
[91] Bao H, Ma Z, Roskilly AP. An optimised chemisorption cycle for power generation using low grade heat. Applied Energy. 2017;186:251-61.
[92] Bao H, Ma Z, Roskilly AP. A chemisorption power generation cycle with multi-stage expansion driven by low grade heat. Energy Conversion and Management. 2017;150:956-65.
[93] Lu Y, Roskilly AP, Tang K, Wang Y, Jiang L, Yuan Y, et al. Investigation and performance study of a dual-source chemisorption power generation cycle using scroll expander. Applied Energy. 2017;204:979-93.
[94] Seyedkavoosi S, Javan S, Kota K. Exergy-based optimization of an organic Rankine cycle (ORC) for waste heat recovery from an internal combustion engine (ICE). Applied Thermal Engineering. 2017;126:447-57.
[95] Girgin I, Ezgi C. Design and thermodynamic and thermoeconomic analysis of an organic Rankine cycle for naval surface ship applications. Energy Conversion and Management. 2017;148:623-34.
[96] Saloux E, Sorin M, Nesreddine H, Teyssedou A. Reconstruction procedure of the thermodynamic cycle of organic Rankine cycles (ORC) and selection of the most appropriate working fluid. Applied Thermal Engineering. 2018;129:628-35.
[97] Zhou Y, Zhang F, Yu L. Performance analysis of the partial evaporating organic Rankine cycle (PEORC) using zeotropic mixtures. Energy Conversion and Management. 2016;129:89-99.
[98] Yang S-C, Hung T-C, Feng Y-Q, Wu C-J, Wong K-W, Huang K-C. Experimental investigation on a 3kW organic Rankine cycle for low-grade waste heat under different operation parameters. Applied Thermal Engineering. 2017;113:756-64.
[99] Aljundi IH. Effect of dry hydrocarbons and critical point temperature on the efficiencies of organic Rankine cycle. Renewable Energy. 2011;36:1196-202.
[100] Li H, Hu D, Wang M, Dai Y. Off-design performance analysis of Kalina cycle for low temperature geothermal source. Applied Thermal Engineering. 2016;107:728-37.
[101] Hua J, Li G, Chen Y, Zhao X, Li Q. Optimization of thermal parameters of boiler in triple-pressure Kalina cycle for waste heat recovery. Applied Thermal Engineering. 2015;91:1026-31.
[102] Modi A, Haglind F. Thermodynamic optimisation and analysis of four Kalina cycle layouts for high temperature applications. Applied Thermal Engineering. 2015;76:196-205.

[103] Wang J, Yan Z, Zhou E, Dai Y. Parametric analysis and optimization of a Kalina cycle driven by solar energy. Applied Thermal Engineering. 2013;50:408-15.
[104] Roy JP, Mishra MK, Misra A. Performance analysis of an Organic Rankine Cycle with superheating under different heat source temperature conditions. Applied Energy. 2011;88:2995-3004.
[105] Demirkaya G, Padilla R, Fontalvo A, Lake M, Lim Y. Thermal and Exergetic Analysis of the Goswami Cycle Integrated with Mid-Grade Heat Sources. Entropy. 2017;19:416.
[106] Wang J, Wang J, Zhao P, Dai Y. Thermodynamic analysis of a new combined cooling and power system using ammonia–water mixture. Energy Conversion and Management. 2016;117:335-42.
[107] Muye J, Ayou DS, Saravanan R, Coronas A. Performance study of a solar absorption power-cooling system. Applied Thermal Engineering. 2016;97:59-67.
[108] Mohammadi A, Kasaeian A, Pourfayaz F, Ahmadi MH. Thermodynamic analysis of a combined gas turbine, ORC cycle and absorption refrigeration for a CCHP system. Applied Thermal Engineering. 2017;111:397-406.
[109] Jawahar CP, Saravanan R, Bruno JC, Coronas A. Simulation studies on gax based Kalina cycle for both power and cooling applications. Applied Thermal Engineering. 2013;50:1522-9.
[110] Padilla RV, Demirkaya G, Goswami DY, Stefanakos E, Rahman MM. Analysis of power and cooling cogeneration using ammonia-water mixture. Energy. 2010;35:4649-57.
[111] Kumar GP, Saravanan R, Coronas A. Experimental studies on combined cooling and power system driven by low-grade heat sources. Energy. 2017;128:801-12.
[112] Ghaebi H, Parikhani T, Rostamzadeh H. Energy, exergy and thermoeconomic analysis of a novel combined cooling and power system using low-temperature heat source and LNG cold energy recovery. Energy Conversion and Management. 2017;150:678-92.
[113] Mohtaram S, Chen W, Lin J. Investigation on the combined Rankine-absorption power and refrigeration cycles using the parametric analysis and genetic algorithm. Energy Conversion and Management. 2017;150:754-62.
[114] Wang Z, Han W, Zhang N, Liu M, Jin H. Proposal and assessment of a new CCHP system integrating gas turbine and heat-driven cooling/power cogeneration. Energy Conversion and Management. 2017;144:1-9.
[115] Chen Y, Han W, Jin H. Investigation of an ammonia-water combined power and cooling system driven by the jacket water and exhaust gas heat of an internal combustion engine. International Journal of Refrigeration. 2017;82:174-88.
[116] Rashidi J, Ifaei P, Esfahani IJ, Ataei A, Yoo CK. Thermodynamic and economic studies of two new high efficient power-cooling cogeneration systems based on Kalina and absorption refrigeration cycles. Energy Conversion and Management. 2016;127:170-86.
[117] Jiang L, Wang L, Wang R, Gao P, Song F. Investigation on cascading cogeneration system of ORC (Organic Rankine Cycle) and CaCl2/BaCl2 two-stage adsorption freezer. Energy. 2014;71:377-87.
[118] Wang L, Roskilly AP, Wang R. Solar Powered Cascading Cogeneration Cycle with ORC and Adsorption Technology for Electricity and Refrigeration. Heat Transfer Engineering. 2014;35:1028-34.
[119] Lu Y, Wang Y, Dong C, Wang L, Roskilly AP. Design and assessment on a novel integrated system for power and refrigeration using waste heat from diesel engine. Applied Thermal Engineering. 2015;91:591-9.
[120] Jiang L, Lu H, Wang R, Wang L, Gong L, Lu Y, et al. Investigation on an innovative cascading cycle for power and refrigeration cogeneration. Energy Conversion and Management. 2017;145:20-9.
[121] Sah RP, Choudhury B, Das RK. A review on adsorption cooling systems with silica gel and carbon as adsorbents. Renewable and Sustainable Energy Reviews. 2015;45:123-34.
[122] Shmroukh AN, Ali AHH, Ookawara S. Adsorption working pairs for adsorption cooling chillers: A review based on adsorption capacity and environmental impact. Renewable and Sustainable Energy Reviews. 2015;50:445-56.
[123] Aristov YI. Challenging offers of material science for adsorption heat transformation: A review. Applied Thermal Engineering. 2013;50:1610-8.

[124] Li SL, Wu JY, Xia ZZ, Wang RZ. Study on the adsorption performance of composite adsorbent of CaCl2 and expanded graphite with ammonia as adsorbate. Energy Conversion and Management. 2009;50:1011-7.
[125] Daou K, Wang RZ, Xia ZZ. Development of a new synthesized adsorbent for refrigeration and air conditioning applications. Applied Thermal Engineering. 2006;26:56-65.
[126] Askalany AA, Salem M, Ismael IM, Ali AHH, Morsy MG, Saha BB. An overview on adsorption pairs for cooling. Renewable and Sustainable Energy Reviews. 2013;19:565-72.
[127] Ali SM, Chakraborty A. Adsorption assisted double stage cooling and desalination employing silica gel+water and AQSOA-Z02+water systems. Energy Conversion and Management. 2016;117:193-205.
[128] Gediz Ilis G. Influence of new adsorbents with isotherm Type V on performance of an adsorption heat pump. Energy. 2017;119:86-93.
[129] Elsayed E, Al-Dadah R, Mahmoud S, Anderson PA, Elsayed A, Youssef PG. CPO-27(Ni), aluminium fumarate and MIL-101(Cr) MOF materials for adsorption water desalination. Desalination. 2017;406:25-36.
[130] Youssef PG, Dakkama H, Mahmoud SM, Al-Dadah RK. Experimental investigation of adsorption water desalination/cooling system using CPO-27Ni MOF. Desalination. 2017;404:192-9.
[131] Du SW, Li XH, Yuan ZX, Du CX, Wang WC, Liu ZB. Performance of solar adsorption refrigeration in system of SAPO-34 and ZSM-5 zeolite. Solar Energy. 2016;138:98-104.
[132] Wang D, Zhang J, Yang Q, Li N, Sumathy K. Study of adsorption characteristics in silica gel–water adsorption refrigeration. Applied Energy. 2014;113:734-41.
[133] Ng KC, Thu K, Saha BB, Chakraborty A. Study on a waste heat-driven adsorption cooling cum desalination cycle. International Journal of Refrigeration. 2012;35:685-93.
[134] Hui T. Chua KCN, Anutosh Chakraborty, Nay M. Oo, and Mohamed A. Othman. Adsorption Characteristics of Silica Gel + Water Systems. J Chem Eng Data. 2002;47:1177-81.
[135] Kayal S, Baichuan S, Saha BB. Adsorption characteristics of AQSOA zeolites and water for adsorption chillers. International Journal of Heat and Mass Transfer. 2016;92:1120-7.
[136] Sayılgan ŞÇ, Mobedi M, Ülkü S. Effect of regeneration temperature on adsorption equilibria and mass diffusivity of zeolite 13x-water pair. Microporous and Mesoporous Materials. 2016;224:9-16.
[137] Habib K, Saha BB, Rahman KA, Chakraborty A, Koyama S, Ng KC. Experimental study on adsorption kinetics of activated carbon/R134a and activated carbon/R507A pairs. International Journal of Refrigeration. 2010;33:706-13.
[138] Wu JW, Madani SH, Biggs MJ, Phillip P, Lei C, Hu EJ. Characterizations of Activated Carbon–Methanol Adsorption Pair Including the Heat of Adsorptions. Journal of Chemical & Engineering Data. 2015;60:1727-31.
[139] Saha BB, El-Sharkawy II, Miyazaki T, Koyama S, Henninger SK, Herbst A, et al. Ethanol adsorption onto metal organic framework: Theory and experiments. Energy. 2015;79:363-70.
[140] Ma L, Yang H, Wu Q, Yin Y, Liu Z, Cui Q, et al. Study on adsorption refrigeration performance of MIL-101-isobutane working pair. Energy. 2015;93:786-94.
[141] Dakkama HJ, Youssef PG, Al-Dadah RK, Mahmoud S. Adsorption ice making and water desalination system using metal organic frameworks/water pair. Energy Conversion and Management. 2017;142:53-61.
[142] Sharma R, Anil Kumar E. Measurement of thermodynamic properties of ammoniated salts and thermodynamic simulation of resorption cooling system. International Journal of Refrigeration. 2016;67:54-68.
[143] Tso CY, Chao CYH. Activated carbon, silica-gel and calcium chloride composite adsorbents for energy efficient solar adsorption cooling and dehumidification systems. International Journal of Refrigeration. 2012;35:1626-38.
[144] Bao J, Zhao L. A review of working fluid and expander selections for organic Rankine cycle. Renewable and Sustainable Energy Reviews. 2013;24:325-42.

[145] Qiu G, Liu H, Riffat S. Expanders for micro-CHP systems with organic Rankine cycle. Applied Thermal Engineering. 2011;31:3301-7.
[146] Yahya S. Turbines Compressors and Fans. Tata McGraw-Hill Education. 2010.
[147] Aungier RH. Turbine Aerodynamics; Axial-flow and radial-inflow turbine design and analysis 2006.
[148] Clemente S, Micheli D, Reini M, Taccani R. Bottoming organic Rankine cycle for a small scale gas turbine: A comparison of different solutions. Applied Energy. 2013;106:355-64.
[149] Mendoza LC, Ayou DS, Navarro-Esbrí J, Bruno JC, Coronas A. Small capacity absorption systems for cooling and power with a scroll expander and ammonia based working fluids. Applied Thermal Engineering. 2014;72:258-65.
[150] Maurizio Cambi RT, Luca Cioccolanti, Enrico Bocci. Converting a commercial scroll compressor into an expander: experimental and analytical performance evaluation. Energy Procedia. 2017;129:363-70.
[151] Rahbar K, Mahmoud S, Al-Dadah RK. Mean-line modeling and CFD analysis of a miniature radial turbine for distributed power generation systems. International Journal of Low-Carbon Technologies. 2016;11:157-68.
[152] Nithesh KG, Chatterjee D, Oh C, Lee Y-H. Design and performance analysis of radial-inflow turboexpander for OTEC application. Renewable Energy. 2016;85:834-43.
[153] Ventura CAM, Jacobs PA, Rowlands AS, Petrie-Repar P, Sauret E. Preliminary Design and Performance Estimation of Radial Inflow Turbines: An Automated Approach. Journal of Fluids Engineering. 2012;134:031102.
[154] Sauret E, Gu Y. Three-dimensional off-design numerical analysis of an organic Rankine cycle radial-inflow turbine. Applied Energy. 2014;135:202-11.
[155] Fiaschi D, Innocenti G, Manfrida G, Maraschiello F. Design of micro radial turboexpanders for ORC power cycles: From 0D to 3D. Applied Thermal Engineering. 2016;99:402-10.
[156] Rahbar K, Mahmoud S, Al-Dadah RK, Moazami N. Parametric analysis and optimization of a small-scale radial turbine for Organic Rankine Cycle. Energy. 2015;83:696-711.
[157] Costall AW, Gonzalez Hernandez A, Newton PJ, Martinez-Botas RF. Design methodology for radial turbo expanders in mobile organic Rankine cycle applications. Applied Energy. 2015;157:729-43.
[158] Li Y, Ren X-d. Investigation of the organic Rankine cycle (ORC) system and the radial-inflow turbine design. Applied Thermal Engineering. 2016;96:547-54.
[159] Al Jubori A, Al-Dadah RK, Mahmoud S, Bahr Ennil AS, Rahbar K. Three dimensional optimization of small-scale axial turbine for low temperature heat source driven organic Rankine cycle. Energy Conversion and Management. 2017;133:411-26.
[160] Al Jubori A, Daabo A, Al-Dadah RK, Mahmoud S, Ennil AB. Development of micro-scale axial and radial turbines for low-temperature heat source driven organic Rankine cycle. Energy Conversion and Management. 2016;130:141-55.
[161] Daabo AM, Al Jubori A, Mahmoud S, Al-Dadah RK. Parametric study of efficient small-scale axial and radial turbines for solar powered Brayton cycle application. Energy Conversion and Management. 2016;128:343-60.
[162] Kang SH. Design and experimental study of ORC (organic Rankine cycle) and radial turbine using R245fa working fluid. Energy. 2012;41:514-24.
[163] Pei G, Li J, Li Y, Wang D, Ji J. Construction and dynamic test of a small-scale organic rankine cycle. Energy. 2011;36:3215-23.
[164] Al Jubori AM, Al-Dadah RK, Mahmoud S, Daabo A. Modelling and parametric analysis of small-scale axial and radial-outflow turbines for Organic Rankine Cycle applications. Applied Energy. 2017;190:981-96.
[165] White M, Sayma AI. System and component modelling and optimisation for an efficient 10 kWe low-temperature organic Rankine cycle utilising a radial inflow expander. Proceedings of the Institution of Mechanical Engineers, Part A: Journal of Power and Energy. 2015;229:795-809.

[166] Nithesh KG, Chatterjee D. Numerical prediction of the performance of radial inflow turbine designed for ocean thermal energy conversion system. Applied Energy. 2016;167:1-16.
[167] Rahbar K, Mahmoud S, Al-Dadah RK, Moazami N, Mirhadizadeh SA. Development and experimental study of a small-scale compressed air radial inflow turbine for distributed power generation. Applied Thermal Engineering. 2017;116:549-83.
[168] Rezk ARM, Al-Dadah RK. Physical and operating conditions effects on silica gel/water adsorption chiller performance. Applied Energy. 2012;89:142-9.
[169] Hui T. Chua KCN, Anutosh Chakraborty, Nay M. Oo,† and Mohamed A. Othman. Adsorption Characteristics of Silica Gel + Water Systems. J Chem Eng Data. 2002;47:177-1181.
[170] Association IZ. http://wwwiza-onlineorg/. 2017.
[171] Saha D, Deng S. Ammonia adsorption and its effects on framework stability of MOF-5 and MOF-177. J Colloid Interface Sci. 2010;348:615-20.
[172] Rezk A, Al-Dadah R, Mahmoud S, Elsayed A. Investigation of Ethanol/metal organic frameworks for low temperature adsorption cooling applications. Applied Energy. 2013;112:1025-31.
[173] Youssef PG, Mahmoud SM, Al-Dadah RK. Performance analysis of four bed adsorption water desalination/refrigeration system, comparison of AQSOA-Z02 to silica-gel. Desalination. 2015;375:100-7.
[174] Elsayed E, Wang H, Anderson PA, Al-Dadah R, Mahmoud S, Navarro H, et al. Development of MIL-101(Cr)/GrO composites for adsorption heat pump applications. Microporous and Mesoporous Materials. 2017;244:180-91.
[175] Elsayed E, Al-Dadah R, Mahmoud S, Elsayed A, Anderson PA. Aluminium fumarate and CPO-27(Ni) MOFs: Characterization and thermodynamic analysis for adsorption heat pump applications. Applied Thermal Engineering. 2016;99:802-12.
[176] Mitra S, Aswin N, Dutta P. Scaling analysis and numerical studies on water vapour adsorption in a columnar porous silica gel bed. International Journal of Heat and Mass Transfer. 2016;95:853-64.
[177] Gao L, Li CY, Yung H, Chan KY. A functionalized MIL-101(Cr) metal-organic framework for enhanced hydrogen release from ammonia borane at low temperature. Chem Commun (Camb). 2013;49:10629-31.
[178] Saha BB, Chakraborty A, Koyama S, Lee JB, He J, Ng KC. Adsorption characteristics of parent and copper-sputtered RD silica gels. Philosophical Magazine. 2007;87:1113-21.
[179] Hong SW, Ahn SH, Chung JD, Bae KJ, Cha DA, Kwon OK. Characteristics of FAM-Z01 compared to silica gels in the performance of an adsorption bed. Applied Thermal Engineering. 2016;104:24-33.
[180] Ehrenmann J, Henninger SK, Janiak C. Water Adsorption Characteristics of MIL-101 for Heat-Transformation Applications of MOFs. European Journal of Inorganic Chemistry. 2011;2011:471-4.
[181] Elsayed A, Elsayed E, Al-Dadah R, Mahmoud S, Elshaer A, Kaialy W. Thermal energy storage using metal–organic framework materials. Applied Energy. 2017;186:509-19.
[182] Jeremias F, Fröhlich D, Janiak C, Henninger SK. Advancement of sorption-based heat transformation by a metal coating of highly-stable, hydrophilic aluminium fumarate MOF. RSC Adv. 2014;4:24073-82.
[183] Intini M, Goldsworthy M, White S, Joppolo CM. Experimental analysis and numerical modelling of an AQSOA zeolite desiccant wheel. Applied Thermal Engineering. 2015;80:20-30.
[184] Mitsubishi. Mitsubishi Chemical AQSOA™. https://wwwm-chemicalcojp/en/products/departments/mcc/aquachem/product/1201185_8078html.
[185] Rezk A, Al-Dadah R, Mahmoud S, Elsayed A. Characterisation of metal organic frameworks for adsorption cooling. International Journal of Heat and Mass Transfer. 2012;55:7366-74.
[186] Ferreira RB, Scheetz PM, Formiga ALB. Synthesis of amine-tagged metal–organic frameworks isostructural to MIL-101(Cr). RSC Advances. 2013;3:10181.
[187] Wang Y, Qu Q, Liu G, Battaglia VS, Zheng H. Aluminum fumarate-based metal organic frameworks with tremella-like structure as ultrafast and stable anode for lithium-ion batteries. Nano Energy. 2017;39:200-10.

[188] Rezk ARM. THEORETICAL AND EXPERIMENTAL INVESTIGATION OF SILICA GEL / WATER ADSORPTION REFRIGERATION SYSTEMS [PhD thesis]: University of Birmingham; 2012.
[189] Surfae Measurement Systems Ltd UK. https://www.surfacemeasurementsystems.com/; 1996-2008.
[190] Hassan HZ, Mohamad AA, Alyousef Y, Al-Ansary HA. A review on the equations of state for the working pairs used in adsorption cooling systems. Renewable and Sustainable Energy Reviews. 2015;45:600-9.
[191] Saha BB, Chakraborty A, Koyama S, Yoon S-H, Mochida I, Kumja M, et al. Isotherms and thermodynamics for the adsorption of n-butane on pitch based activated carbon. International Journal of Heat and Mass Transfer. 2008;51:1582-9.
[192] Sun B, Chakraborty A. Thermodynamic formalism of water uptakes on solid porous adsorbents for adsorption cooling applications. Applied Physics Letters. 2014;104:201901.
[193] Saha BB, Koyama S, Kashiwagi T, Akisawa A, Ng KC, Chua HT. Waste heat driven dual-mode, multi-stage, multi-bed regenerative adsorption system. International Journal of Refrigeration. 2003;26:749-57.
[194] Cai D, Jiang J, He G, Li K, Niu L, Xiao R. Experimental evaluation on thermal performance of an air-cooled absorption refrigeration cycle with NH3–LiNO3 and NH3–NaSCN refrigerant solutions. Energy Conversion and Management. 2016;120:32-43.
[195] Gomri R. Simulation study on the performance of solar/natural gas absorption cooling chillers. Energy Conversion and Management. 2013;65:675-81.
[196] Xu ZY, Wang RZ. Simulation of solar cooling system based on variable effect LiBr-water absorption chiller. Renewable Energy. 2017;113:907-14.
[197] Mitra S, Thu K, Saha BB, Srinivasan K, Dutta P. Modeling study of two-stage, multi-bed air cooled silica gel+water adsorption cooling cum desalination system. Applied Thermal Engineering. 2017;114:704-12.
[198] Krzywanski J, Grabowska K, Herman F, Pyrka P, Sosnowski M, Prauzner T, et al. Optimization of a three-bed adsorption chiller by genetic algorithms and neural networks. Energy Conversion and Management. 2017;153:313-22.
[199] Modi A, Kærn MR, Andreasen JG, Haglind F. Thermoeconomic optimization of a Kalina cycle for a central receiver concentrating solar power plant. Energy Conversion and Management. 2016;115:276-87.
[200] Chen T, Zhuge W, Zhang Y, Zhang L. A novel cascade organic Rankine cycle (ORC) system for waste heat recovery of truck diesel engines. Energy Conversion and Management. 2017;138:210-23.
[201] Sun W, Yue X, Wang Y. Exergy efficiency analysis of ORC (Organic Rankine Cycle) and ORC-based combined cycles driven by low-temperature waste heat. Energy Conversion and Management. 2017;135:63-73.
[202] Wang X, Chua HT. A comparative evaluation of two different heat-recovery schemes as applied to a two-bed adsorption chiller. International Journal of Heat and Mass Transfer. 2007;50:433-43.
[203] Saha BB, Elisa C. Boelman, and Takao Kashiwagi. Computational analysis of an advanced adsorption-refrigeration cycle. Energy. 1995;20:983-94.
[204] Akahira A, Alam KCA, Hamamoto Y, Akisawa A, Kashiwagi T. Mass recovery adsorption refrigeration cycle—improving cooling capacity. International Journal of Refrigeration. 2004;27:225-34.
[205] Hamamoto Y, Amanul Alam KC, Akisawa A, Kashiwagi T. Performance evaluation of a two-stage adsorption refrigeration cycle with different mass ratio. International Journal of Refrigeration. 2005;28:344-52.
[206] Koronaki IP, Papoutsis EG, Papaefthimiou VD. Thermodynamic modeling and exergy analysis of a solar adsorption cooling system with cooling tower in Mediterranean conditions. Applied Thermal Engineering. 2016;99:1027-38.
[207] Zhai H, Dai YJ, Wu JY, Wang RZ. Energy and exergy analyses on a novel hybrid solar heating, cooling and power generation system for remote areas. Applied Energy. 2009;86:1395-404.

[208] Bellos E, Tzivanidis C, Antonopoulos KA. Exergetic, energetic and financial evaluation of a solar driven absorption cooling system with various collector types. Applied Thermal Engineering. 2016;102:749-59.
[209] Rezk A, Al-Dadah RK, Mahmoud S, Elsayed A. Effects of contact resistance and metal additives in finned-tube adsorbent beds on the performance of silica gel/water adsorption chiller. Applied Thermal Engineering. 2013;53:278-84.
[210] Saha BB, Koyama S, Lee JB, Kuwahara K, Alam KCA, Hamamoto Y, et al. Performance evaluation of a low-temperature waste heat driven multi-bed adsorption chiller. International Journal of Multiphase Flow. 2003;29:1249-63.
[211] Chang WS, Wang CC, Shieh CC. Experimental study of a solid adsorption cooling system using flat-tube heat exchangers as adsorption bed. Applied Thermal Engineering. 2007;27:2195-9.
[212] Brownell Limited Company https://brownell.co.uk/non-indicating-silica-gel.html.
[213] Safarian S, Aramoun F. Energy and exergy assessments of modified Organic Rankine Cycles (ORCs). Energy Reports. 2015;1:1-7.
[214] Collings P, Yu Z, Wang E. A dynamic organic Rankine cycle using a zeotropic mixture as the working fluid with composition tuning to match changing ambient conditions. Applied Energy. 2016;171:581-91.
[215] Rahbar K, Mahmoud S, Al-Dadah RK, Moazami N. Modelling and optimization of organic Rankine cycle based on a small-scale radial inflow turbine. Energy Conversion and Management. 2015;91:186-98.
[216] Baines NC. Fundamentals of turbocharging 2005.
[217] H. Moustapha MFZ, N. C. Baines, and D. Japikse. Axial and radial turbines. White River Junction, USA: Concepts NREC; 2003.
[218] Whitfield ANCB. Design of radial turbomachines. 1990.
[219] Al Jubori AM, Al-Dadah R, Mahmoud S. Performance enhancement of a small-scale organic Rankine cycle radial-inflow turbine through multi-objective optimization algorithm. Energy. 2017;131:297-311.
[220] Dixon SL, C. H. Fluid mechanics and thermodynamics of turbomachinery. 2013.
[221] Turton BRK. Principles of Turbomachinery. London: CHAPMAN & HALL; Second edition 1995.
[222] Suhrmann J, D. Peitsch, M. Gugau, T. Heuer and U. Tomm (2010). Validation and development of loss models for small size radial turbines. Proceedings of ASME Turbo Expo : Power for land, sea and Air GT2010, Glasgow, UK. 2010.
[223] Japikse D BN. Introduction to turbomachinery1994.
[224] Fiaschi D, Manfrida G, Maraschiello F. Design and performance prediction of radial ORC turboexpanders. Applied Energy. 2015;138:517-32.
[225] GZassman AtJ. Computer program for design analysis of radial-inflow turbines. WASHINGTON, D. C: NASA February 1976
[226] ANSYS. Workbench User's Guide. In: 16.2 R, editor.July 2015.
[227] Hirsch C. Numerical Computation of Internal and External Flows: The Fundamentals of Computational Fluid Dynamics. 2 ed: Elsevier; 2007.
[228] ANSYS. ANSYS TurboGrid Tutorials. In: 16.0 R, editor.January 2015.
[229] ANSYS. ANSYS CFX-Solver Modeling Guide. November 2013.
[230] Daabo AM, Mahmoud S, Al-Dadah RK, Al Jubori AM, Bhar Ennil A. Numerical analysis of small scale axial and radial turbines for solar powered Brayton cycle application. Applied Thermal Engineering. 2017;120:672-93.
[231] ANSYS. ANSYS CFX-Solver Theory Guide. In: 15.0 R, editor.November 2013.
[232] Wu W, Shi W, Wang J, Wang B, Li X. Experimental investigation on NH3–H2O compression-assisted absorption heat pump (CAHP) for low temperature heating under lower driving sources. Applied Energy. 2016;176:258-71.
[233] K. C. Fundamentals of test measurement instrumentation. ISA-Instrumentation, Systems, and Automation Society. 2006.

[234] Ronald E. Walpole RHM, Sharon L. Myers, Keying Ye. Probability & Statistics for Engineers & Scientists. eight ed: Pearson Education International 2007.